The Impact of Biodiesel-based Na on the Durability of Cu-Zeolite SCR Catalysts and Other Diesel Aftertreatment Devices

A Dissertation Presented for the
Doctor of Philosophy
Degree
The University of Tennessee, Knoxville

Daniel William Brookshear
May 2013

DEDICATION

I dedicate this work to the family and friends who have supported me in my personal life so that I may succeed in my professional life, especially my loving parents.

ACKNOWLEDGEMENTS

I would like to thank my advisor, Dr. Ke Nguyen, for his support and guidance throughout the duration of this project, and for making this work possible. I would also like to express my gratitude to Dr. Todd Toops for sharing his knowledge and insight into the research area of catalysis, and for ensuring that I had access to the necessary facilities and resources at the Oak Ridge National Laboratory. I also would like to thank my graduate committee members, Dr. Jay Frankel, Dr. Roger Parsons, Dr. David Irick, and Dr. Robert Counce, for their valuable input into the writing of my dissertation. At the National Transportation Research Center I would like to thank Vitaly Prikhodko and Josh Pihl for their guidance during experiments and for their kind words of encouragement. In addition, I want to thank Wil Rohr, my laboratory colleague at the University of Tennessee, for his friendship during this work.

Lastly, I want to express my appreciation to the United States Department of Energy (DOE) for their financial support of this research.

ABSTRACT

Biodiesel fuel has increased in popularity in recent years as an alternative fuel choice, but there are concerns related to the impact it will have on diesel engines and aftertreatment systems relative to conventional diesel fuel. One major concern is the presence of sodium (Na) in finished biodiesel fuel due to the use of Na-hydroxyl as a liquid-phase catalyst during biodiesel synthesis. The current study focuses on determining the impact of biodiesel-based Na on the performance and materials characterization of diesel aftertreatment devices including lean NO_x traps (LNT), diesel oxidation catalysts (DOC), diesel particulate filters (DPF), and Cu-zeolite selective catalytic reduction (SCR) catalysts. Long-term engine aged LNT, DOC, and DPF samples are provided by research partners, while a 517 cc single-cylinder Hatz diesel engine is used to perform accelerated Na-aging of aftertreatment systems consisting of a DOC, SCR, and DPF in either the light-duty (DOC-SCR-DPF) or heavy-duty (DOC-DPF-SCR) configuration.

Bench-flow reactor (BFR) evaluations reveal that the performance of LNT and DOC catalysts is negligibly affected by exposure to Na, but that Cu-zeolite SCR in the light-duty configuration suffers a drastic reduction in nitrogen oxide (NO_x) performance. The performance loss can be avoided by placing the SCR downstream of the DPF in the heavy-duty aftertreatment configuration, but electron microprobe analysis (EPMA) of the DPF from this configuration identifies excessive Na ash buildup and migration of Na into the DPF substrate.

EPMA analysis of the Na-aged SCR determined that the contamination pattern is similar to that observed in the long-term engine-aged DOC and LNT samples, providing credibility to the accelerated Na-aging process. Materials characterization techniques including diffuse-reflective infrared Fourier transform spectroscopy (DRIFTS), scanning electron microscopy (SEM) with energy dispersive spectroscopy (EDS), and BET surface area measurements determined that loss of catalyst surface area and a decrease in the number of active Cu sites for ammonia (NH_3) adsorption and SCR reactions are the most likely cause of the reduced nitrogen oxides (NO_x) performance in the light-duty configuration accelerated Na-aged SCR. Finally, mathematical modeling successfully predicts the performance of fresh SCR catalysts, but is less accurate for catalysts exposed to elevated levels of Na.

TABLE OF CONTENTS

CHAPTER I Introduction and General Information 1
1.1 Diesel Engines 1
1.2 Biodiesel Fuel 3
1.3 Mobile Emissions Regulation 4
1.4 Regulated Emissions 7
1.4.1 Unburned Hydrocarbons and Carbon Monoxide 8
1.4.2 Sulfur Oxides 8
1.4.3 Nitrogen Oxides 8
1.4.4 Particulate Matter 9
1.5 Diesel Aftertreatment Devices 10
1.5.1 Selective Catalytic Reduction of Nitrogen Oxides by Ammonia 10
1.5.2 Lean NO_x Trap 11
1.5.3 Diesel Oxidation Catalyst 12
1.5.4 Diesel Particulate Filter 12
1.6 Scope of Investigation 13
CHAPTER II Literature Review 16
2.1 Biodiesel Combustion 16
2.2 Cu-Zeolite SCR 21
2.2.1 Cu-Zeolite Catalyst Structure and Formulation 21
2.2.2 Reaction Mechanism for NH_3 SCR of NO_x Over Cu-Zeolite 24
2.2.3 Cu-Zeolite SCR Catalyst Performance and Durability 26
2.3 Durability of LNT, DOC, and DPF Aftertreatment Devices 34
CHAPTER III Materials and Methods 39
3.1 Catalysts 39
3.2 Engine Bench for Accelerated Na Engine-Aging 41
3.3 Bench Flow Reactor Overview and Components 45
3.3.1 Bench Flow Reactor Overview 45
3.3.2 Mass Flow Controllers 49
3.3.3 Stainless Steel Tubing and Heating Tapes 49
3.3.4 Steam Generator and Peristaltic Pumps 50
3.3.5 Reactor Setup 50
3.3.6 University of Tennessee Analyzer Bench 51
3.3.7 University of Tennessee Gas Analyzers 52
3.3.8 National Transportation Research Center FTIR Spectrometer 53
3.3.9 Data Acquisition System 53
3.4 Bench Flow Reactor Startup and Performance Evaluations 54
3.4.1 Bench Flow Reactor Startup Procedures 54
3.4.2 De-greening of Fresh Catalysts 55
3.4.3 SCR Performance Evaluations 55
3.4.4 LNT Performance Evaluations 57
3.4.5 DOC Performance Evaluations 57
3.5 Materials Characterization Techniques 58
3.5.1 Electron Probe Microanalysis 58

3.5.2 Inductively Coupled Plasma Spectroscopy 61
3.5.3 Scanning Electron Microscopy and Energy Dispersive Spectroscopy 61
3.5.4 Scanning Transmission Electron Microscopy 63
3.5.5 BET Surface Area Measurements 64
3.5.6 Diffuse-Reflective Infrared Fourier Transform Spectroscopy 66
3.6 Mathematical Modeling of Cu-zeolite SCR 68
3.6.1 Overview of Fortran SCR Model 68
3.6.2 Gas-Phase Energy Balance 72
3.6.3 Gas-Phase Species Balance 73
3.6.4 Solid-Phase Energy Balance 74
3.6.5 Solid-Phase Species Balance 75
3.6.6 Livermore ODE Solver 76
CHAPTER IV Results and Discussion 78
4.1 Fresh and Engine-aged LNT 78
4.1.1 Engine-aging of LNT 79
4.1.2 Performance Evaluations 79
4.1.3 Materials Characterization 83
4.2 Engine-aged and Accelerated Na-aged DPF 89
4.2.1 GM Engine-aging and Accelerated Na-aging of DPFs 89
4.2.2 Materials Characterization 92
4.3 Fresh, Engine-aged, and Accelerated Na-aged DOC 102
4.3.1 Long-term Engine-aging and Accelerated Na-aging of DOCs 102
4.3.2 Performance Evaluations 105
4.3.3 Materials Characterization 110
4.4 Fresh and Accelerated Na-aged Cu-zeolite SCR 118
4.4.1 Accelerated Na-aging of Cu-zeolite SCR 119
4.4.2 SCR Performance Evaluations 122
4.4.3 SCR Materials Characterization 134
4.4.4 Mathematical Modeling of Cu-zeolite SCR 158
CHAPTER V Conclusions and Recommendations 166
LIST OF REFERENCES 173
Vita 181

LIST OF TABLES

Table 1.3.1 EPA Emission Standards for Heavy-Duty Diesel Engines, Model Year 1988-2003, in g/bhp-hr [7]. 5

Table 1.3.2 Tier 2 Emissions Standards for Light-Duty Vehicles [8]. 6

Table 3.1.1 Catalyst Information and Aging Approaches. 40

Table 3.4.1 CLEERS transient SCR protocol for SCR evaluations. 56

Table 3.6.1 Symbol key for energy and species balance equations. 70

Table 3.6.2 Constants of reaction rates employed in SCR model..... 71

Table 4.1.1 ICP Measurements of Na in Fresh and Accelerated Na-aged SCR catalysts..... 147

LIST OF FIGURES

Figure 1.1.1 Total U.S. Greenhouse Gas Emissions by Economic Sector in 2010 [4] 3

Figure 1.5.1 Flow Explanation in a SiC Diesel Particulate Filter [19, p. 213] 13

Figure 2.1.1 PM, DS, and NSF emissions with different biodiesel blends (n=1500 min-1) [41, p. 1483]. 18

Figure 2.1.2 NO_x emissions with different biodiesel blends (n=1500 min-1) [41, p. 1484]. 20

Figure 2.2.1 Structures of (a) small-pore CHA, (b) medium-pore MFI, and (c) large-pore MOR zeolite structures [53, p. 5]. 22

Figure 2.2.2 Selective catalytic reduction of NO by NH_3 over Cu-exchanged Na- and H-form ZSM-5 zeolites [57, p. 66]. 24

Figure 2.2.3 Reduction-oxidation cycle of Cu species during NH_3 SCR of NO over Cu-zeolite [61, p. 327] 26

Figure 2.2.4 NO-only performance of Cu-zeolite SCR with 500 ppm NO, 500 ppm NH_3, 8% O2 and 0-5% H_2O, and N_2 balance [55, p. 185]. 27

Figure 2.2.5 Effect of varying the NO_2/NO_x ratio over Cu-zeolite with 500 ppm NO_x, 500 ppm NH_3, 2% O_2, 3% H_2O, and N_2 balance [64, p. 228] 28

Figure 2.2.6 Standard SCR NO_x performance after hydrothermal aging at 950ºC [65, p. 483]. 29

Figure 2.2.7 Impact of Na contamination on (a) standard and (b) fast SCR performance over Cu-zeolite [16, p. 11]. 33

Figure 2.3.1 Impact of Na contamination on T-50 light-off temperature for (a) CO and (b) HC performance in DOCs [16, p. 6]. 37

Figure 3.2.1 Single-cylinder Hatz diesel engine for accelerated Na-aging [1, p. 44]. 42

Figure 3.2.2 Schematic of engine bench for accelerated Na-aging 43

Figure 3.3.1 Schematic of bench flow reactor at the University of Tennessee ... 46

Figure 3.3.2 Thermocouple locations in evaluation cores [1, p. 28]. 48

Figure 3.5.1 Cameca SC-52 EPMA device [17, p. 58]. 59

Figure 3.5.2 TEM used for fresh and engine-aged LNT analysis.. 63

Figure 3.5.3 DRIFTS setup for SCR surface analysis [84, p. 247]. 66

Figure 4.1.1 NO_x concentration in fresh LNT during last five evaluation cycles at 300ºC. 80

Figure 4.1.2 NO_x conversion over fresh and engine-aged LNTs. 81

Figure 4.1.3 Impact of soot oxidation and desulfation treatments on performance of engine-aged LNT catalysts. 82

Figure 4.1.4 TEM images of Pt particles in (a) fresh and (b) engine-aged LNT catalysts. 83

Figure 4.1.5 ImageJ analysis of particle size distribution in fresh and engine-aged LNT samples. 84

Figure 4.1.6 EPMA micrographs of (a) Na, (b) S, and (c) P contamination in engine-aged LNT. (d) Backscatter images shown for clarity. 86

Figure 4.1.7 EPMA Line Scans of Na, S, and P contamination at inlet of engine-aged LNT. 87

Figure 4.1.8 EPMA Line Scans of Na, S, and P contamination at middle of engine-aged LNT. 87

Figure 4.1.9 EPMA Line Scans of Na, S, and P contamination at exit of engine-aged LNT. 88

Figure 4.2.1 DPF temperature during accelerated Na-aging protocols for light-duty arrangement. 90

Figure 4.2.2 DPF temperature during accelerated Na-aging protocols for control arrangement. 91

Figure 4.2.3 DPF temperature during accelerated Na-aging protocols for heavy-duty arrangement. 91

Figure 4.2.4 Average inlet temperature, average exit temperature, and maximum temperature in DPFs during accelerated Na-aging. 92

Figure 4.2.5 EPMA micrographs of (a) Na, (b) P, and (c) Ca contamination in GM provided long-term engine-aged SiC-based DPF. (d) Backscatter images shown for clarity. 93

Figure 4.2.6 EPMA line scan of ash plug in GM provided long-term engine-aged DPF. 94

Figure 4.2.7 EPMA micrographs of (a) Na, (b) P, and (c) S contamination in light-duty configuration accelerated Na-aged DPF. (d) Backscatter images shown for clarity. 96

Figure 4.2.8 EPMA micrographs of (a) Na, (b) P, and (c) S contamination in heavy-duty configuration accelerated Na-aged DPF. (d) Backscatter images shown for clarity. 97

Figure 4.2.9 EPMA micrographs of (a) Na, (b) P, and (c) S contamination in control DPF. (d) Backscatter images shown for clarity (white circles seen in BSE images represent fibers used to mark the channels). 98

Figure 4.2.10 EPMA line scans of light-duty accelerated Na-aged DPF at (a) middle and (b) rear. 100

Figure 4.2.11 EPMA line scans of heavy-duty accelerated Na-aged DPF at (a) middle and (b) rear. 101

Figure 4.3.1 DOC temperature during accelerated Na-aging protocols for light-duty arrangement. 103

Figure 4.3.2 DOC temperature during accelerated Na-aging protocols for control arrangement. 103

Figure 4.3.3 DOC temperature during accelerated Na-aging protocols for heavy-duty arrangement. 104

Figure 4.3.4 Average inlet temperature, average exit temperature, and maximum temperature in DOCs during accelerated Na-aging. 105

Figure 4.3.5 DOC catalyst temperature profiles during aging in the temperature range from 100 to 400°C. 106

Figure 4.3.6 Ethylene oxidation in fresh, long-term engine-aged, light-duty accelerated Na-aged, and control DOCs. 107

Figure 4.3.7 CO oxidation in fresh, long-term engine-aged, light-duty accelerated Na-aged, and control DOCs. 108

Figure 4.3.8 NO oxidation in fresh, long-term engine-aged, light-duty accelerated Na-aged, and control DOCs. 109

Figure 4.3.9 EPMA micrographs of (a) Na, (b) S, and (c) P contamination in long-term engine-aged DOC. (d) Backscatter images shown for clarity. 112

Figure 4.3.10 EPMA micrographs of (a) Na, (b) S, and (c) P contamination in light-duty configuration accelerated Na-aged DOC. (d) Backscatter images shown for clarity. 113

Figure 4.3.11 EPMA line scans of Na, S, and P contamination at inlet of long-term engine-aged DOC. 114

Figure 4.3.12 EPMA line scans of Na, S, and P contamination at middle of long-term engine-aged DOC. 114

Figure 4.3.13 EPMA line scans of Na, S, and P contamination at exit of long-term engine-aged DOC. 115

Figure 4.3.14 EPMA line scans of Na, S, and P contamination at inlet of light-duty accelerated Na-aged DOC. 116

Figure 4.3.15 EPMA line scans of Na, S, and P contamination at middle of light-duty accelerated Na-aged DOC. 116

Figure 4.3.16 EPMA line scans of Na, S, and P contamination at exit of light-duty accelerated Na-aged DOC. 117

Figure 4.4.1 SCR temperature during accelerated Na-aging protocols for light-duty arrangement. 120

Figure 4.4.2 SCR temperature during accelerated Na-aging protocols for control arrangement. 120

Figure 4.4.3 SCR temperature during accelerated Na-aging protocols for heavy-duty arrangement. 121

Figure 4.4.4 Average inlet temperature, average exit temperature, and maximum temperature in DPFs during accelerated Na-aging. 122

Figure 4.4.5 SCR catalyst temperature profiles during aging in the temperature range from 150 to 650°C. 123

Figure 4.4.6 Standard SCR NO_x performance in fresh and accelerated Na-aged SCR catalysts. 124

Figure 4.4.7 Impact of varying the NH_3/NO_x ratio on the standard SCR NO_x performance of fresh and accelerated Na-aged Cu-zeolite SCR catalysts. 127

Figure 4.4.8 Standard SCR NO performance in fresh and accelerated Na-aged SCR catalysts. 128

Figure 4.4.9 NO to NO_2 oxidation in fresh and accelerated Na-aged SCR catalysts. 129

Figure 4.4.10 NH_3 storage capacity in fresh and accelerated Na-aged SCR catalysts. 130

Figure 4.4.11 NH_3 oxidation in fresh and accelerated Na-aged SCR catalysts. 133

Figure 4.4.12 EPMA micrographs of Na, S, and P presence in fresh SCR catalyst. (d) Backscatter images shown for clarity. 135

Figure 4.4.13 EPMA line scan of Na in fresh SCR catalyst. 135

Figure 4.4.14 EPMA micrographs of (a) Na, (b) S, and (c) P contamination in light-duty configuration accelerated Na-aged SCR. (d) Backscatter images shown for clarity. 137

Figure 4.4.15 EPMA micrographs of (a) Na, (b) S, and (c) P contamination in heavy-duty configuration accelerated Na-aged SCR. (d) Backscatter images shown for clarity. 138

Figure 4.4.16 EPMA micrographs of (a) Na, (b) S, and (c) P contamination in control SCR. (d) Backscatter images shown for clarity (rear of control SCR unavailable for analysis). 139

Figure 4.4.17 EPMA line scans of Na, S, and P contamination at inlet of light-duty configuration accelerated Na-aged SCR. 141

Figure 4.4.18 EPMA line scans of Na, S, and P contamination at middle of light-duty configuration accelerated Na-aged SCR. 141

Figure 4.4.19 EPMA line scans of Na, S, and P contamination at exit of light-duty configuration accelerated Na-aged SCR. 142

Figure 4.4.20 EPMA line scans of Na, S, and P contamination at inlet of heavy-duty configuration accelerated Na-aged SCR. 143

Figure 4.4.21 EPMA line scans of Na, S, and P contamination at middle of heavy-duty configuration accelerated Na-aged SCR. 143

Figure 4.4.22 EPMA line scans of Na, S, and P contamination at exit of heavy-duty configuration accelerated Na-aged SCR. 144

Figure 4.4.23 EPMA line scans of Na, S, and P contamination at inlet of control SCR..... 145

Figure 4.4.24 EPMA line scans of Na, S, and P contamination at inlet of control SCR..... 145

Figure 4.4.25 Na line scans at inlet of SCR samples. 146

Figure 4.4.26 BET surface area measurements of fresh and accelerated Na-aged SCR catalysts..... 149

Figure 4.4.27 DRIFTS absorbance spectra for fresh and accelerated Na-aged SCRs during NO exposure for dry and wet conditions 151

Figure 4.4.28 DRIFTS absorbance spectra for fresh and accelerated Na-aged SCRs during NO_2 exposure for dry and wet conditions..... 152

Figure 4.4.29 EPMA backscatter image and Na micrograph for NREL Na-aged Cu-chabazite SCR sample. 153

Figure 4.4.30 Cu content in fresh, NREL ULSD-aged, and NREL Na-aged Cu-chabazite SCR catalysts..... 154

Figure 4.4.31 CuO particles on the surface of the washcoat in the NREL Na-aged Cu-chabazite SCR catalyst. 155

Figure 4.4.32 CuO particles on the surface of the washcoat in the light-duty configuration accelerated Na-aged SCR catalyst. 157

Figure 4.4.33 EDS measurement of washcoat surface in light-duty accelerated Na-aged SCR where CuO particles are present..... 157

Figure 4.4.34 Fortran model simulations of NH3 oxidation in fresh Cu-zeolite SCR. 159

Figure 4.4.35 Fortran model simulations of NO to NO_2 oxidation in fresh Cu-zeolite SCR. 159

Figure 4.4.36 Fortran model simulations of standard SCR performance in fresh Cu-zeolite SCR. 161

Figure 4.4.37 Fortran model simulations of fast SCR performance in fresh Cu-zeolite SCR. 161

Figure 4.4.38 Fortran model simulations of NH_3 oxidation in fresh and light-duty configuration accelerated Na-aged Cu-zeolite SCR catalysts. 163

Figure 4.4.39 Fortran model simulations of NO oxidation in fresh and light-duty configuration accelerated Na-aged Cu-zeolite SCR catalysts. 163

Figure 4.4.40 Fortran model simulations of standard SCR in fresh and light-duty configuration accelerated Na-aged Cu-zeolite SCR catalysts. 165

Figure 4.4.41 Fortran model simulations of fast SCR in fresh and light-duty configuration accelerated Na-aged Cu-zeolite SCR catalysts..... 165

CHAPTER I

INTRODUCTION AND GENERAL INFORMATION

1.1 Diesel Engines

Developed by Rudolf Diesel in 1893, the diesel engine has played an important role in power production for over a century. Its popularity, particularly in the last forty years, is a result of both its large power output and its inherently high efficiency. Unlike gasoline engines, diesel engines do not require spark ignition, instead relying on high compression ratios to initiate the combustion of the fuel. Diesel engines operate with lean air/fuel ratios and are un-throttled, which means that a higher percentage of fuel is consumed during the power stroke, thus producing a higher work output [1]. Additionally, the efficiency of diesel engines is currently around 45%, which is a vast improvement over the 30% efficiency seen in typical spark-ignition engines, and with future advances in technology it is believed that diesel engines could reach efficiencies as high as 63% [2].

While the economic advantages of high-power, fuel efficient engines are obvious, another primary motivator in the push to use diesel engines is the ability to reduce the negative environmental impact of burning fossil fuels for transportation purposes. According to an assessment published in April 2012 by the Environmental Protection Agency (EPA), greenhouse gas emissions in the United States have increased by 10.5% since 1990, and U.S. emissions in general rose by 3.2% between 2009 and 2010. Furthermore, the average

temperature of the Earth has risen 1.4°F in the past century, and projections estimate that the next one hundred years will see another increase of anywhere between 2 and 11.5°F. With transportation accounting for 27% of the United States' total greenhouse gas emissions in 2010, as shown in Figure 1.1.1, the pressure to reduce fossil fuel consumption and slow climate change is clear [3]. Diesel engines can help reach these goals due to lower fuel consumption enabled by higher efficiencies. However, there are still issues that must be addressed as the prevalence of diesel engines increases. Lean-burn engine operation results in an excess of nitrogen oxide (NO_x) formation, along with excessive particulate matter (PM) exiting the tailpipe. NO_x is a known contributor to acid rain and smog, and PM has been linked to excess deaths and health problems. Thus, in order to reap the benefits provided by diesel engines, diesel aftertreatment technology must meet the demands of stringent emissions regulations.

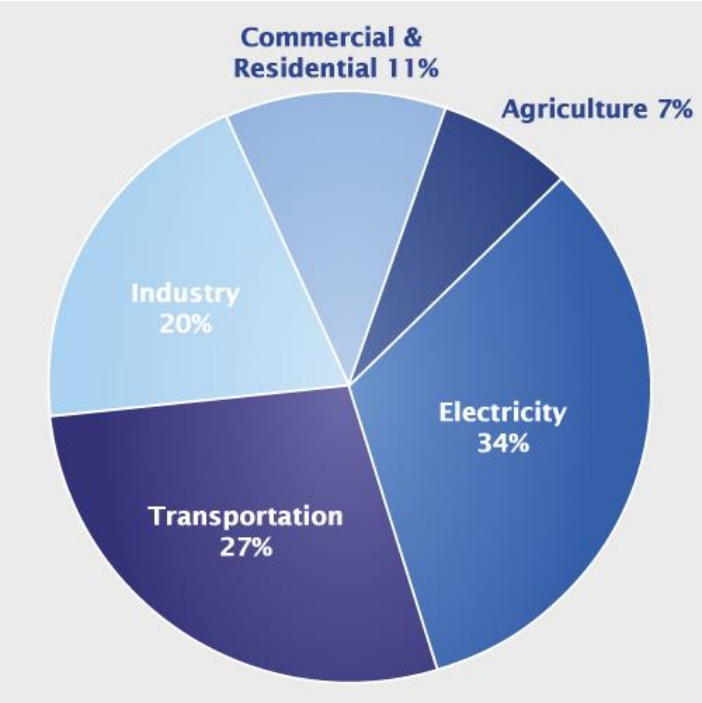

Figure 1.1.1 Total U.S. Greenhouse Gas Emissions by Economic Sector in 2010 [4]**.**

1.2 Biodiesel Fuel

Biodiesel has emerged as a popular renewable fuel choice in recent years due to its similarities with conventional diesel fuel and its potential to reduce dependence on imported oil in the United States. It can be derived from an array of sustainable sources, and it possesses a higher energy density than many alternative fuel options such as ethanol. However, as with other alternative fuels, the primary barrier with regards to the widespread introduction of biodiesel is concern over what effects biodiesel use will have on the performance and durability of diesel engines and emissions aftertreatment devices. One particular concern is the presence of trace amounts of sodium and/or potassium in finished

biodiesel fuel product due to the use of either NaOH or KOH as a liquid phase catalyst in biodiesel synthesis and the difficulty of removing these alkalis from the finished fuel product. Current ASTM standards require that less than a combined total of 5 ppm Na + K appear in pure biodiesel fuel [5], but even at such low concentrations there are still concerns that these organics will have a significant impact on emissions control systems

1.3 Mobile Emissions Regulation

The history of emissions regulation with regards to mobile sources began when congress passed the first major Clean Air Act (CAA) in 1970, which originally mandated a 90% reduction in harmful emissions from new vehicles by 1975. Early technologies in emissions control developed throughout the 1970's, including the invention of exhaust gas recirculation (EGR) valves to reduce NO_x emissions in 1972, and the first generation of catalytic converters in 1975 which necessitated the introduction of unleaded gasoline due to the deactivating effect of lead on the catalyst. However, despite these technological innovations in emissions control, it was not until 1981 that new cars were able to meet an amended version of the original CAA. The first Inspection and Maintenance (I/M) programs followed in 1983 in areas with high air pollution, and by the end of the 1980's the emissions regulations shown in Table 1.3.1 were defined for heavy-duty diesel engines in trucks and buses for model years 1988-2003 [6].

Table 1.3.1 EPA Emission Standards for Heavy-Duty Diesel Engines, Model Year 1988-2003, in g/bhp-hr [7]**.**

Year	HC	CO	NO_x	PM
Heavy-Duty Diesel Truck Engines				
1988	1.3	15.5	10.7	0.60
1990	1.3	15.5	6.0	0.60
1991	1.3	15.5	5.0	0.25
1994	1.3	15.5	5.0	0.10
1998	1.3	15.5	4.0	0.10
Urban Bus Engines				
1991	1.3	15.5	5.0	0.25
1993	1.3	15.5	5.0	0.10
1994	1.3	15.5	5.0	0.07
1996	1.3	15.5	5.0	0.05*
1998	1.3	15.5	4.0	0.05*
* – in-use PM standard 0.07				

In 1990 the CAA was amended to introduce emissions regulations for all mobile pollution sources, including light-duty vehicles such as passenger cars, light-duty trucks, minivans, and sport utility vehicles. Emissions standards for light-duty vehicles were divided into two sets of standards: Tier 1 and Tier 2. The Tier 1 standards were finalized on June, 5, 1991 and phased in progressively from 1994 until 1997 before being superseded by the National Low Emission Vehicle (NLEV) standards in 2001 nationwide. In turn, the NLEV was made obsolete by the Tier 2 standards, which were approved in 1999 and phased in between 2004 and 2009. These standards are shown in Table 1.3.2.

Table 1.3.2 Tier 2 Emissions Standards for Light-Duty Vehicles [8]**.**

Bin#	Intermediate life (5 years / 50,000 mi)					Full useful life				
	NMOG*	CO	NOx	PM	HCHO	NMOG*	CO	NOx†	PM	HCHO
Temporary Bins										
11 MDPV[c]						0.280	7.3	0.9	0.12	0.032
10[a,b,d,f]	0.125 (0.160)	3.4 (4.4)	0.4	–	0.015 (0.018)	0.156 (0.230)	4.2 (6.4)	0.6	0.08	0.018 (0.027)
9[a,b,e,f]	0.075 (0.140)	3.4	0.2	–	0.015	0.090 (0.180)	4.2	0.3	0.06	0.018
Permanent Bins										
8[b]	0.100 (0.125)	3.4	0.14	–	0.015	0.125 (0.156)	4.2	0.20	0.02	0.018
7	0.075	3.4	0.11	–	0.015	0.090	4.2	0.15	0.02	0.018
6	0.075	3.4	0.08	–	0.015	0.090	4.2	0.10	0.01	0.018
5	0.075	3.4	0.05	–	0.015	0.090	4.2	0.07	0.01	0.018
4	–	–	–	–	–	0.070	2.1	0.04	0.01	0.011
3	–	–	–	–	–	0.055	2.1	0.03	0.01	0.011
2	–	–	–	–	–	0.010	2.1	0.02	0.01	0.004
1	–	–	–	–	–	0.000	0.0	0.00	0.00	0.000

* for diesel fueled vehicle, NMOG (non-methane organic gases) means NMHC (non-methane hydrocarbons)
† average manufacturer fleet NOx standard is 0.07 g/mi for Tier 2 vehicles

a – Bin deleted at end of 2006 model year (2008 for HLDTs)
b – The higher temporary NMOG, CO and HCHO values apply only to HLDTs and MDPVs and expire after 2008
c – An additional temporary bin restricted to MDPVs, expires after model year 2008
d – Optional temporary NMOG standard of 0.195 g/mi (50,000) and 0.280 g/mi (full useful life) applies for qualifying LDT4s and MDPVs only
e – Optional temporary NMOG standard of 0.100 g/mi (50,000) and 0.130 g/mi (full useful life) applies for qualifying LDT2s only
f – 50,000 mile standard optional for diesels certified to bins 9 or 10

Heavy-duty diesel engines were also subjected to an increase in the strictness of emissions regulations in 2004 due to standards published by the EPA in October of 1997. The defined useful life of heavy-duty diesel engines was increased for model year 2004, and new combined limit of 2.4 g/bhp-hr for NO_x plus non-methane hydrocarbons (NMHC) went into effect. Standards again changed for model year 2007 based on a 2001 EPA decision, and currently the EPA requires the following limits on harmful emissions from heavy-duty diesel engines: 0.01 g/hbp-hr PM, 0.20 g/bhp-hr NO_x, and 0.14 g/bhp-hr NHMC. These standards must be maintained for the useful life of the vehicle as defined by the EPA in 2004, which is 110,000 miles or 10 years for light heavy-duty diesel engines (LHDDE), 185,000 miles or 10 years for medium heavy-duty diesel engines (MHDDE), and 435,000 miles or 10 years/22,000 hours for heavy heavy-duty diesel engines (HHDDE) [7-8].

1.4 Regulated Emissions

Several byproducts of diesel combustion are harmful to both human health and the environment, and for this reason the Environmental Protection Agency (EPA) regulates the amount of dangerous substances exiting the tailpipe of diesel vehicles. Emissions regulated by the EPA include unburned hydrocarbons (HC), carbon monoxide (CO), sulfur oxides (SO_x), particulate matter (PM), and nitrogen oxides (NO_x).

1.4.1 Unburned Hydrocarbons and Carbon Monoxide

Both unburned HC and CO are results of incomplete combustion. While the lean operating condition of diesel engines typically minimizes these emissions relative to standard spark-ignition engines, some fuel is still trapped in crevices around the cylinder or near the wall where combustion is incomplete [9]. The effects of HC vary depending on which specific HC escape the tail pipe, but an increased risk of cancer is one known health concern [10]. Meanwhile, CO can cause chest pain in those with heart disease, and is known to cause vision problems or even death due to long exposure. It is also a contributor to the formation of smog [11].

1.4.2 Sulfur Oxides

The formation of SO_x, of which sulfur dioxide (SO_2) is the most prevalent, occurs when the sulfur present in diesel fuel experiences oxidation due to the high temperature of combustion. In the environment SO_2 leads to the formation of acid rain and contributes to reduced visibility from air pollution in many portions of the U.S. The health effects of SO_x are due to the formation of sulfates when SO_2 particles react with chemicals in the air to form sulfates which can be inhaled and increase the susceptibility of the lung to respiratory diseases [12].

1.4.3 Nitrogen Oxides

NO_x emissions from diesel engines, consisting primarily of nitric oxide (NO), nitrogen dioxide (NO_2), and nitrous oxide (N_2O), pose a difficult problem for automobile manufacturers. These compounds are formed when nitrogen is

oxidized at high temperatures during combustion, and for diesel vehicles these emissions are inherently high due to the extra availability of oxygen created by the lean operating conditions of a diesel engine. The environmental impacts of NO_x include global warming, acid rain, and increased nitrogen content in water bodies which upsets the natural chemical balance of aquatic ecosystems. NO_x in the air also leads to the formation of ozone gas, which can agitate respiratory problems such as lung disease and asthma in the young and elderly [13].

1.4.4 Particulate Matter

Diesel particulate matter is a mixture of different components including soot, ash, metallic, silicates, and other miscellaneous materials which escape the tailpipe during diesel vehicle operation. These particles are typically separated into two different classifications depending on size: inhalable coarse particles which range in size from 2.5 to 10 micrometers, and fine particles which are smaller in diameter than 2.5 micrometers. Possible health effects of particulate matter inhalation include decreased lung function, increased respiratory symptoms, and heart-related issues such as irregular heartbeat or nonfatal heart attacks. In the environment PM has been linked to reduced visibility along with particle contamination of water bodies and soil [14].

1.5 Diesel Aftertreatment Devices

In order to handle the various pollutants released during diesel combustion, a number of aftertreatment devices are employed in typical diesel exhaust configurations. These devices include the selective catalytic reduction catalyst (SCR), lean NO_x trap (LNT), diesel oxidation catalyst (DOC), and diesel particulate filter (DPF).

1.5.1 Selective Catalytic Reduction of Nitrogen Oxides by Ammonia

Numerous formulations have been investigated over the past two decades for the SCR of NO_x by NH_3 including noble metals, metal oxides, and zeolite based catalysts. Noble metal catalysts operate well at low temperatures but show poor selectivity at higher temperatures. Metal oxide catalysts operate well in the temperature range from 350 to 450°C, but outside of this temperature range their performance lessens. In mobile emissions control, where operation occurs over a wide range of temperatures, the use of zeolite-based catalysts which have been ion exchanged with iron (Fe) or copper (Cu) has become the norm [1]. The focus of the current study is on Cu-zeolite SCR catalysts, which usually consist of a honeycomb cordierite substrate covered with a Cu-zeolite washcoat.

NO_x reduction by NH_3 typically takes place according to one of three reactions, depending on the availability of NO and NO_2 in the exhaust feed.

These chemical reactions [15, p. 84] are shown in Eqs. 1.5.1 to 1.5.3, and are known as the standard, fast, and slow SCR reactions, respectively.

$$4NO + 4NH_3 + O_2 \rightarrow 4N_2 + 6H_2O \tag{1.5.1}$$

$$2NO_2 + 4NH_3 + O_2 \rightarrow 3N_2 + 6H_2O \tag{1.5.2}$$

$$NO + NO_2 + 2NH_3 \rightarrow 2N_2 + 3H_2O \tag{1.5.3}$$

Aside from the SCR reactions, there are numerous other reactions taking place over SCR catalysts. NO to NO_2 oxidation occurs, along with the direct oxidation of NH_3 as shown in Eqs. 1.5.4 to 1.5.6 [16, p. 4].

$$4NH_3 + 3O_2 \rightarrow 2N_2 + 6H_2O \tag{1.5.4}$$

$$4NH_3 + 5O_2 \rightarrow 4NO + 6H_2O \tag{1.5.5}$$

$$4NH_3 + 7O_2 \rightarrow 4NO_2 + 6H_2O \tag{1.5.6}$$

All three of the NH_3 oxidation reactions are undesirable, as Eq. 1.5.4 results in reduced NH_3 availability for the SCR reactions while Eqs. 1.5.5 and 1.5.6 lead to NO_x remake. NO to NO_2 oxidation can improve SCR performance as long as the ratio of NO_2 to NO remains below a value of one to avoid the slow SCR reaction from occurring.

1.5.2 Lean NO_x Trap

The LNT is an alternative to SCR for NO_x emissions control and functions as an adsorber catalyst. Most LNTs consist of a honeycomb cordierite substrate dipped in a washcoat containing a platinum group metal (PGM) and a storage material such as Ba, Na, or K. LNT operation is carried out during cyclic operation with alternative lean and rich exhaust phases. During the lean exhaust

phase NO is oxidized to NO_2 over a platinum group metal (PGM) and is stored in the NO_x storage media until the trapping capacity of the storage material is reached. A rich exhaust phase is then initiated and adsorbed NO_x is released to react with reductants such as HC, H_2, and CO. This lean/rich cycling continuously repeats as needed for NO_x abatement [17].

1.5.3 Diesel Oxidation Catalyst

The primary function of the DOC is the oxidation of unburned hydrocarbons and carbon monoxide to form water vapor (H_2O) and carbon dioxide (CO_2). The catalyst typically consists of a ceramic honeycomb substrate such as cordierite coated with a Pt and/or Pd containing washcoat to catalyze the oxidation processes. The chemical reactions which take place over the DOC are shown in Eqs. 1.5.7 and 1.5.8.

$$C_nH_{2m} + \left(n + \frac{m}{2}\right) O_2 \rightarrow CO_2 + H_2O \qquad (1.5.7)$$

$$CO + \frac{1}{2} O_2 \rightarrow CO_2 \qquad (1.5.8)$$

Another side reaction which can be of importance for certain SCR catalysts is the oxidation of NO to NO_2 over the DOC, as shown in Eq. 1.5.9 [18].

$$NO + \frac{1}{2} O_2 \rightarrow NO_2 \qquad (1.5.9)$$

1.5.4 Diesel Particulate Filter

The DPF removes dangerous particulates from the exhaust stream before the exhaust exits the tailpipe. A DPF functions by using SiC/cordierite plugs to

alternately block the flow of exhaust through channels and force exhaust gases to flow through the substrate walls, thereby trapping any solid particulates in the inlet channels and allowing the exhaust gas to exit through the adjacent channel. An image of a typical DPF is shown in Figure 1.5.1 for clarity.

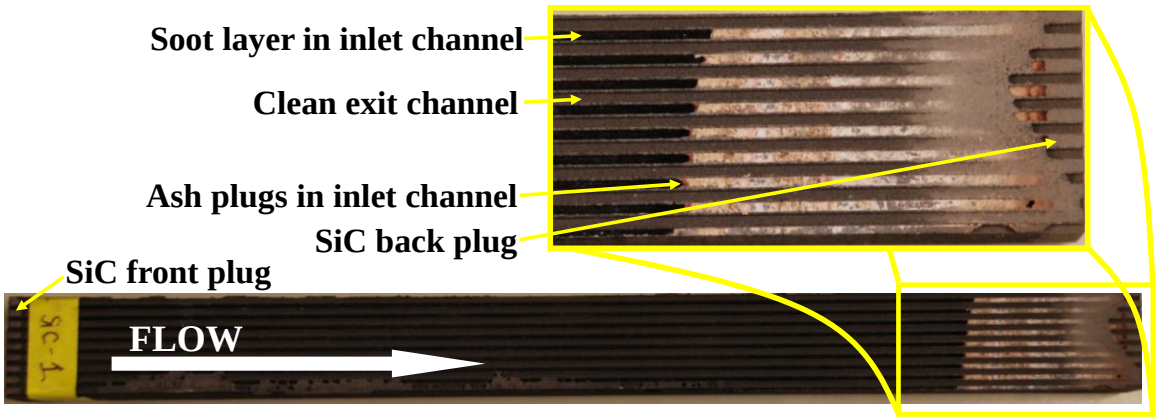

Figure 1.5.1 Flow Explanation in a SiC Diesel Particulate Filter [19, p. 213]**.**

1.6 Scope of Investigation

The current study examines the effects of biodiesel-based Na on the performance and materials characteristics of diesel aftertreatment devices. The primary focus of the project is Cu-zeolite SCR, but attention is also given to DOC, LNT, and DPF performance and/or materials characterization.

An LNT aged long-term on a four cylinder engine was provided by the National Renewable Energy Laboratory (NREL) and the Manufacturers of Emissions Control Association (MECA), while an engine-aged Pt/Al_2O_3-based DOC and SiC-based DPF were supplied by General Motors (GM) for evaluation.

Engine-aged Cu-chabazite SCR catalysts contaminated with Na were obtained through a collaboration between ORNL, MECA, NREL, and Ford. However, the main focus of the study involves the accelerated Na-aging of a beta Cu-zeolite SCR catalyst in an aftertreatment system also consisting of a washcoated Pt/Al_2O_3-based DOC and cordierite DPF, all of which were provided by BASF. The accelerated Na-aging took place on a 517 cm^3 single-cylinder Hatz diesel engine, and was carried out three separate times. Two aging configurations, DOC-SCR-DPF (light-duty) and DOC-DPF-SCR (heavy-duty), utilized B20 fuel doped with dioctylsulfosuccinate to achieve increased levels of Na corresponding to 435,000 miles, while in the third run the samples were aged in the DOC-SCR-DPF configuration with in-spec B20 to provide a control set of samples. Performance evaluations for the DOC, SCR, and LNT samples are carried out on a bench flow reactor (BFR) using protocols put forth by the Cross-Cut Lean Exhaust Emissions Reductions Simulations (CLEERS) research project. Trends observed during fresh Cu-zeolite SCR performance evaluations are compared against a 1-D Fortran-based model built and provided by ORNL.

Aside from performance evaluations, multiple materials characterization techniques are utilized on the catalysts in order to observe the effects of the aging processes and Na contamination on the structure of the aftertreatment devices. All samples are subjected to electron microprobe analysis (EPMA) to provide qualitative and quantitative measurements on the levels of contaminants present after aging. Transmission electron microscopy (TEM) is used to observe the possibility of PGM sintering in the engine-aged LNT, while scanning electron

microscopy is applied to examine Cu-chabazite SCR structure and to perform energy dispersive spectroscopy (EDS) to measure pollutants trapped in the washcoat. Finally, Brunauer, Emmet, and Teller (BET) surface area analysis is performed on fresh and accelerated Na-aged beta Cu-zeolite SCR catalysts to measure any change in surface area brought about by aging, while diffuse-reflective infrared Fourier transform spectroscopy (DRIFTS) is applied to the same samples to study NO_x and nitrate adsorption on the surface of the catalysts.

The objective of this work is to gain an improved understanding of the effect Na in biodiesel fuel will have on the operation of diesel aftertreatment devices, with an emphasis on the impact of Na on SCR chemistry. It is hoped that the accelerated aging approach will provide a valuable tool for the evaluation of new catalyst formulations, and also some insight into whether the current standard of less than 5 ppm Na+K in finished biodiesel fuel is adequate to prevent the deterioration of emissions reduction performance through the aftertreatment system.

CHAPTER II

LITERATURE REVIEW

This chapter contains a review of the literature pertinent to the objectives of the current study. In Section 2.1, the combustion of biodiesel is highlighted regarding the changes in emissions relative to standard ultra-low sulfur diesel. Section 2.2 is reserved for a detailed discussion on pertinent literature related to the Cu-zeolite SCR catalysts which are the primary focus of the current study, while Section 2.3 includes a description of the Fortran model used to predict and study SCR performance. Finally, Section 2.4 contains a brief summary regarding the durability of DOC, LNT, and DPF aftertreatment devices also examined in the project.

2.1 Biodiesel Combustion

As the popularity of biodiesel as an alternative fuel rises, it becomes increasingly important to understand how biodiesel combustion differs from that of conventional ultra-low sulfur diesel (ULSD). While biodiesel shares many similarities with conventional ULSD, there are differences which can be significant in light of the stringent emissions regulations now in place in the United States. A recent literature survey in 2011 by Xue et al. [20] attempts to consolidate and summarize research since 2000 pertaining to these issues

One of the primary concerns regarding biodiesel use is the loss of engine power reported by numerous researchers [21-25]. A study by Carraretto et al. [26] determined that engine power and torque decreased over the entire speed range in a 6-cylinder direct-injection diesel engine as the percentage of biodiesel in the blend increased from 20 to 100%, while Murillo et al. [27] observed a similar trend on a single-cylinder, four-stroke direct injection diesel engine. This loss in power is often attributed to the higher viscosity and lower heating value of most biodiesel blends relative to conventional diesel fuel [25, 28]. Biodiesel operation has also been shown to result in reduced fuel economy relative to standard diesel fuel, which is again typically blamed on the lower heating value of biodiesel which requires excessive fuel consumption in order to compensate for decreased engine power [29-31]. However, despite these changes in engine performance the durability of diesel engines operating on biodiesel fuel seems to be minimally affected [32-33], and many researchers believe that what durability concerns exist (fuel filter plugging, injector coking, etc.) can be overcome with relative ease [34-35].

The combustion of biodiesel in diesel engines also changes the composition of emissions exiting through the exhaust system. Some of these changes are beneficial, while others have the potential to lead to emissions control difficulties. A vast majority of research has found that PM emissions are significantly reduced as the content of biodiesel in fuel is increased, and that this decrease occurs for all different biodiesel fuels regardless of feed stock [36-40]. A study by Wu et al. [41] confirmed this finding by evaluating the emissions

performance of five different biodiesel blends including soybean methyl ester (SME), rapeseed methyl ester (RME), cottonseed methyl ester (CME), palm oil methyl ester (PME), and waste cooking oil methyl ester (WME). They found that PM emissions with biodiesel fuel were reduced by 53-69% on average compared to conventional diesel, as shown in Figure 2.1.1.

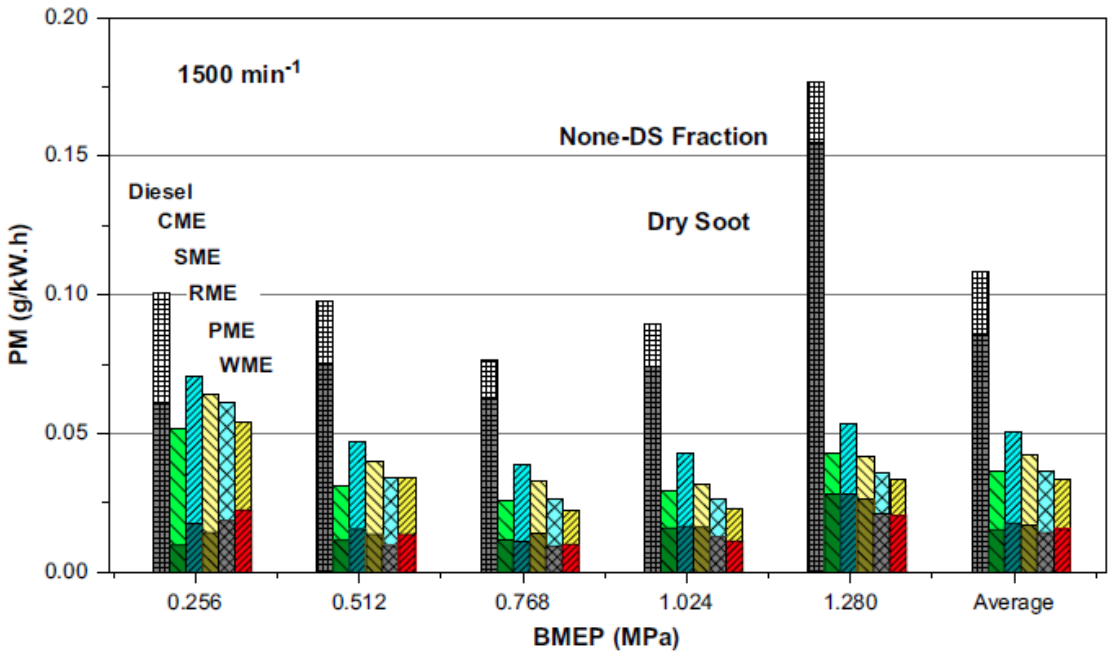

Figure 2.1.1 PM, DS, and NSF emissions with different biodiesel blends (n=1500 min^{-1}) [41, p. 1483]**.**

One of the primary factors believed to contribute to reduced PM emissions is the increased oxygen content of biodiesel fuel [20], which promotes soot oxidation and results in more complete combustion. This theory was investigated by Frijters and Baert [42] who determined that there is a strong correlation between increased fuel oxygen content and reduced PM emissions. Lower amounts of

aromatic and sulfur compounds have also been highlighted as factors which reduce PM emissions when utilizing biodiesel fuel [43-44].

Similar to PM performance during biodiesel combustion, HC and CO emissions have also been found to decrease substantially as biodiesel content in fuel increases [21, 25, 27, 45]. CO emissions were found to decrease anywhere between 50 and 94% relative to standard ULSD [46-47], while HC emissions reductions were slightly lower in an average range of 45 to 67% [41, 45-46]. These trends are again primarily attributed to increased oxygen content resulting in more complete combustion and thus less unburned hydrocarbons and lower CO formation [20, 25, 27]. Additionally, Graboski et al. [48] performed a study which found that the longer chain length and saturation level of many biodiesel blends also contributed to decreased HC emissions. Overall, biodiesel seems to benefit from increased oxygen content relative to ULSD which leads to significant reductions in PM, CO, and HC emissions during combustion.

Although biodiesel combustion has been shown to be beneficial for PM, CO, and HC emissions, the majority of scientists have found that the opposite is true in the case of NO_x emissions [20-21, 23, 49]. Wu et al. [41] found that this increase in NO_x was common amongst biodiesel blends from multiple feedstock sources, as shown in Figure 2.1.2.

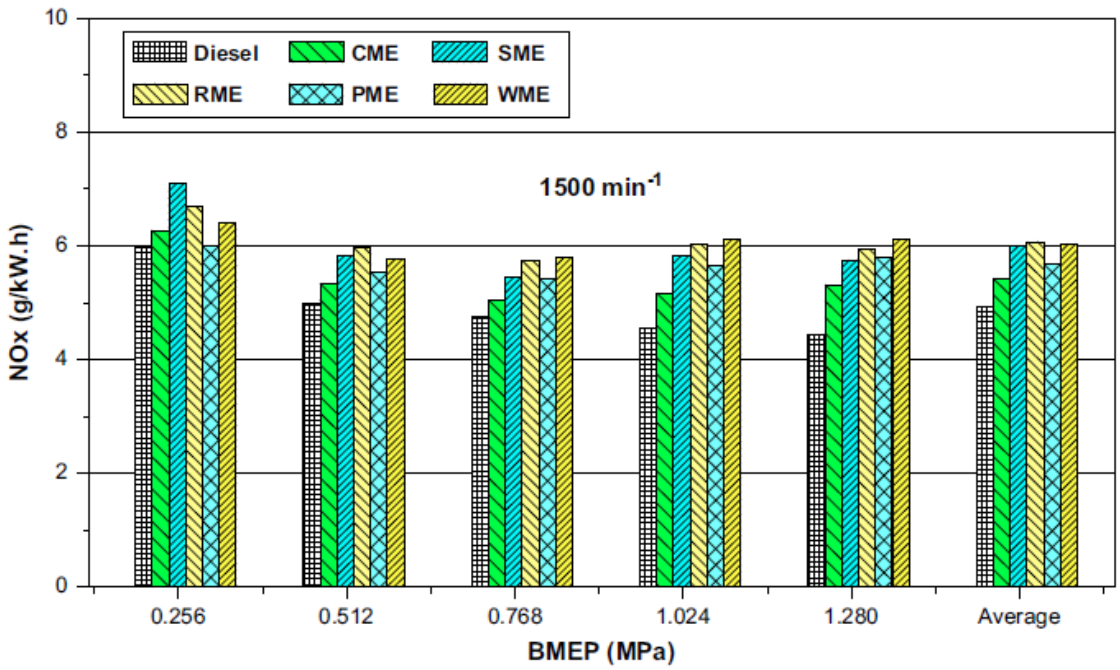

Figure 2.1.2 NO_x emissions with different biodiesel blends (n=1500 min^{-1}) [41, p. 1484]**.**

Ozsezen [45] obtained similar results, with NO_x emissions increasing anywhere between 6 and 22%. In the research, two factors have emerged as the primary contributors to this trend. First, the increased oxygen content which is beneficial for PM, CO, and HC emissions has been shown by Labeckas and Slavinskas [50] to result in increased NO_x emissions. Second, an advance in injection timing due to the increased bulk modulus of most biodiesel fuels has been studied by Tat et al. [51] and Szybist et al. [52], both of whom agreed that there is a definitive correlation between this phenomenon and increased NO_x emissions. While the increase in NO_x emissions is relatively small on average, the impact on the performance of an LNT or SCR system could be significant due to the

difficulty in treating NO_x emissions in a diesel exhaust aftertreatment system under strict emissions regulations.

2.2 Cu-Zeolite SCR

Section 2.2 highlights literature related to Cu-zeolite SCR, with an emphasis on beta model Cu-zeolite and other similar Cu-based zeolites. The structure and formulation of Cu-zeolite SCR is described in Section 2.2.1, while ammonia SCR chemistry is investigated in Section 2.2.2. Finally, the durability and failure mechanisms typical of Cu-zeolite SCR catalysts are detailed in Section 2.2.3.

2.2.1 Cu-Zeolite Catalyst Structure and Formulation

A commonly used configuration for Cu-zeolite SCR catalysts, and catalytic combustion reactors in general, is that of the monolith or honeycomb reactor consisting of a ceramic substrate with a zeolite washcoat. This structure consists of a honeycomb substrate containing a number of parallel flow channels which have been coated with the desired catalyst [15]. There are numerous advantages to this design, including high surface-to-volume ratios, low pressure drops, and flow uniformity due to the honeycomb matrix distribution. Cordierite, a high-temperature-resistant ceramic material composed primarily of alumina (Al_2O_3), kaolin ($Al_2O_3 \cdot 2SiO_2 \cdot 2H_2O$) and talc ($3MgOAl_2O_3 \cdot 4SiO_2 \cdot H_2O$), is chosen for the monolith substrate in typical zeolite SCR catalysts. It exhibits high temperature stability, good porosity, strong oxidation resistance, and a low coefficient of

thermal expansion, all of which are beneficial properties for a catalytic combustion reactor.

The zeolite material itself is a microporous, crystalline aluminosilicate with a crystalline structure similar to one of the examples for small-, medium-, and large-pore zeolites shown in Figure 2.2.1.

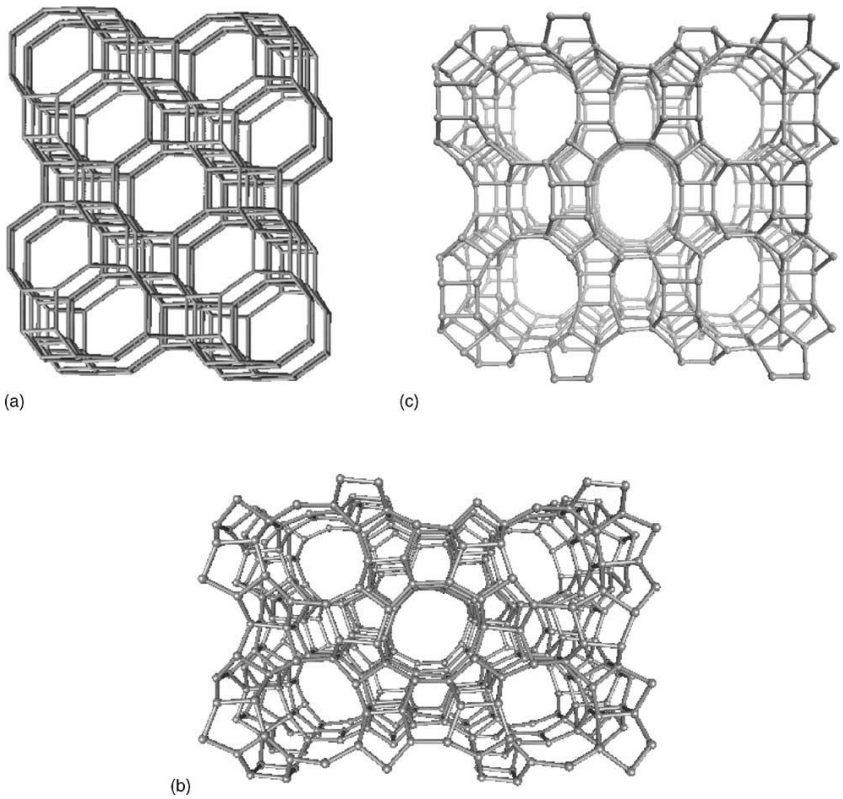

Figure 2.2.1 Structures of (a) small-pore CHA, (b) medium-pore MFI, and (c) large-pore MOR zeolite structures [53, p. 5]**.**

Zeolites can be described by the generalized chemical formula $M_{2/n}O \cdot Al_2O_3 \cdot ySiO_2$, where n is the valence of the cation M and y may vary from 2 to infinity as required [54]. With regards to ammonia SCR, the two key properties

of these materials are the high surface areas achieved by the molecular-sized pores in the crystalline structure, and the high acidity they exhibit relative to amorphous aluminosilicates. High surface areas provide a large number of active sites for the SCR reactions to occur, while increased acidity results in an increased number of the Brønsted acid sites important for NH_3 adsorption. Acidity is inversely proportional to the Si/Al ratio of the zeolite, which makes this an important factor in determining the catalytic properties of the zeolite [55].

Zeolites are not exceptionally active for the ammonia SCR of NO_x by themselves [56], necessitating the addition of an active cation such as Cu via an ion-exchange process. The aqueous ion-exchange process is commonly used for the synthesis of Cu-zeolite for SCR due to its practicality for large scale production [57]. In this method the NH_4-, Na-, or H-form of the zeolite is impregnated onto the monolith structure, which is then placed into a Cu-containing solution such as $Cu(CH_3COO)_2$ for up to 24 hours. The catalysts are then removed for filtering, washing, and drying before being calcined at a high temperature. The degree of ion-exchange plays a large role in determining the effectiveness of the catalyst, and reaching an exchange ratio of 100% is rarely possible. Additionally, the study by Sultana et al. [57] found that the base form of the zeolite utilized for Cu ion exchange played a role in SCR performance for the ZSM-5 zeolite they were investigating. They determined that Cu-exchanged Na-ZSM5 is significantly more active than its HZSM-5 counterpart, as shown in Figure 2.2.2.

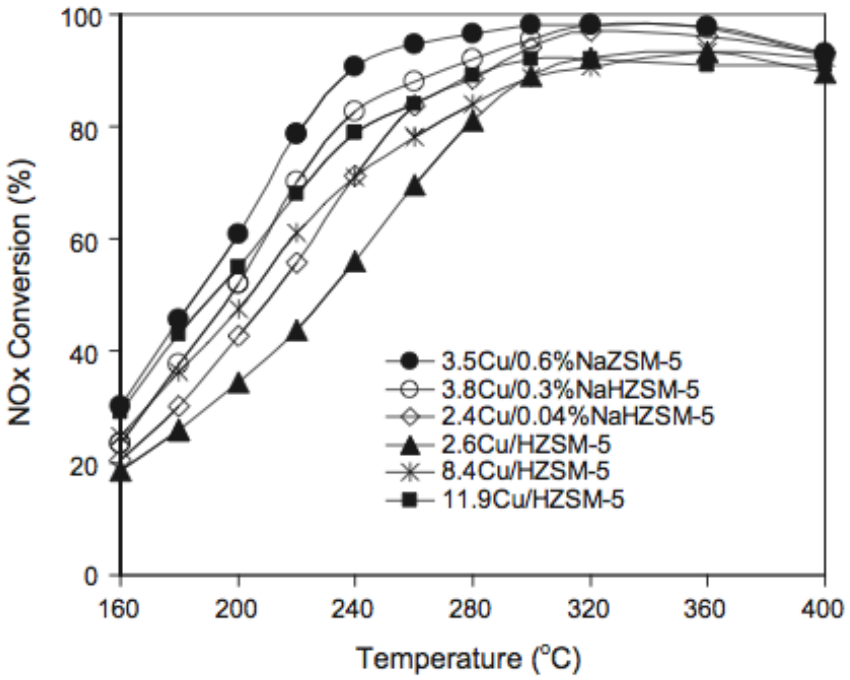

Figure 2.2.2 Selective catalytic reduction of NO by NH_3 over Cu-exchanged Na- and H-form ZSM-5 zeolites [57, p. 66]**.**

This effect was particularly notable in the desirable low-temperature range from 160 to 320°C. They attribute this high performance to the ease of reduction of Cu exchanged into the Na-based zeolite, an increase in the number of Lewis and Brønsted acid sites available when Cu was exchanged into NaZSM-5 relative to HZSM-5, and improved NO to NO_2 oxidation.

2.2.2 Reaction Mechanism for NH_3 SCR of NO_x Over Cu-Zeolite

The NH_3 SCR reaction mechanism is complex, involving both surface and gas-phase species. Many researchers believe that NH_3 SCR over Cu-zeolite follows the Eley-Rideal mechanism, where NH_3 adsorbs to the surface on Lewis and Brønsted acid sites before reacting directly with gas-phase NO_x to produce

N_2 and H_2O [58]. However, recent studies by Sjovall et al. [59] and Wilken et al. [60] have placed an emphasis on Cu sites in the zeolite as the active sties for both NO to NO_2 oxidation and NH_3 SCR. Sjovall et al. [59] utilized Fourier transform infrared spectroscopy to identify surface species on Cu-zeolite during multiples gas flow compositions. During a flow of NH_3 they observed peaks corresponding to the adsorption of NH_3 on both Brønsted and Cu sites, and upon introducing O_2 these peaks diminished as NH_3 began to be consumed by oxidation over Cu. Meanwhile, exposure to NO + O_2, NO_2, or SCR flow conditions resulted in multiple peaks associated with NO^+ and nitrate/nitrite species. Based on these results, they suggested that both gas phase NO and surface nitrates/nitrites on Cu sites in the zeolite play an important role in NH_3 SCR. Wilken et al. [60] agreed with these findings based on their own observations that increased Cu sites, particularly Cu^+, resulted in an increase in SCR activity in the zeolite. These two studies suggest that a Langmuir-Hinshelwood mechanism involving the reaction of two adsorbed surface species is just as important to the SCR performance of a Cu-zeolite catalyst as the Eley-Rideal mechanism.

The chemistry of active Cu sites in NH_3 SCR is explained by a reduction-oxidation (redox) cycle such as the one proposed by Goursot et. al [61] for the SCR of NO shown in Figure 2.2.3 [61-63].

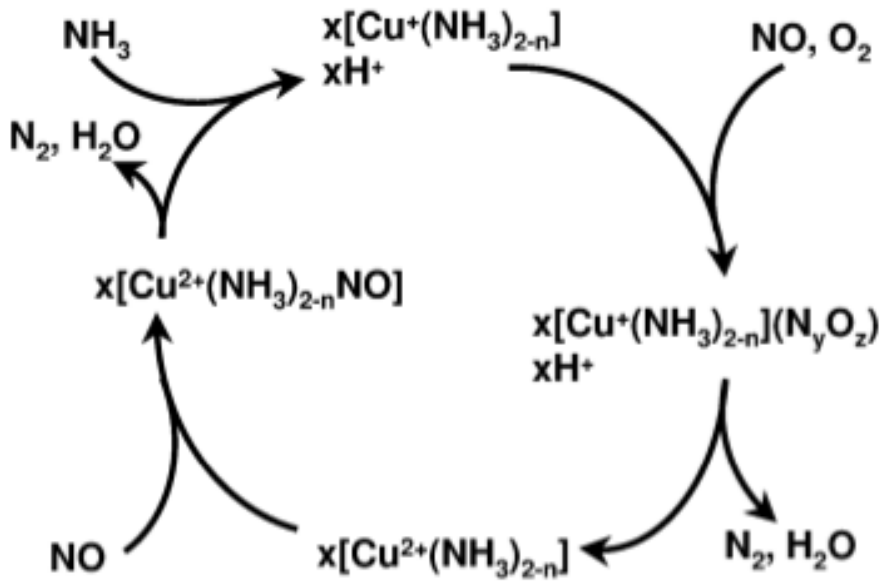

Figure 2.2.3 Reduction-oxidation cycle of Cu species during NH_3 SCR of NO over Cu-zeolite [61, p. 327]**.**

In this cycle Cu^+ with adsorbed NH_3 is oxidized to Cu^{2+} after reaction with NO + O_2 to form N_2 and H_2O. The concomitant reduction to Cu^+ occurs after exposure to NO and NH_3, during which more N_2 and H_2O production occurs. The oxidation step is believed to control the rate at which SCR occurs, meaning the activity of the Cu^+ sites is crucial to the performance of the Cu-zeolite SCR catalyst.

2.2.3 Cu-Zeolite SCR Catalyst Performance and Durability

The use of Cu-zeolite as an NH_3 SCR catalyst stems from its ability to reduce a high percentage of NO_x in exhaust gas over a large temperature range. It has the particular advantage of excellent low temperature conversion in the range of 200 to 300°C. Some typical results for NH_3 SCR over Cu-zeolite from a

study investigating the impact of changing the simulated exhaust gas composition by Sjovall et al. [55] are shown in Figure 2.2.4.

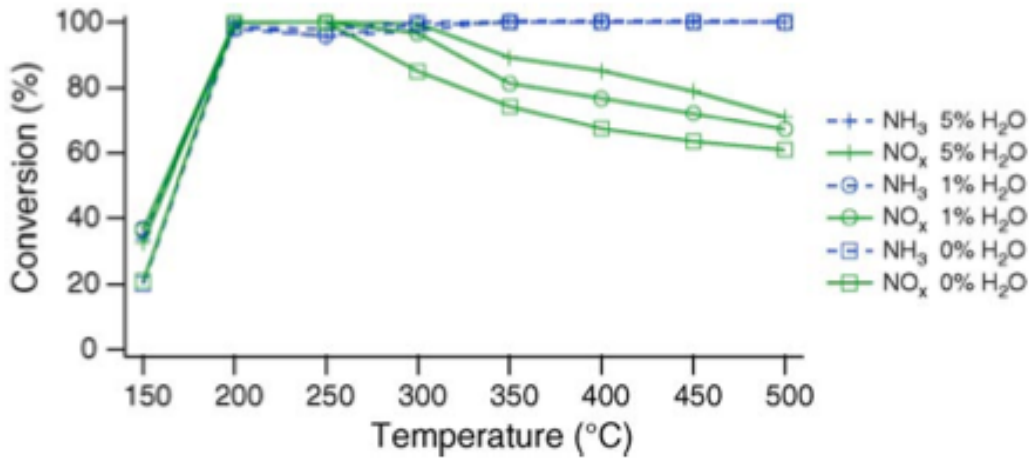

Figure 2.2.4 NO-only performance of Cu-zeolite SCR with 500 ppm NO, 500 ppm NH_3, 8% O_2 and 0-5% H_2O, and N_2 balance [55, p. 185]**.**

NO-only conversion at 150°C is in the range of 20-40%, but upon increasing the temperature to 200°C the NO_x reduction reaches almost 100%. The peak range of conversion is between 200 and 300°C, and at temperatures above 350°C the performance steadily declines with increasing temperature. These results also illustrate the importance of H_2O in the exhaust gas, as increasing the concentration of water from 0 to 5% improves SCR performance, particularly at temperatures above 300°C. Sjovall et al. [55] attributed this observation to a reduction in the blocking of active SCR sites by NH_3 when H_2O is present in the exhaust gas.

Introducing NO_2 into the simulated exhaust feed also has an important effect on SCR performance, as illustrated in results from Colombo et al. [64] shown in Figure 2.2.5.

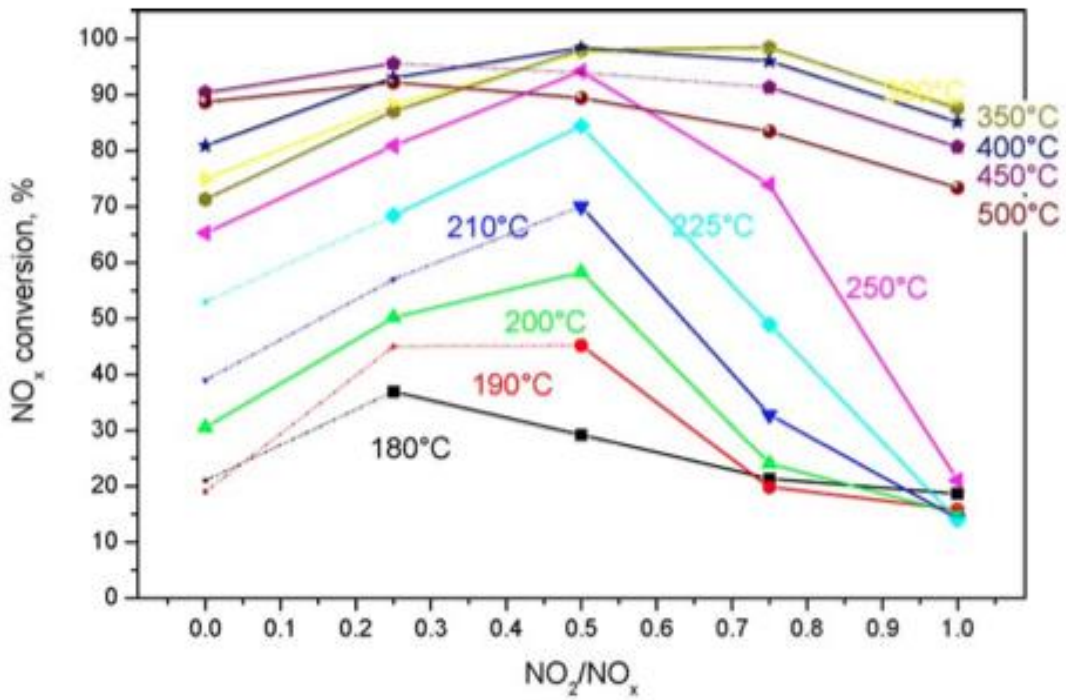

Figure 2.2.5 Effect of varying the NO_2/NO_x ratio over Cu-zeolite with 500 ppm NO_x, 500 ppm NH_3, 2% O_2, 3% H_2O, and N_2 balance [64, p. 228]**.**

They found that in the temperature range from 190 to 400°C increasing the NO_2/NO_x ratio from 0.0 to 0.5 resulted in increased NO_x reduction. This effect is more pronounced at lower temperatures, illustrating the importance of the fast SCR reaction in low temperature NO_x reduction by NH_3. However, NO to NO_2 oxidation over Cu-zeolite SCR is low, typically reaching a maximum of 10% in the temperature range from 500 to 600°C [55]. Therefore, in order to achieve the

highest possible NO_x conversion over a Cu-zeolite catalyst an upstream DOC is often needed to provide adequate NO oxidation in real diesel exhaust.

While Cu-zeolite SCR catalysts exhibit the level of NO_x reduction required to meet modern emissions standards, their durability is a concern due to the necessity that these catalysts maintain that high level of performance over the useful life of a vehicle. A significant amount of research has been devoted to understanding the failure mechanisms of Cu-zeolite SCR, especially with regards to the effects of hydrothermal aging. Cavataio et al. [65] performed hydrothermal aging of Cu-zeolite catalysts using a bench flow reactor and determined the do not exceed temperature to be 900°C. Aging at 950°C results in significant catalyst deactivation, as shown in Figure 2.2.6.

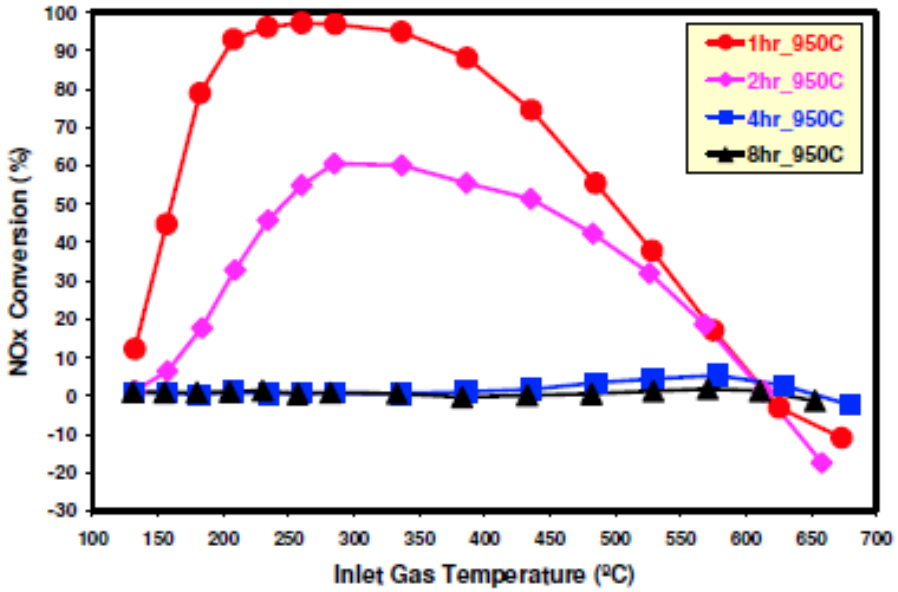

Figure 2.2.6 Standard SCR NO_x performance after hydrothermal aging at 950°C [65, p. 483]**.**

After one hour the catalyst is relatively unaffected, while after two hours performance has declined by as much as 50% across the temperature range. Further aging beyond four hours leads to a complete loss of SCR function. Similar results were obtained by Wilken et al. [60] while characterizing hydrothermally aged Cu-zeolite SCR using X-ray photoelectron spectroscopy (XPS) and X-ray diffraction (XRD). They attributed the performance degradation to a loss of the Cu^+ sites active for NH_3 SCR in Cu-zeolite.

In another recent hydrothermal aging study on beta Cu-zeolite by Cavataio et al. [66] they developed four performance criteria to determine a likely SCR failure: less than 80% NO_x conversion at temperatures between 200 and 400°C for standard or fast SCR, less than 100% NH_3 oxidation between 500 and 700°C, less than 600 mg/L NH_3 storage capacity, and less than 70% normalized BET surface area relative to a reference sample. They performed hydrothermal aging on a bench flow reactor using 8% O_2, 5% H_2O, and 5% CO_2 with N_2 balance at aging temperatures of 600, 700, 800, and 900°C for up to three hours at each temperature. After each aging step, they measured BET surface area, NO_x performance, NH_3 oxidation, and NH_3 storage and compared them against the four performance criteria. Based on their results, they believe borderline catalyst failure occurs under any one of the following hydrothermal conditions: one hour at 1000°C, two hours at 950°C, 8 hours at 900°C, 64 hours at 850°C, and 256 hours at 800°C. They used their results to develop emissions transfer

functions capable of predicting the impact of aging on the four performance criteria within a 10% margin of error.

Aside from hydrothermal aging, many researchers have investigated other potential factors leading to Cu-zeolite SCR failure. Poisoning of the SCR catalyst due to sulfur contamination from diesel fuel is one concern which was investigated by Theis [67] in his study on contamination and desulfation characteristics of Cu-zeolite. He contaminated catalysts by introducing SO_2 flow for 1, 2, 4, and 8 hours in a bench flow reactor. NO_x performance of the catalysts decreased by 10 to 20% after 1 to 4 hours of aging, particularly at temperatures between 200 and 400°C, although further contamination showed little to no effect. Additionally, he found that desulfation at 750°C under lean conditions results in a complete performance recovery, and after multiple poisoning/desulfation cycles the catalyst appears to stabilize with only minimal performance loss.

While sulfur is a fuel-derived source of catalyst poisoning, recent research by Cavataio et al. [68] addresses the possibility that another aftertreatment device could lead to SCR failure in the form of PGM contamination from a DOC. Both light- and heavy-duty diesel aftertreatment arrangements utilize a DOC upstream of the SCR to both eliminate HC and CO, and to oxidize NO to NO_2 in order to promote the fast SCR reaction over Cu-zeolite. During DPF regeneration, the temperature of the DOC may reach up to 850°C and can have the effect of volatizing PGM particles, particularly Pt, which then deposit on the downstream SCR. In the study, contamination was achieved by dipping one inch

Cu-zeolite SCR samples into a solution containing $Pt(NH_3)_4(NO_3)_2$ before drying at 150°C for one hour and calcination at 400°C for four hours. They found that Pt contamination of 0.008 wt% results in a 5-10% reduction in NO_x performance at temperature between 200 and 600°C. Furthermore, contamination of 0.06 wt% causes up to 100% catalyst deactivation during evaluations between 225 and 350°C, and at temperatures above 400°C significant NO_x formation was observed. This is explained by excess NH_3 to NO_x oxidation and N_2O formation over the deposited Pt in the catalyst.

With regards to the investigation which is the focus of this thesis, the most pertinent study available was a 2009 research effort by Cavataio et al. [16] in which the impact of Na and K exposure on Cu-zeolite SCR was analyzed. Catalysts were exposed to either $NaNO_3$ or KNO_3 solution using an incipient wetness technique to achieve contamination levels from 0.1 to 3.0% by weight. Afterwards, the SCR samples were evaluated for NO_x performance (standard and fast) and BET surface area. Additionally, in the case of K, NH_3 storage capacity was measured. The results of the NO_x performance evaluations after Na impregnation are shown in Figure 2.2.7. At Na contamination levels up to 0.50 wt% a steady decline in performance is observed, and at 1.00 wt% complete catalyst deactivation occurs. Corresponding declines in normalized BET surface area follow the same trend as the NO_x performance evaluations, with surface area losses of 10% and 80% at the 0.5 and 1.0 wt% contamination levels, respectively. Finally, NH_3 storage measurements of K contaminated SCR samples shows a linear decline in storage capacity with increasing

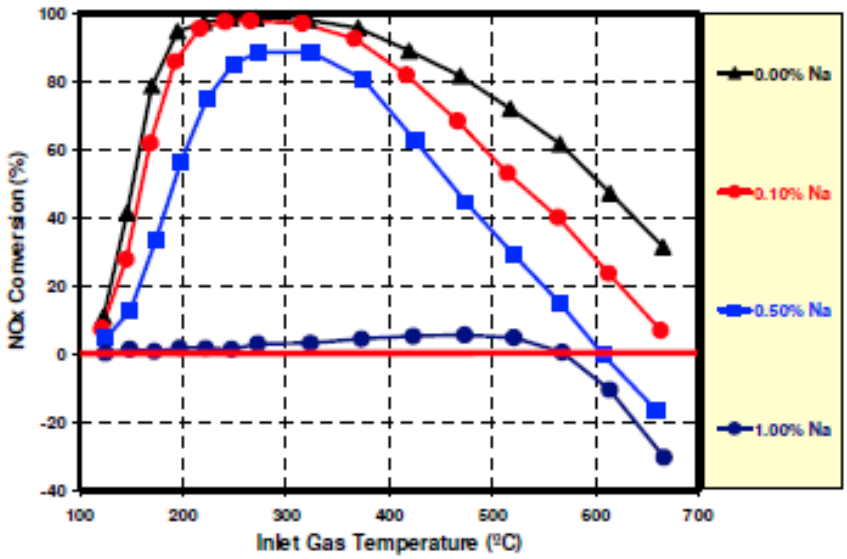

(a)

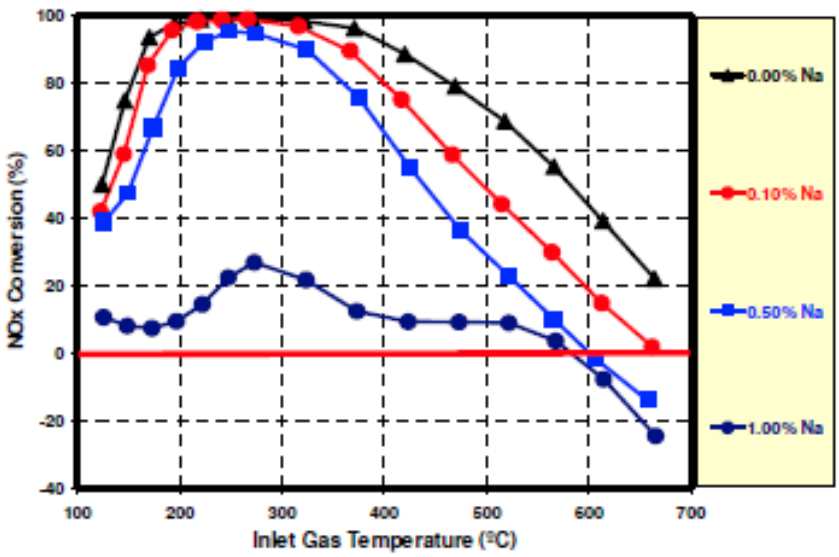

(b)

Figure 2.2.7 Impact of Na contamination on (a) standard and (b) fast SCR performance over Cu-zeolite [16, p. 11]**.**

contamination. In general, the researchers found that the effects of K contamination were less drastic and behaved in a linear fashion, although the

impact was still significant enough to be of concern for emissions control purposes.

In general, it appears that multiple factors including BET surface area, availability of active Cu sites, and NH_3 storage capability determine the performance of Cu-zeolite SCR catalysts. These factors are affected by both hydrothermal aging and catalyst poisoning which occurs as a part of normal day-to-day operation during diesel engine operation.

2.3 Durability of LNT, DOC, and DPF Aftertreatment Devices

LNT catalysts are an alternative to SCR catalysts and rely on a much different approach to NO_x reduction, although both share some common durability concerns. Ottinger et al. [69-70] studied the effects of high-temperature lean/rich cycling and determined that at temperatures above 900°C LNTs experience PGM sintering and significant reductions in surface area, leading to decreased NO_x performance. However, it should be noted that even after aging at 1000°C for 350 cycles the NO_x performance of the catalyst still maintains a level of approximately 70% conversion, a decrease of less than 30% relative to fresh samples. Cheng et al. [71] examined the effect sulfur poisoning on LNTs and determined that although performance is impacted as a result of sulfur contamination, this problem can be typically be reversed through high temperature desulfation under rich engine conditions. While the above results are similar to those seen for SCR catalysts, studies to determine the impact of Na on

LNTs have shown much different outcomes. Dou and Balland [72] found that when alkali metals such as Na are introduced with Ba that a number of positive effects occur, including increased NO_x conversion, higher sulfur resistance, and higher NO_x storage capacity [73]. These effects have been attributed to more facile dissociation due to a weakening of the N-O bond and an increase in the number of sorption sites when Na is present. Such observations are not entirely unexpected due to the fact that Na can function as a storage material similar to Ba.

DOC performance loss is typically quantified by increases in light-off temperature for CO, HC, and NO to NO_2 oxidation. Thermal aging of DOCs has been shown to cause sintering of PGM particles resulting in decreased Pt particle surface area and increases of up to 100°C in the temperature required to achieve 50% conversion (T-50 light-off temperature) for CO, HC, and NO [74]. Meanwhile, Kolli at al. [75] investigated the effects of sulfur exposure and found that decreases in specific surface area and the formation of sulfates on active sites in the DOC after contamination increase CO and HC T-50 light-off temperatures by 20°C relative to fresh samples. In the same study it was determined that Ca has a negligible impact on DOC performance. Another failure mechanism for DOCs is soot buildup on the surface of the catalyst, which masks the active sites and can result in 20 to 30°C increases in T-50 light off temperature for HC and CO [76]. However, soot can be removed by exposing the catalyst to an oxidizing environment at 500°C.

Regarding the subject of this thesis, the most pertinent results were obtained by Cavataio et al. [16] in their study on Na exposure DOC catalysts. The CO and HC T-50 light-off temperatures for three different DOC formulations (Pd-only, Pd:Pt non-zeolite, and Pd:Pt zeolite) contaminated with Na at the 1.0 and 3.0 wt% levels are shown in Figure 2.3.1. As can be seen from the figures, the Pd-only formulation of DOC is relatively resistant to Na contamination up to 1.0 wt%, but CO and HC T-50 light-off temperatures are increased by 30°C at the 3.0 wt% contamination level. Both the non-zeolite and zeolite Pt:Pd DOC formulations are sensitive to Na exposure, with increases of 35 to 50°C in CO and HC T-50 light-off temperatures at 1.0% wt contamination and up to 70°C increases after 3.0 wt% contamination. NO to NO_2 oxidation also suffers in the Pt containing DOCs, where the amount of oxidation decreases by 23 and 35% for 1.0 and 3.0 wt% Na contamination, respectively. These changes in performance for the Pt-containing DOCs correlate with reduced BET surface area as the level of Na contamination increases, while the Pd-only DOC showed little to no reduction in surface area after Na exposure.

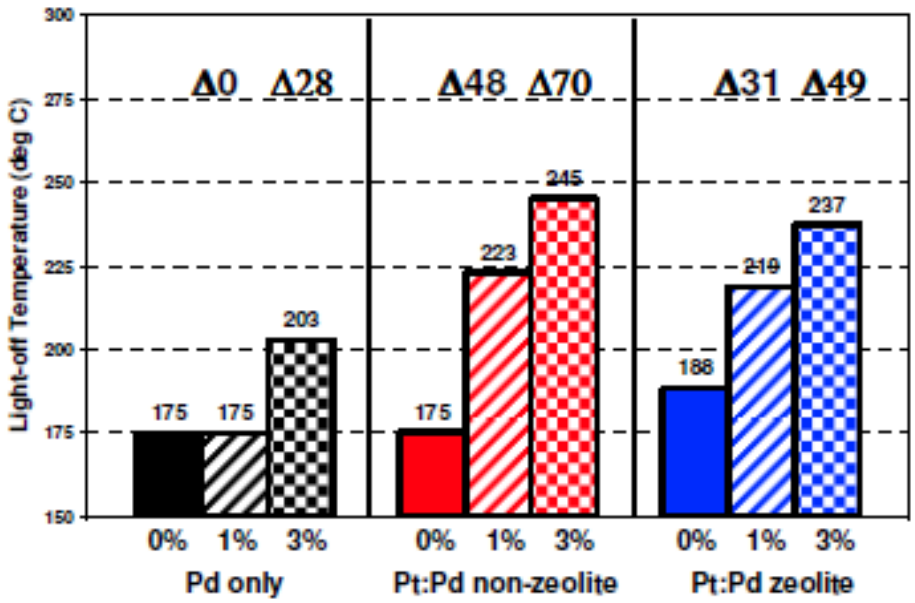

(a)

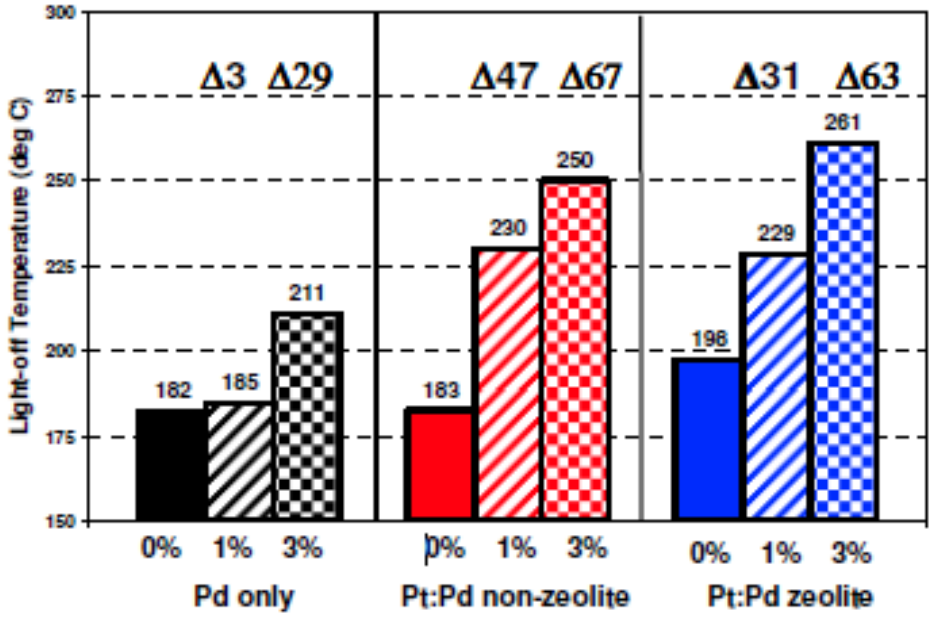

(b)

Figure 2.3.1 Impact of Na contamination on T-50 light-off temperature for (a) CO and (b) HC performance in DOCs [16, p. 6]**.**

DPFs serve as filters instead of catalysts, so their durability is characterized in terms of increased regeneration frequency and excessive ash buildup which can require physical removal of a DPF from an aftertreatment system for cleaning. Sulfur content in fuel is one factor that has been shown to contribute to excessive ash formation and increased backpressure, particularly when barium is also present in the fuel due to the formation of barium sulfate [77]. Biodiesel combustion in diesel engines can affect the DPF by increasing regeneration rates, resulting in higher fuel consumption up to 3% for B20 fuel [78]. Biodiesel fuel also leads to the presence of Na and K ash in the DPF, which requires that the regeneration temperature be controlled in order to avoid melting of these materials which can then have adverse effects on the integrity of the substrate material and thus the filtering performance of the DPF [79].

CHAPTER III

MATERIALS AND METHODS

This chapter describes the experimental procedures and apparatus used in the present investigation, along with information on the SCR, LNT, DOC, and DPF aftertreatment devices which were investigated. Section 3.1 contains details about the catalysts evaluated during the study, including physical characteristics and any aging performed before delivery to the laboratory. In Section 3.2 an overall description of bench flow reactor (BFR) operation is given along with descriptions of the important BFR components, while Section 3.3 explains BFR startup and evaluation procedures. Section 3.4 describes the engine bench located at the National Transportation Research Center (NTRC) which was used for accelerated Na-aging. Section 3.5 contains descriptions of the multiple materials characterization techniques utilized during the study, and the chapter concludes in Section 3.6 with a brief description of the Fortran model used for predicting the performance of Fresh Cu-zeolite SCR.

3.1 Catalysts

A wide range of catalysts and emissions control devices were evaluated and characterized in the current investigation, as shown in Table 3.1.1. Fresh and engine-aged LNT catalysts were provided for evaluation by the Manufacturers of Emissions Controls Association (MECA) through a National Renewable Energy Laboratory (NREL) study. The engine-aged LNT was part of

a diesel emissions control system which consisted of an upstream DOC, an LNT, and a downstream DPF (the DOC and DPF were unavailable for analysis). The long-term engine-aged

Table 3.1.1 Catalyst Information and Aging Approaches.

Catalysts	Supplier	Aging Approach	Configuration	Fuel	Engine	Fresh Sample Available
Lean NO_x Trap	NREL/MECA	Long Term Engine-Aging	DOC-LNT-DPF	ULSD with 20% Biodiesel	In-line 4-Cylinder Turbocharged System	Yes
Pt/Al_2O_3-based DOC	General Motors	Long Term Engine-Aging	DOC-DPF	In-Spec B20	Details Not Provided	No
SiC-based DPF	General Motors	Long Term Engine-Aging	DOC-DPF	In-Spec B20	Details Not Provided	No
Cu-chabazite SCR Catalyst	NREL	100 h Engine Aging	Front and Rear DOC - Front and Rear SCR - DPF	B20 + 14 ppm Na	Caterpillar C9	No
Cu-zeolite SCR Catalyst	BASF	1. Accelerated Na-Aging 2. Accelerated Na-Aging 3. Accelerated Control Case	1. DOC-SCR-DPF 2. DOC-DPF-SCR 3. DOC-SCR-DPF	1. Na-doped B20 2. Na-doped B20 3. B20	Direct Injection 517 cm^3 Single-Cylinder Hatz Diesel Engine	Yes
Washcoated Pt/Al_2O_3-based DOC	BASF	1. Accelerated Na-Aging 2. Accelerated Na-Aging 3. Accelerated Control Case	1. DOC-SCR-DPF 2. DOC-DPF-SCR 3. DOC-SCR-DPF	1. Na-doped B20 2. Na-doped B20 3. B20	Direct Injection 517 cm^3 Single-Cylinder Hatz Diesel Engine	Yes
Cordierite DPF	BASF	1. Accelerated Na-Aging 2. Accelerated Na-Aging 3. Accelerated Control Case	1. DOC-SCR-DPF 2. DOC-DPF-SCR 3. DOC-SCR-DPF	1. Na-doped B20 2. Na-doped B20 3. B20	Direct Injection 517 cm^3 Single-Cylinder Hatz Diesel Engine	Yes

Pt/Al_2O_3-based DOC and SiC-based DPF catalysts were supplied by General Motors (GM). The aging procedure utilized B20 with normal Na levels, < 5 ppm, in a vehicle system with a DOC and a DPF, i.e. without a NO_x control catalyst, and was operated for a 150,000 equivalent miles. The exhaust temperature was periodically elevated to greater than 600°C to regenerate the DPF, i.e., oxidize the collected carbonaceous particulate. Engine-aged Cu-chabazite SCR samples were provided by NREL after 100 h, or 150,000 equivalent miles, aging on a Caterpillar C9 engine using B20 fuel with 14 ppm Na content. The aging

configuration during these tests consisted of an upstream front and rear DOC, front and rear SCR bricks, and a downstream DPF.

For the accelerated aging, an uncatalyzed DPF and washcoated model DOC and SCR catalysts were obtained from BASF. The DPF was a porous cordierite-based monolith with alternate channels plugged for wall filtration. The DOC was a Pt/Al_2O_3-based catalyst washcoated on a cordierite monolith. The SCR catalysts were a model Cu-zeolite (beta formulation) supported on a cordierite substrate. Since the SCR catalyst was not an integral part of the NREL/MECA and GM diesel emissions control systems, the validity of the implemented accelerated Na-aging protocol was qualitatively assessed from the Na location and distribution in the LNT samples from NREL/MECA, the DOC/DPF provided by GM, and the Cu-chabazite SCR samples from NREL.

3.2 Engine Bench for Accelerated Na Engine-Aging

Accelerated Na engine-aging is carried out by an engine operator on a bench-mounted naturally aspirated, direct injection 517 cm^3 single-cylinder Hatz diesel engine located at the National Transportation Research Center (NTRC). This engine and its components have been described in detail elsewhere [80], and a photograph of the setup is shown in Figure 3.2.1. An electric induction motor and drive are used to control engine speed and load, producing consistent and repeatable exhaust temperatures during the periodic DPF regeneration. Two

different configurations of the emissions control system are used in the accelerated Na engine-aging. One configuration, DOC-SCR-DPF, is typically

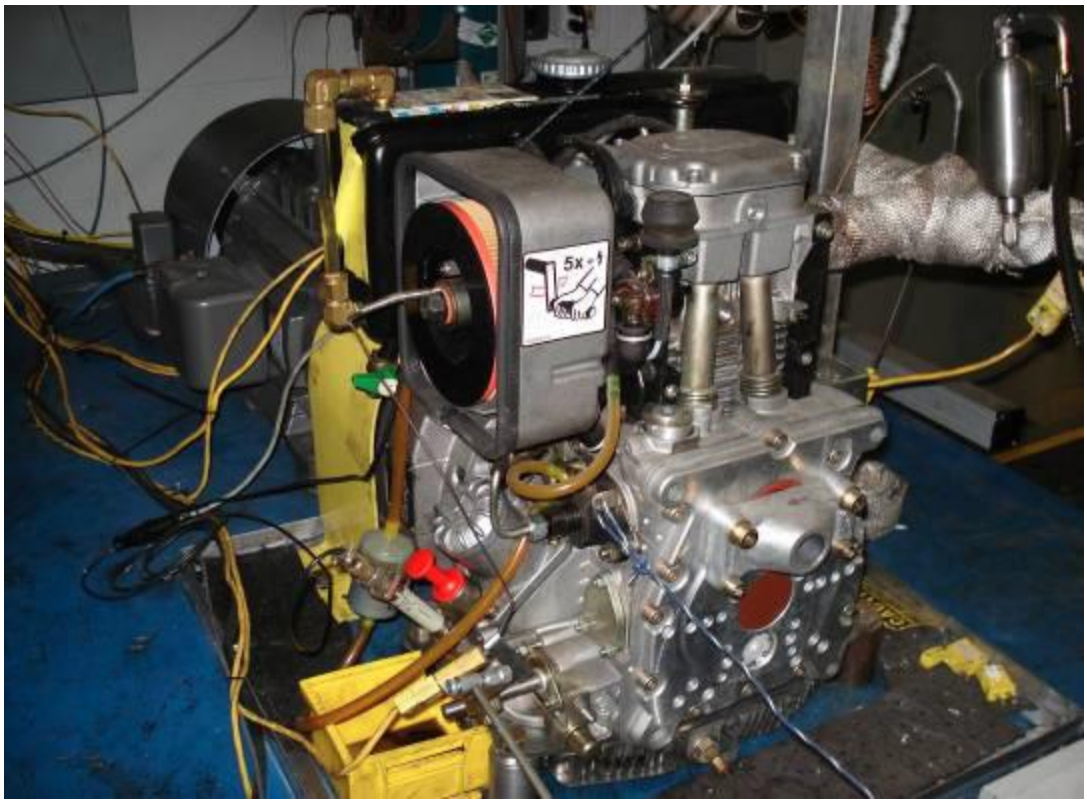

Figure 3.2.1 Single-cylinder Hatz diesel engine for accelerated Na-aging protocol [1, p. 44]**.**

used in light-duty applications, while the other, DOC-DPF-SCR, in heavy duty. The heavy-duty diesel aftertreatment system is implemented to investigate the ability of the upstream DPF to protect the SCR from performance degradation. In addition to the accelerated Na engine-aging, aging is also carried out on the light-duty configuration (DOC-SCR-DPF) without Na salt added to the biodiesel and ULSD mixture and is referred to as the control case. In all three cases the engine

is operated for the amount of time required to consume 8L of B20 fuel. Figure 3.2.2 is a schematic of the engine bench with the light-duty emissions control system.

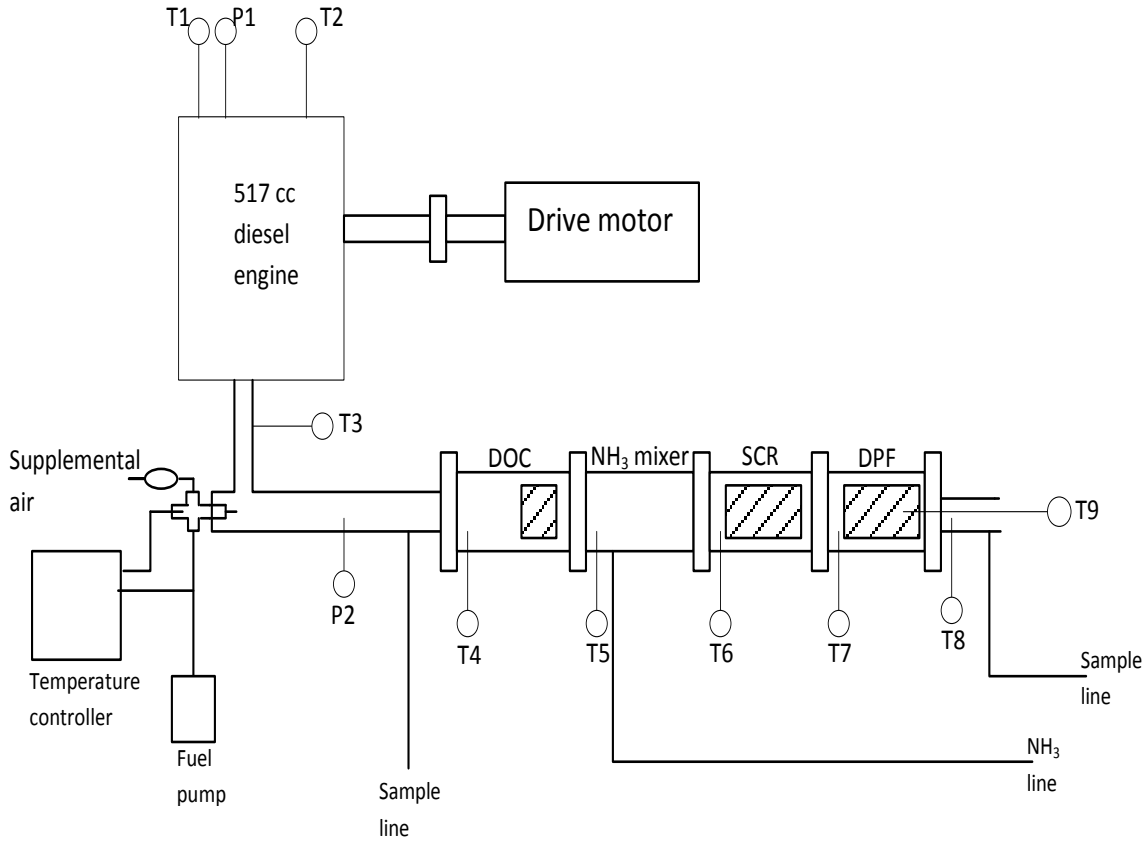

Figure 3.2.2 Schematic of engine bench for accelerated Na-aging.

A fuel injection system installed approximately 0.3 m downstream of the exhaust manifold is used to inject fuel into the engine exhaust to initiate the exotherms for active DPF regeneration. The fuel is pumped through a 1.6 mm stainless steel tube into a vaporizer using a FMI (Fluid Metering, Inc.) laboratory pump. The fuel is vaporized by a cartridge heater maintained at 375°C. The

evaporated fuel is then injected into the exhaust gas through a nozzle using compressed air at a flow rate of 1000 sccm/min as a sweeper gas.

An NH_3 injection line is connected to the front of the NH_3/exhaust mixer through a Swagelok fitting to provide NH_3 for the SCR reactions. The line is comprised of a 1.5 m long Teflon tubing connected to a 0.5 m stainless steel tubing with a solenoid valve connecting the two separate materials. Flow from a 5% NH_3 in N_2 gas cylinder is controlled by a Teledyne Hastings MFC. Heat tape is wrapped around the line to ensure the temperature is maintained above 200ºC to avoid the formation of ammonium nitrate when the NH_3 enters the mixer.

Each catalyst is mounted in a 7.6 cm diameter steel can. Before being placed in the cans, the catalysts are wrapped in a vermiculite-coated fiber mat which provides insulation and prevents gas slippage at the edges of the catalyst. The exhaust pipe is also wrapped in insulation to minimize heat losses from the emissions control system. Omega type-K thermocouples with a range from -200 to 1250°C and an accuracy of 2.2°C are located at the inlet and exit of each catalyst to provide temperature profiles of the catalysts during the aging process.

The high-level of Na in the biodiesel is obtained by adding approximately 190 g of dioctyl sulfosuccinate (with ratio of Na to S in the Na salt of approximately one) to two gallons of Haltermann Products ultra-low sulfur diesel fuel (ULSD) with SoyGold 1100 soy B20 fuel to produce approximately 5000 ppm of Na and 5000 ppm of S in the fuel. Thus, in the accelerated Na engine-aging protocol the amount of Na exposure in the aftertreatment system is elevated to a level corresponding to 435,000 miles in less than eight hours.

3.3 Bench Flow Reactor Overview and Components

3.3.1 Bench Flow Reactor Overview

Two separate bench flow reactors were utilized in the current investigation. One is located at the University of Tennessee at Knoxville (UTK), and the other is at the National Transportation Research Center (NTRC). Both setups include five main components: a mass flow controller (MFC) bank for introduction of simulated diesel exhaust, a steam generator, tubular reactors, a data acquisition system (DAQ), and an instrument for gas concentration measurements. The only significant difference between the two systems is the method of gas analysis. At UTK, a gas analyzer bench consisting of four analyzers is used, while at NTRC gas analysis is performed with an FTIR spectrometer. A diagram of the UTK BFR is shown in Figure 3.3.1. The NTRC BFR is essentially identical except the exclusion of an NH_3 scrubber and the replacement of the analyzer bench with an FTIR.

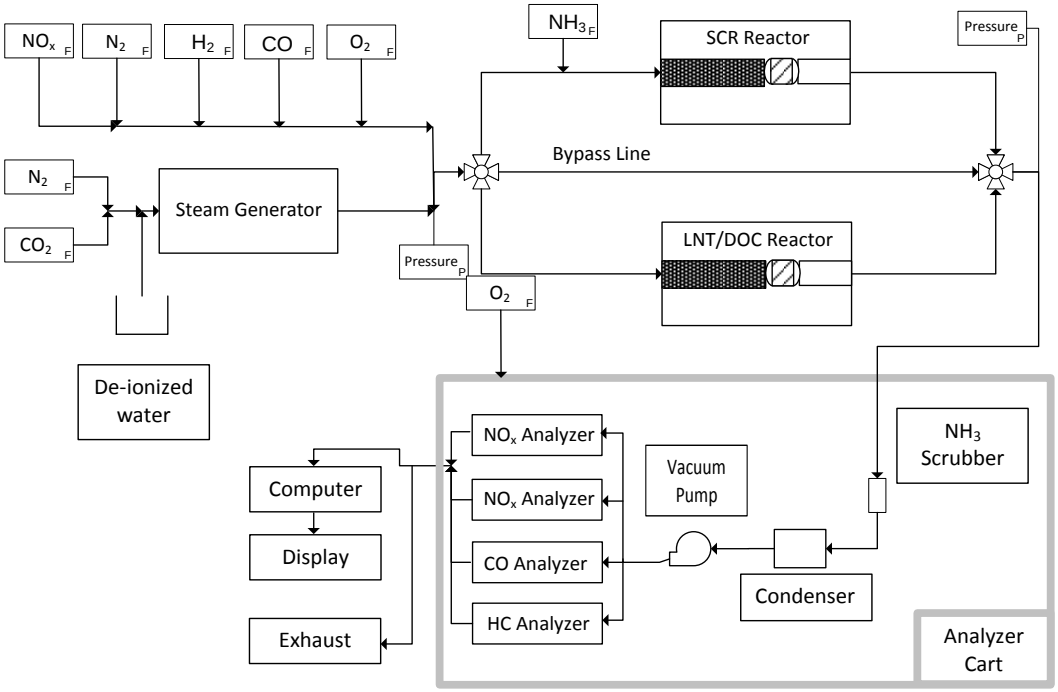

Figure 3.3.1 Schematic of bench flow reactor at University of Tennessee.

Before operation of a BFR calculations are made in Microsoft Excel to determine the necessary MFC inputs for the LabVIEW-based DAQ. These calculations are based on the desired flow composition and gas hourly space velocity (GHSV) for the reactor. The gas hourly space velocity is defined according to Eq. 3.3.1, where Q is the total volumetric flow rate of the simulated diesel exhaust gases and V_s is the volume of the catalyst channels in the reactor through which the gases will flow.

$$GHSV = \frac{Q}{V_s} \tag{3.3.1}$$

The GHSV and gases which comprise the simulated diesel exhaust flow are dependent on which type of catalyst (SCR, LNT, or DOC) is being evaluated and

what reaction is currently under investigation for the given catalyst. Gases are supplied from gas cylinders located in the laboratory, and each gas is assigned to an individual MFC based on the required flow rate for the experiment. Flow rate through the MFCs is controlled by a 0-5 V signal sent from the computer through the DAQ.

Water vapor is the only component of the simulated diesel exhaust introduced outside of the DAQ and is supplied via a pump and steam generator. N_2 and CO_2 are used as carrier gases to sweep the liquid water introduced by the pump through the steam generator where evaporation occurs to the produce the water vapor. At the exit of the steam generator the remaining gases, except for NH_3, enter the BFR and are then directed by a three-way valve to either the bypass line or the desired reactor. NH_3 is introduced directly upstream of the SCR reactor through a separate line heated to 200ºC to avoid the formation of unwanted ammonium nitrate in the BFR.

A catalyst sample from a fresh or engine-aged SCR, LNT, or DOC of one inch in diameter is core-drilled from fresh and engine-aged catalysts for evaluation on a BFR. The sample is wrapped with insulation to ensure a tight fit and inserted into a tubular quartz reactor. The inlet of the reactor is filled with 5 mm quartz beads to provide heating and mixing of the simulated diesel exhaust gases. The reactor is placed inside a Lindberg Minimite tubular furnace which provides temperature control during evaluation. Omega type-K thermocouples measure the temperatures inside the reactor at the inlet, middle, and exit of the catalyst. The UTK BFR also has thermocouples located at the one- and three-

quarter catalyst length locations, as shown in Figure 3.3.2. Cole Parmer pressure transducers measure pressure at the inlet and exit of the BFR system.

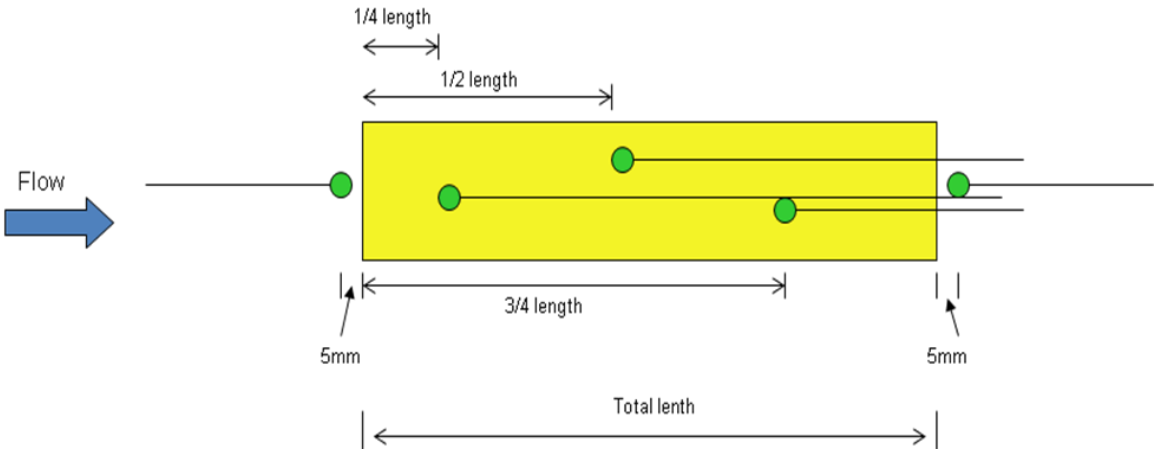

Figure 3.3.2 Thermocouple locations in evaluation cores [1, p. 28]**.**

At UTK, a gas analyzer bench measures the concentration of gases exiting the BFR. There are four analyzers in the bench: a Horiba CO/CO_2 analyzer, a Horiba flame ionization detector (FID) HC analyzer, a Horiba chemiluminescent NO_x analyzer, and a California Analytical Instruments (CAI) chemiluminescent NO_x analyzer. Gas analysis at NTRC is performed with an MKS FTIR spectrometer which comes preloaded with reference spectra to determine gas composition.

In both UTK and NTRC bench-flow reactors, temperature and pressure data are acquired and stored in a LabVIEW-based DAQ. The interface provides a virtual control panel which controls the MFC flow rates as well. The gas analyzer bench at UTK is also connected to the LabVIEW DAQ in order to store the gas

concentration measurements as a function of time. The MKS FTIR at NTRC uses its own software for gas analysis, data acquisition and data storage. This software is provided with the FTIR and operates independently of the LabVIEW program.

3.3.2 Mass Flow Controllers

Mass flow controllers (MFC) are used to precisely regulate the flow rate of the simulated diesel exhaust gases from gas cylinders. The MFCs used in the current investigation have maximum flow rates ranging from 0.1 to 10 LPM and are controlled by the virtual control panel in LabVIEW. The MFCs are calibrated using N_2, and the flow rates of other gases are adjusted in terms of N_2 flow rate by a correction factor knows as the K factor. The K factor corrects for differences in molecular weight between the target gas and N_2. The input voltage to the MFCs from the personal computer (PC) operating LabVIEW vary between 0 and 5 V, with 0 V corresponding to zero flow and 5 V corresponding to the maximum flow rate of the given MFC. An internal feedback system from the MFCs to the PC ensures that the specified flow rates are achieved.

3.3.3 Stainless Steel Tubing and Heating Tapes

The BFR tubing is 0.25 in stainless steel, and Swagelok® fittings are used for junctions and component connections. Omega heating tapes controlled by Variac variable voltage transformers are wrapped around the stainless steel tubing to maintain the desired temperature throughout the BFR. All lines are heated to at least 100ºC to avoid water condensation, and the lines into and out

of the steam generator are kept above 200ºC to minimize water pulsation from the peristaltic pump and steam generator. The inlets and exits of the reactors are Swagelok VCR-type connectors which use graphite gasket fittings to prevent leakage.

3.3.4 Steam Generator and Peristaltic Pumps

De-ionized water is injected into the BFR through a Tygon tube attached to a peristaltic pump. At UTK, this pump is a Cole Parmer Masterflex™ model capable of flow rates between 0.1 and 580 cc/min, while at NTRC a PUMP DETAILS is used. The steam generator consists of a 0.5 in outer diameter stainless steel tube placed inside a Lindberg Minimite furnace to provide heating. The inlet of the tube is filled with quartz wool and the remainder is packed with quartz beads. The injected water is absorbed onto the quartz wool, evaporates, and is then swept through the quartz beads where mixing occurs before entering the BFR.

3.3.5 Reactor Setup

The reactor is a 44.5 cm long quartz tube with an inner diameter of 2.22 cm and an outer diameter of 2.54 cm. The catalyst is placed inside the reactor after being wrapped in FiberFrax™ glass wool to ensure that no gas is able to flow around the edges of the sample. A wire mesh screen located upstream of the catalyst prevents the quartz beads used to mix the gas from sliding down to the catalyst inlet. The end caps for the reactor each have three Swagelok fittings welded in place which are used to insert the Omega type-K thermocouples which

measure the temperature at the inlet, middle, and rear of the catalyst sample. Graphite ferrule fittings create a compression seal between the quartz tube and end caps to prevent leakage at the edges of the quartz tube.

3.3.6 University of Tennessee Analyzer Bench

The UTK analyzer bench contains several important components of the BFR including the gas analyzers, analyzer matrix switches, vacuum pump, NH_3 trap, and cooling coil with water trap. Both NO_x analyzers are located inside the analyzer bench, along with the CO and HC analyzers. Details will be provided for these instruments in Section 3.3.7. The analyzer matrix switch allows the operator to direct flow to the desired analyzers, and the amount of flow to each analyzer can be controlled by three-way solenoid valves located on the front of the bench. Overall pressure in the BFR itself and in the analyzer bench is controlled by a throttling valve and pressure regulator located on the bench. A pressure of approximately 1.0 psig is maintained in the reactor during evaluation, while the analyzer bench is kept at a pressure of 9.0 psig. The vacuum pump ensures that the pressure in the system does not exceed the desired level.

The Perma Pure NH_3 trap is filled with a scrubber material which reacts with the NH_3 before the simulated exhaust gas reaches the cooling coil. NH_3 must be removed from the system before reaching the cooling coil in order to avoid the formation of ammonium nitrate in the analyzer bench. Additionally, NH_3 is detrimental to the performance of the NO_x analyzers in the form of decreased NO_2 to NO conversion. The scrubber material must be replaced once every

month for continued operation. The cooling coil is contained in a water bath which is maintained below 45 ºC to ensure condensation of the water vapor in the simulated diesel exhaust gas. At the end of experiments, any water which has condensed into the trap is drained and disposed of.

3.3.7 University of Tennessee Gas Analyzers

Four analyzers are utilized for gas analysis in the UTK BFR. A California Analytical Instruments (CAI) Model 400-HCLD measures total NO_x ($NO+NO_2$), while a Horiba Model CLA-220 measures NO. Both analyzers are based on the chemiluminescent method of NO_x detection. O_2 is supplied to the analyzers from a gas bottle and is used to generate ozone (O_3) which reacts with NO to produce NO_2 and O_2. The amount of light emitted by this chemiluminscent reaction is directly proportional to the concentration of NO in the simulated exhaust gas. An NO_2 to NO converter allows for total NO_x measurement when desired.

DOC evaluations are performed using a Horiba FMA-220 flame ionization detector (FID) for HCs and a Horiba AIA-210 Infrared detector for CO. The flame in the FID is generated from a gas cylinder of 40% hydrogen in helium which reacts with air from a separate cylinder. When HC reaches the hydrogen flame the heat of combustion causes the HC to undergo ionization. By applying a DC voltage between two electrodes on either side of the flame it is possible to measure the flow of ions, which is proportional to the number of carbon atoms in the HC. In the CO analyzer, an infrared source emits light as the sample flows

through the sample cell. The concentration of CO is calculated based on the measurement of the infrared absorption spectrum.

3.3.8 National Transportation Research Center FTIR Spectrometer

Gas analysis at NTRC is performed by an MKS MultiGas2030 Continuous Gas Analyzer Fourier transform infrared spectrometer (FTIR). The spectrometer collects infrared spectra at a set sampling interval and compares them against preloaded reference spectra in the accompanying software to determine the concentration of target species as a function of time. The results of the measurements are saved to text files for data analysis. The FTIR at NTRC is capable of measuring concentrations of NO, NO_2, N_2O, and NH_3 on the order of parts per million.

3.3.9 Data Acquisition System

The BFR is controlled by LabVIEW operating on a Dell PC. Inside the LabVIEW program a virtual interface (VI) is constructed which allows the user to control the set point of MFCs and, in the case of LNT evaluation, to govern the switching valve used to alternate between lean and rich flow conditions. Feedback from thermocouples and pressure transducers is visually displayed in the VI. Additionally, at UTK the measurements obtained by the gas analyzers are also displayed in the VI. All data gathered by the program are saved into text files for data analysis.

3.4 Bench Flow Reactor Startup and Performance Evaluations

This section begins by outlining the startup procedures for BFR operation at UTK and NTRC, and then describes the evaluation protocols used for each catalyst.

3.4.1 Bench Flow Reactor Startup Procedures

BFR startup for both the UTK and NTRC BFRs begins by turning on the heat tapes, steam generator furnace, and reactor furnace. At UTK, the gas analyzers are calibrated while waiting for the system to warm up. For SCR and LNT evaluations a gas cylinder containing 1000 ppm NO in ultra-high purity (UHP) N_2 is used to calibrate the NO_x analyzers. DOC evaluations require that the HC analyzer be given two hours to stabilize the flame after ignition, and calibration is performed with a bottle of 300 ppm C_3H_8 in UHP N_2. While operating the BFR at NTRC, time waiting for the heat tapes to warm is used to prepare the FTIR for operation. The detector must be filled with liquid nitrogen, and a background spectrum must be acquired while flowing pure N_2 through the sample cell. The remainder of the startup procedure is identical for both BFRs.

After the BFR system reaches the required temperature, a flow of N_2 is introduced at 1.0 LPM through the bypass line and the vacuum pump is activated to prevent pressure buildup. Once the pump is operational simulated diesel exhaust gas containing N_2, O_2, CO_2 is introduced to the bypass. The water pump is also activated to allow water vapor into the system. Before flowing through the reactor, concentration measurements of the target species for the catalyst being

evaluated are made. For SCR and LNT evaluations this includes NO, NO_2, and NH_3, while for DOC evaluations CO and HC concentrations are measured. These values are recorded and will be used as references while calculating conversion percentages. Once this process is complete, a simulated diesel exhaust flow consisting of N_2, O_2, CO_2, and water vapor is directed through the reactor and the furnace temperature is adjusted until the thermocouple at the middle of the catalyst sample reaches the initial evaluation temperature. At this point performance evaluations may begin.

3.4.2 De-greening of Fresh Catalysts

Prior to performance evaluations for fresh SCR, LNT, and DOC samples it is necessary to perform a de-greening of the catalyst. This process ensures that the catalyst is stable and that experimental results will be repeatable. De-greening is performed at a GHSV of 30,000 h^{-1} with a flow composition consisting of 5% H_2O, 14% O_2, and N_2 balance.

3.4.3 SCR Performance Evaluations

Performance evaluations of fresh and engine-aged Cu-zeolite SCR catalysts are done according to the CLEERS transient SCR protocol shown in Table 3.4.1. SCR evaluations are always performed with a 3-in core at a GHSV of 30,000 h^{-1}.

Table 3.4.1 CLEERS transient SCR protocol for SCR evaluations.

Step	Gas concentrations	Temperature	Description
0(a)	14% O_2	650ºC	Pretreat
0(b)	14% O_2	650ºC → 150ºC	Cool
0(c)	350ppm NH_3	150 ºC	NH_3 adsorption
0(d)		150ºC → 650ºC	NH_3 TPD (10ºC/min)
0(e)	14% O_2	650ºC	Pretreat
1(a)	14% O_2	650ºC → T(n)	Cool
1(b)	350ppm NH_3, 14% O_2	T(n)	NH_3 storage, NH_3 oxidation
1(c)	175ppm NO, 175ppm NO_2, 350 ppm NH_3, 14% O_2	T(n)	NO+NO2 SCR α = 1.0
1(d)	350ppm NO, 350ppm NH_3, 14% O_2	T(n)	NO SCR α = 1.0
1(e)	350ppm NO, 315ppm NH_3, 14% O_2	T(n)	NO SCR α = 0.9
1(f)	350ppm NO, 385ppm NH_3, 14% O_2	T(n)	NO SCR α = 1.1
1(g)	350ppm N, 14% O_2	T(n)	NO storage, NO oxidation
2(a)	14% O_2	T(n) → T(n-1)	Cool
…	Repeat (a-g) for all temperatures	T(n-1)…150 ºC	
n(g)	350ppm NO, 14% O_2	150ºC	NO storage, NO oxidation
n+1(a)		150ºC → 650ºC	TPD (10ºC/min)

Note: all steps includes 5% CO_2, 5% H_2O

Prior to SCR evaluation, an NH_3 adsorption test is performed at 150ºC, followed by a temperature programmed desorption (TPD) at a heating rate of 10ºC/min up to 650ºC. During the adsorption the flow consists of 5% H_2O, 5% CO_2, 350 ppm NH_3, and N_2 balance. During the TPD NH_3 is removed from the flow, but otherwise the composition is unchanged. Following the TPD the catalyst is pretreated with 5% H_2O, 5% CO_2, 14% O_2, and N_2 balance to remove any remaining NH_3 possibly stored in the catalyst.

The SCR performance evaluations consist of six phases which are repeated at 600, 500, 400, 300, 250, 200, and 150ºC. All six phases include 5% H_2O, 5% CO_2, 14% O_2, and N_2 in the simulated diesel exhaust gas. During the NH_3 storage and oxidation evaluation, 350 ppm NH_3 is introduced to the flow. This phase is followed by a fast SCR reaction evaluation during which 175 ppm

NO and 175 ppm NO_2 are added to the 350 ppm NH_3 in the exhaust gas. In phases 3-5 the flow includes 350 ppm NO and 315-385 ppm NH_3 to investigate the standard SCR reaction and the effect of the NH_3/NO ratio on NO_x performance. Finally, in the sixth phase NH_3 is removed while the 350 ppm NO remains to examine NO to NO_2 oxidation over the catalyst. The objective of this protocol is to provide a wealth of knowledge about the performance of the catalyst and any mechanisms which could reflect influence changes in performance for engine-aged Cu-zeolite SCR catalysts.

3.4.4 LNT Performance Evaluations

LNT evaluations are performed at 200, 300, and 400ºC on a 3-in sample with a GHSV of 30,000 h^{-1}. The evaluation cycle consists of a 60s lean phase followed by a 5s rich phase. During the lean phase the simulated diesel exhaust consists of 5% H_2O, 5% CO_2, 10% air, 300 ppm NO, and N_2 balance. The rich phase flow composition is comprised of 5% H_2O, 5% CO_2, 1.13% CO, 0.68% H_2, 300 ppm NO, and N_2 balance. Steady state is defined as the point at which the average cycle-to-cycle NO_x concentration remains unchanged for five minutes.

3.4.5 DOC Performance Evaluations

DOC performance evaluations are conducted on a 2-in core with a GHSV of 80,000 h^{-1}. The catalysts are evaluated in the temperature range from 200 to 400°C in 25°C increments to ensure that the temperatures required to reach 50 and 80% conversion, or the T-50 and T-80 light-off temperatures, respectively, can be accurately identified from performance curves. Simulated diesel exhaust

gas during DOC evaluations consists of 5% CO_2, 10% H_2O, 10% O_2, 1000 ppm NO, 500 ppm CO, 300 ppm C_2H_4, and N_2 balance. With this flow composition it is possible to identify HC conversion, CO conversion, and NO to NO_2 oxidation capability of the catalysts.

3.5 Materials Characterization Techniques

A number of materials characterization techniques were utilized in the current study to investigate physical and chemical changes in the catalyst. Section 3.5.1 describes electron probe microanalysis (EPMA), while Section 3.5.2 discusses inductively coupled plasma (ICP) mass spectrometry. Section 3.5.3 details scanning electron microscopy (SEM) and energy dispersive spectroscopy (EDS), followed by Section 3.5.4 which describes scanning transmission electron microscopy (STEM). In Section 3.5.5 the process for BET surface area measurements is outlined, and the section concludes in Section 3.5.6 with a discussion of diffuse-reflective infrared Fourier transform spectroscopy (DRIFTS).

3.5.1 Electron Probe Microanalysis

Electron probe microanalysis (EPMA) is used to determine the chemical composition of SCR, LNT, DOC, and DPF samples through the acquisition of physical maps called micrographs and quantitative measurements known as line scans. Samples are placed inside an ultra-high vacuum chamber and bombarded

by a finely focused beam of electrons which upon contact with the sample surface energizes electrons to a higher unstable energy state. When these excited electrons return to their normal energy state X-ray radiation and dislocated electrons are released and measured by detectors. Each element possesses unique states of energy and by measuring the wavelengths of the emitted X-rays it is possible to identify which elements are present and in what concentration.

The instrument utilized in this study is a Cameca Model SC-52 EPMA device and is located at the University of Tennessee. An image of this device is shown in Figure 3.5.1.

Figure 3.5.1 Cameca SC-52 EPMA device [17, p. 58]**.**

The intensities of dislocated electrons are measured by a backscatter detector which creates a qualitative plot of average atomic number. Backscatter images are used to easily identify materials changes such as cracking or dealumination in the catalyst. Five wavelength-dispersive spectrometers on the EPMA device measure the X-ray radiation released and make it possible to plot both line scans and elemental micrographs of the catalyst. Line scans are plots of the elemental concentration against location taken at 3 μm intervals from the cordierite substrate through the washcoat to the surface. Elemental micrographs are images which show a qualitative distribution of elements in the catalyst. The elements chosen for analysis differ from catalyst to catalyst, although all scans typically include Na, K, S, and P as these are typical contaminants associated with engine aging and biodiesel use.

Preparation of EPMA samples is crucial to the accuracy of the analysis. The ideal surface for analysis is flat, smooth, and polished. SCR, LNT, DOC, or DPF samples are cut and placed in a 1-in rubber ring and covered in epoxy. A vacuum pump is used to pump down the samples in order to remove as many air bubbles as possible. The epoxy is allowed to harden overnight before the front 1 mm of the samples is removed with a low-speed Buehler Minimet diamond saw. The samples are sanded by hand and then polished with diamond polish to a 1 μm finish.

3.5.2 Inductively Coupled Plasma Spectroscopy

Inductively coupled plasma (ICP) mass spectroscopy is a technique used to detect and measure the concentration of elements within a sample [81]. A torch sustains the inductively coupled plasma and the sample is typically transported to the plasma by an argon gas stream. The plasma atomizes and immediately ionizes the analyte elements in the sample. The ions produced by the plasma are then sampled and extracted from the plasma and measured in a quadrupole mass spectrometer to determine the concentration of the target elements based on reference materials.

In the current study ICP was used to measure the relative concentrations of Na in the accelerated Na-aged SCR catalysts. Powder samples of the SCR catalysts between 5 and 10g in mass were shipped to American Assay Laboratories (AAL) where the ICP mass spectroscopy was performed. AAL digested the powder samples into a solution and performed ICP using a Bruker ICP-MS to measure concentrations of Na.

3.5.3 Scanning Electron Microscopy and Energy Dispersive Spectroscopy

Scanning electron microscopy (SEM) and energy dispersive spectroscopy (EDS) function in a similar fashion to EPMA. A sample in a UHV chamber is bombarded with a high-energy electron beam resulting in the release of electrons and X-ray radiation. A detector counts the number of incident particles on the detector for each discretized area of the sample. The total number of counts is interpreted by a computer which allocates numerical values to an image

generating routine to display an image based on the relative X-ray and electron intensities [1]. This method produces two forms of information in the form of secondary and backscattered electrons. Backscattered electrons are incident electrons which have been deflected into the detector. The intensity of these reflected electrons corresponds to the atomic number of elements in the sample. Secondary electrons are electrons emitted from the atoms at the top surface of the sample and yield information related to surface morphology and topography.

EDS is a crucial utility of SEM machines which is used to measure the concentration of elements present in the top atomic layers of the sample surface. Like in EPMA, the X-rays emitted by the surface are unique to each element and therefore by detecting the energy emitted in these X-rays it is possible to create energy spectra with which to elements can be identified [82].

The SEM used for the current study is located in the High Temperature Materials Laboratory (HTML) at the Oak Ridge National Laboratory (ORNL). This machine is a Hitachi 4800 FEG-SEM with an EDAX Apollo XL detector. SEM was performed on both the light-duty configuration accelerated Na-aged beta Cu-zeolite SCR samples and the Cu-chabazite SCR samples which were engine-aged by NREL using B20 fuel with 14 ppm Na in order to study the distribution of Na contamination in the SCR catalysts which were exposed to elevated levels of Na during aging processes.

3.5.4 Scanning Transmission Electron Microscopy

Scanning transmission electron microscopy (STEM) functions in a slightly different way than SEM. In TEM, a beam of electrons is focused by electromagnetic lenses into a fine beam which is directed at an ultra-thin sample. When this beam passes through the sample, some electrons are scattered while some transmit through the sample onto a fluorescent screen. An image is formed by the transmitted electrons and is then digitized with a camera for analysis [17].

A Hitachi HF-3300 cold FE-STEM/TEM located at HTML on the ORNL campus is used in the current study. This TEM is equipped with a cold field emission electron source which aids in nanoscale analysis due to its high energy resolution and brightness. A photograph of this machine is shown in Figure 3.5.2.

Figure 3.5.2 TEM used for fresh and engine-aged LNT analysis.

The TEM in this study was used to investigate the possibility of PGM sintering in the NREL engine-aged LNT samples.

3.5.5 BET Surface Area Measurements

BET is a technique used to determine the surface area of porous materials which is named after Stephen Brunauer, Paul Hugh Emmett, and Edward Teller, who first published an article on the subject [83]. The theory is based on the Langmuir equation for monolayer adsorption, given as Eq. 3.5.1, which relates the adsorption of molecules on a solid surface to the concentration of concentration of a medium above that solid surface at a fixed temperature.

$$\theta = \frac{\alpha P}{1 + \alpha P} \tag{3.5.1}$$

In this equation, θ is the fraction coverage of the surface, α is a constant, and P is the gas pressure or concentration.

The BET theory extends the Langmuir theory from monolayer to multilayer adsorption using the following three hypotheses: gas molecules physically adsorb on a solid in layers infinitely, there is no interaction between each adsorption layer, and the Langmuir theory can separately be applied to each adsorption layer. The resulting BET equation based on these hypotheses is shown in Eq. 3.5.2.

$$\frac{1}{v[(P_0/P) - 1]} = \frac{c - 1}{v_m c}\left(\frac{P}{P_0}\right) + \frac{1}{v_m c} \tag{3.5.2}$$

In this equation, P and P_0 are the equilibrium and saturation pressures of the adsorbates at the adsorption temperature, v is the adsorbed gas quantity, v_m is the monolayer adsorbed gas quantity, and c is the BET constant calculated with Eq. 3.5.3.

$$c = exp\left(\frac{E_1 - E_L}{RT}\right) \tag{3.5.3}$$

E_1 and E_L are the heats of adsorption in the first and succeeding monolayers, respectively, while R is the ideal gas constant and T is the adsorption temperature. The BET plot is constructed by plotting the left-hand side of Equation 3.5.2 against P/P_0. The slope of this plot is equal to $\frac{c-1}{v_m c}$ and may be approximated as $\frac{1}{v_m}$ since c is always much greater than one. Once the value of v_m is known it is simple to calculate the BET surface area according to Eq. 3.5.4.

$$A_{BET} = \frac{v_m N}{s} \tag{3.5.4}$$

In this equation, N is the Avogadro's number and s is the cross sectional area of the adsorbate gas.

BET surface area analysis for this study is performed at the National Transportation Research center and is applied to powdered samples from the fresh, control and accelerated Na-aged SCR catalysts. Ar is used as the adsorbant at concentrations ranging from 1.5% to 7.5% with He as the balance gas for a total flow rate of 100 sccm. The sample is lowered into a liquid nitrogen bath and once adsorption is completed the sample is removed and allowed to

return to room temperature. Concentration data is collected with a Stanford Research System Residual Gas Analyzer (SRS-RGA 100) mass spectrometer.

3.5.6 Diffuse-Reflective Infrared Fourier Transform Spectroscopy

The diffuse-reflective infrared Fourier Transform spectroscopy (DRIFTS) setup used in the current study has previously been described in detail elsewhere, and is specifically designed for in situ analysis of sample surfaces in a temperature controlled gas cell environment as shown in Figure 3.5.3 [84].

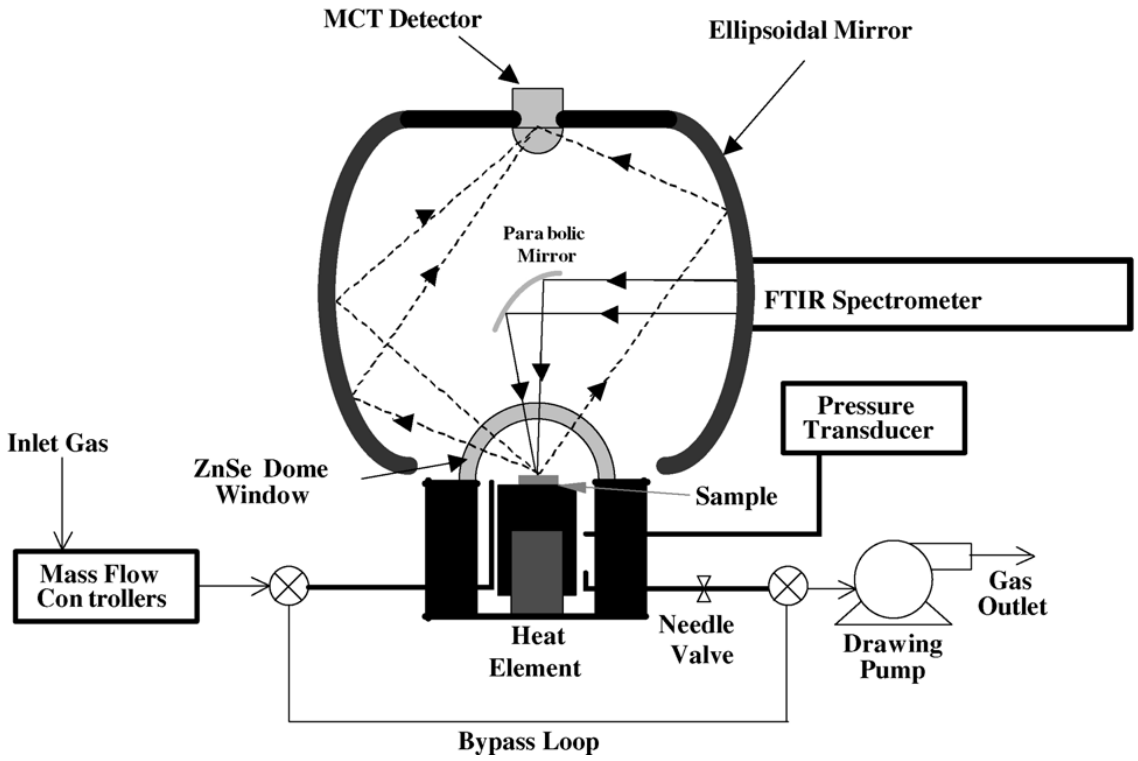

Figure 3.5.3 DRIFTS setup for SCR surface analysis [84, p. 247]**.**

The system consists of a Harrick Scientific ellipsoidal DRIFT accessory coupled to a MIDAC model M2500 FTIR spectrometer. A collimated infrared beam is emitted by the FTIR and focused by a parabolic mirror onto the sample surface which is positioned at one focus of the barrel ellipsoid, while an Infra Red Associates mercury-cadmium-telluride (MCT) detector is positioned at the opposing focus. The ellipsoidal mirror maximizes detection of light diffusely scattered at azimuthal angles from the sample surface while at the same time the parabolic focusing mirror blocks detection of specularly reflected light. Spectra generated from the collected infrared light are converted to absorbance units for analysis.

Samples for DRIFTS analysis in this investigation are taken from fresh and accelerated Na-aged Cu-zeolite SCR catalysts. A small piece of catalyst is trimmed from a core and gently sanded in order to ensure the analysis surface is as flat as possible. Samples are placed into a vacuum reaction chamber and are heated by a 100W Chromalox cartridge heater for temperature control. The reaction chamber is covered by a zinc selenide (ZnSe) dome through which the infrared light passes. A type K thermocouple placed directly on the sample surface measures temperature, while a manifold of Tylan General FC-280S MFCs provides the gas mixture consisting of 10% O_2, 300 ppm NO_x, Ar balance, and in the 'wet' case 5% H_2O to the sample chamber. The objective of the DRIFTS work in this study is to identify adsorbed NO, NO_2, and nitrate species on the SCR catalyst surface.

3.6 Mathematical Modeling of Cu-zeolite SCR

Section 3.6 presents a discussion of the mathematical model used to predict results of Cu-zeolite SCR performance evaluations. Section 3.6.1 provides a summary of the model along with a brief description of the equations and chemical reactions included in the model. Sections 3.6.2 to 3.6.5 provide derivations for the gas phase energy balance, gas phase species balance, solid phase energy balance, and solid phase species balance equations, respectively. Finally, the section concludes in Section 3.6.6 with a brief description of the ODE solver implemented in Fortran.

3.6.1 Overview of Fortran SCR Model

The Fortran model used in the current study was developed by Gao et al. [85] at the National Transportation Research Center. It simulates SCR reactions in a single monolith channel of a plug flow reactor under the assumptions of one-dimensional, fully-developed laminar flow for a 6-in catalyst length and a time span of 180s. The differential equations used to solve for temperature and reactant concentrations are the gas phase energy balance, gas phase species balance, solid phase energy balance, and solid phase species balance given in Eqs. 3.6.1-3.6.4, respectively [15, 85].

$$\rho_g c_{pg} \varepsilon \left(\frac{\partial T_g}{\partial t} + u_g \frac{\partial T_g}{\partial z} \right) = h_g G_m \left(T_s - T_g \right) \tag{3.6.1}$$

$$\frac{\partial x_{g_i}}{\partial t} + u_g \frac{\partial x_{g_i}}{\partial z} = \frac{h_m G_m}{\varepsilon} \left(x_{s_i} - x_{g_i} \right) \tag{3.6.2}$$

$$\rho_s c_{ps}(1-\varepsilon)\frac{\partial T_s}{\partial t} = k_s(1-\varepsilon)\frac{\partial^2 T_s}{\partial z^2} + h_g G_m\left(T_g - T_s\right) + h_a G_a(T_a - T_s) + \sum_{k=1}^{n} R^k \cdot \Delta H^k \tag{3.6.3}$$

$$\frac{\partial x_{s_i}}{\partial t} = \frac{h_m G_m}{\varepsilon'(1-\varepsilon)}\left(x_{g_i} - x_{s_i}\right) + \frac{1}{\rho_m \varepsilon'(1-\varepsilon)}\sum_k \alpha_i^k R^k \tag{3.6.4}$$

The symbols are described in Table 3.6.1.

Included in the model are the three SCR reactions (Eqs. 1.5.1-1.5.3) and NO to NO_2 oxidation (Eq. 1.5.9), along with NH_3 surface adsorption and surface reaction according to Eqs. 3.6.5 and 3.6.6 where *S* represents a surface site.

$$NH_3 + S \Leftrightarrow NH_3S \tag{3.6.5}$$

$$2NH_3S + 1.5O_2 \Leftrightarrow N_2 + 3H_2O + 2S \tag{3.6.6}$$

Reaction rates, *R*, for these equations are obtained according to Eqs. 3.6.7-3.6.12

$$R_{std-SCR} = k_{std-SCR} C_{NO} \theta_{NH_3S} \Psi_{NH_3} \tag{3.6.7}$$

$$R_{fast-SCR} = k_{fast-SCR} C_{NO} C_{NO_2} \theta_{NH_3S} \Psi_{NH_3} \tag{3.6.8}$$

$$R_{slow-SCR} = k_{slow-SCR} C_{NO_2} \theta_{NH_3S} \Psi_{NH_3} \tag{3.6.9}$$

$$R_{NH_3-S} = k_{NH_3-S,f} C_{NH_3}\left(1-\theta_{NH_3S}\right)\Psi_{NH_3} - k_{NH_3-S,b} C_{NH_3} \theta_{NH_3S} \Psi_{NH_3} \tag{3.6.10}$$

$$R_{NH_3S-O_2} = k_{NH_3S-O_2} C_{O_2} \theta_{NH_3S} \Psi_{NH_3} \tag{3.6.11}$$

$$R_{NO-O_2} = k_{NO-O_2,f} C_{NO} C_{O_2}^{0.5} - k_{NO-O_2,f} C_{NO_2} / K_{eq,NO-O_2} \tag{3.6.12}$$

In these equations *C* represents mole concentration, *θ* represents coverage of adsorption, and *Ψ* is ammonia storage capacity per unit volume. The initial reaction rate parameters used in the model are shown in Table 3.6.2.

Table 3.6.1 Symbol key for energy and species balance equations.

Symbol	Definition	Units
T_g	gas temperature	*K*
T_s	solid temperature	*K*
T_a	ambient air temperature around catalyst	*K*
ρ_g	gas mass density	*kg/m^3*
c_{pg}	gas specific heat	*J/kg-K*
ε	hole space fraction of monolith	*N/A*
h_g	gas heat transfer coefficient	*W/m^2-K*
G_m	specific surface area per volume of monolith	*1/m*
u_g	exhaust gas velocity	*m/s*
x_{g_i}	mole fraction of species *i* in gas phase	*N/A*
x_{s_i}	mole fraction of species *i* in solid surface phase	*N/A*
h_m	mass transfer coefficient	*m/s*
ρ_s	solid wall density	*kg/m^3*
c_{ps}	solid wall specific heat	*W/m^2-K*
k_s	Sold wall thermal conductivity	*W/K*
h_a	heat transfer coefficient between ambient air and catalyst surface	*W/m^2-K*
G_a	specific external heat transfer surface per volume	*W/m^2*
R^k	*k*-step chemical reaction rate	*mol/s*
ΔH^k	Heat generated at chemical reaction *k*	*W*
ρ_m	gas mole density	*mol/m^3*
α_i^k	Stoichiometric coefficient of species *i* in *k*-step chemical reaction	*N/A*
ε'	Effective porosity of channel wall surface	*N/A*

Table 3.6.2 Constants of reaction rates employed in SCR model.

Rate Constant	Pre-exponential Factor	Activation Energy (J/mol)
$k_{std-SCR}$	2.3×10^{8}	85.0×10^{3}
$k_{fast-SCR}$	1.9×10^{12}	85.0×10^{3}
$k_{slow-SCR}$	1.0×10^{6}	55.0×10^{3}
$k_{NH_3-S,f}$	0.93	0
$k_{NH_3-S,b}$	1.0×10^{11}	$181.5 \times 10^{3} \times (1 - 0.98\theta_{NH_3S})$
$k_{NH_3S-O_2}$	1.2×10^{11}	162.4×10^{3}
$k_{NO-O_2,f}$	2.0×10^{4}	48.0×10^{3}

3.6.2 Gas-Phase Energy Balance

The gas-phase energy balance assumes that no reactions occur in the gas phase, and therefore no term for heat generated by gas-phase chemical reactions is included.

Heat accumulated due to gas flow through control volume

$$= Q_V \rho_g c_{pg} \varepsilon \Delta T_g \tag{3.6.13}$$

Heat added to the gas-phase from surface convection

$$= h_g A_s \left(T_s - T_g\right) \tag{3.6.14}$$

Time rate of change in gas -phase energy content

$$= \Delta V \rho_g c_{pg} \varepsilon \frac{\partial T_g}{\partial t} \tag{3.6.15}$$

Thus, the overall energy balance in the gas-phase is

$$Q_V \rho_g c_{pg} \varepsilon \Delta T_g + \Delta V \rho_g c_{pg} \varepsilon \frac{\partial T_g}{\partial t} = h_g A_s \left(T_s - T_g\right) \tag{3.6.16}$$

Dividing this equation by ΔV gives

$$u_g \rho_g c_{pg} \varepsilon \frac{\Delta T_g}{\Delta z} + \rho_g c_{pg} \varepsilon \frac{\partial T_g}{\partial t} = h_g G_m \left(T_s - T_g\right) \tag{3.6.17}$$

Finally, taking the limit as $\Delta z \to 0$ gives the overall gas-phase energy balance.

$$\rho_g c_{pg} \varepsilon \left(\frac{\partial T_g}{\partial t} + u_g \frac{\partial T_g}{\partial z} \right) = h_g G_m \left(T_s - T_g\right) \tag{3.6.18}$$

3.6.3 Gas-Phase Species Balance

The gas-phase energy balance assumes that no reactions occur in the gas phase, and therefore no term for species *i* produced or reacted due to gas-phase chemical reactions is included.

Change in mole fraction of species *i* due to gas flow through control volume

$$= Q_V \varepsilon \Delta x_{g_i} \tag{3.6.19}$$

Change in mole fraction of species *i* due to transport from catalyst surface

$$= h_m A_s \left(x_{s_i} - x_{g_i} \right) \tag{3.6.20}$$

Time rate of change in mole fraction of species *i*

$$= \Delta V \varepsilon \frac{\partial x_{g_i}}{\partial t} \tag{3.6.21}$$

Putting these terms together gives the overall energy balance

$$\Delta V \varepsilon \frac{\partial x_{g_i}}{\partial t} + Q_V \varepsilon \Delta x_{g_i} = h_m A_s \left(x_{s_i} - x_{g_i} \right) \tag{3.6.22}$$

Dividing this equation by ΔV and taking the limit as $\Delta z \to 0$, along with moving ε to the other side, gives

$$\frac{\partial x_{g_i}}{\partial t} + u_g \frac{\partial x_{g_i}}{\partial z} = \frac{h_m G_m}{\varepsilon} \left(x_{s_i} - x_{g_i} \right) \tag{3.6.23}$$

3.6.4 Solid-Phase Energy Balance

The solid-phase energy balance assumes that conduction heat transfer varies in the *z*-direction only, and that convection heat transfer occurs both internally with flowing gases and externally with ambient air.

Energy from conduction heat transfer along catalyst surface

$$= A_c k_s (1-\varepsilon)\frac{\partial T_s}{\partial z} \tag{3.6.24}$$

Energy from convection heat transfer with flowing gas

$$= h_g A_s \left(T_g - T_s\right) \tag{3.6.25}$$

Energy from convection heat transfer with external ambient air

$$= h_a A_a (T_a - T_s) \tag{3.6.26}$$

Energy due to chemical reaction *k*

$$= \Delta V \sum_{k=1}^{n} R^k \cdot \Delta H^k \tag{3.6.27}$$

Time rate of change of energy in the solid-phase control volume

$$= \Delta V \rho_g c_{pg} (1-\varepsilon)\frac{\partial T_s}{\partial t} \tag{3.6.28}$$

The overall energy balance after combining terms is

$$\Delta V \rho_g c_{pg} (1-\varepsilon)\frac{\partial T_s}{\partial t} = A_c k_s (1-\varepsilon)\frac{\partial T_s}{\partial z} + h_g A_s \left(T_g - T_s\right) + h_a A_a (T_a - T_s) + \Delta V \sum_{k=1}^{n} R^k \cdot \Delta H^k \tag{3.6.29}$$

Dividing this equation by ΔV gives

$$\rho_g c_{pg}(1-\varepsilon)\frac{\partial T_s}{\partial t} = k_s(1-\varepsilon)\frac{1}{\Delta z}\frac{\partial T_s}{\partial z} + h_g G_m\left(T_g - T_s\right) + h_a G_a(T_a - T_s) + \sum_{k=1}^{n} R^k \cdot \Delta H^k \tag{3.6.30}$$

Taking the limit as $\Delta z \to 0$ gives energy balance in the solid phase as

$$\rho_g c_{pg}(1-\varepsilon)\frac{\partial T_s}{\partial t} = k_s(1-\varepsilon)\frac{\partial^2 T_s}{\partial z^2} + h_g G_m\left(T_g - T_s\right) + h_a G_a(T_a - T_s) + \sum_{k=1}^{n} R^k \cdot \Delta H^k \tag{3.6.31}$$

3.6.5 Solid-Phase Species Balance

The solid-phase species balance accounts for transport between the gas phase and the catalyst surface, along with species *i* generated or consumed by chemical reaction.

Change in mole fraction of species *i* due chemical reaction

$$= \frac{\Delta V}{\rho_m}\sum_k \alpha_i^k R^k \tag{3.6.32}$$

Change in mole fraction of species *i* due to transport from gas phase

$$= h_m A_s\left(x_{g_i} - x_{s_i}\right) \tag{3.6.33}$$

Time rate of change in mole fraction of species *i*

$$= \Delta V \varepsilon'(1-\varepsilon)\frac{\partial x_{s_i}}{\partial t} \tag{3.6.34}$$

Combining terms gives the overall surface species balance as

$$\Delta V \varepsilon'(1-\varepsilon)\frac{\partial x_{s_i}}{\partial t} = h_m A_s\left(x_{g_i} - x_{s_i}\right) + \frac{\Delta V}{\rho_m}\sum_k \alpha_i^k R^k \tag{3.6.35}$$

Dividing this equation by ΔV and rearranging terms produces the solid-phase species balance as

$$\frac{\partial x_{s_i}}{\partial t} = \frac{h_m G_m}{\varepsilon'(1-\varepsilon)}\left(x_{g_i} - x_{s_i}\right) + \frac{1}{\rho_m \varepsilon'(1-\varepsilon)}\sum_k \alpha_i^k R^k \tag{3.6.36}$$

3.6.6 Livermore ODE Solver

The Livermore Solver for Ordinary Differential Equations (LSODE) is a Fortran subroutine package written by Alan C. Hindmarsh of the Center for Applied Scientific Computing at the Lawrence Livermore National Laboratory, with details available elsewhere [86]. The solver is designed to determine a numerical solution of an initial value problem for a system of first-order ordinary differential equations (ODE). In general such a system can be written in the form shown in Eqs. 3.6.37-3.6.38.

$$\underline{\dot{y}} \equiv \frac{d\underline{y}}{d\xi} = \underline{f}\left(\underline{y}(\xi), \xi\right) \tag{3.6.37}$$

$$\underline{y}(\xi_0) = \underline{y}_0 \tag{3.6.38}$$

In the above equations $\underline{y}$, $\underline{y}_0$, $\underline{\dot{y}}$, and $\underline{f}$ are column vectors containing N (≥1) components and ξ is the independent variable. The equations can be written in

component form according to Eqs. 3.6.39-3.6.40.

$$\frac{dy_i(\xi)}{d\xi} = f_i(y_1(\xi), \dots, y_N(\xi), \xi) \tag{3.6.39}$$

$$y_i(\xi_0) = y_{i,0} \tag{3.6.40}$$

The initial value problem is to find the solution function $\underline{y}$ at the desired values of ξ on the interval $[\xi_0, \xi_{end}]$ where $\underline{y}_0$ at $\xi = \xi_0$ is known.

A key feature of the LSODE algorithm is its ability to solve “stiff” ODEs. “Stiff” ODEs are ODEs in which the target solution is varying slowly, but nearby solutions are changing rapidly. This requires that the numerical solver take small steps in order to obtain accurate results. In the Fortran code developed by Gao et al. [85] the LSODE solver is used to numerically determine temperature and species concentrations starting with initial values for surface temperature, gas temperature, and species concentrations. Stiffness can be an issue in this SCR model due to the fact that species concentrations can vary rapidly before approaching steady-state values with little to no variation.

CHAPTER IV

RESULTS AND DISCUSSION

This chapter contains a discussion of the results obtained during the current investigation. Section 4.1 addresses the performance and materials characterization of fresh and engine-aged LNT samples which were not involved in the accelerated Na-aging protocols. In Section 4.2 results of EPMA analysis on both the GM engine-aged and accelerated Na-aged DPFs are highlighted. Performance evaluations and materials characterization of fresh, GM engine-aged, and accelerated Na-aged DOC samples are given in Section 4.3. Finally, the chapter concludes in Section 4.4 with an in depth discussion on the impact Na has on the performance and materials characterization of accelerated Na-aged Cu-zeolite SCR relative to fresh samples, along with an analysis of the trends observed during mathematical modeling of the SCR.

4.1 Fresh and Engine-aged LNT

This section discusses the performance evaluations and materials characterization of fresh and engine-aged LNT catalysts. Section 4.1.1 describes the engine-aging details of the LNT provided by NREL, while Section 4.1.2 is focused on the results of NO_x performance evaluations for both the fresh and engine-aged samples. Finally, in Section 4.1.3 the results of EPMA and STEM analysis on the engine-aged LNT are discussed.

4.1.1 Engine-aging of LNT

The engine-aged LNT is provided by Delphi Umicore through an NREL study, and was part of an aftertreatment system consisting of an upstream DOC and a downstream DPF. The engine used for aging was an in-line 4 cylinder, turbocharged, common-rail system direct injected engine, with details available elsewhere [87-88]. During aging, the engine was operated with in-specification B20 fuel and the LNT was aged to end of life conditions. No further details regarding the aging process were provided by NREL.

4.1.2 Performance Evaluations

Although no LNT catalysts were involved in the accelerated Na-aging study, analysis of the fresh and engine-aged LNTs is included to illustrate the distribution of Na contamination in a catalyst after normal engine-aging exposure, and to introduce thermal aging effects. In general it is not expected that Na would contribute to the deactivation of an LNT based on the studies discussed in Chapter 2 [72-73]. BFR performance evaluation of LNT catalysts results in transient NO_x concentrations across lean/rich cycles such as those shown for the evaluation of a fresh LNT at 300ºC shown in Figure 4.1.1. The troughs in the plot correspond to storage during the lean phase, while the large NO_x excursions forming the peaks represent the rich phase. Conversion is calculated based on the average total NO_x concentration measured during the last five cycles.

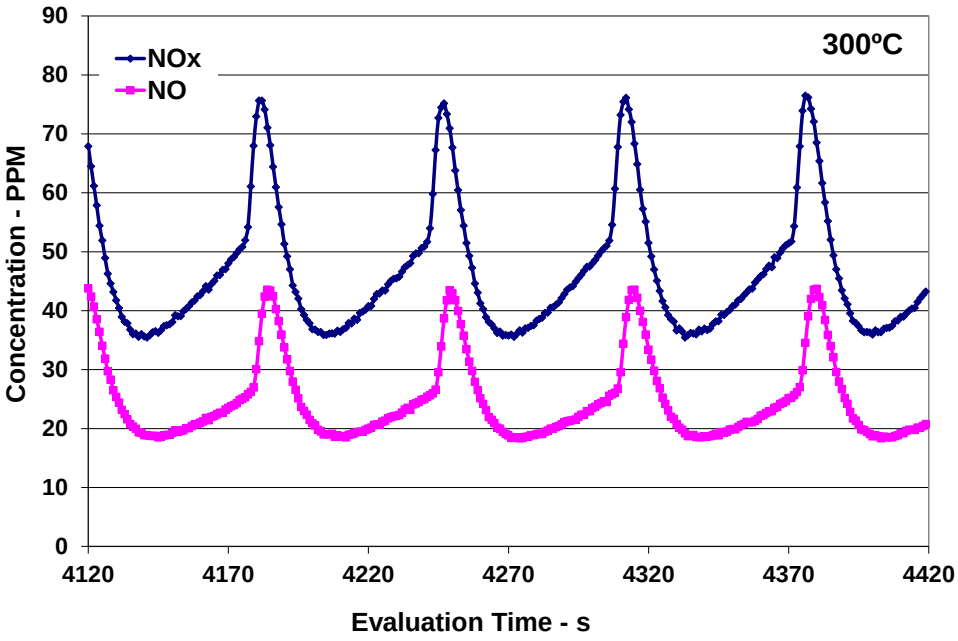

Figure 4.1.1 NO_x concentration in fresh LNT during last five evaluation cycles at 300ºC.

The NO_x performance of the engine-aged LNT catalyst, both front and rear halves, as received from NREL, is shown in Figure 4.1.2. Initially, conversion is reduced by as much as 35% in the front half and 25% in the rear half relative to the fresh sample. However, by subjecting the engine-aged LNT to 1h under lean conditions at 600ºC for soot oxidation followed by desulfation at 4h under rich conditions at 700ºC significant performance recovery is seen in both halves, as shown in Figure 4.1.3. This performance recovery effect is most evident during evaluations at 300 and 400 ºC, where conversion is highest even for the fresh catalyst. Similar results were obtained by Cheng et al. [71] while investigating the impact of thermal aging on LNT catalysts. In their studies, they determined

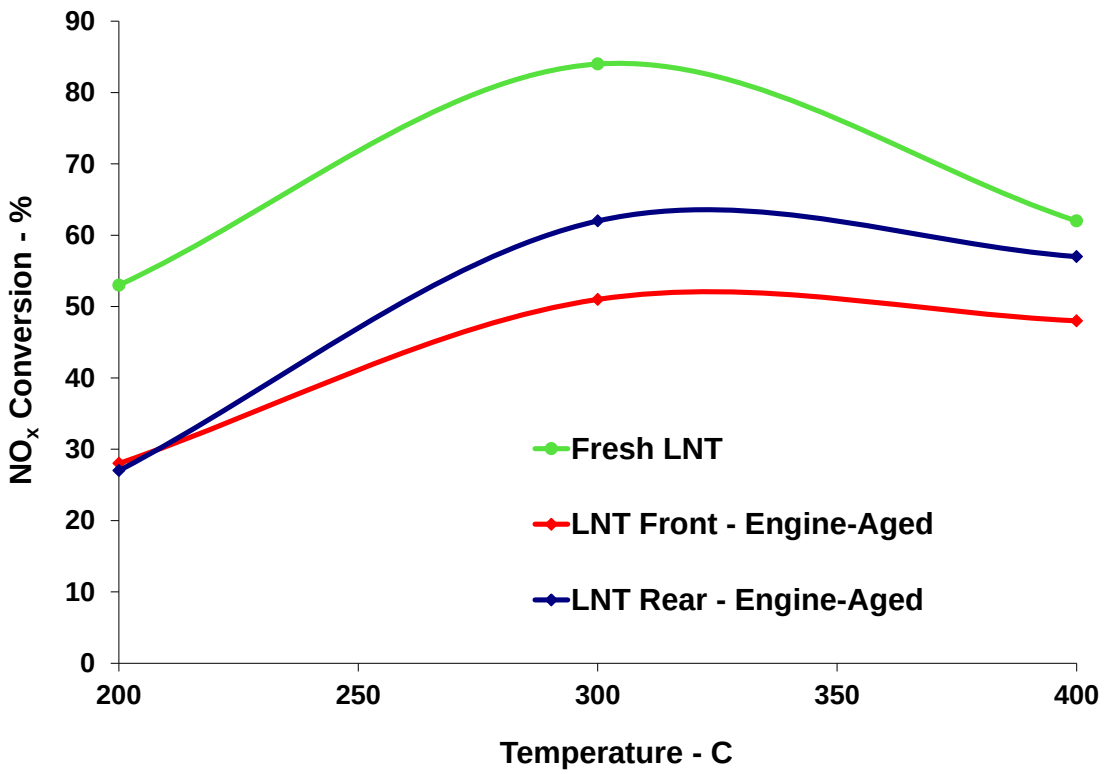

Figure 4.1.2 NO_x conversion over fresh and engine-aged LNTs.

that sulfur removal treatments reversed performance losses, while thermal aging effects were permanent. Additionally, high temperature LNT performance is limited by stable storage sites while low temperature conversion is limited by catalytic activity [73]. This view is reflected in the results presented here, as desulfation was shown to recover high temperature performance, but low temperature performance has been irreversibly damaged as a result of thermal aging. Therefore, based on the results of these LNT evaluations it is likely that the reduction in performance of the engine-aged LNT samples is due to repeated exposure to high temperature lean/rich cycling resulting in the sintering of PGM particles rather than Na contamination.

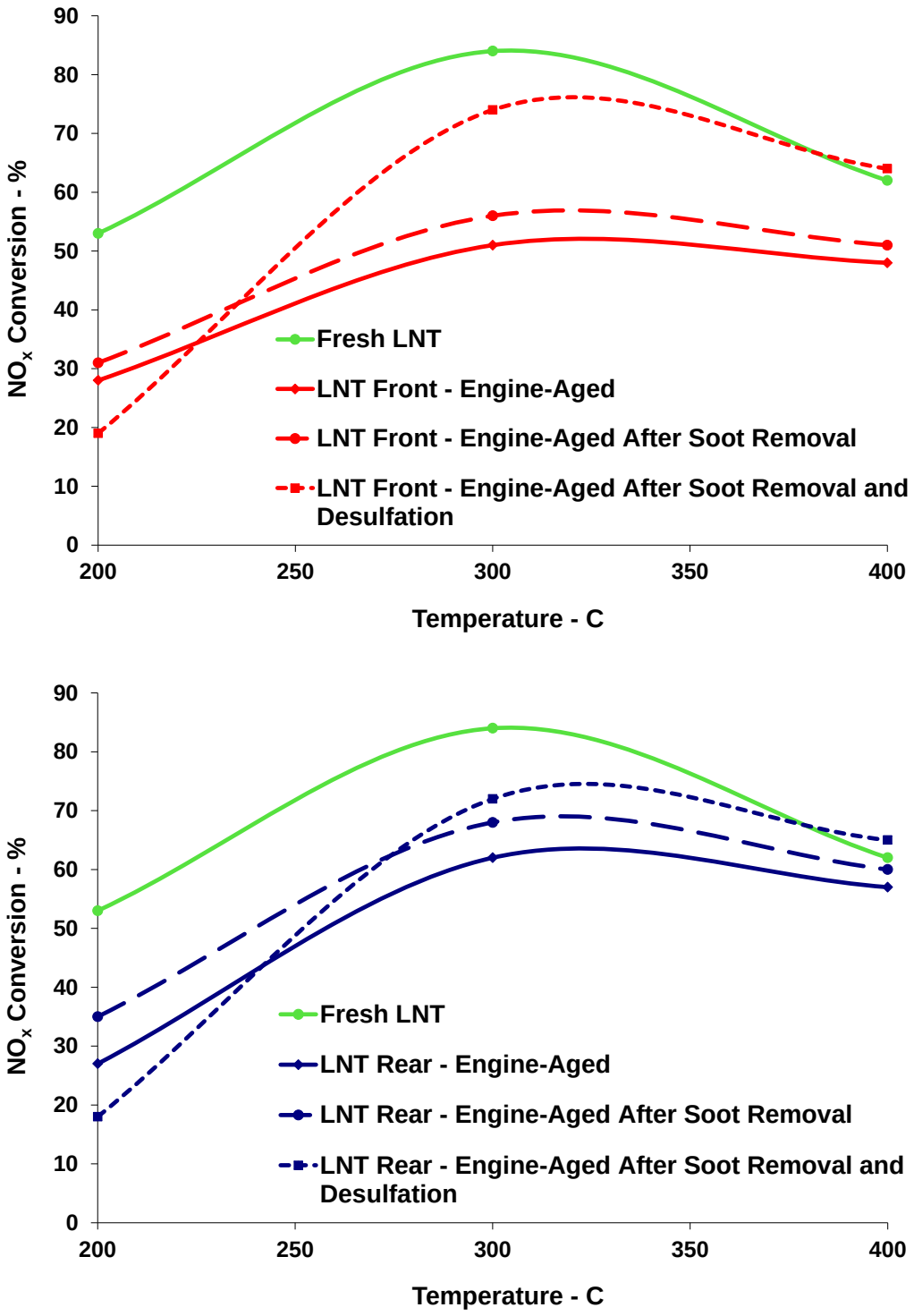

Figure 4.1.3 Impact of soot oxidation and desulfation treatments on performance of engine-aged LNT catalysts.

4.1.3 Materials Characterization

In order to confirm the sintering of PGM particles, STEM was utilized to capture images of Pt particles in powdered fresh and engine-aged LNT samples such as those in Figure 4.1.4.

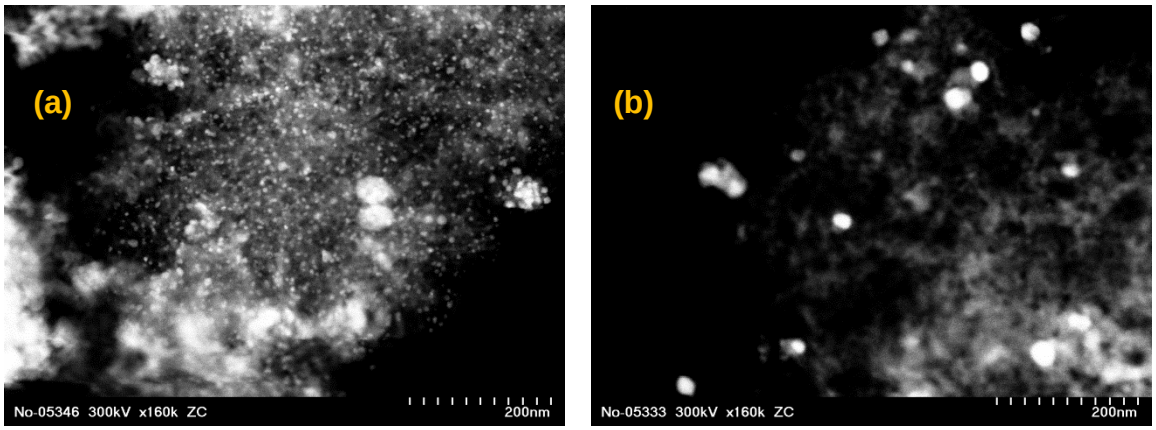

Figure 4.1.4 TEM images of Pt particles in (a) fresh and (b) engine-aged LNT catalysts.

These images are analyzed using a software package known as ImageJ, which enables the user to identify and measure Pt particles based on user input. For ImageJ analysis, depending on the TEM image quality the minimum particle diameter is specified; the better the quality of the image the smaller the initially specified particle diameter. Based on the specified particle diameter, ImageJ highlights all objects with diameters equal or larger than the specified diameter. It is then necessary to select particles of diameter smaller than the originally specified diameter for inclusion in the analysis or to remove highlighted objects

which are noise instead of particles. However, it is possible that some of the smallest particles contained in the image are excluded from the analysis.

It is therefore important to keep this limitation in mind with the results of the ImageJ analysis shown in Figure 4.1.5.

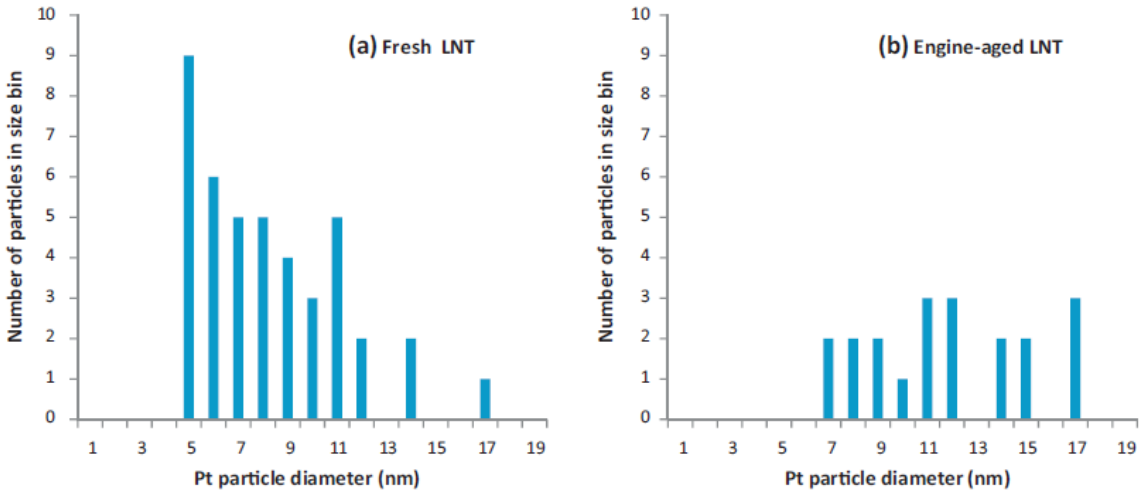

Figure 4.1.5 ImageJ analysis of particle size distribution in fresh and engine-aged LNT samples.

In the fresh sample, the size distribution is skewed towards the range of 5–10 nm with an average size of 9 nm, while in the aged sample the bulk of the particles fall in the range of 10–17 nm with the average size being 12 nm. While the difference is small, there is clear sign of Pt particle growth in the engine-aged LNT sample. The small difference in the average Pt particle size in the fresh and aged samples is possibly due to the resolution of the TEM, and it is likely that the actual average size of Pt particles in the fresh sample is much smaller.

To determine the distribution of Na and other contaminants in the engine-aged LNT, EPMA analysis was performed at the inlet, middle, and rear of the catalyst. Micrographs of Na, S, and P contamination are shown in Figure 4.1.6, along with backscatter images of the channels to illustrate the transition from substrate to washcoat. P contamination is more concentrated than that of Na and appears at a higher relative scale in the EPMA images, but like Na it is confined to the surface of the washcoat. The amounts of both S and P decrease from front to back in the LNT, similar to the concentration gradient of Na. EPMA line scans shown in Figures 4.1.7-4.1.9 of the engine-aged LNT catalyst taken at the locations corresponding to the micrographs confirm the trends. As seen in both the line scans and the micrographs, Na contamination is concentrated on the washcoat surface at each location, with the catalyst inlet experiencing the highest Na-level by weight percentage. Based on the EPMA analysis of the LNT, it appears that S from the biodiesel fuel and P are significantly more prevalent in the LNT than Na. This is due to the longevity of the aging of the LNT, since it was exposed to longer engine run times it was exposed to more S and/or P from the fuel and natural consumption of lubricant. In other words, since the engine was run for long periods of time the contribution from other components is likely to be observed.

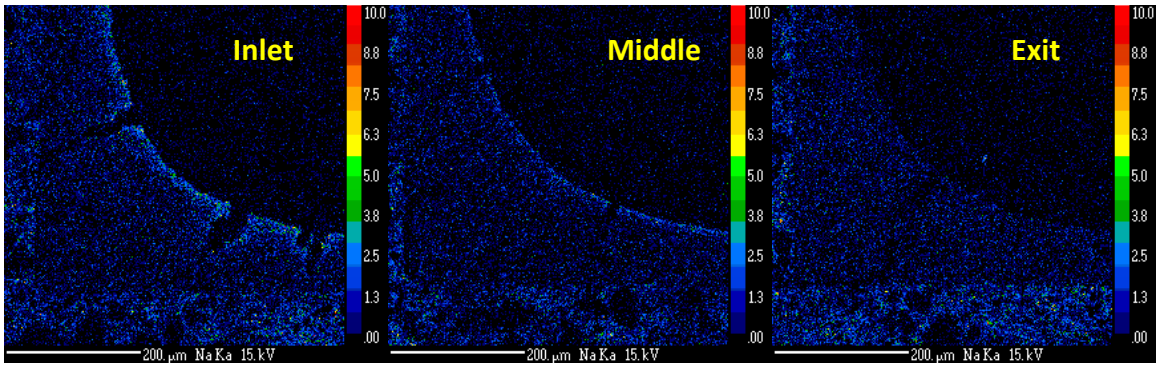

(a)

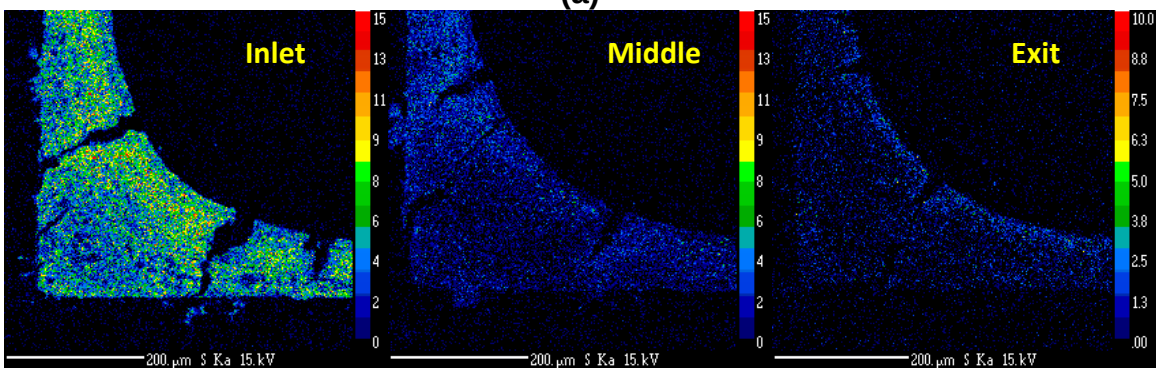

(b)

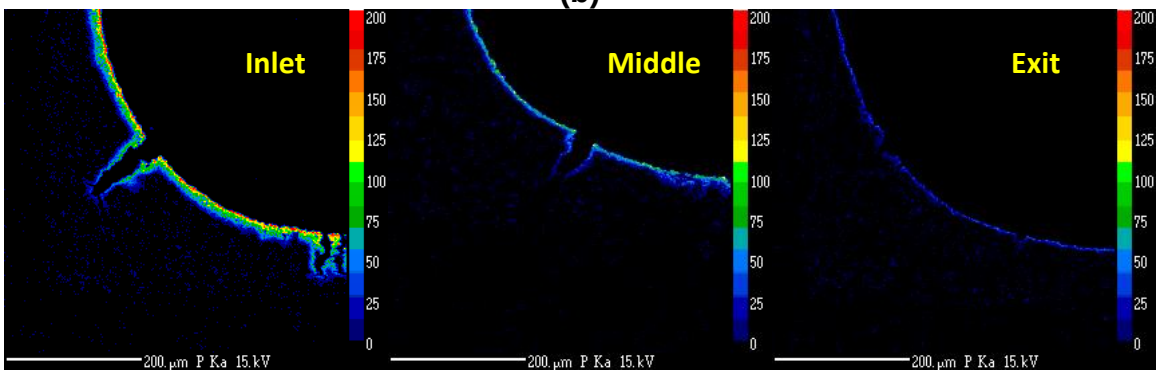

(c)

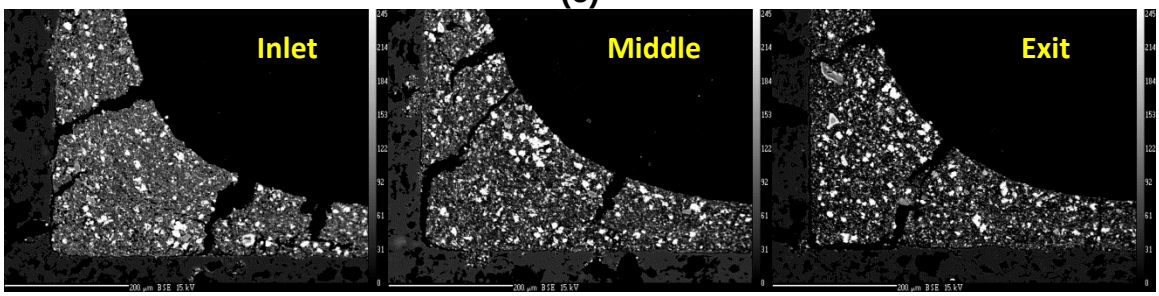

(d)

Figure 4.1.6 EPMA micrographs of (a) Na, (b) S, and (c) P contamination in engine-aged LNT. (d) Backscatter images shown for clarity.

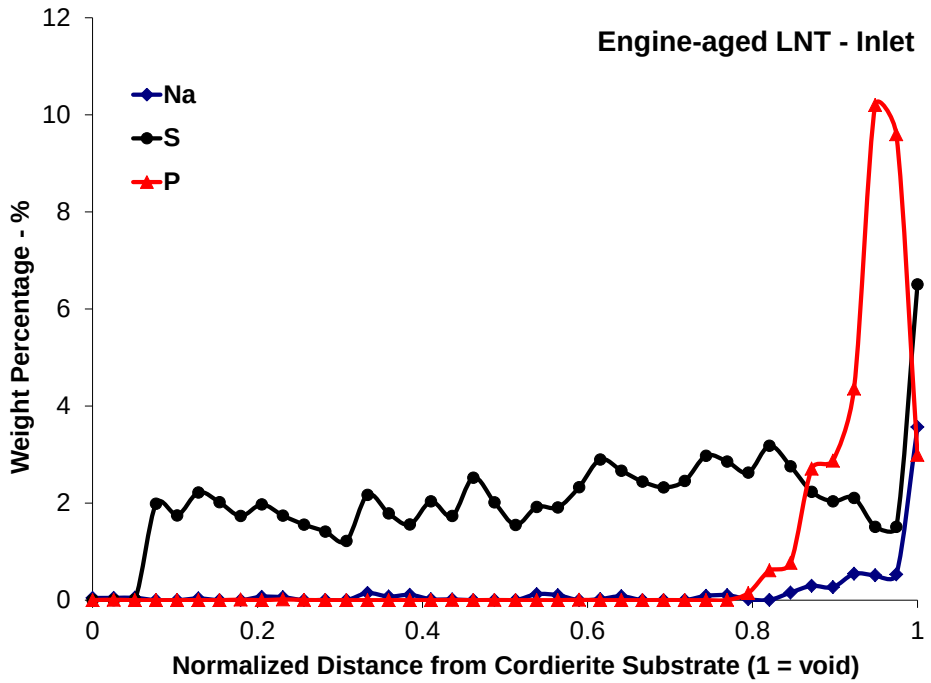

Figure 4.1.7 EPMA Line Scans of Na, S, and P contamination at inlet of engine-aged LNT.

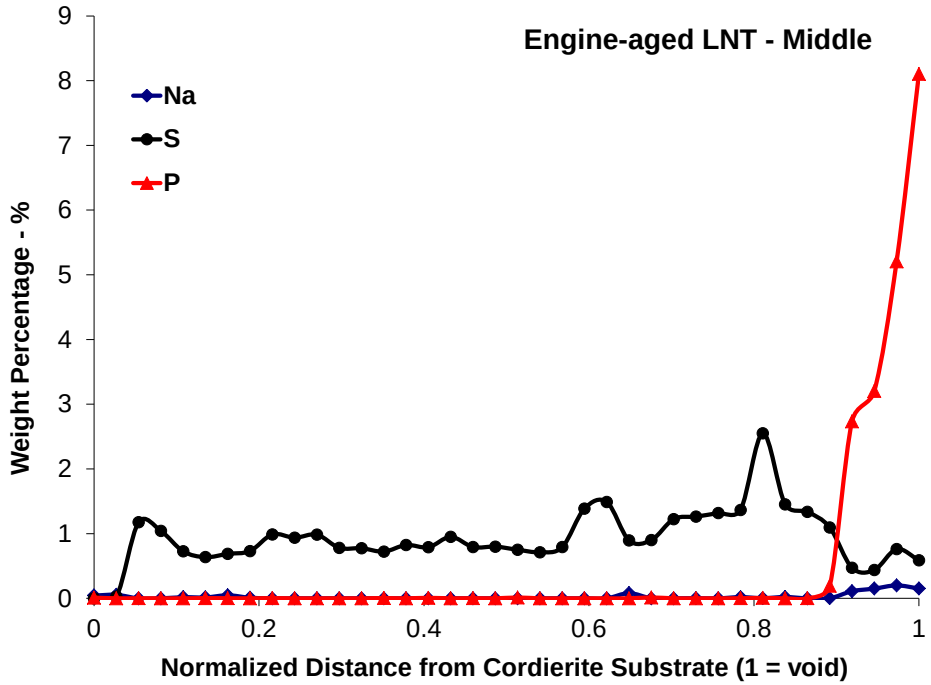

Figure 4.1.8 EPMA Line Scans of Na, S, and P contamination at middle of engine-aged LNT.

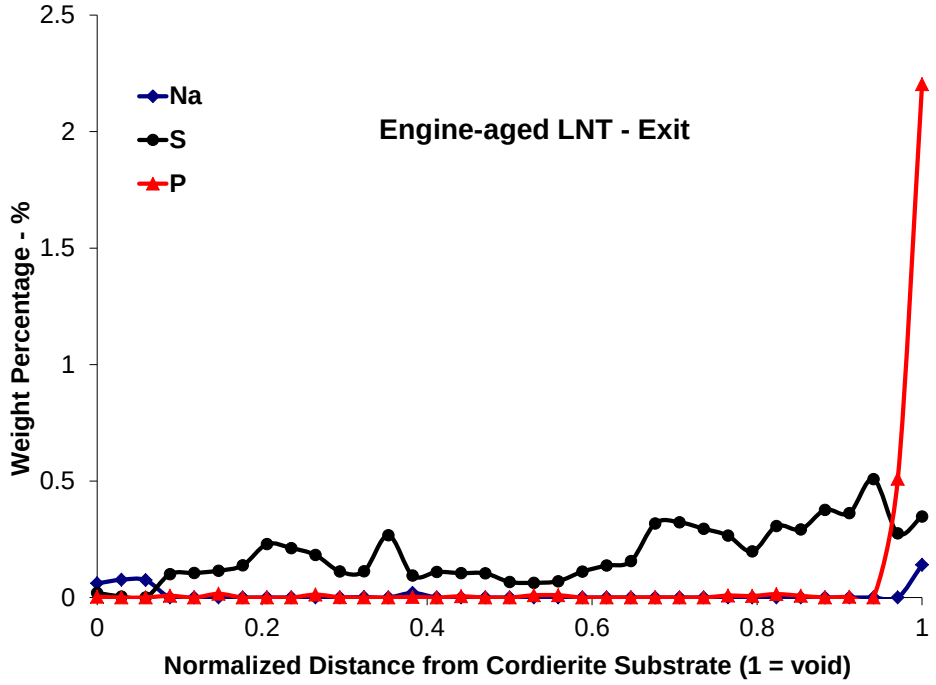

Figure 4.1.9 EPMA Line Scans of Na, S, and P contamination at exit of engine-aged LNT.

4.2 Engine-aged and Accelerated Na-aged DPF

This section discusses EPMA characterization of the engine-aged and accelerated Na-aged DPFs. Section 4.2.1 provides details on engine-aging of the SiC-based DPF and accelerated Na-aging of the cordierite-based DPF, while Section 4.2.2 discusses the results of EPMA analysis on these DPFs after aging.

4.2.1 GM Engine-aging and Accelerated Na-aging of DPFs

Regarding the SiC-based DPF provided by GM after a long-term engine-aging project, only minimal details were provided. The DPF was part of an emissions control arrangement which also included an upstream Pt/Al_2O_3-based DOC and the system was aged with an engine operating on in-specification B20 fuel. No further details were providing regarding aging temperatures or engine details.

The cordierite-based DPFs in the light-duty and heavy-duty configurations were aged as part of the accelerated Na-aging protocol discussed in Chapter 3. Temperature profiles for the cordierite DPFs during aging are shown in Figures 4.2.1-4.2.3. Regeneration produces steady-state temperature fluctuations which range from 400 to 600°C in the control DPF, and between 500 and 700°C for both the light-duty and heavy-duty accelerated Na-aging arrangements. The average inlet, average exit, and maximum DPF temperatures are shown in Figure 4.2.4. The maximum temperatures inside accelerated Na-aged DPFs reach 750 and 700°C for the light-duty and heavy-duty arrangement, respectively, while the average temperature across both DPFs is 600°C.

Meanwhile, the control DPF sees a maximum temperature of just over 600°C and an average temperature of 500°C.

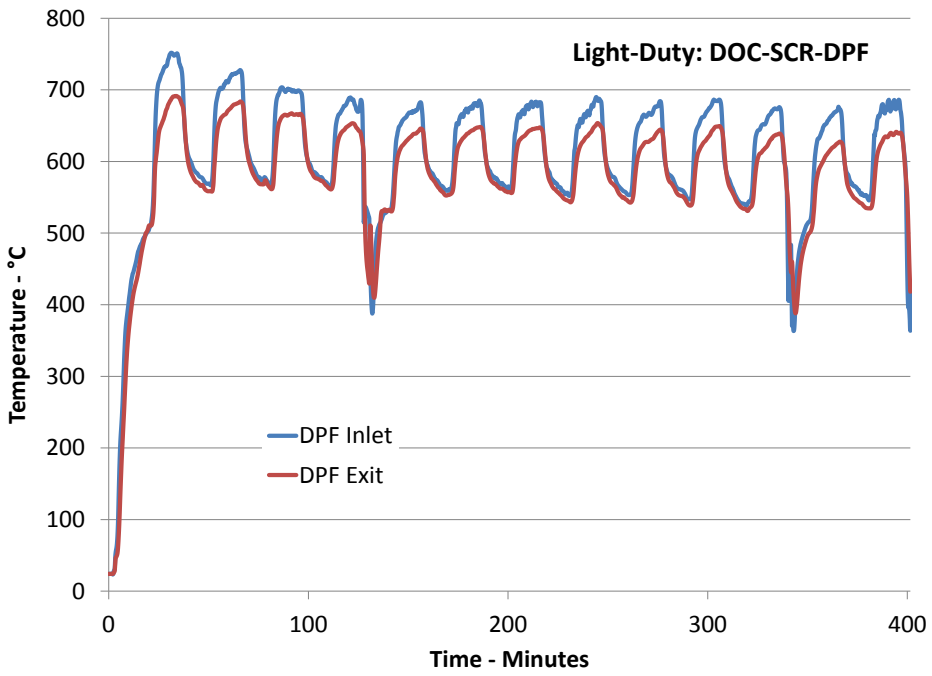

Figure 4.2.1 DPF temperature during accelerated Na-aging protocols for light-duty arrangement.

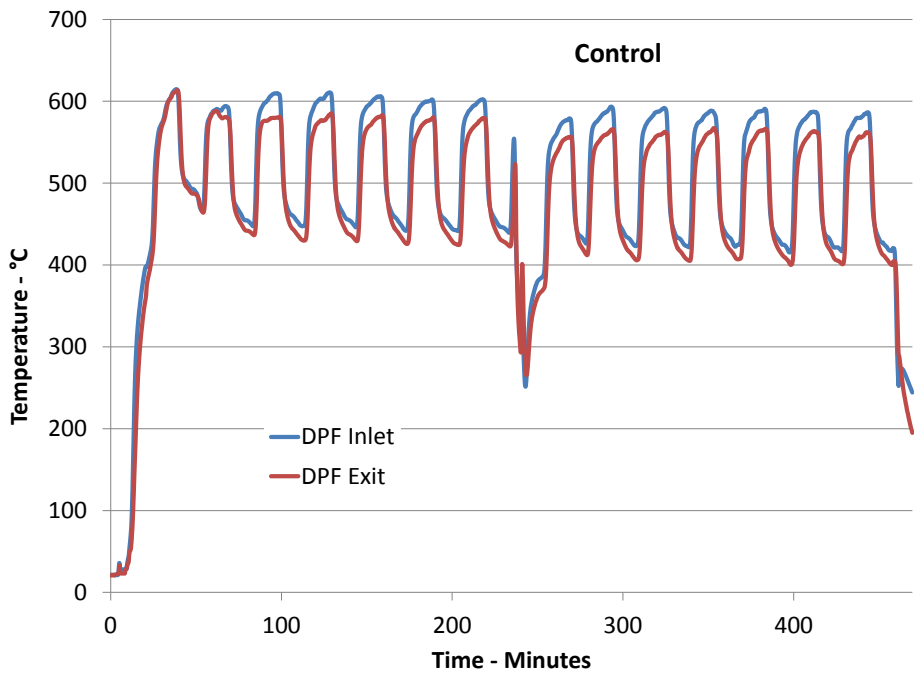

Figure 4.2.2 DPF temperature during accelerated Na-aging protocols for control arrangement.

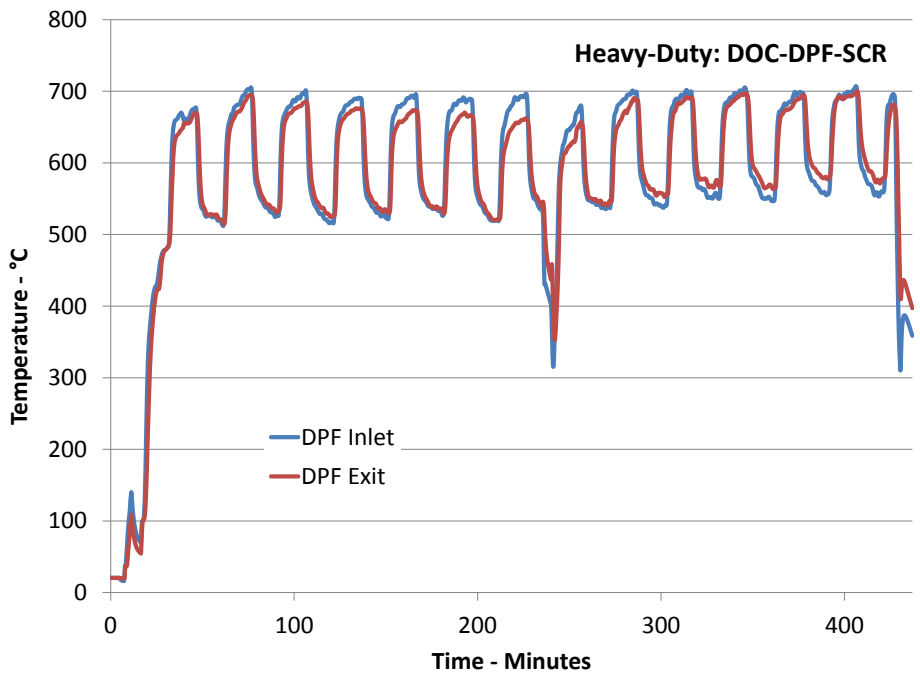

Figure 4.2.3 DPF temperature during accelerated Na-aging protocols for heavy-duty arrangement.

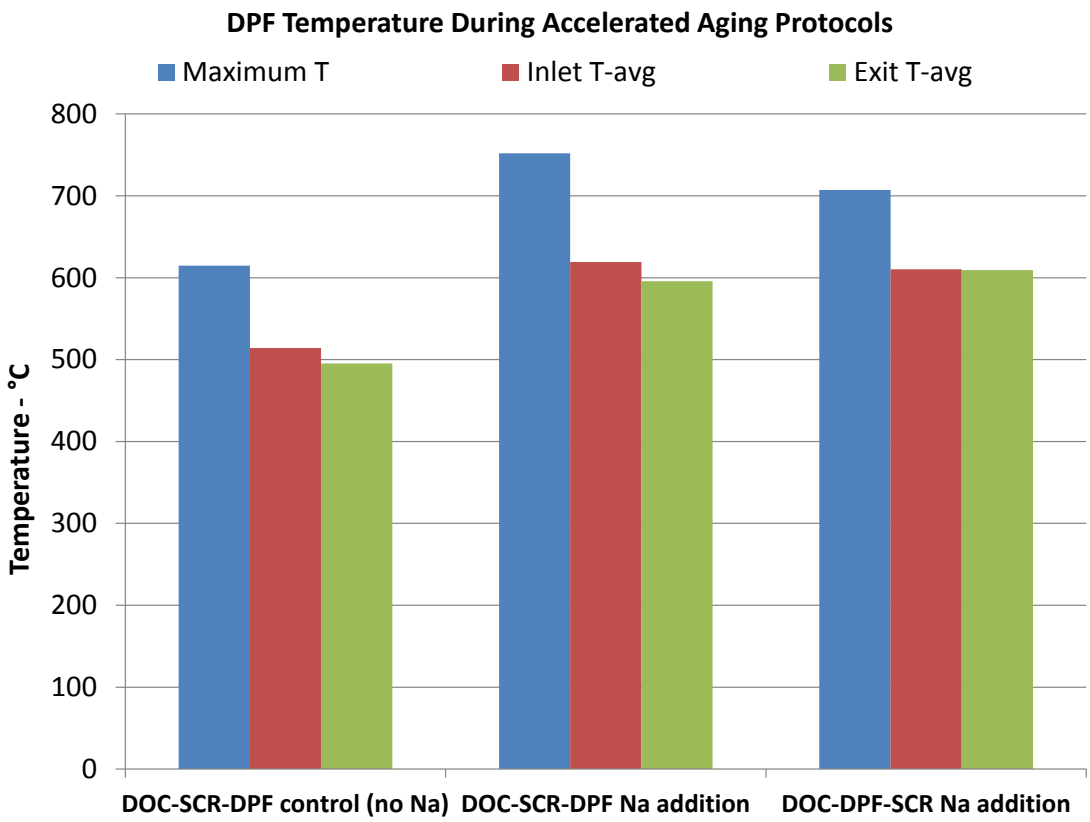

Figure 4.2.4 Average inlet temperature, average exit temperature, and maximum temperature in DPFs during accelerated Na-aging.

4.2.2 Materials Characterization

EPMA analysis was performed on the GM provided long-term engine-aged SiC-based DPF in order to determine the concentration and distribution of contaminants, most notably Na, in a DPF from a long-term engine aging project. Micrographs of Na, P, and Ca taken at the inlet, middle, and at the front of ash plugs observed in the SiC DPF are shown in Figure 4.2.5. Minimal contamination is present at the inlet of the DPF, and only small amounts of Na, P, and Ca appear at the middle.

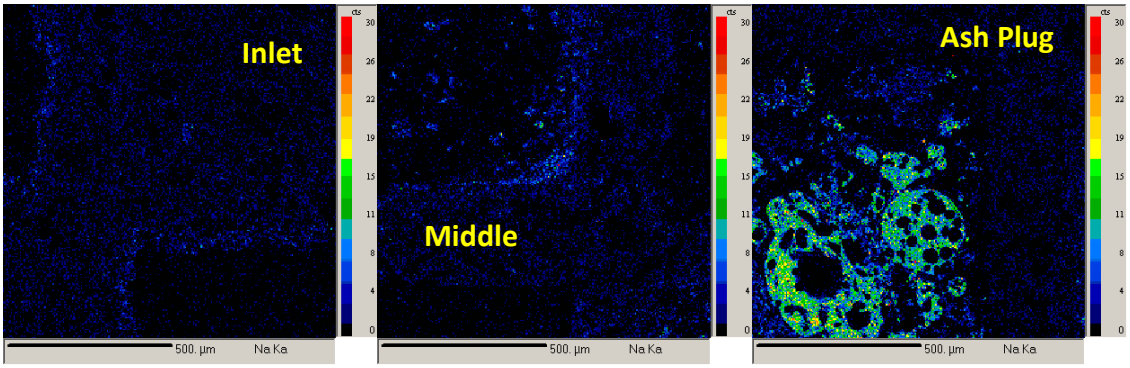

(a)

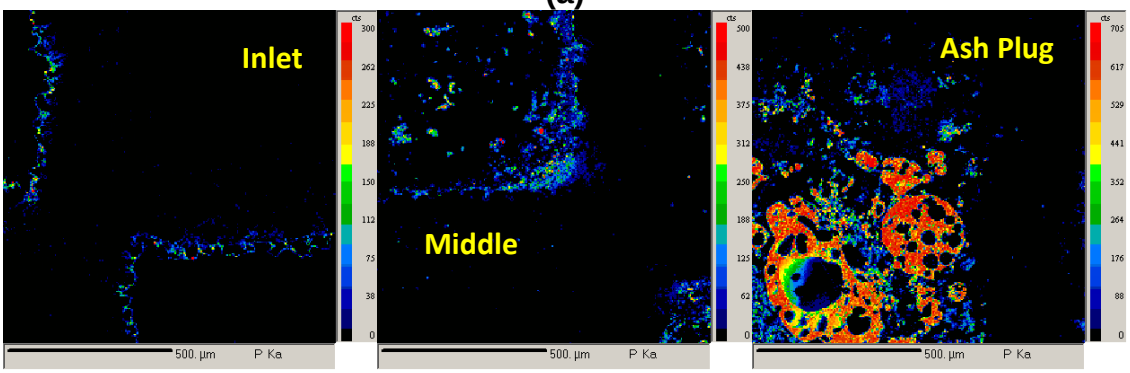

(b)

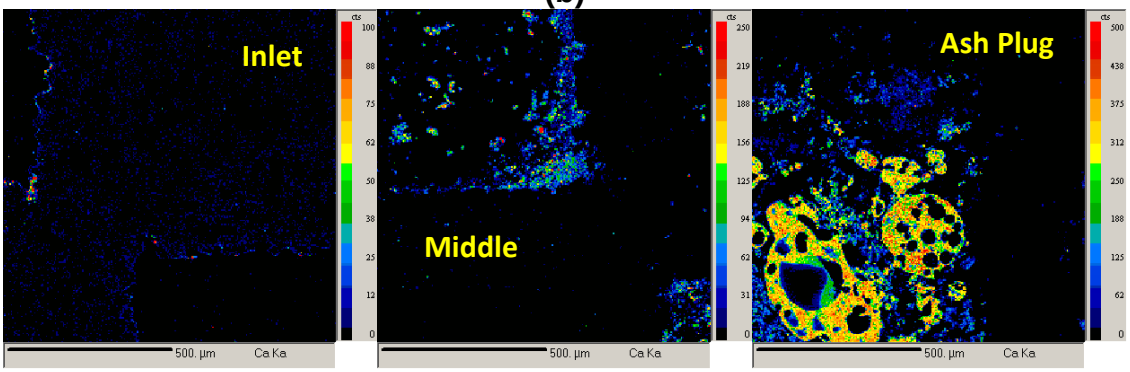

(c)

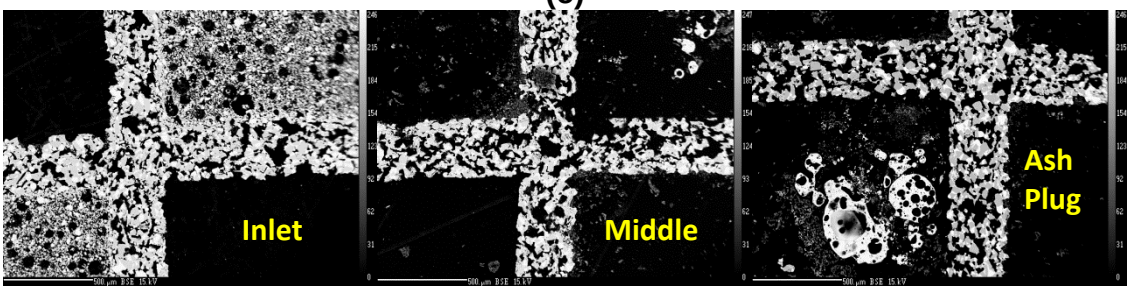

(d)

Figure 4.2.5 EPMA micrographs of (a) Na, (b) P, and (c) Ca contamination in GM provided long-term engine-aged SiC-based DPF. (d) Backscatter images shown for clarity.

The bulk of the contamination is contained in the ash plugs, as seen in the micrographs. In order to determine the relative levels of contamination in the ash plug, an EPMA line scan taken through the plug is shown in Figure 4.2.6.

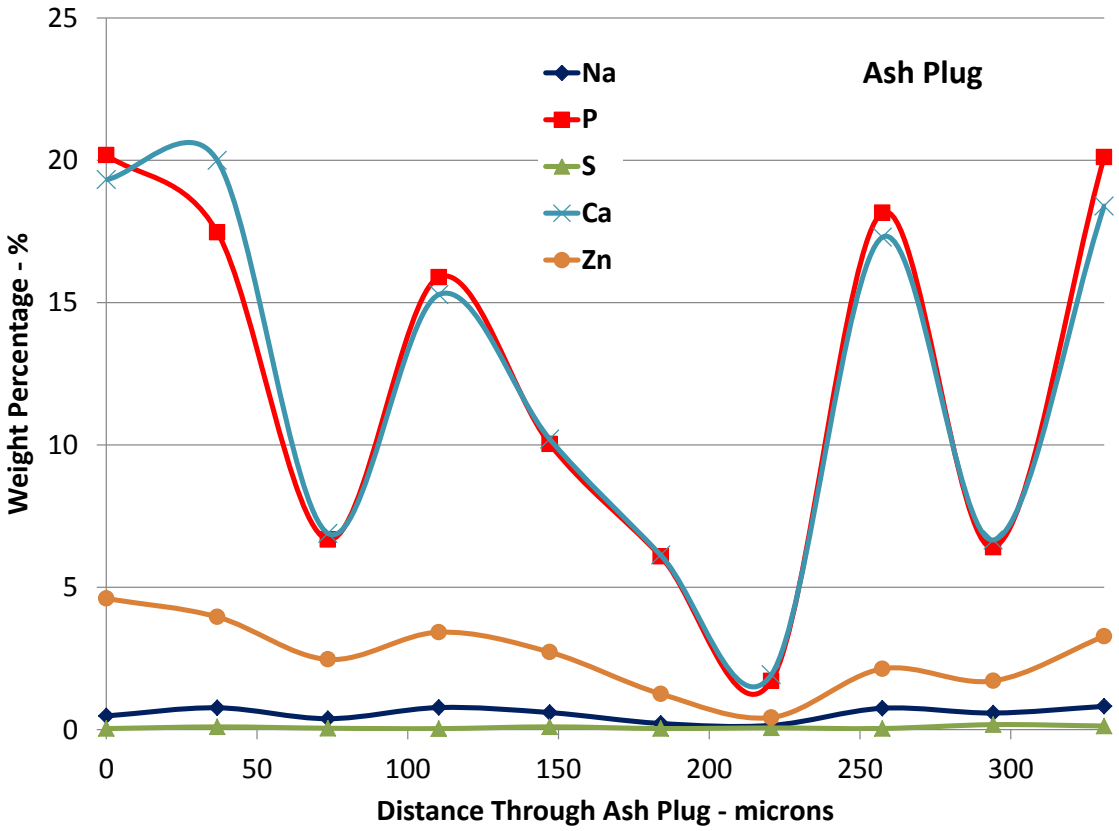

Figure 4.2.6 EPMA line scan of ash plug in GM provided long-term engine-aged DPF.

With concentrations as high as 20% by weight, P and Ca are clearly the primary ash components in the plug. Zn is also prevalent, with levels as high as 5% by weight. Meanwhile, the contribution of Na is between 0.5 and 1% by weight, and S content is negligible. Based on these results it appears that lube oil is the primary source of ash in the GM-provided engine-aged DPF, as the levels of P

and Ca are approximately 20 times that of Na. Additionally, in the case of the GM provided engine-aged DPF it appears that little to no penetration of Na into the substrate wall is occurring, and that the majority of the Na is confined to the ash plug near the rear of the DPF.

EPMA analysis was also performed on the accelerated Na-aged and control DPFs. Micrographs of Na, P, and S contamination are shown for the light-duty configuration accelerated Na-aged DPF, heavy-duty configuration accelerated Na-aged DPF, and control DPF in Figures 4.2.7-4.2.9, respectively. In both accelerated Na-aged samples Na and S can be seen down the length of the catalyst, particularly at the middle and rear upstream of the cordierite plugs. In the DPF from the light-duty configuration, both Na and S appear in the layer of ash on the substrate. However, the DPF from the heavy-duty configuration shows clear penetration of Na into the actual walls of the cordierite substrate. Similar results were observed in a recent study by Williams et al. [89], who identified K and Na in the cordierite substrate after 150,000 simulated miles of aging which further spread to the exit of the DPF after 435,000 simulated miles. Meanwhile, the control sample shows no evidence of Na or S contamination in the DPF. Additionally, the level of P is low in all three samples, which can be attributed to minimal lube oil contamination due to the short aging times associated with the accelerated aging protocol.

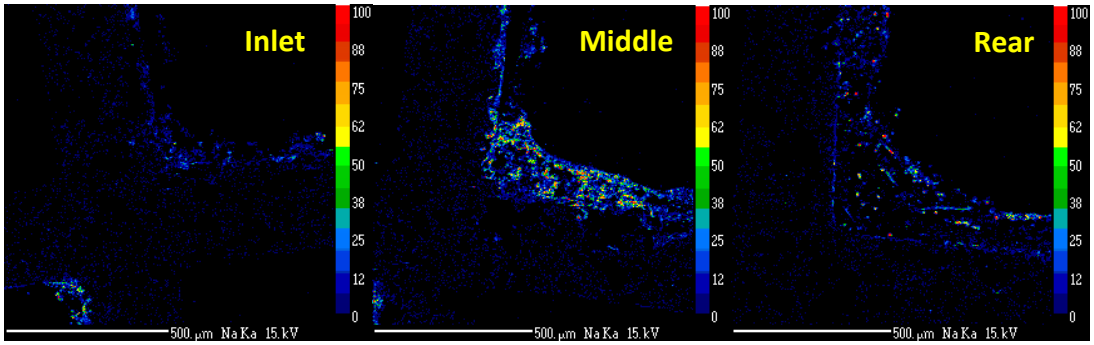

(a)

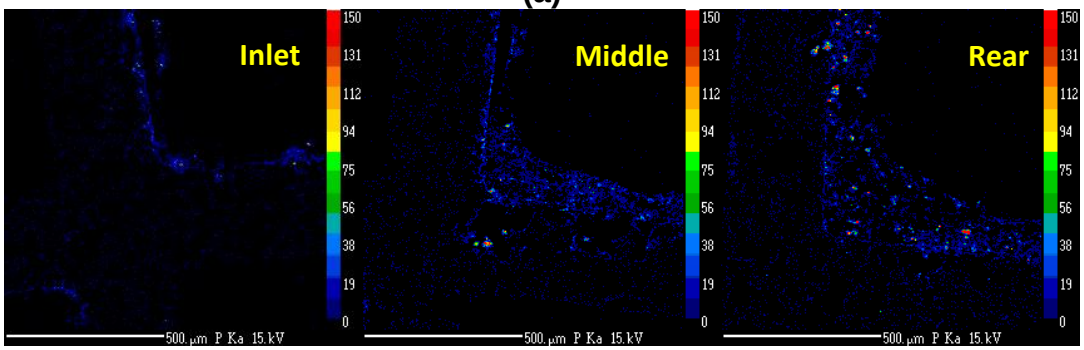

(b)

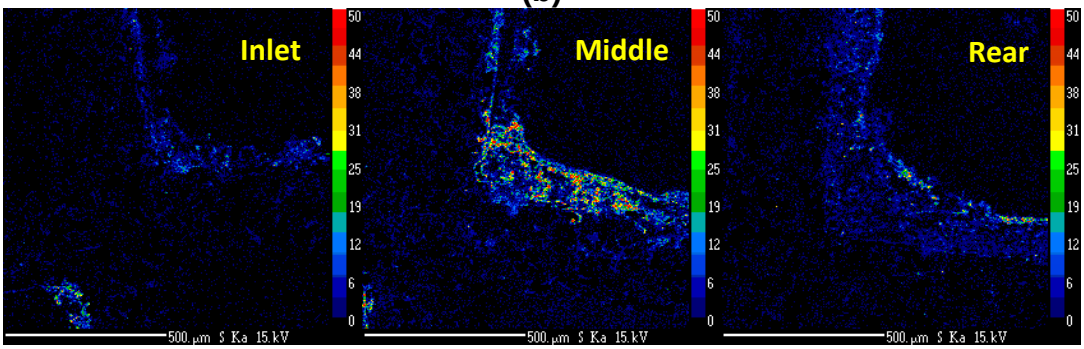

(c)

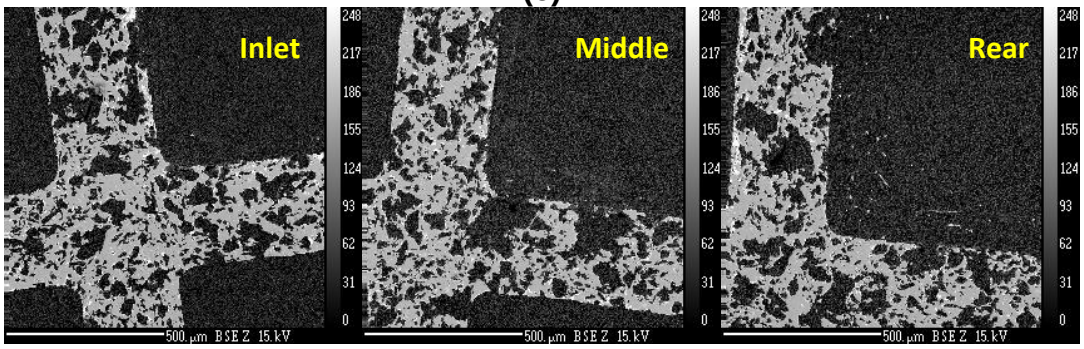

(d)

Figure 4.2.7 EPMA micrographs of (a) Na, (b) P, and (c) S contamination in light-duty configuration accelerated Na-aged DPF. (d) Backscatter images shown for clarity.

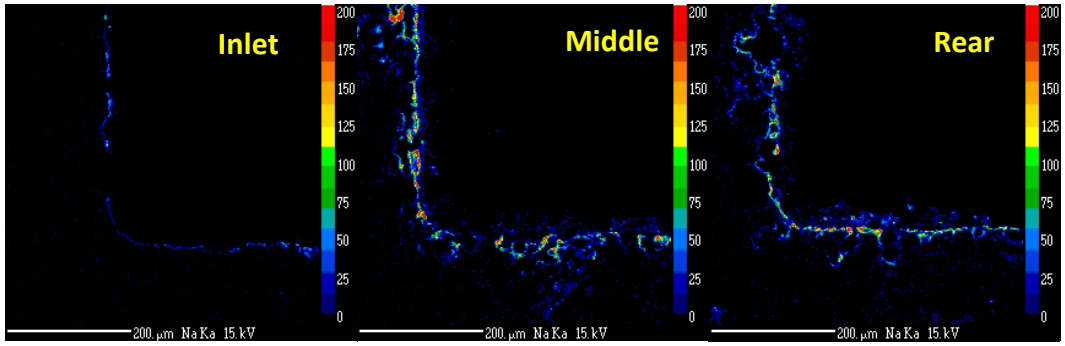

(a)

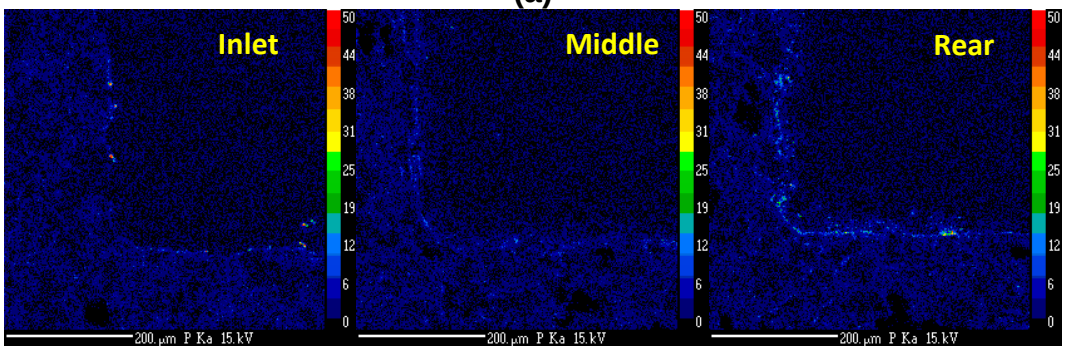

(b)

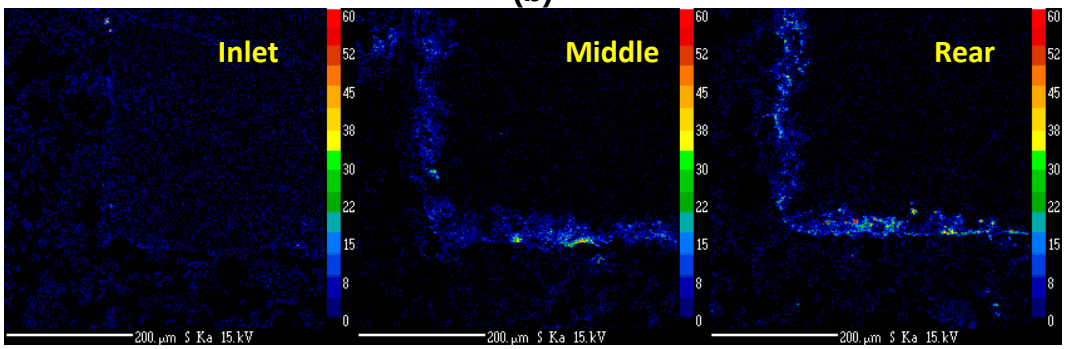

(c)

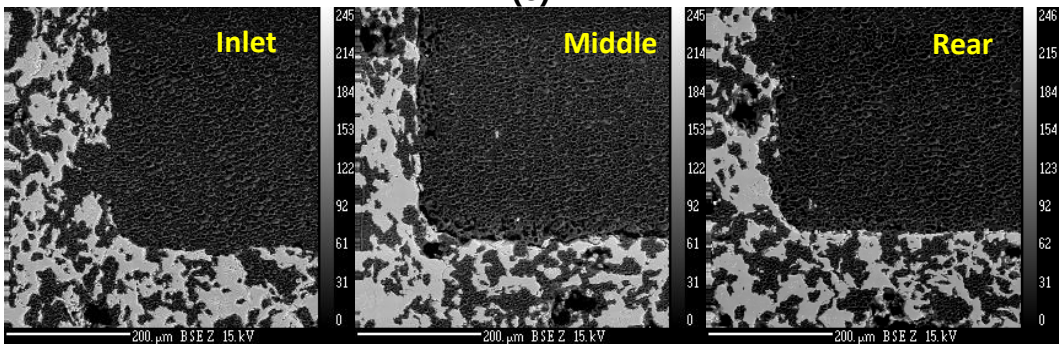

(d)

Figure 4.2.8 EPMA micrographs of (a) Na, (b) P, and (c) S contamination in heavy-duty configuration accelerated Na-aged DPF. (d) Backscatter images shown for clarity.

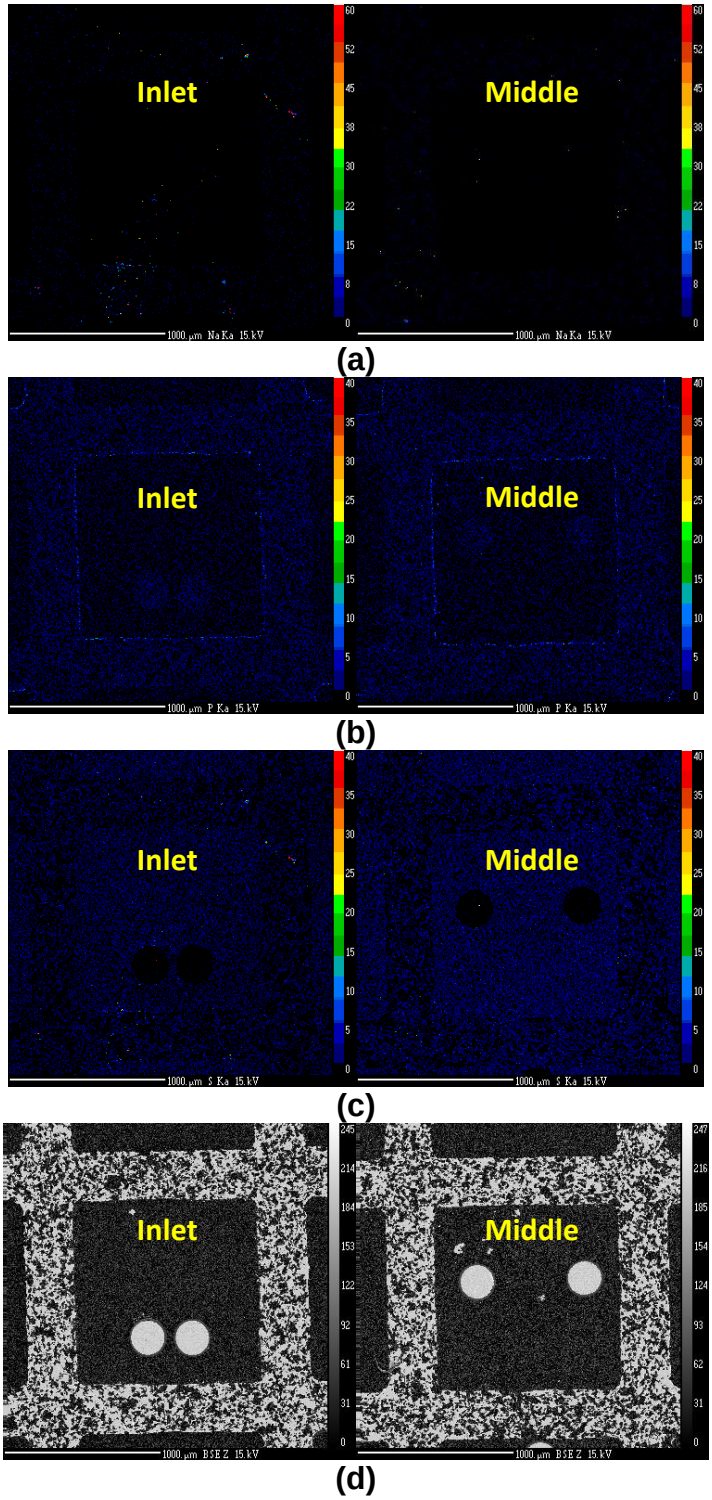

Figure 4.2.9 EPMA micrographs of (a) Na, (b) P, and (c) S contamination in control DPF. (d) Backscatter images shown for clarity (white circles seen in BSE images represent fibers used to mark the channels).

During EPMA analysis, line scans were taken at the middle and rear of the accelerated Na-aged DPFs from both the light-duty and heavy-duty configurations as shown in Figures 4.2.10 and 4.2.11, respectively. These lines scans provide insight into the effect DPF position in the aftertreatment system has on the level of contamination in the filter. The DPF from the light-duty arrangement shows levels of contamination as high as 3% by weight at the middle, and as high as 2% by weight at the rear. However, as observed in the micrographs, high levels of Na contamination are only seen as ash on the surface of the DPF, with only a small amount of Na present in the substrate. Meanwhile, the DPF from the heavy-duty configuration shows much higher levels overall, particularly in the middle where Na has penetrated the cordierite substrate with concentrations as high as 5% by weight even at a depth of 40 microns below the substrate surface. Based on these results, it appears that placing the DPF upstream of the SCR in the heavy-duty arrangement leads to an excess of Na ash buildup in the DPF which causes Na to penetrate into the substrate. Additionally, both DPFs show similar levels of S contamination which is confined to ash on the surface of the washcoat regardless of the arrangement. Finally, when comparing the levels of Na in the accelerated Na-aged DPFs against those found in the long-term engine-aged SiC DPF, it is apparent that the accelerated aging protocol introduces a much greater amount of Na to the DPF. This is expected, as the long-term engine-aging process targeted 150,000 miles equivalent operation, while the accelerated Na-aging approach was designed to reach an equivalent of 435,000 miles of Na exposure.

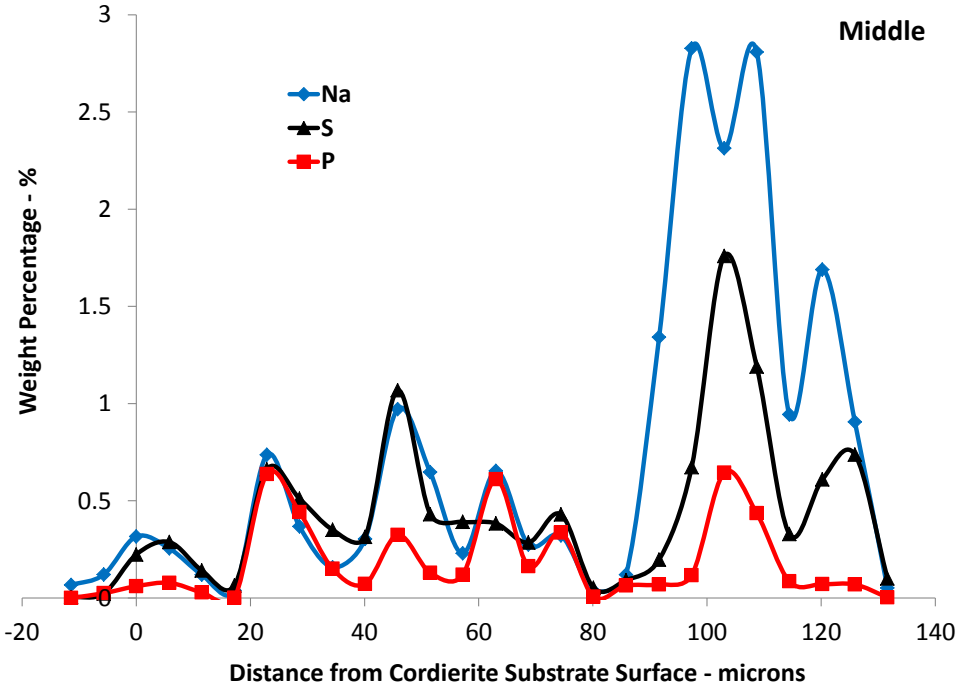

(a)

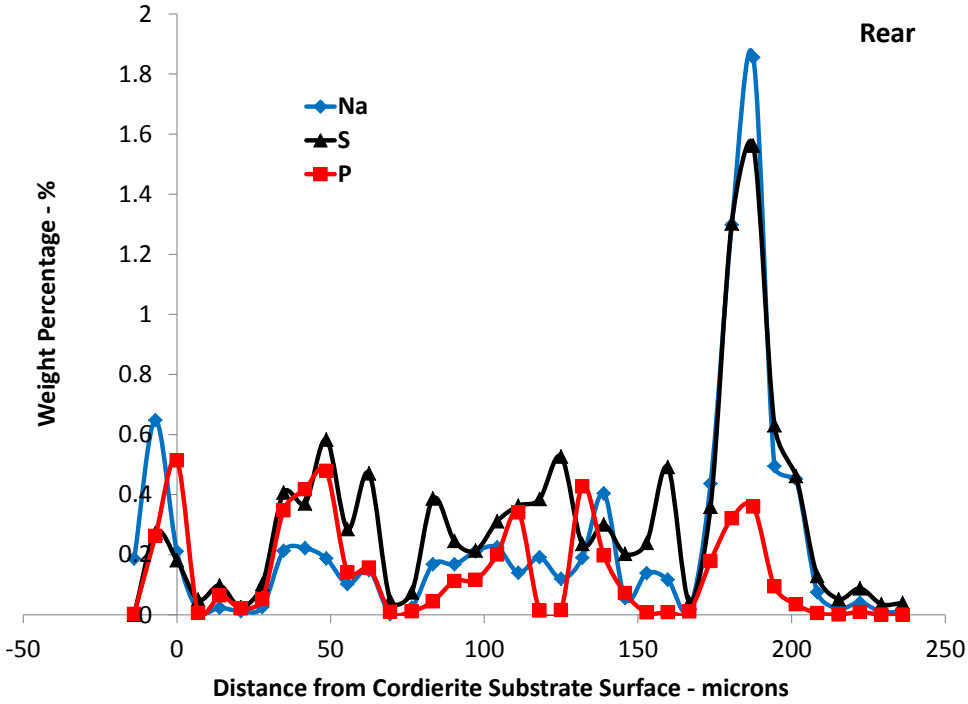

(b)

Figure 4.2.10 EPMA line scans of light-duty accelerated Na-aged DPF at (a) middle and (b) rear.

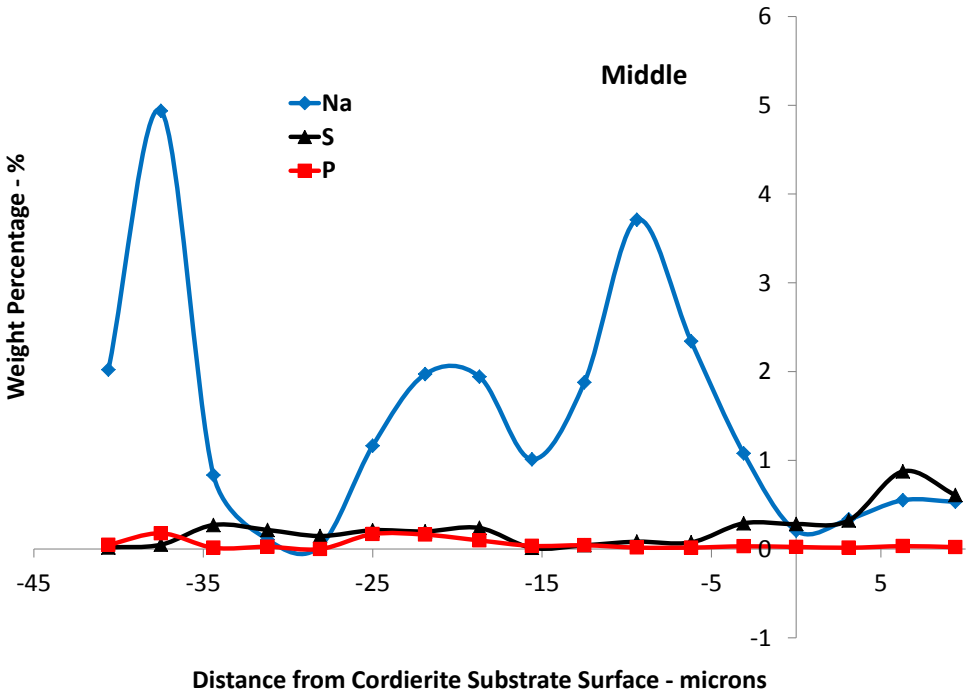

(a)

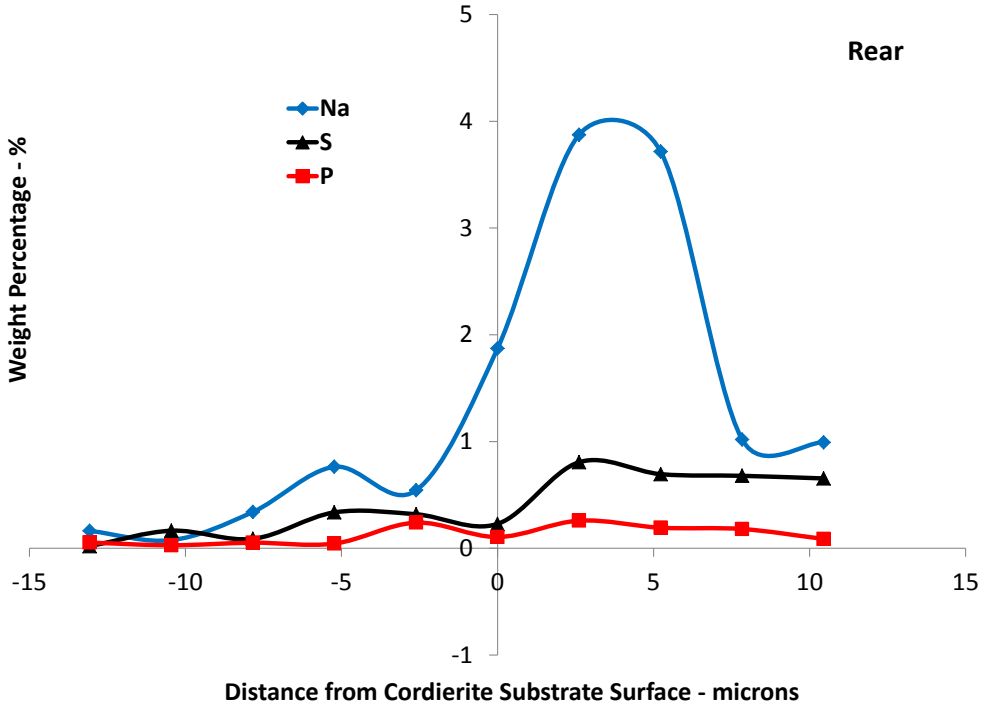

(b)

Figure 4.2.11 EPMA line scans of heavy-duty accelerated Na-aged DPF at (a) middle and (b) rear.

4.3 Fresh, Engine-aged, and Accelerated Na-aged DOC

This section discusses the results of performance evaluations and materials characterization of fresh, long-term engine-aged, and accelerated Na-aged DOC catalysts. Section 4.3.1 provides information regarding the long-term engine aging process and the accelerated Na-aging protocols, while Section 4.3.2 discusses the results of performance evaluations on these same catalysts. The section concludes in 4.3.3 with a comparative analysis of EPMA results obtained for the long-term engine-aged and light-duty accelerated Na-aged DOCs.

4.3.1 Long-term Engine-aging and Accelerated Na-aging of DOCs

The long-term engine-aged DOC was part of the DOC-DPF system provided by GM. The Pt/Al_2O_3-based DOC was upstream of the SiC DPF in the aftertreatment system which was aged with an engine operating on in-specification B20 fuel. No further information was provided regarding aging temperatures or engine details.

The DOCs aged as part of the accelerated Na-aging protocols described in Chapter 3 are also Pt/Al_2O_3-based. Temperature profiles for the DOCs during aging are shown in Figures 4.3.1-4.3.3. Due to the location of the DOC catalysts at the front of the aftertreatment systems, temperatures are much more consistent at the inlet of the DOC and remain between 400 and 500ºC for all three runs, although the control sample does experience the lowest temperatures. However, regeneration still causes temperatures at the exit of the

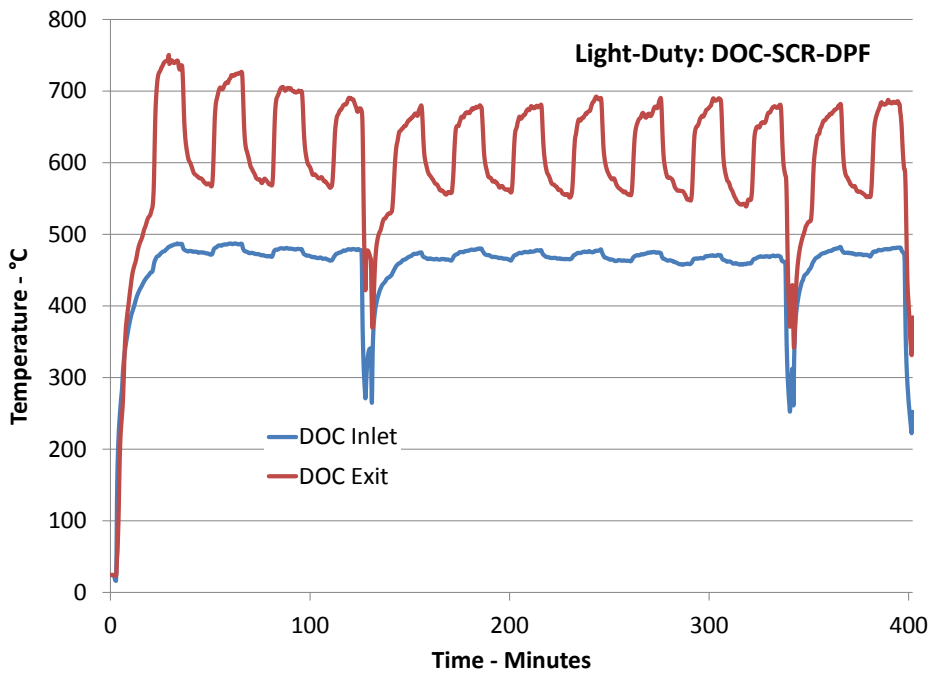

Figure 4.3.1 DOC temperature during accelerated Na-aging protocols for light-duty arrangement.

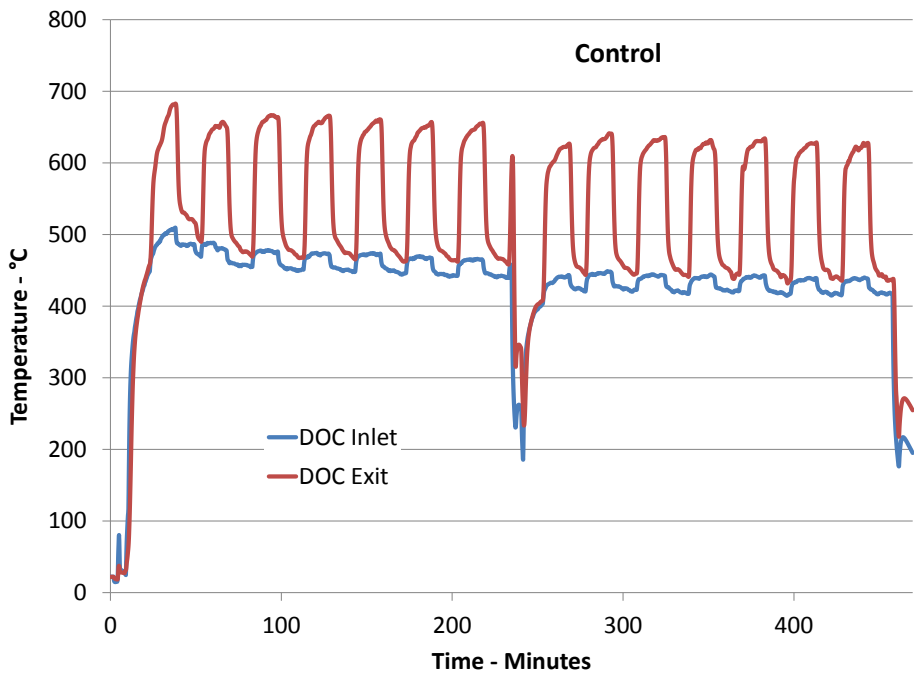

Figure 4.3.2 DOC temperature during accelerated Na-aging protocols for control arrangement.

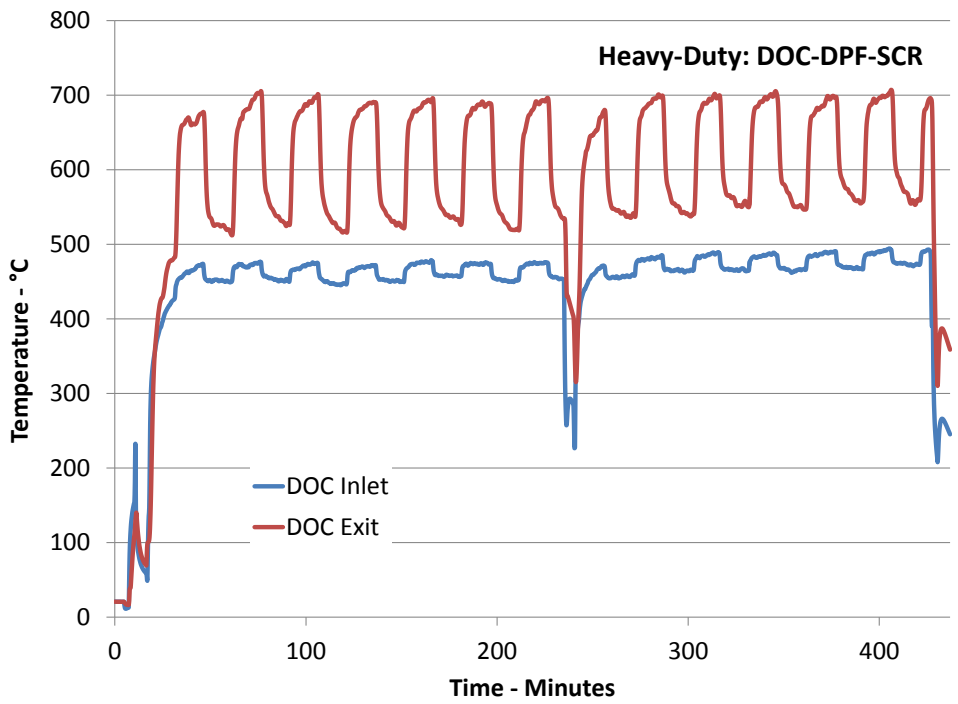

Figure 4.3.3 DOC temperature during accelerated Na-aging protocols for heavy-duty arrangement.

DOCs to fluctuate between 500 and 700ºC in all three arrangements. The average inlet, average exit, and maximum DOC temperatures are shown in Figure 4.3.4. The maximum temperatures in the DOCs fall in the range between 680 and 750ºC, which is a much smaller temperature window than the range observed in the accelerated Na-aged DPFs. Additionally, while average inlet and exit temperatures across the DPFs were consistent, there are large temperature gradients between the inlet and exit of the DOCs. The average inlet temperature for the DOCs is approximately 460ºC, while the exit temperatures range from 450-680ºC in the control DOC and 510-730ºC in the accelerated Na-aging configurations. These large temperature gradients are a result of the DPF

regeneration cycles significantly impacting the DOC exit temperatures, while the DOC inlet temperatures are relatively unaffected.

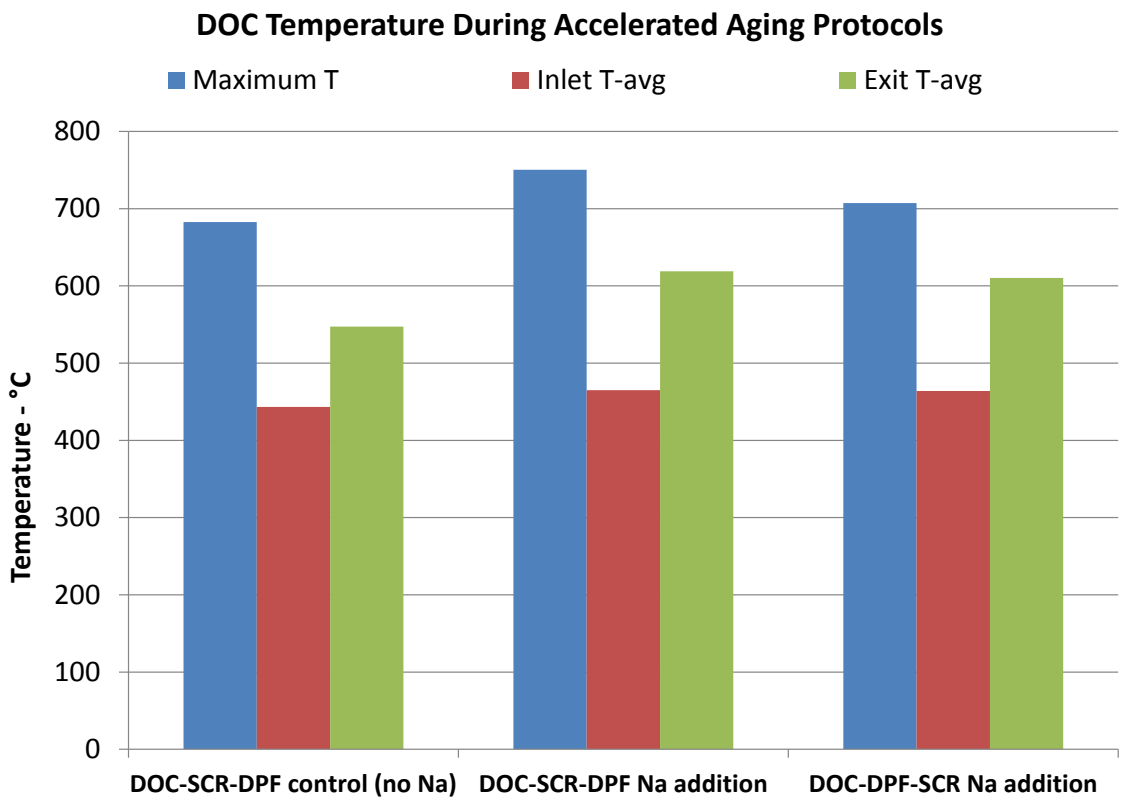

Figure 4.3.4 Average inlet temperature, average exit temperature, and maximum temperature in DOCs during accelerated Na-aging.

4.3.2 Performance Evaluations

BFR performance evaluations were performed at the University of Tennessee on the fresh, long-term engine-aged, control, and light-duty accelerated Na-aged DOC catalysts. Evaluations were done in the temperature range between 100 and 400°C, where the temperature recorded by the thermocouple at the middle of the catalyst was used as the basis for evaluation

temperature. Temperature profiles across the length of the DOC catalyst are shown in Figure 4.3.5.

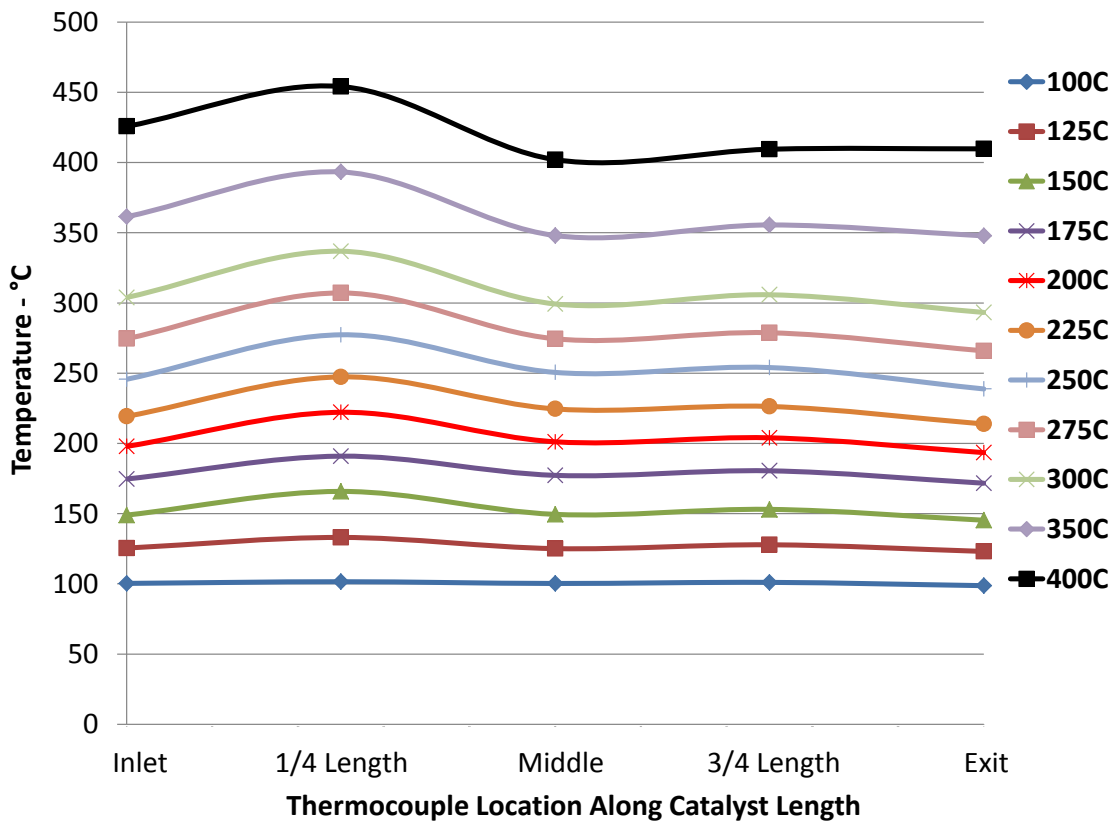

Figure 4.3.5 DOC catalyst temperature profiles during aging in the temperature range from 100 to 400°C.

There is some variation in temperature across the 2” DOC core during evaluation, particularly at temperatures above 200°C. The inlet of the DOC typically sees a slightly higher temperature than the target evaluation temperature, most likely due to chemical reactions, and the highest temperature consistently appears at the quarter length of the catalyst. These variations

appear due to the temperature gradients across the tubular furnace reactor during evaluation, which are largest at high temperatures.

The ethylene oxidation behavior of the DOC catalysts is shown in Figure 4.3.6.

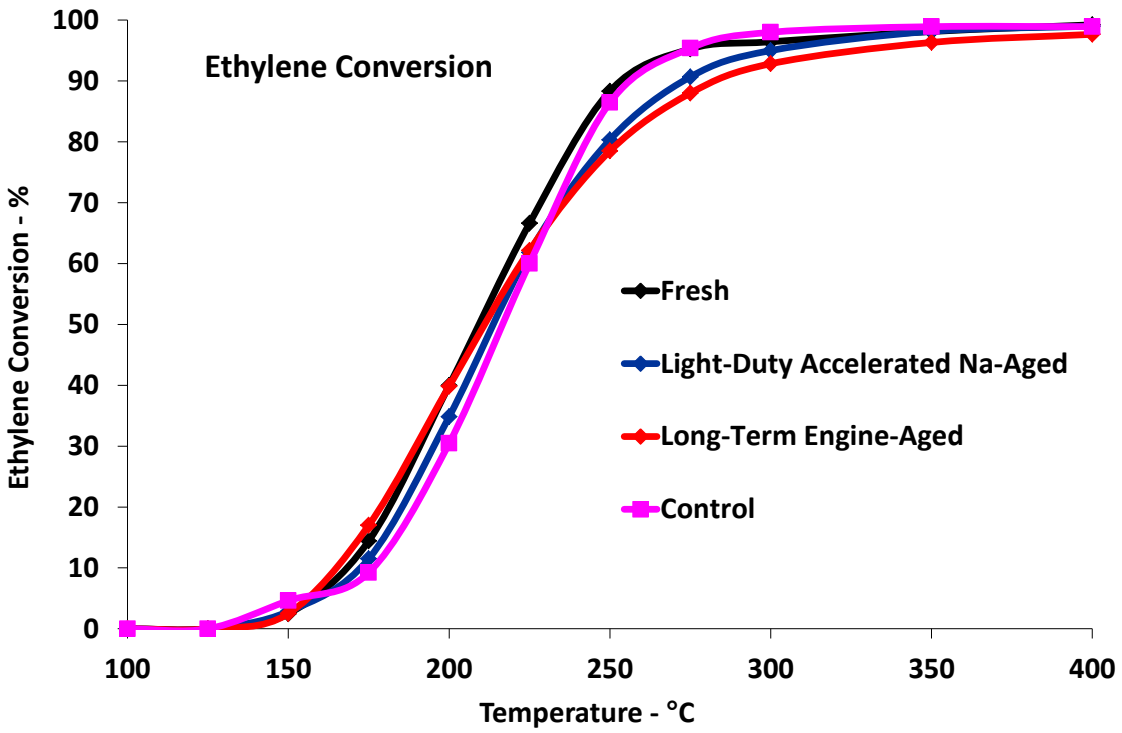

Figure 4.3.6 Ethylene oxidation in fresh, long-term engine-aged, light-duty accelerated Na-aged, and control DOCs.

Overall, the impact of aging and Na contamination on the performance of the DOCs is minimal. Relative to the fresh sample T-50 light-off temperatures for the aged samples increases by no more than 15°C, and T-80 light temperatures increase by less than 20°C. In the study by Cavataio [16] on Na contamination of DOCs they observed increases of 31 and 63°C for the Pt:Pd zeolite DOC at Na contamination levels of 1% and 3% weight respectively. For the samples

evaluated in the current study, Na content is well below one percent, which is reflected in the lack of performance reduction in the aged samples. With regards to CO oxidation, it is difficult to draw conclusions based on the results shown in Figure 4.3.7.

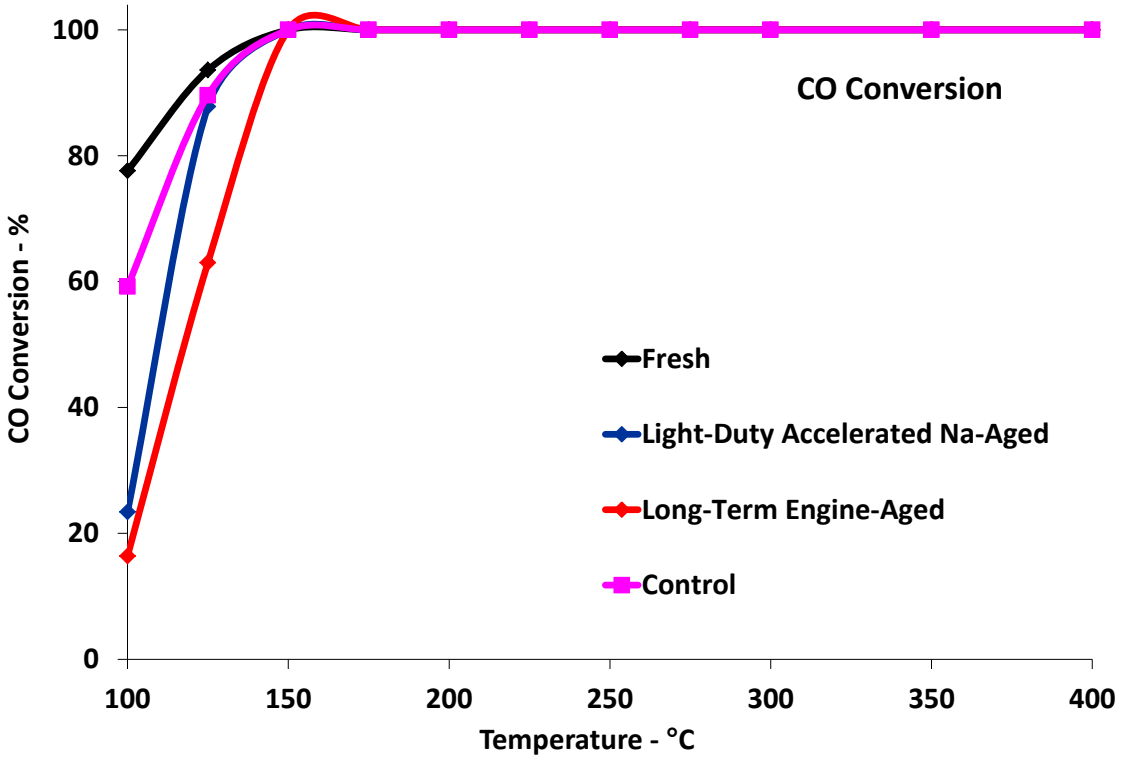

Figure 4.3.7 CO oxidation in fresh, long-term engine-aged, light-duty accelerated Na-aged, and control DOCs.

CO oxidation activity is extremely high over all four DOC samples, with 100% conversion occurring in all samples at temperatures above 150°C. It does appear there is some aging effect at 100 and 125°C, but the overall impact on performance is negligible due to the high conversion across the remainder of the evaluation temperature range.

The NO to NO_2 oxidation results shown in Figure 4.3.8 reveal that the NO oxidation of the aged samples is actually improved compared to the fresh sample.

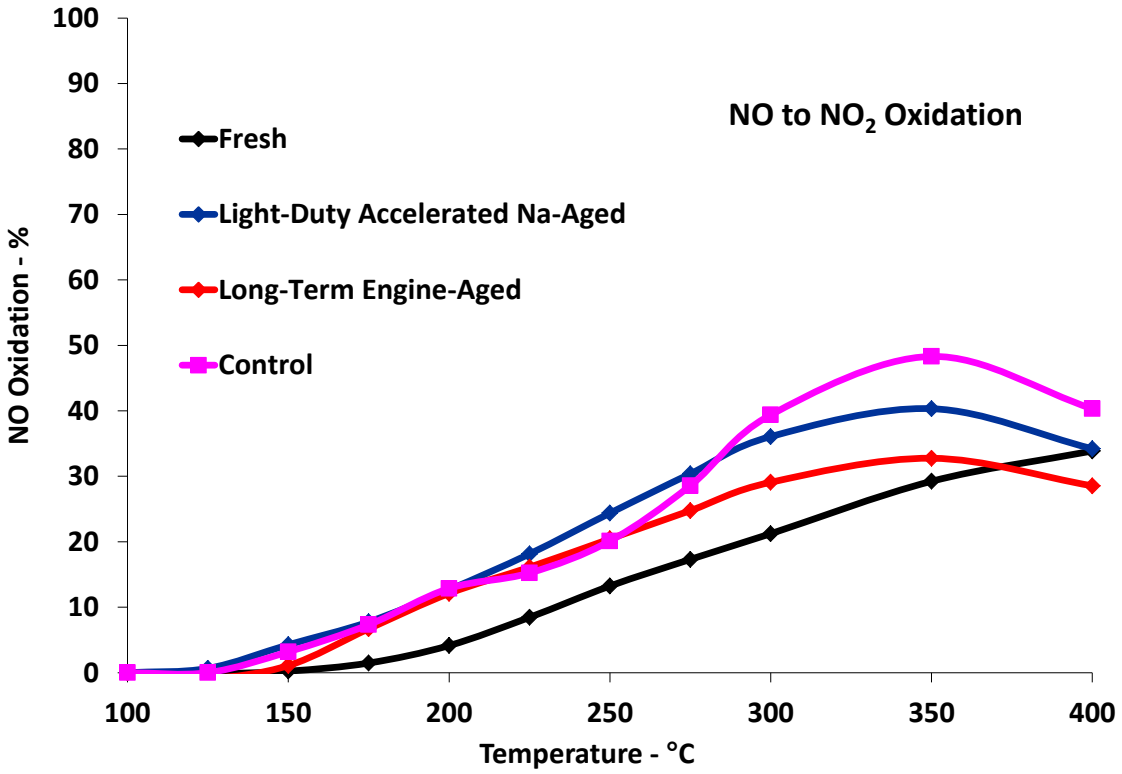

Figure 4.3.8 NO oxidation in fresh, long-term engine-aged, light-duty accelerated Na-aged, and control DOCs.

Oxidation over the fresh sample is below that of all three aged samples across the entire temperature range except for 400°C, where it slightly surpasses the long-term engine-aged sample with a conversion of 34%. All three aged samples show peak conversion at 350°C, with the control showing the highest oxidation potential at just under 50%. A likely explanation of the increase in NO oxidation is attributed to a common aging phenomenon, the sintering of Pt particles. It has

been shown that larger Pt particles have increased NO_x reduction activity especially when normalized to the exposed Pt atoms on the surface. This has been demonstrated in past investigations which suggested the increased activity for the Pt sites for the oxidation of NO is due to the relative inability of larger Pt particles to form deactivating oxides in comparison to smaller Pt particles which are easily oxidized [90-92]. This is more likely to occur on smaller Pt particles where more Pt/metal oxide interfaces occur. Finally, it is important to notice that oxidation over the DOCs in the peak SCR range of 200 to 300°C is less than 35% for all four samples, which is well below the 50% conversion required to achieve the 1:1 NO_2/NO_x ratio required for fast SCR conditions in the downstream SCR catalyst.

4.3.3 Materials Characterization

EPMA analysis was applied to the long-term engine-aged and light-duty configuration accelerated Na-aged DOC samples primarily for the purpose of comparing the level of Na contamination in the two samples. Micrographs for Na, S, and P contamination for the long-term engine-aged and light-duty accelerated Na-aged DOCs are shown in Figures 4.3.9 and 4.3.10, respectively. In the long-term engine-aged DOC a layer of Na is present on the surface of the washcoat at the inlet of the DOC catalyst, but this layer diminishes in intensity down the length of the catalyst. P contamination follows a similar pattern of contamination but at a much higher concentration, while S contamination is present throughout the washcoat at the inlet but is barely detectable at the middle and exit. In the

accelerated Na-aged DOC, Na is also present in a thin layer on the washcoat surface, but the intensity of the Na contamination does not diminish down the length of the catalyst. This same trend is also observed for S contamination in the accelerated Na-aged DOC. Meanwhile, the concentration of the P layer is much smaller than that seen in the long-term engine-aged DOC due to the minimal lube oil contamination which occurs during accelerated aging.

In order to examine the relative quantities of contaminants in the DOC washcoats line scans taken at the inlet, middle, and exit of the long-term engine-aged DOC and accelerated Na-aged DOCs are shown in Figures 4.3.11-4.3.13 and Figures 4.3.14-4.4.16 respectively. The line scans confirm observations from the micrographs. Phosphorous is the primary contaminant in the long-term engine-aged DOCs, with concentrations as high as 6% at the washcoat surface. Na levels reach 0.2% by weight at the washcoat surface in the inlet of the long-term engine-aged DOC and are less than 0.1% by weight at the middle and exit, while S contamination is approximately 1.0% by weight throughout the washcoat at the inlet and is negligible elsewhere. In the accelerated Na-aged DOC the concentration of Na at the surface of the washcoat is high as 0.5% by weight, and there is clear penetration into the washcoat at peak levels between 0.2 and 0.3% by weight. Sulfur contamination appears throughout the entirety of the DOC washcoat along the entire length of the catalyst in comparable concentrations to the surface levels of Na contamination, with maximum values between 0.25 and 0.6% by weight. The presence of P at the washcoat surface is minimal, with a maximum value of less than 0.1% by weight at the DOC inlet.

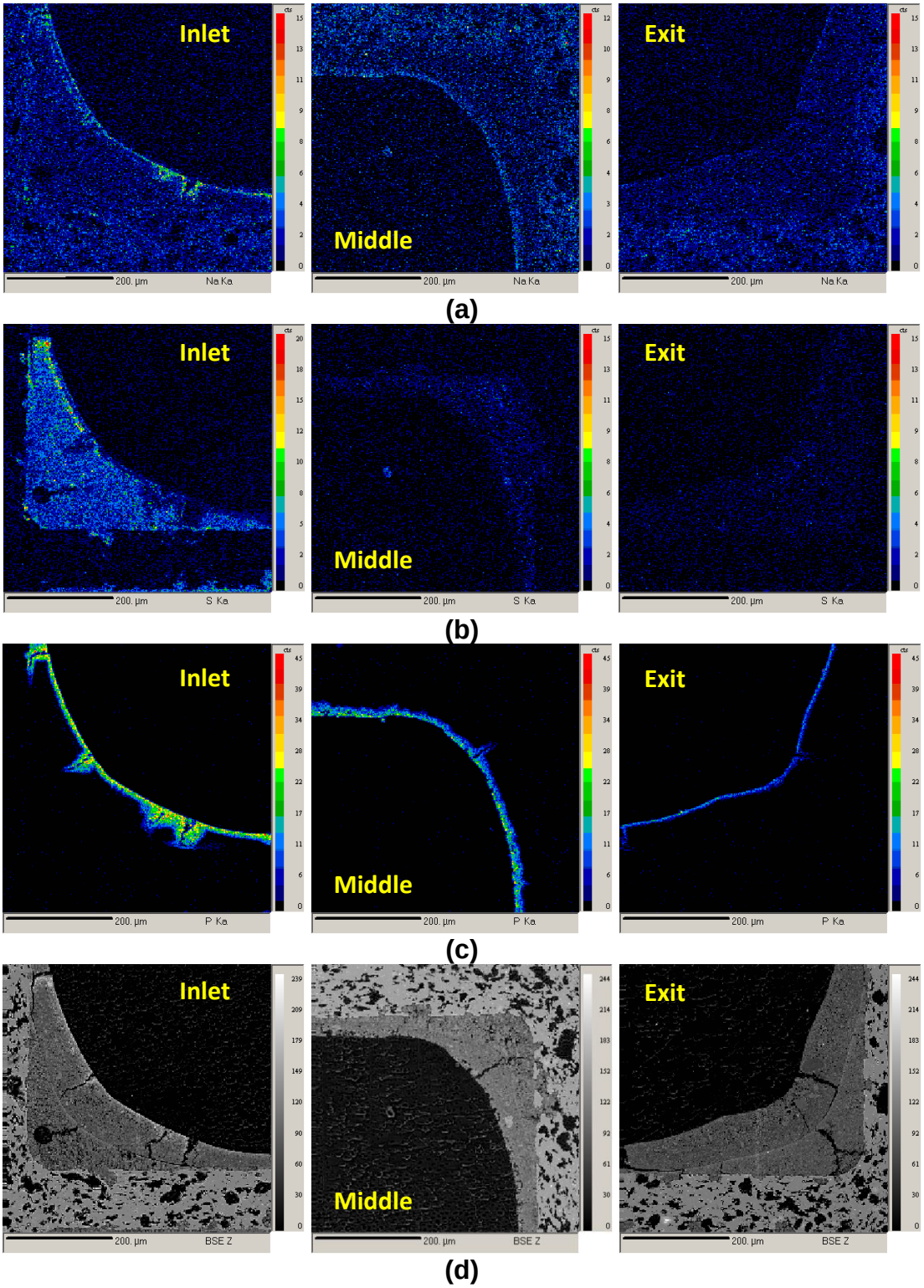

Figure 4.3.9 EPMA micrographs of (a) Na, (b) S, and (c) P contamination in long-term engine-aged DOC. (d) Backscatter images shown for clarity.

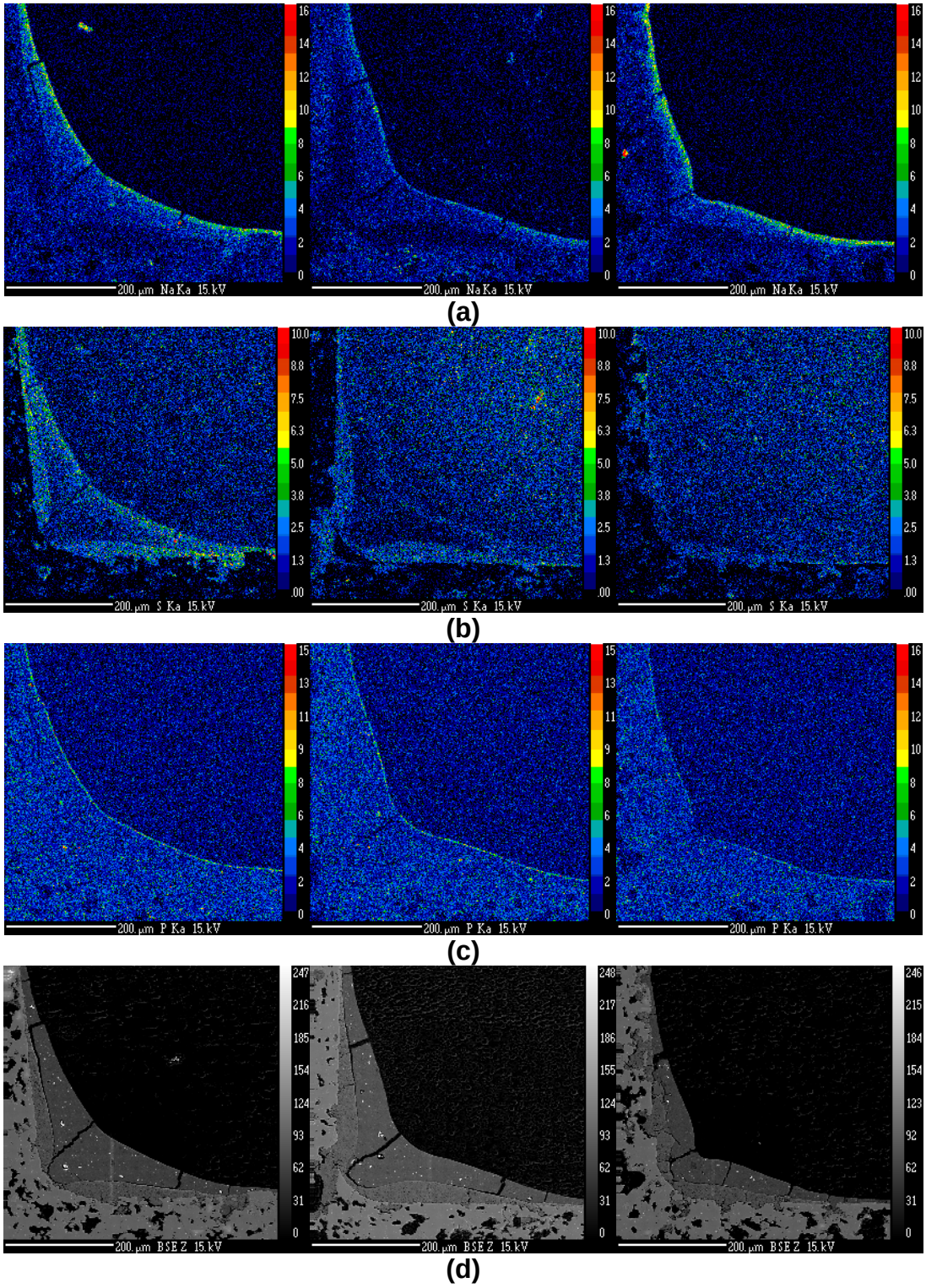

Figure 4.3.10 EPMA micrographs of (a) Na, (b) S, and (c) P contamination in light-duty configuration accelerated Na-aged DOC. (d) Backscatter images shown for clarity.

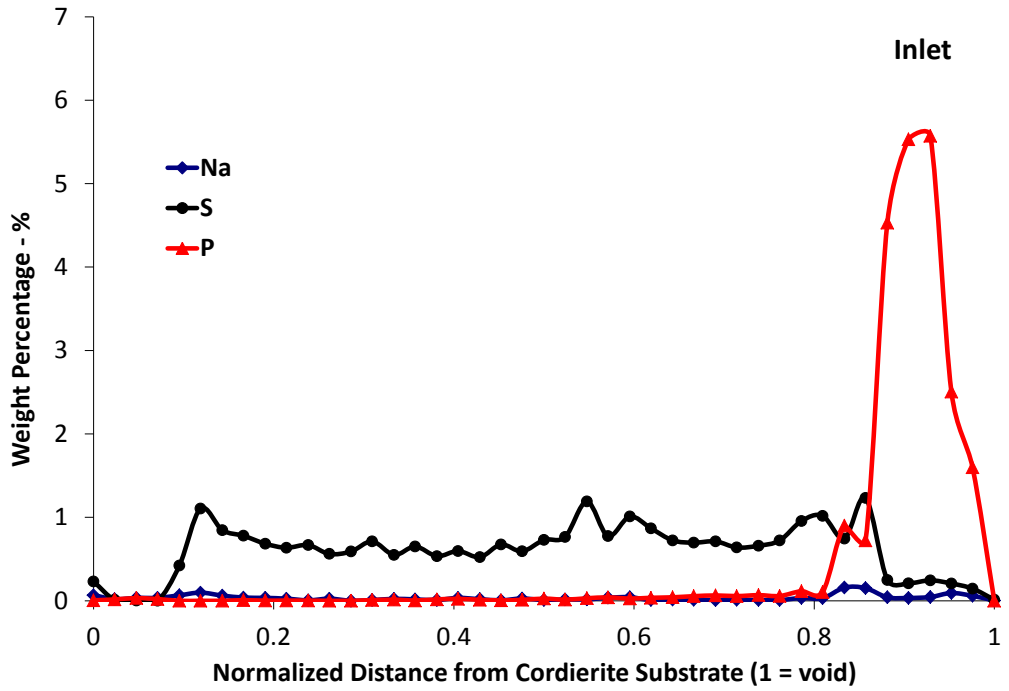

Figure 4.3.11 EPMA line scans of Na, S, and P contamination at inlet of long-term engine-aged DOC.

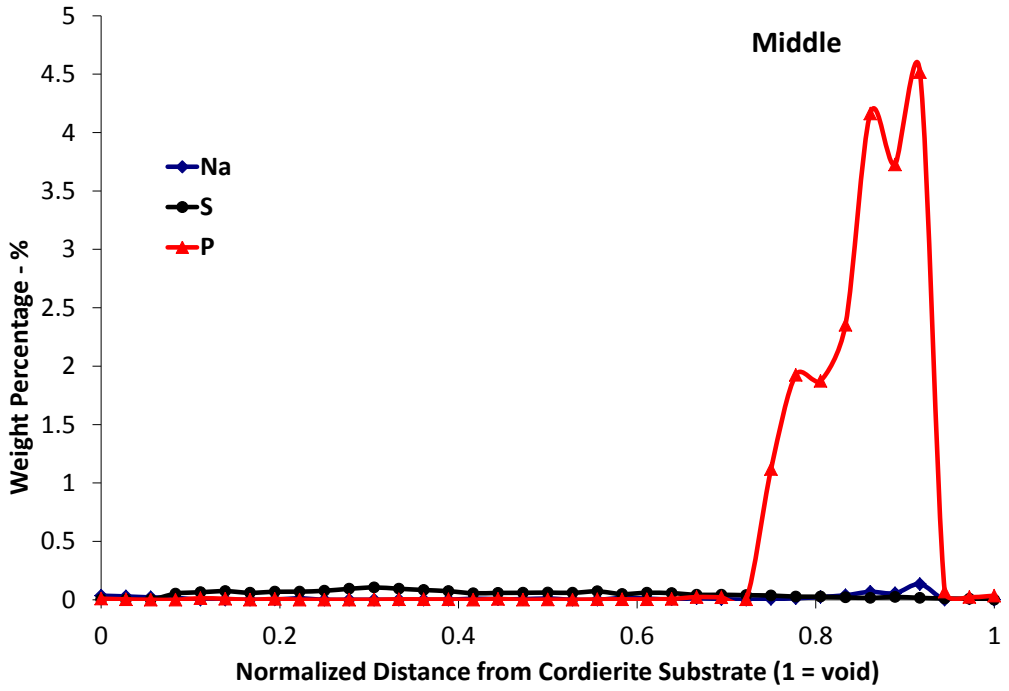

Figure 4.3.12 EPMA line scans of Na, S, and P contamination at middle of long-term engine-aged DOC.

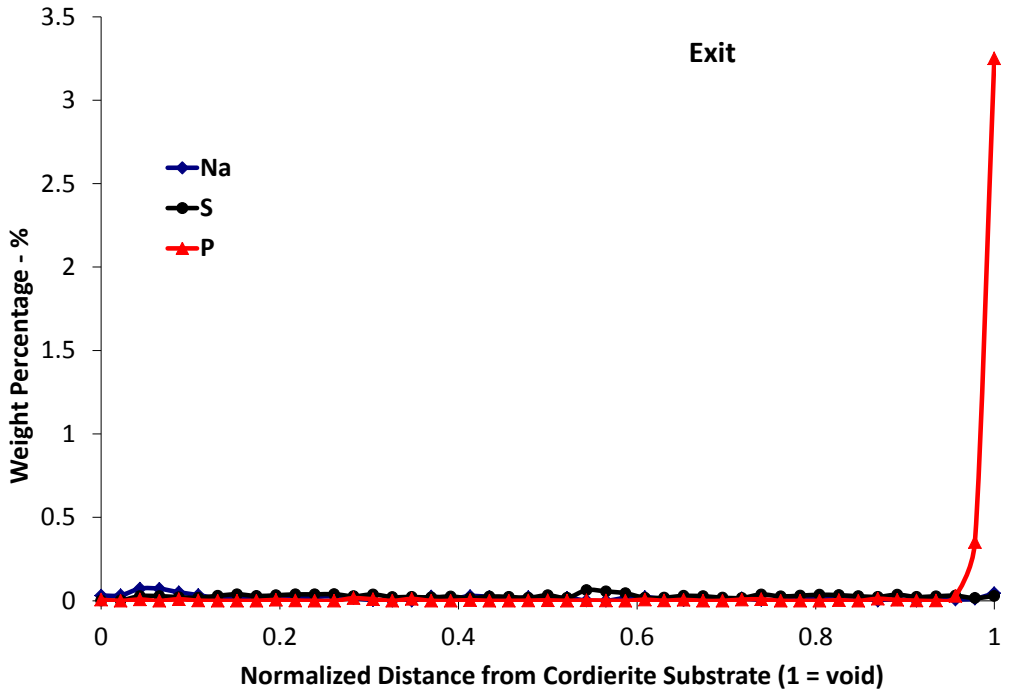

Figure 4.3.13 EPMA line scans of Na, S, and P contamination at exit of long-term engine-aged DOC.

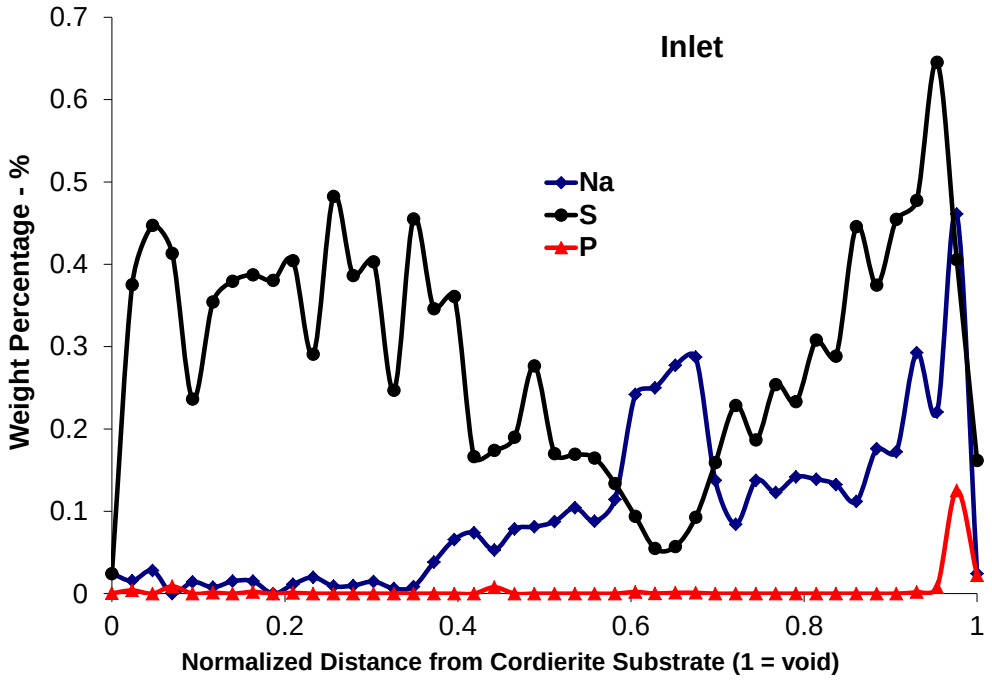

Figure 4.3.14 EPMA line scans of Na, S, and P contamination at inlet of light-duty accelerated Na-aged DOC.

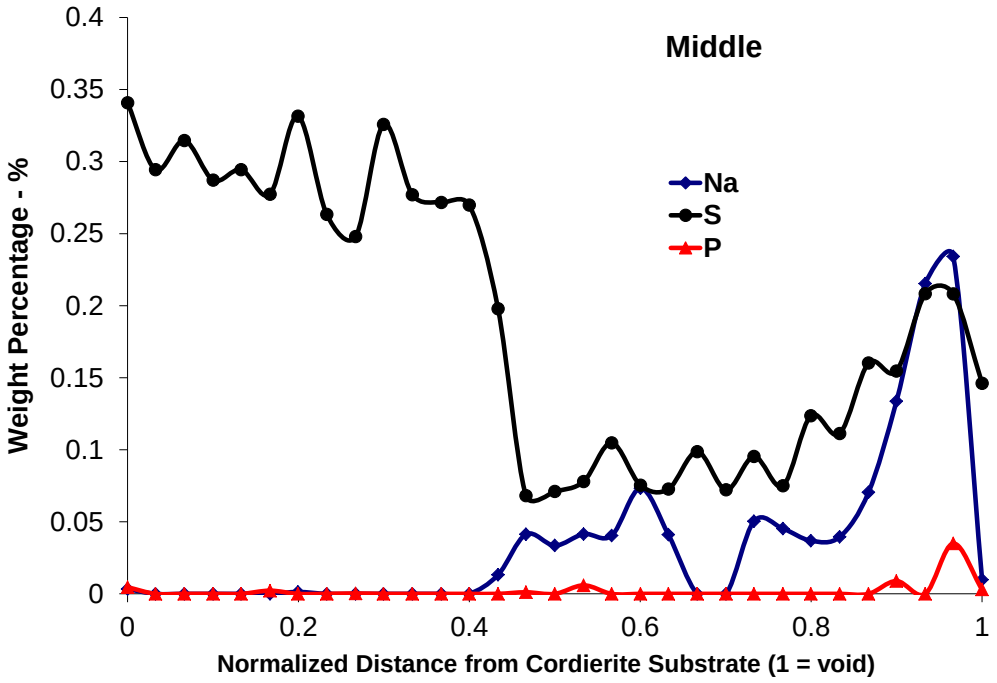

Figure 4.3.15 EPMA line scans of Na, S, and P contamination at middle of light-duty accelerated Na-aged DOC.

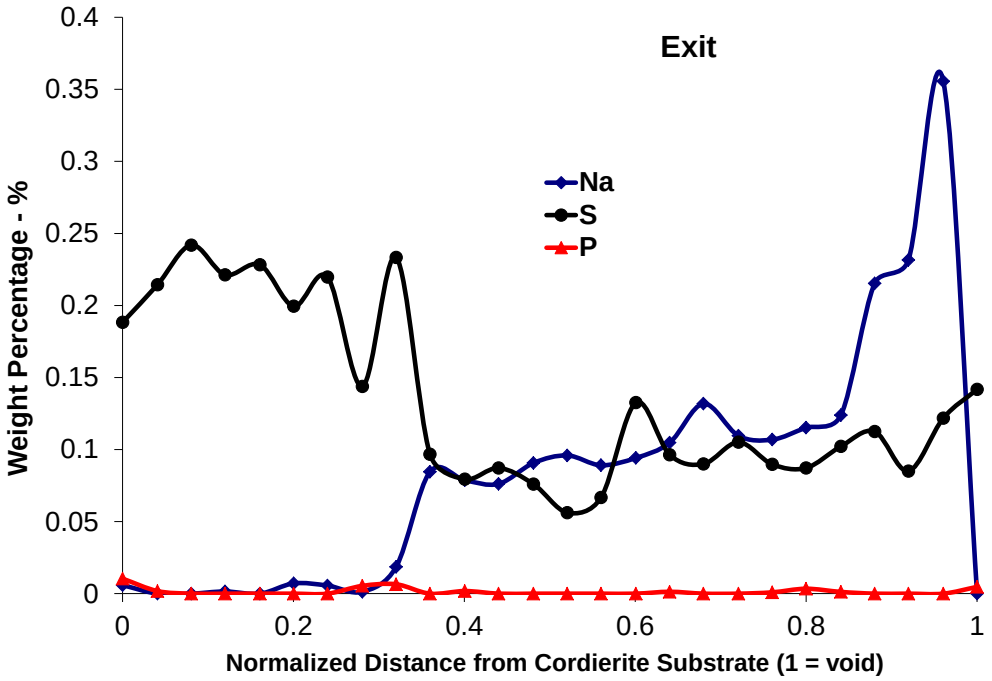

Figure 4.3.16 (continued) EPMA line scans of Na, S, and P contamination at exit of light-duty accelerated Na-aged DOC.

Overall, the distribution of Na contamination in the washcoat is similar for the two DOC catalysts, with the exception of the presence of Na down the entire length of the accelerated Na-aged DOC as opposed to appearing primarily at the inlet in the long-term engine-aged DOC. However, this difference can be explained by the difference in targeted equivalent miles for the aging protocols. The long-term engine-aging project at GM was performed to achieve 150,000 equivalent miles of exposure, while the accelerated Na-aging protocol aimed to achieve 435,000 miles of exposure. Therefore, it is expected that Na would appear in higher concentrations throughout the catalyst for the accelerated Na-aged DOC. Based on these results along with those from the DOC performance evaluations, it is believed that the accelerated Na-aging approach implemented in the current study is in line with long-term exposure approach.

4.4 Fresh and Accelerated Na-aged Cu-zeolite SCR

This section discusses performance evaluation, materials characterization, and mathematical modeling of fresh and accelerated Na-aged Cu-zeolite SCR catalysts. Section 4.4.1 provides the details of the accelerated Na-aging process, while Section 4.4.2 describes the results of the performance evaluations done according to the CLEERS transient SCR protocol. In Section 4.4.3 EPMA analysis, ICP measurements, BET surface area measurements, DRIFTS studies, and SEM-EDS are discussed, and the chapter concludes in Section 4.4.4 with results obtained using the SCR mathematical model.

4.4.1 Accelerated Na-aging of Cu-zeolite SCR

The beta formulation Cu-zeolite SCR catalysts were aged during the accelerated Na-aging protocol discussed in Chapter 3. Temperature profiles for the SCRs during aging are shown in Figures 4.4.1-4.4.3. During the light-duty configuration accelerated Na-aging run the inlet and exit of the SCR experience almost identical temperatures which fluctuate in the range between 550 and 700°C during the DPF regeneration. In the control case the temperature fluctuations due to regeneration are much higher, and the inlet of the SCR consistently sees higher temperatures than the exit. At the SCR inlet, temperatures range between 450 and 650°C, while at the SCR exit temperatures fall in the range from 400-600°C. The difference in temperatures between the inlet and exit of the SCR is highest in the heavy-duty configuration accelerated Na-aging arrangement, where the inlet temperature fluctuates between 525 and 700°C, while the exit temperature range is lower with values between 480 and 625°C. These large variations in the heavy-duty arrangement are most likely due to the position of the SCR at the end of the exhaust aftertreatment system.

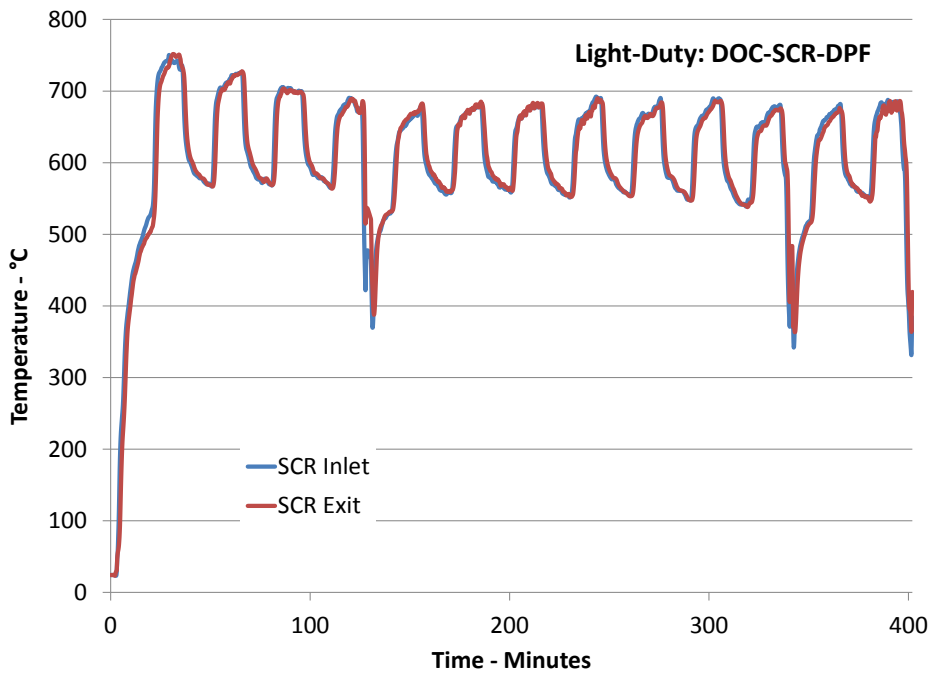

Figure 4.4.1 SCR temperature during accelerated Na-aging protocols for light-duty arrangement.

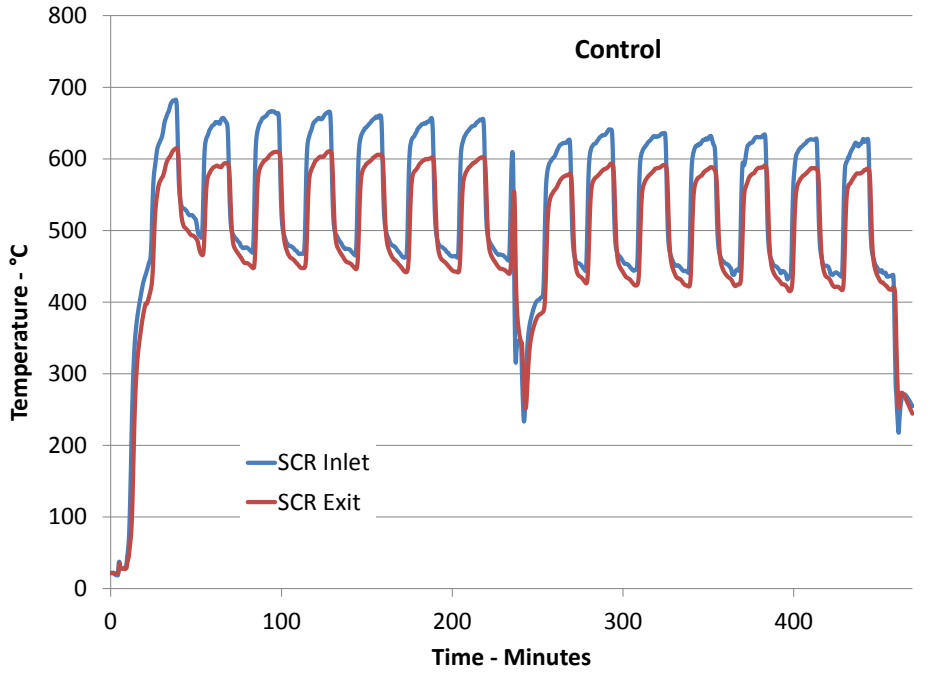

Figure 4.4.2 SCR temperature during accelerated Na-aging protocols for control arrangement.

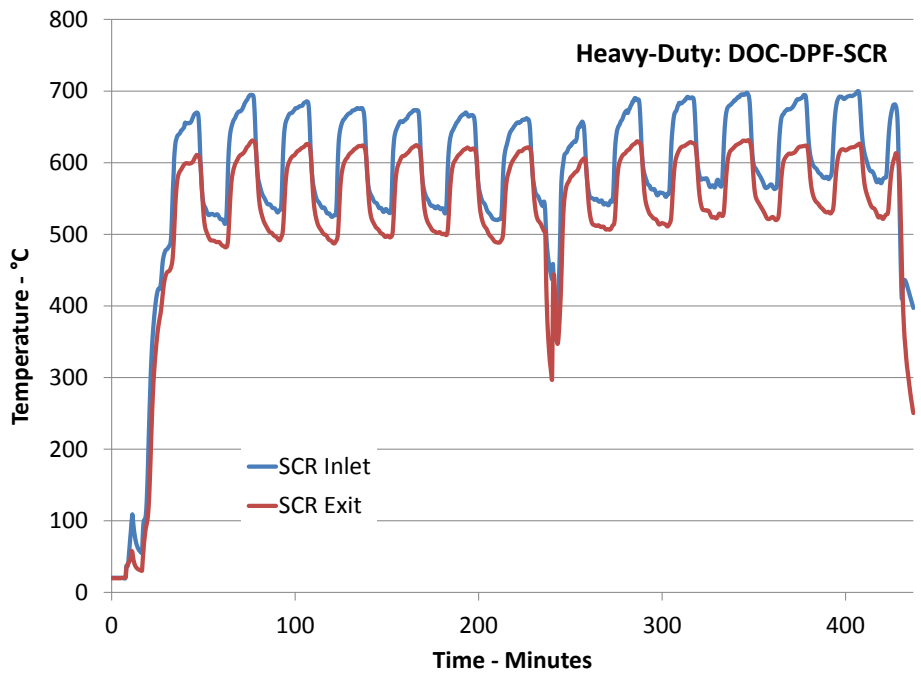

(c)

Figure 4.4.3 SCR temperature during accelerated Na-aging protocols for heavy-duty arrangement.

The average inlet, average exit, and maximum SCR temperatures are shown in Figure 4.4.4. The maximum temperature of the light-duty configuration accelerated Na-aged SCR reaches 750°C during the initial regeneration period, but subsequent regenerations produces temperatures at a maximum of 700°C similar to the maximum temperatures in the other two aging runs. The average temperature across the light-duty configuration accelerated Na-aged SCR is slightly above 600°C, while the control SCR catalyst experiences average temperatures at the inlet and exit of 550 and 510°C, respectively. In the heavy-duty configuration accelerated Na-aged SCR, the average inlet temperature is

similar to that observed in the light duty arrangement, although the exit average exit temperature is less at just over 550°C.

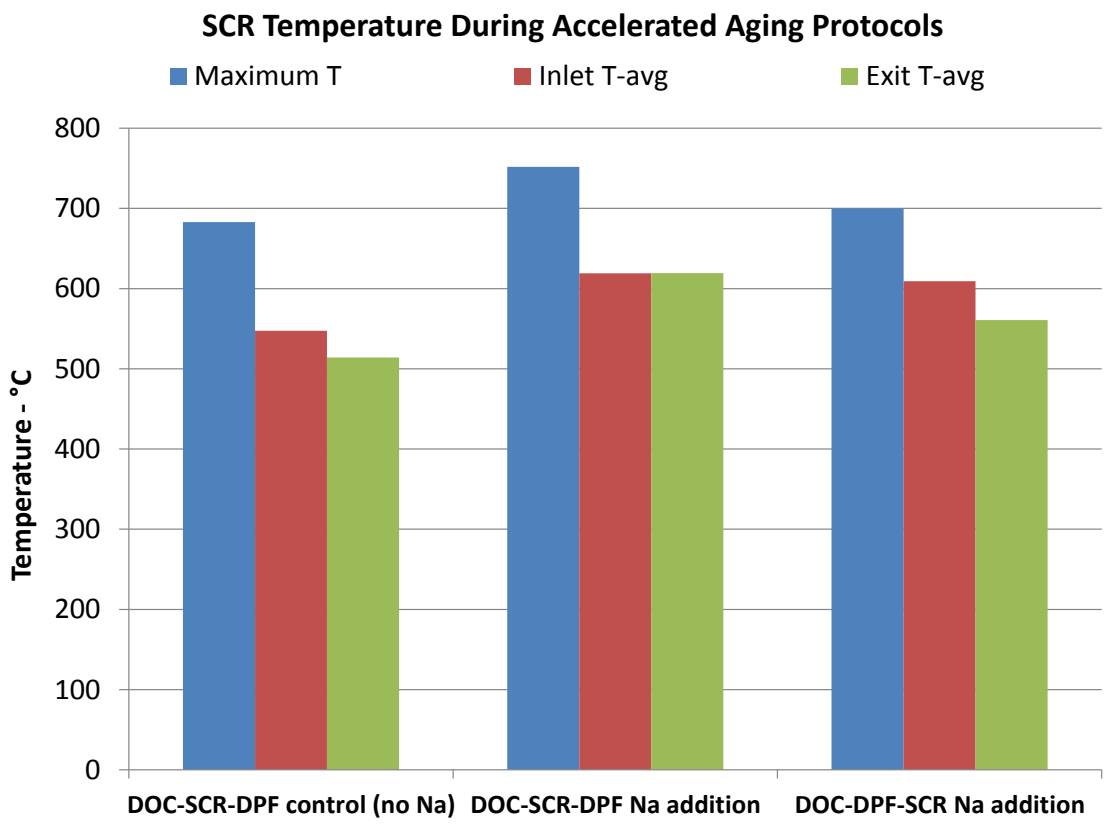

Figure 4.4.4 Average inlet temperature, average exit temperature, and maximum temperature in DPFs during accelerated Na-aging.

4.4.2 SCR Performance Evaluations

Performance evaluations were carried out on the fresh, control, light-duty configuration accelerated Na-aged, and heavy-duty configuration accelerated Na-aged SCR catalysts. These evaluations were performed on a BFR at NTRC according to the transient CLEERS SCR protocol, and gas analysis was performed by an MKS FTIR spectrometer capable of measuring NO, NO_2, N_2O

and NH_3. As with the DOC performance evaluations, the thermocouple located at the middle of the SCR sample was used as a basis for evaluation temperature in the evaluation range between 150 and 600ºC. Typical temperatures across the catalyst are shown in Figure 4.4.5.

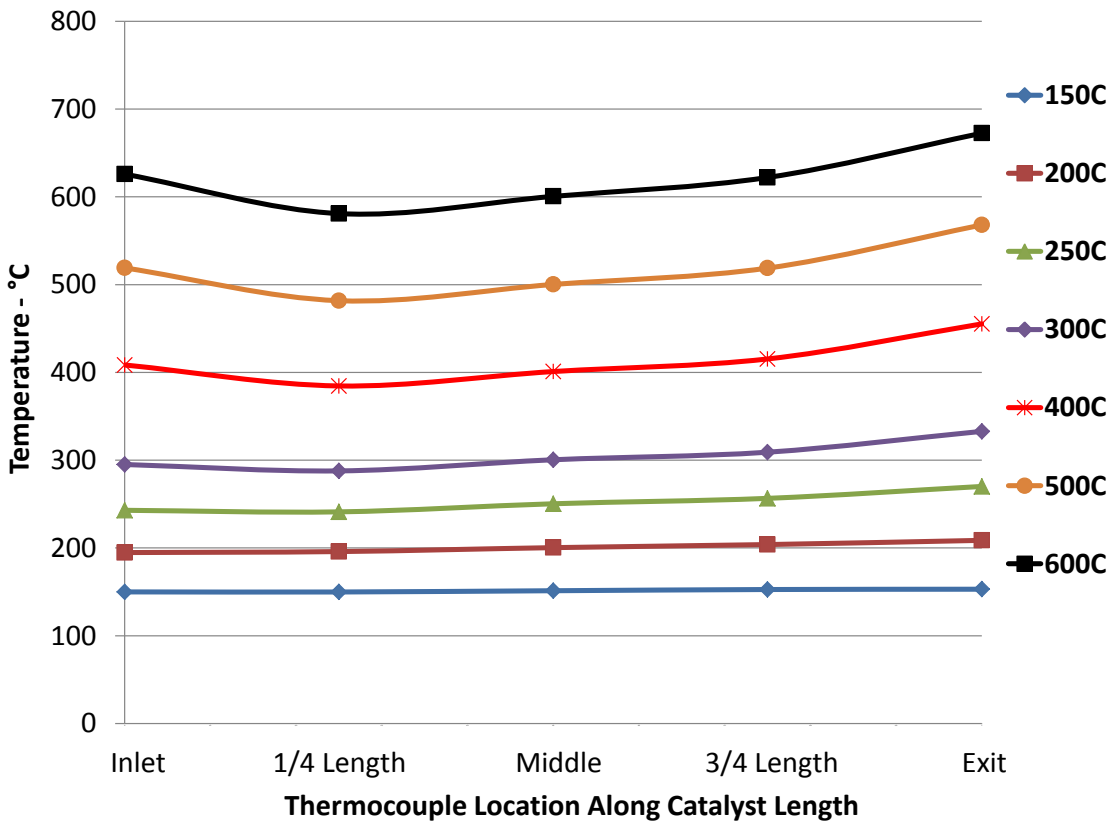

Figure 4.4.5 SCR catalyst temperature profiles during aging in the temperature range from 150 to 650°C.

During SCR evaluations, temperatures are typically lowest at the one quarter length of the catalyst, although even at 600ºC the difference between the middle and quarter length locations is only approximately 20ºC. Temperatures are highest at the exit of the SCR catalyst, with a maximum temperature difference

between middle and exit of 75ºC during evaluation at 600ºC. As with the DOC, these temperature variations are due to temperature gradients within the tubular furnace.

The BFR performance evaluation results of the standard NO-only NO_x conversion with an NH_3/NO_x ratio of 1:1 are shown in Figure 4.4.6.

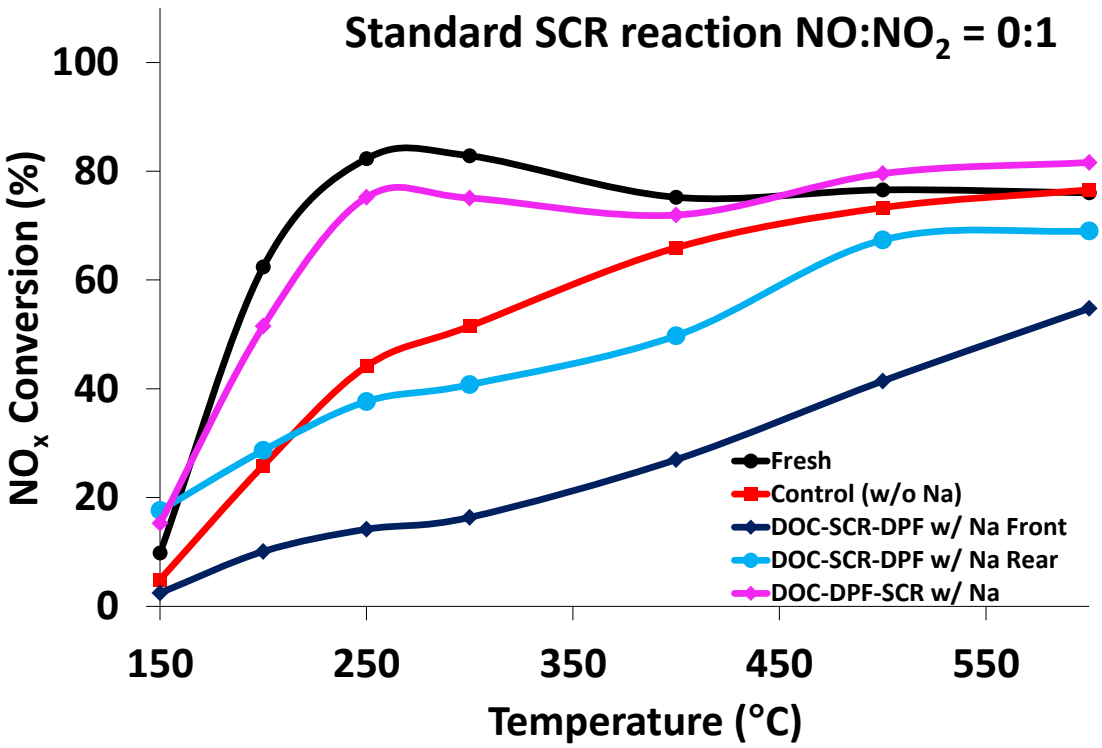

Figure 4.4.6 Standard SCR NO_x performance in fresh and accelerated Na-aged SCR catalysts.

The Na-contaminated SCR sample from the light-duty configuration accelerated Na-aging configuration experiences significant performance loss in both the front and rear halves of the catalyst relative to the fresh sample. The front half of the sample shows the highest performance loss with, reductions in NO_x conversion

as high as 70% in the peak SCR performance temperature range between 200 and 300ºC. The rear half exhibits less deactivation, but NO_x reduction is still decreased by as much as 45% in the peak temperature range and is significantly below that of the fresh catalyst across the entire range of evaluation temperatures. The performance of the control sample, also aged in the light-duty configuration, is impacted as well, although the decrease in performance impact is less with the control sample with NO_x conversions between those of the light-duty configuration accelerated Na-aged and fresh SCR samples. This implies that there are some thermal aging effects taking place in the light-duty aftertreatment arrangement. On the other hand, with the DPF positioned upstream of the SCR in the heavy-duty accelerated Na-aging arrangement, the performance of the SCR remains comparable to that of the fresh sample. Based on these performance results and EPMA analysis of the DPFs in Section 4.2.2, it appears that the upstream DPF in the heavy-duty configuration is retaining the majority of the Na from the biodiesel fuel and preventing Na contamination in the downstream SCR. Additionally, the performance of the control SCR relative to that of the heavy-duty configuration accelerated Na-aged catalyst suggests that the upstream DPF also lessens the thermal aging effects in the downstream SCR in the heavy-duty arrangement. Thus, the decrease in NO_x performance observed in the light-duty configuration accelerated Na-aged SCR samples indicates that Na contamination has a detrimental impact on the performance of Cu-zeolite SCR at the exposure levels brought about by the accelerated Na-

aging protocol, but that thermal aging effects also play a role in SCR deactivation in the light-duty arrangement.

During standard SCR performance evaluations, the NH_3/NO_x ratio was varied between 0.9 and 1.1 in order to determine the effect of NH_3 availability on SCR performance. The results of these tests are shown in Figure 4.4.7. In the fresh SCR, increasing the concentration of NH_3 in the simulated exhaust gases increases NO_x conversion by 6-8% at all temperatures above 250ºC. However, in both halves of the light-duty configuration accelerated Na-aged SCR, the impact of increased NH_3 is minimal, with only small increases of 1-2% at temperatures above 500ºC. The trends in the control sample fall in between those of the fresh and light-duty configuration accelerated Na-aged SCR catalysts, with minimum performance increases of 2% at 400ºC and maximum performances increases of 6% at 600ºC. Meanwhile, the sample from the heavy-duty configuration accelerated Na-aged SCR catalysts shows a correlation between NH_3 availability and NO_x conversion performance similar to that of the fresh SCR catalyst. These results imply that it is not NH_3 availability which is impacting performance, but rather the inability of the control and light-duty configuration accelerated Na-aged SCR catalysts to utilize the NH_3 for the SCR reaction. The results are corroborated by the significant amount of NH_3 slip observed during the standard SCR reaction in these two catalysts, particularly for the light-duty configuration accelerated Na-aged SCR. Furthermore, the fact that the light-duty configuration accelerated Na-aged SCR sees the smallest performance increase as a result of increased NH_3 availability, even relative to the control SCR, implies that Na is

contributing to the deactivation of this catalyst along with the thermal aging effects observed in the control SCR.

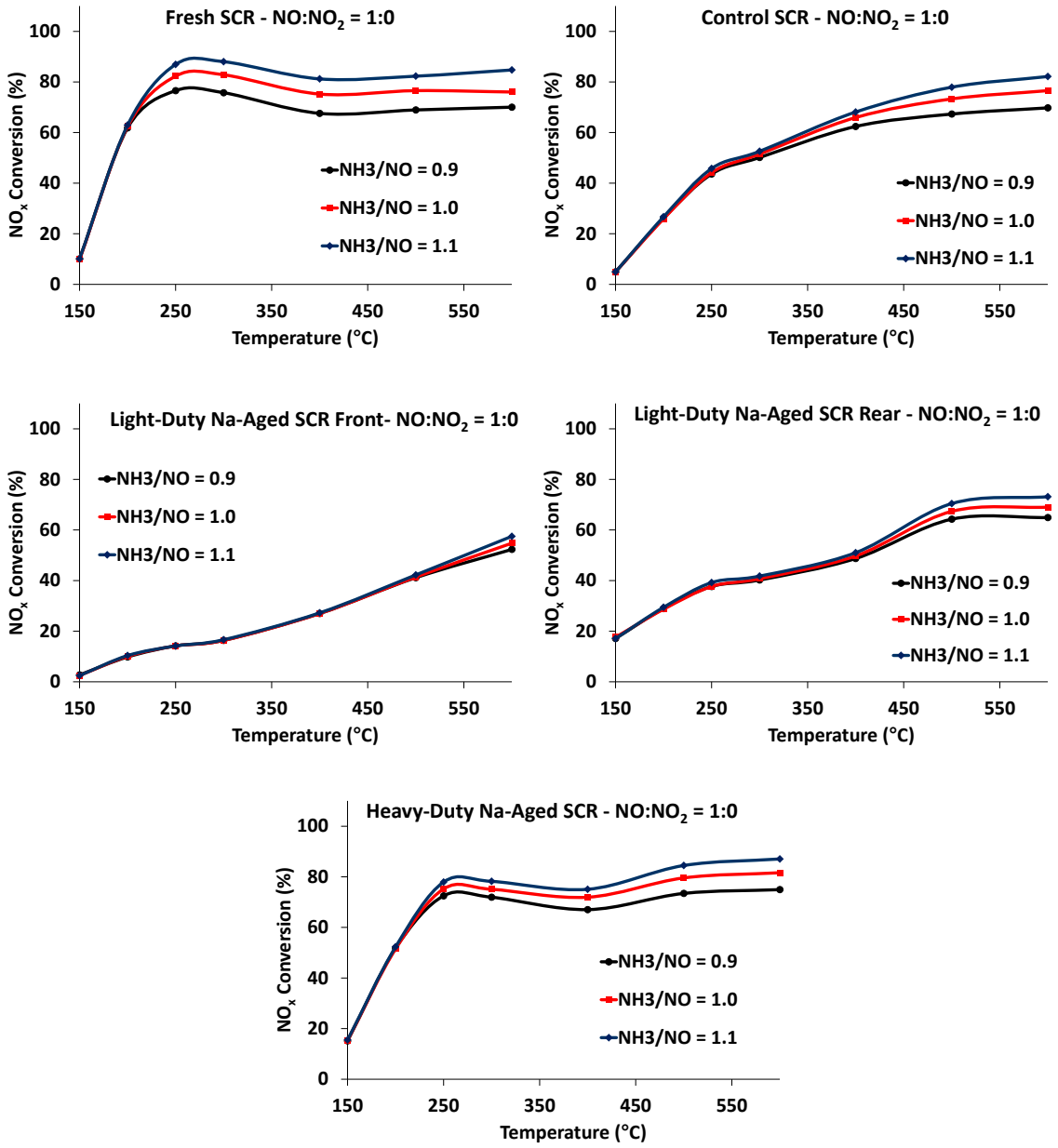

Figure 4.4.7 Impact of varying the NH_3/NO_x ratio on the standard SCR NO_x performance of fresh and accelerated Na-aged Cu-zeolite SCR catalysts.

Results of fast SCR performance evaluations where the ratio of NO to NO_2 is unity in the simulated exhaust feed are shown in Figure 4.4.8.

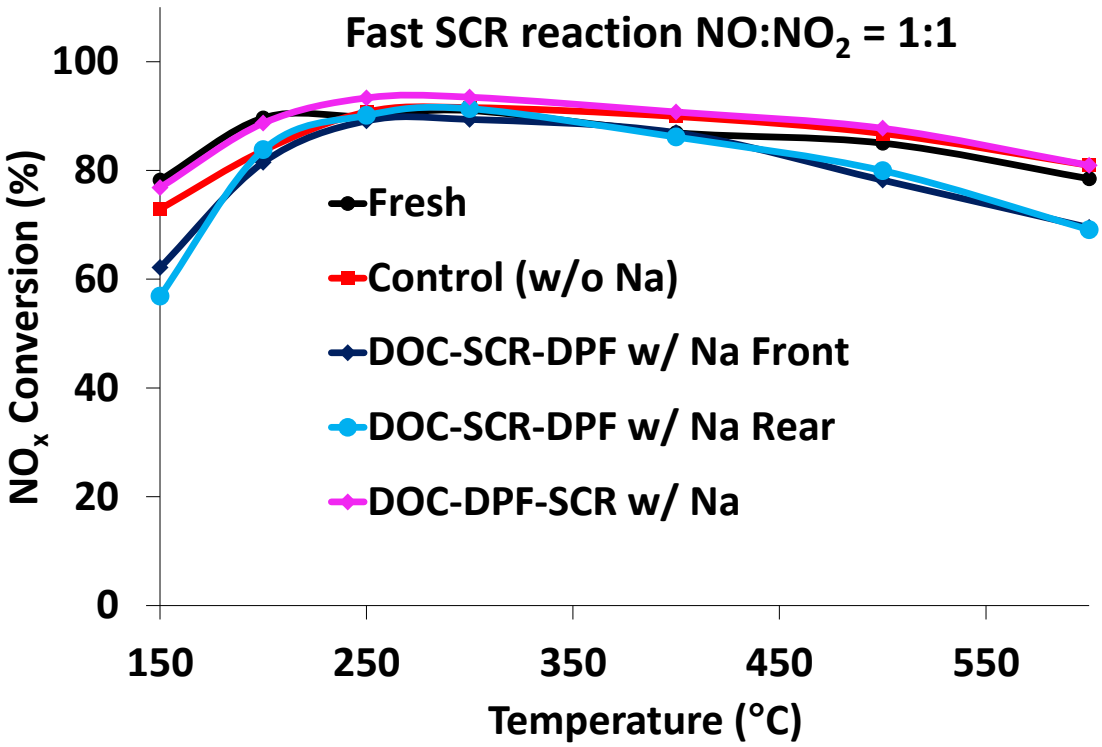

Figure 4.4.8 Standard SCR NO performance in fresh and accelerated Na-aged SCR catalysts.

As expected for fast SCR conditions, the performance of all five SCR samples is dramatically increased, particularly in the temperature range of 150 to 200ºC. The control and light-duty configuration accelerated Na-aged SCR samples show the biggest performance gains, where the disparity between these two catalysts and the fresh catalysts is greatly diminished. However, the light-duty configuration accelerated Na-aged SCR sample still shows significant deactivation at temperatures of 150, 500, and 600ºC.

In trying to isolate the impact of Na on the functionality of the SCR catalysts, NO to NO_2 oxidation, NH_3 oxidation, and NH_3 storage capacity were each independently evaluated during the transient CLEERS SCR protocol. The results of the NO to NO_2 oxidation experiments are shown in Figure 4.4.9.

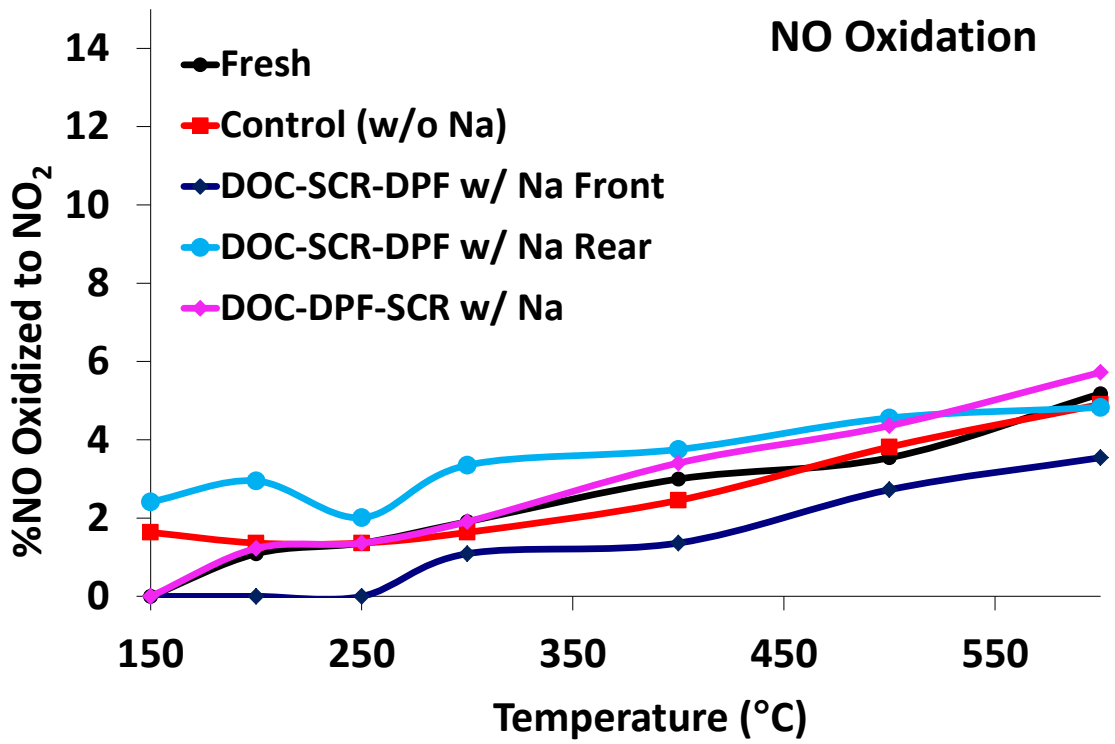

Figure 4.4.9 NO to NO_2 oxidation in fresh and accelerated Na-aged SCR catalysts.

As can be seen in the figure, both the fresh and aged Cu-zeolite SCR catalysts show very poor oxidation performance for NO, with a maximum conversion of 6% at 600 ºC. The SCR with worst NO to NO_2 oxidation activity is the front half of the light-duty configuration accelerated Na-aged SCR, but the rear half of the same

catalyst shows the highest activity across the evaluation temperature range. Performance for the remainder of the SCR catalysts falls within the bounds of these two samples. Due to the fact that all of the SCR samples showed poor NO to NO_2 oxidation capability, along with the fact that that both halves of the light-duty configuration accelerated Na-aged SCR catalysts showed significant NO_x performance deactivation but not NO to NO_2 deactivation, it is not possible to imply that Na contamination is directly impacting this functionality.

The NH_3 storage capacity measurements taken during BFR evaluations are shown in Figure 4.4.10.

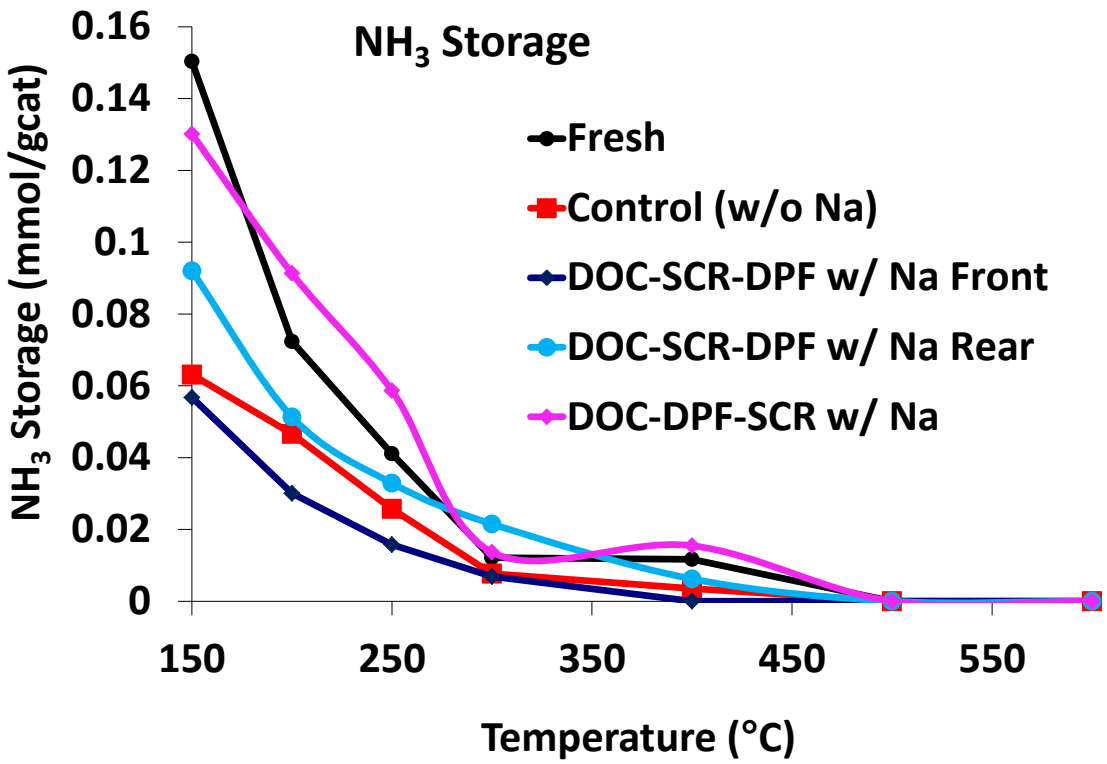

Figure 4.4.10 NH_3 storage capacity in fresh and accelerated Na-aged SCR catalysts.

The storage of NH_3 is greatest at 150ºC, although significant NH_3 storage still occurs at 200 and 250ºC. At temperatures above 400ºC only minimal storage is observed due to the prevalence of NH_3 oxidation at high temperatures. For simplicity, it is easiest to compare the results at 150ºC where trends are easily observed. In the front half of the light-duty configuration accelerated Na-aged SCR catalyst NH_3 storage capacity is significantly reduced from 0.15 to 0.058 mmol/g_{cat}. The impact on the rear half of this catalyst is less pronounced, where the storage is reduced to 0.093 mmol/g_{cat}. Meanwhile, the NH_3 storage capacity of the heavy-duty configuration accelerated Na-aged SCR is comparable to that of the fresh SCR, with a value of 0.13 versus 0.15 mmol/g_{cat} in the fresh sample. Surprisingly, the control sample shows a similar reduction in NH_3 storage capacity to the front half of the light-duty configuration accelerated Na-aged SCR, with a value of 0.062 mmol/g_{cat}. The temperature values recorded for the accelerated-aging process shown in Figure 4.4.4 show that the maximum and average temperatures across all three SCR catalysts were similar in each aging protocol, with the control case seeing the mildest conditions, followed by the heavy-duty configuration accelerated Na-aged SCR and then the light-duty configuration accelerated Na-aged SCR. Again there appear to be competing deactivation mechanisms which are difficult to fully correlate to the presence of Na. If Na was the primary contributor to decreased NH_3 storage capacity then the rear half of the light-duty configuration accelerated Na-aged SCR should exhibit lower storage capacity than the control case. On the other hand, if thermal aging effects were the primary deactivation mechanism then the SCR from the heavy-

duty configuration accelerated Na-aged SCR should have a lower storage capacity than the control SCR. Based on these results, it appears that both Na contamination and thermal aging effects are contributing to reduction in NH_3 storage capacity, but since the results do not directly correlate to the NO_x performance losses observed in Figure 4.4.6, it is not possible to suggest NH_3 storage capacity as the limiting factor in the deactivated SCR catalysts.

The oxidation of NH_3 over Cu-zeolite is an undesirable side reaction during SCR and can significantly impact the performance of SCR catalysts due to reduced availability of NH_3, and in some cases NO_x can be produced. However, investigating NH_3 oxidation can provide insight into which chemistry is impacted by the presence of Na contamination in the SCR samples. The results of NH_3 oxidation tests over the fresh and accelerated Na-aged SCR catalyst is shown in Figure 4.4.11. NH_3 oxidation is similar for all SCR samples at temperatures below 400ºC, but differences are observed beginning at temperatures above 500ºC. The front half of the light-duty configuration accelerated Na-aged SCR catalyst again shows the lowest activity, while the NH_3 oxidation in the rear half generally follows the trends seen in the control sample. Meanwhile, NH_3 oxidation in the heavy-duty configuration accelerated Na-aged SCR catalyst is comparable to the fresh at 500ºC and approximately 10% below the fresh at 600ºC. Of the three main mechanisms investigated in the study (NO to NO_2 oxidation, NH_3 storage, and NH_3 oxidation), the results of the NH_3 oxidation study most closely resemble those observed in the standard NO-only SCR performance evaluations. This suggests that the portion of performance loss associated directly with Na

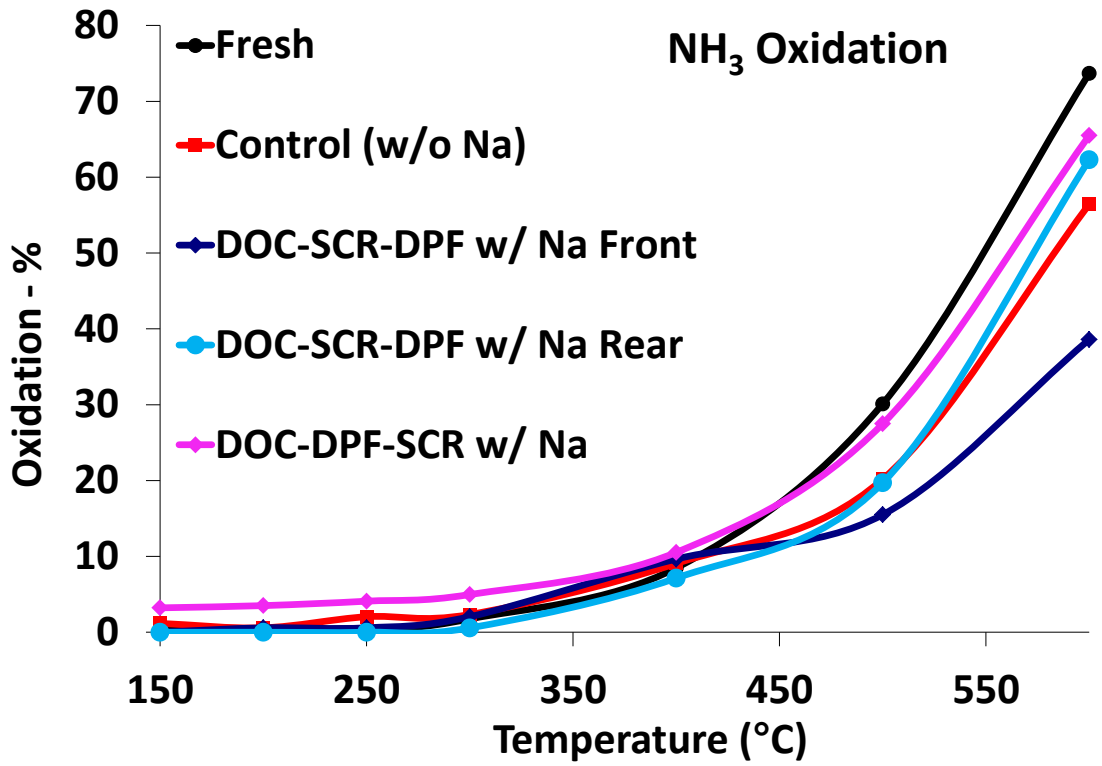

Figure 4.4.11 NH_3 oxidation in fresh and accelerated Na-aged SCR catalysts.

contamination could be related to a deactivation of and/or a reduction in the number of the Cu sites responsible for NH_3 oxidation. Wilken et al. [60] observed deactivation of Cu-zeolite which they attributed to a loss of active Cu sites in their study on thermal aging. The possibility that Na contamination is either masking or deactivating these active Cu sites beyond normal thermal aging effects would account for the significant decline in NO_x performance observed in the light-duty configuration accelerated Na-aged SCR catalyst, along with the difference in performance observed between this sample and the control sample.

Overall, the results obtained during the SCR performance evaluations appear to agree with those obtained by Cavataio et al. [16] in their study on the

deactivation of Cu-zeolite due to Na contamination. Na contamination has a clear impact on the performance of Cu-zeolite SCR, but it is difficult to point to a single mechanism as the source of the deactivation. The standard SCR reaction is significantly impacted, and there appear to be both thermal aging effects and a performance loss due to the presence of Na. However, it seems that a combination of factors could be leading to the deactivation, including loss of NH_3 storage capacity and a reduction in the number of Cu sites as evidenced by the decrease in NH_3 oxidation activity. Finally, the aftertreatment arrangement plays a significant role in the level of deactivation observed, as the SCR placed downstream of the DPF in the heavy-duty aging configuration appears to be protected from both thermal aging effects and Na contamination by the upstream DPF.

4.4.3 SCR Materials Characterization

EPMA analysis was performed on the fresh and accelerated Na-aged SCR catalysts, including the control SCR sample. Analysis on the fresh sample was performed in order to obtain a baseline level of Na presence in the beta model Cu-zeolite as provided from BASF. The micrographs obtained for the fresh SCR catalyst sample are shown in Figure 4.4.12, while a line scan of Na concentration is shown in Figure 4.4.13. In the fresh condition, no evidence of Na, S, or P is seen in the micrographs of the SCR catalyst channel, either in the

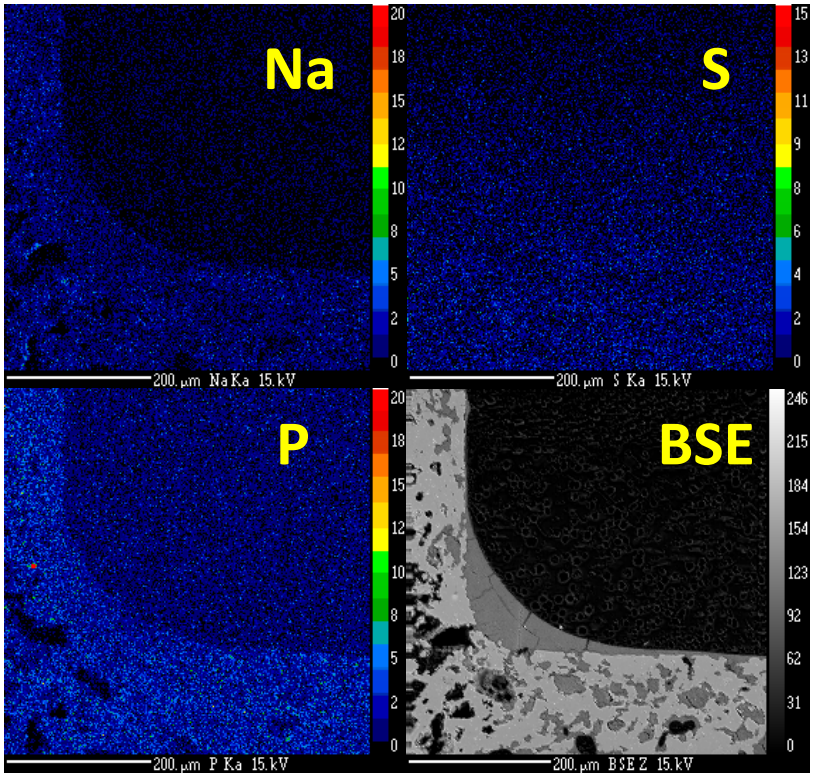

Figure 4.4.12 EPMA micrographs of Na, S, and P presence in fresh SCR catalyst. Backscatter images shown for clarity.

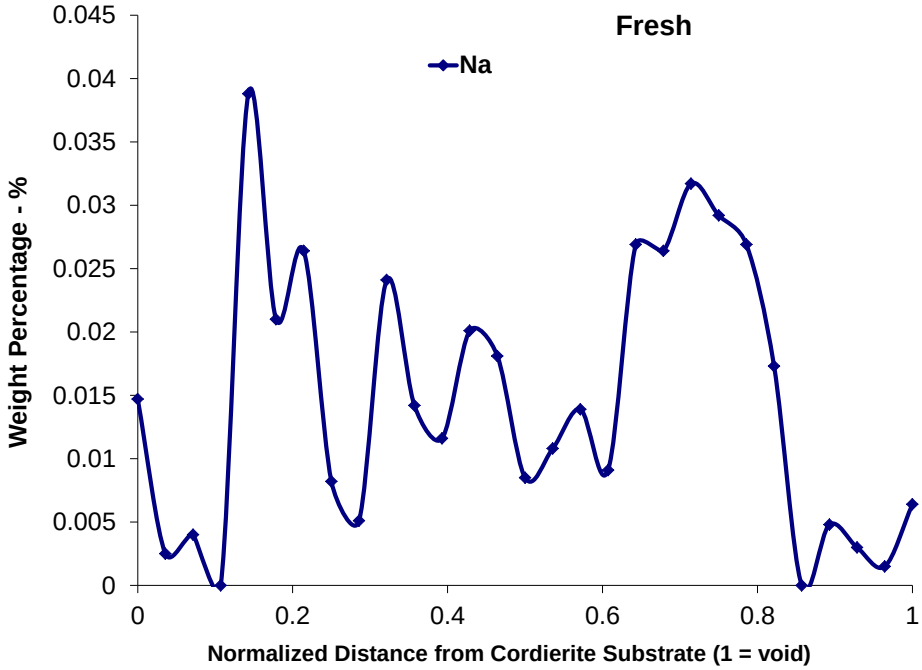

Figure 4.4.13 EPMA line scan of Na in fresh SCR catalyst.

bulk of the washcoat or on the washcoat surface. Meanwhile, the line scan shows that the highest concentration of Na measured in the fresh SCR is below 0.04% by weight, which is at the detection limit of the EPMA apparatus. Thus, prior to aging only a negligible amount of Na is present in the SCR catalyst.

Micrographs of Na, S, and P contamination in the light-duty configuration accelerated Na-aged SCR, heavy-duty configuration accelerated Na-aged SCR, and control SCR are shown in Figures 4.4.14-4.4.16, respectively. In the light-duty configuration accelerated Na-aged SCR catalyst a layer of Na contamination is clearly visible on the surface of the washcoat. Furthermore, this layer does not diminish in intensity down the length of the SCR catalyst. Meanwhile, the SCR catalyst located downstream of the DPF in the heavy-duty accelerated Na-aging configuration shows no evidence of Na contamination either on the surface or in the bulk of the washcoat, indicating that the upstream DPF captures the majority of the Na contamination in the heavy-duty arrangement. The control SCR catalyst also exhibits no signs of Na contamination, which is expected since the fuel was not doped with Na salt during that aging process. With regards to S and P contamination, all three SCR catalysts show negligible amounts of contamination based on the micrograph images. It is important to note that the distribution of Na contamination in the light-duty configuration accelerated Na-aged SCR catalysts is similar to that observed in the light-duty configuration accelerated Na-aged DOC and long-term engine-aged DOC provided by GM. This observation increases confidence that the accelerated Na-aging approach

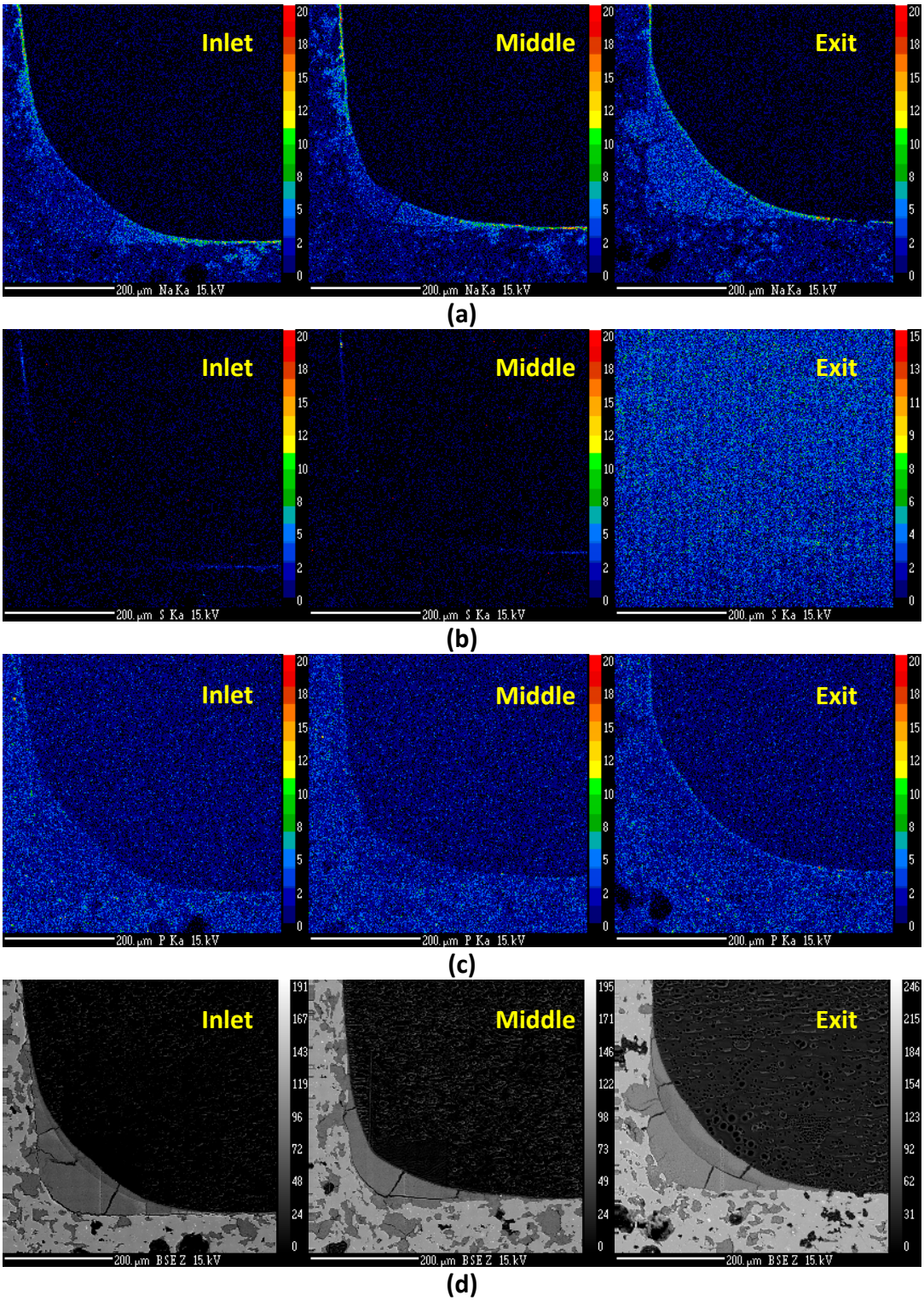

Figure 4.4.14 EPMA micrographs of (a) Na, (b) S, and (c) P contamination in light-duty configuration accelerated Na-aged SCR. (d) Backscatter images shown for clarity.

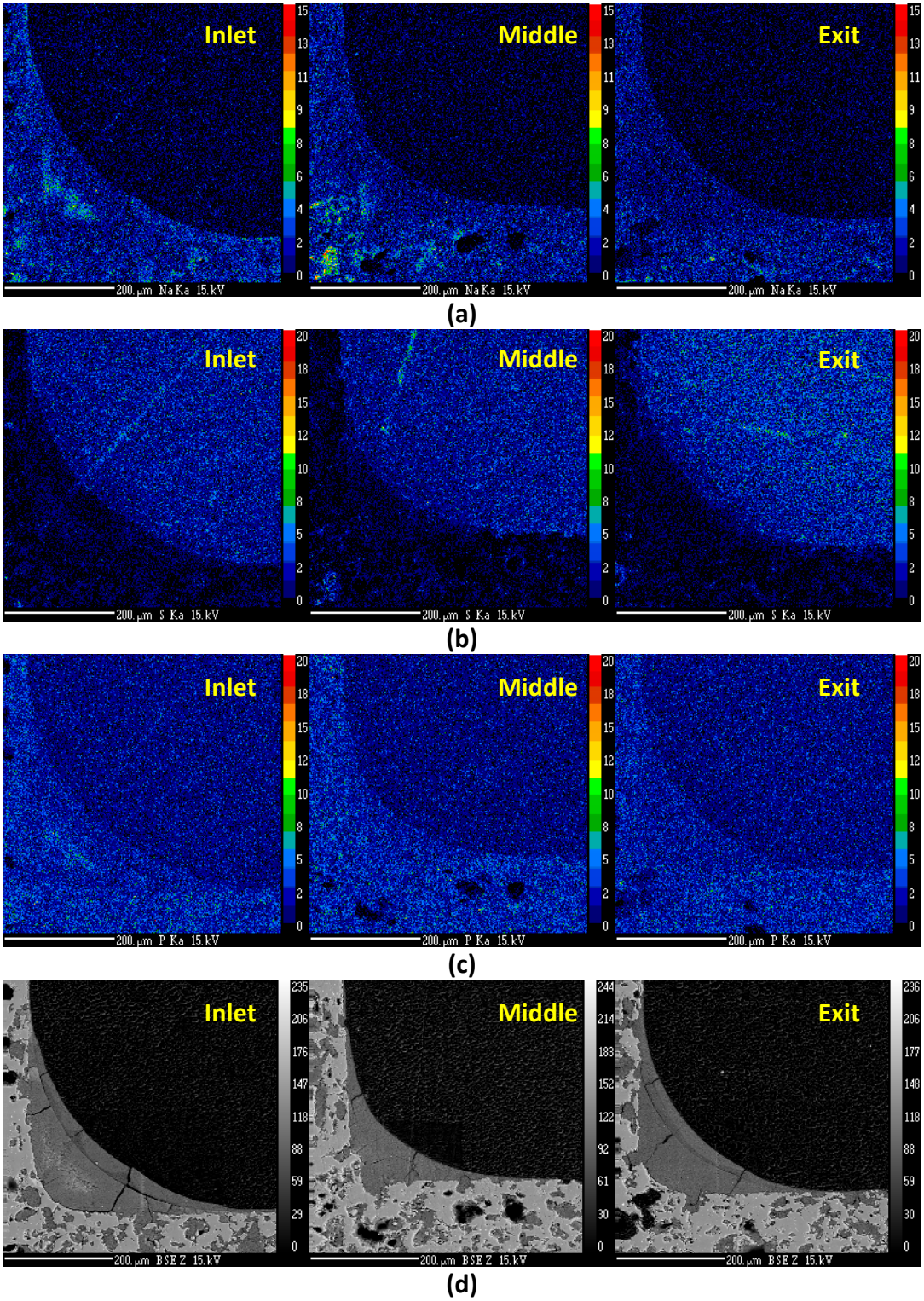

Figure 4.4.15 EPMA micrographs of (a) Na, (b) S, and (c) P contamination in heavy-duty configuration accelerated Na-aged SCR. (d) Backscatter images shown for clarity.

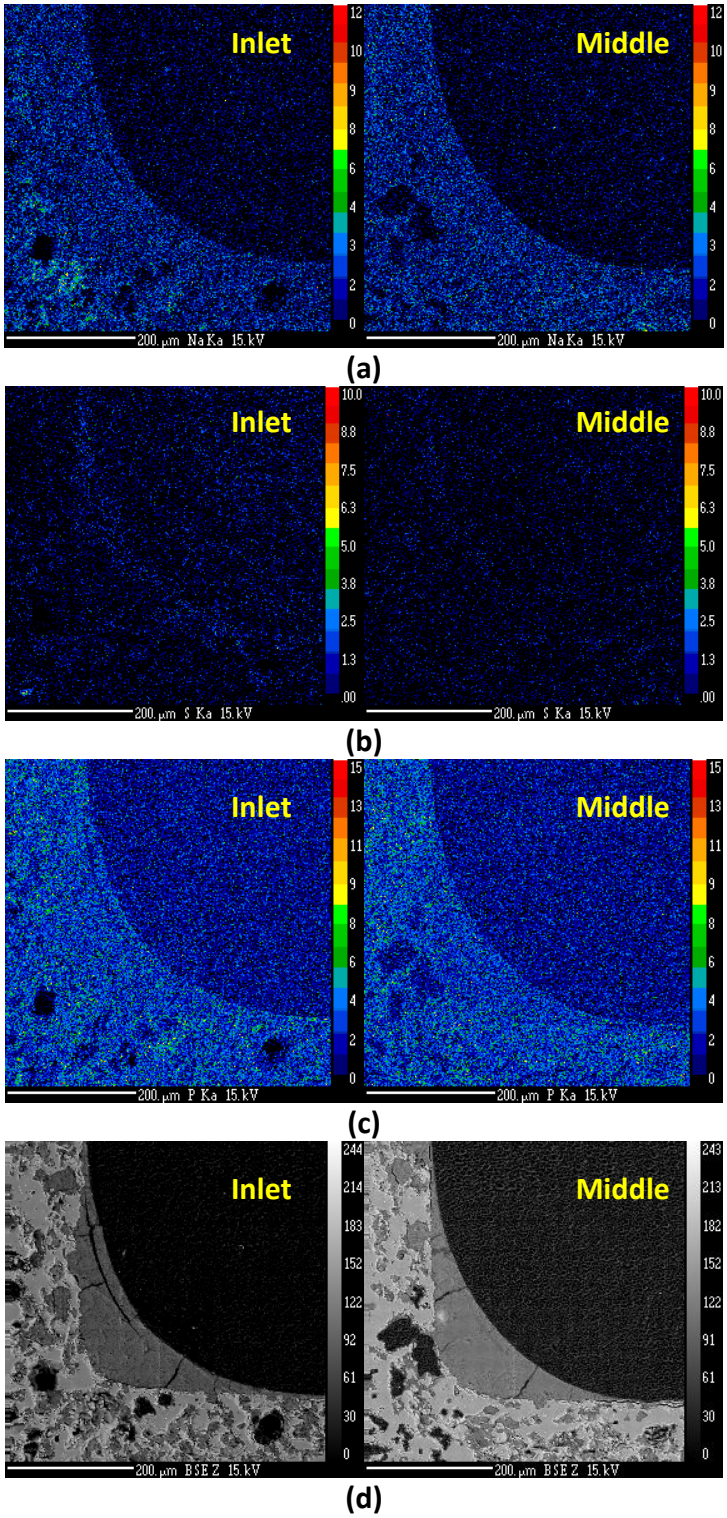

Figure 4.4.16 EPMA micrographs of (a) Na, (b) S, and (c) P contamination in control SCR. (d) Backscatter images shown for clarity (rear of control SCR unavailable for analysis).

provides an accurate representation of Na contamination brought about by the operation of a diesel engine using biodiesel fuel.

Line scan results obtained for Na, S, and P in the light-duty configuration accelerated Na-aged SCR, heavy-duty configuration accelerated Na-aged SCR, and control SCR are shown in Figures 4.4.17-4.4.19, Figures 4.4.20-4.4.22, and Figures 4.4.23-4.4.24, respectively. The inlet and middle of the light-duty configuration accelerated Na-aged SCR shows Na concentrations in the bulk of the washcoat at levels between 0.1 and 0.15% by weight, while the washcoat surface contains levels as high as 0.25% by weight. The exit shows even higher levels of concentration, with the bulk of the washcoat containing as much as 0.25% by weight and the surface showing levels as high as 0.5% by weight. Both S and P contamination are minimal, with S levels reaching a maximum of less than 0.1% by weight and P levels averaging less than 0.03% by weight. Meanwhile, Na contamination in both the heavy-duty configuration accelerated Na-aged SCR and control SCR is minimal. In the heavy-duty arrangement, the inlet of the SCR sees a maximum concentration of 0.11% Na by weight is observed at the SCR inlet, while the majority of the washcoat contains between 0.04 and 0.1% by weight. The middle and exit of this SCR exhibit even less evidence of contamination with Na concentrations of less than 0.04% by weight throughout the washcoat, which is near the detection limit of the EPMA device. The line scans for the control SCR show similar results, with levels of Na contamination below 0.07% by weight in the washcoat for both the inlet and middle samples. The concentrations of S and P in the heavy-duty

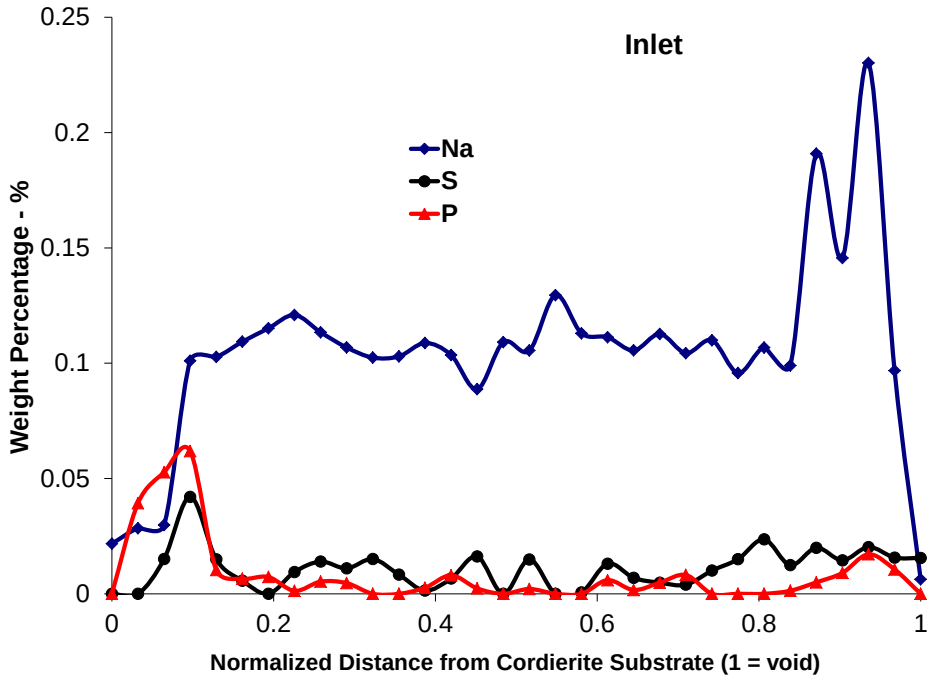

Figure 4.4.17 EPMA line scans of Na, S, and P contamination at inlet of light-duty configuration accelerated Na-aged SCR.

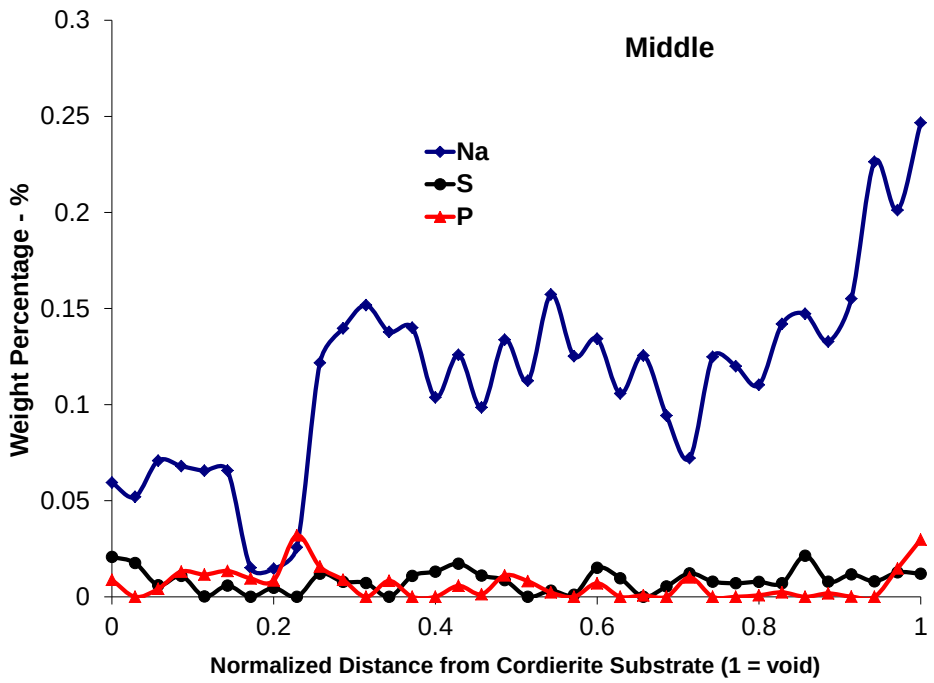

Figure 4.4.18 EPMA line scans of Na, S, and P contamination at middle of light-duty configuration accelerated Na-aged SCR.

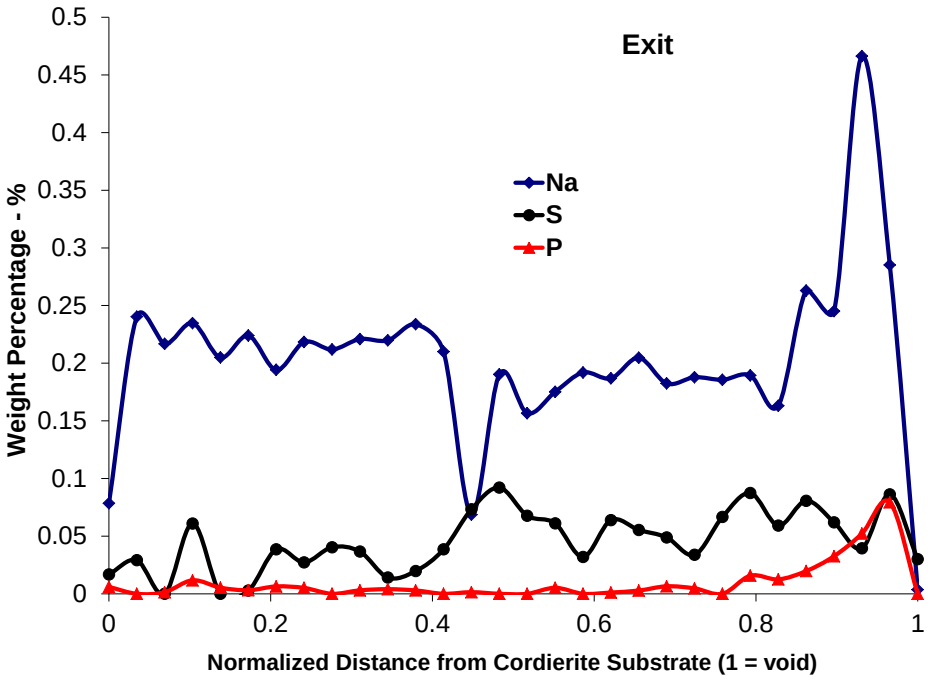

Figure 4.4.19 EPMA line scans of Na, S, and P contamination at exit of light-duty configuration accelerated Na-aged SCR.

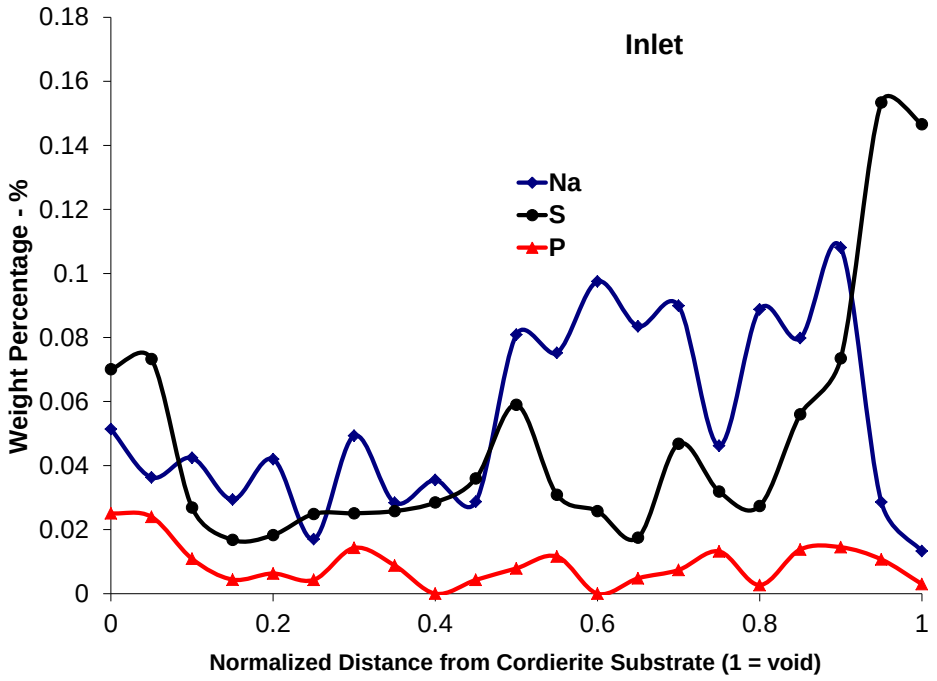

Figure 4.4.20 EPMA line scans of Na, S, and P contamination at inlet of heavy-duty configuration accelerated Na-aged SCR.

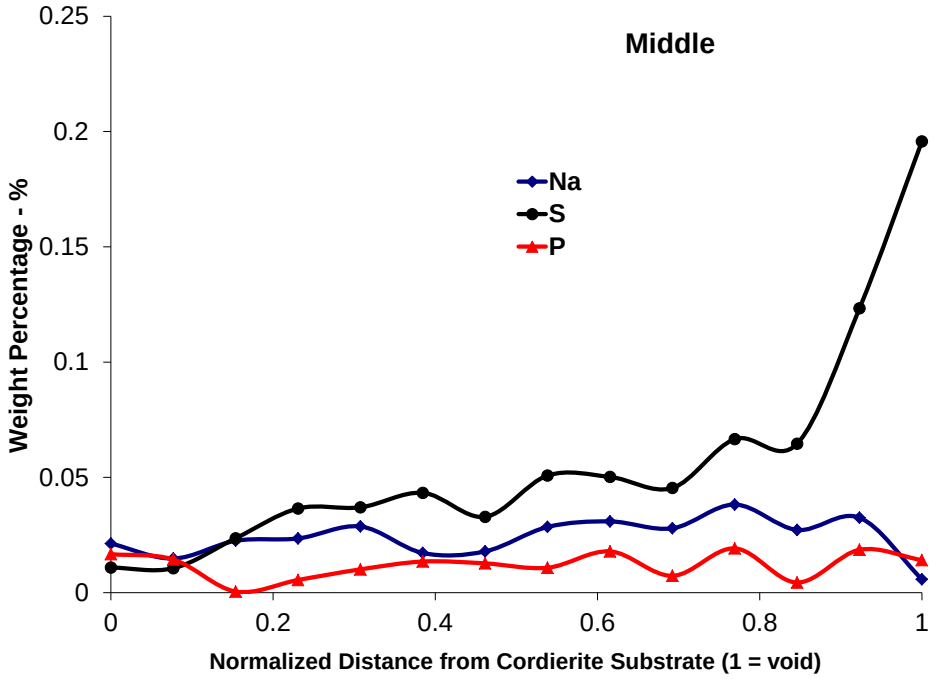

Figure 4.4.21 EPMA line scans of Na, S, and P contamination at middle of heavy-duty configuration accelerated Na-aged SCR.

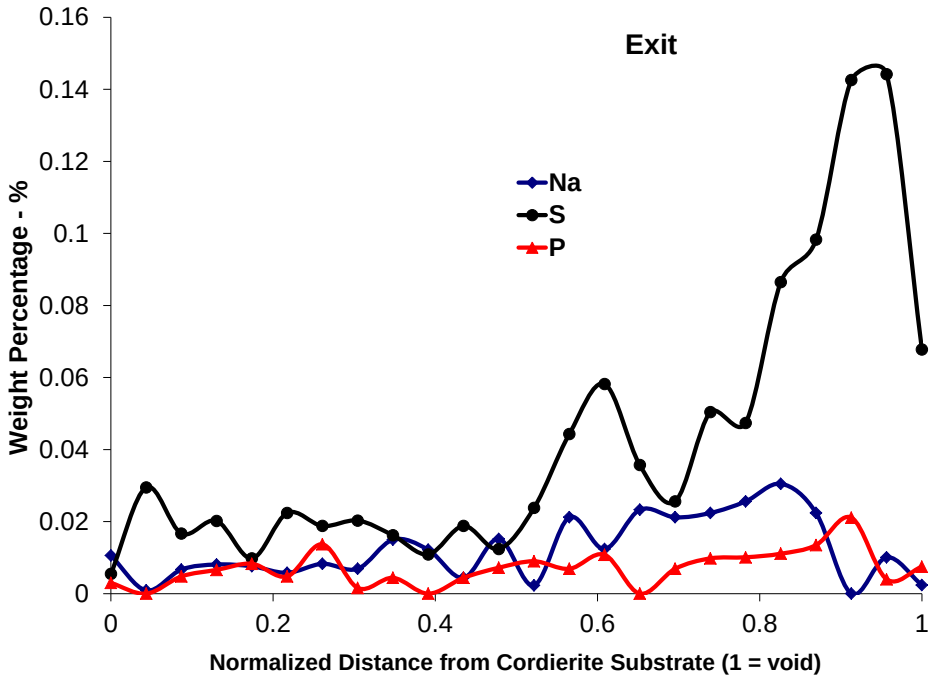

Figure 4.4.22 EPMA line scans of Na, S, and P contamination at exit of heavy-duty configuration accelerated Na-aged SCR.

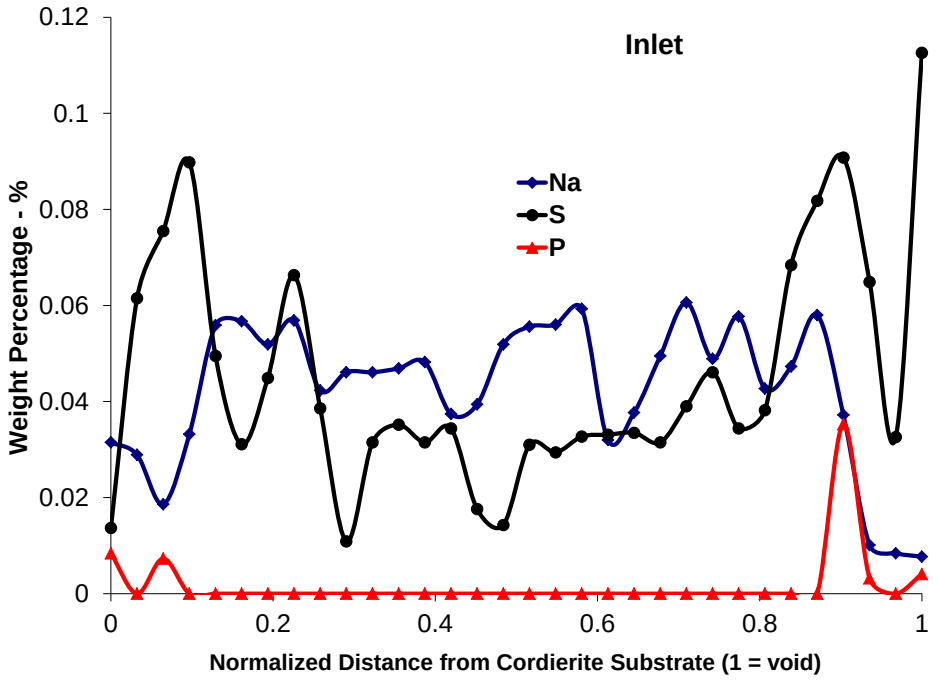

Figure 4.4.23 EPMA line scans of Na, S, and P contamination at inlet of control SCR.

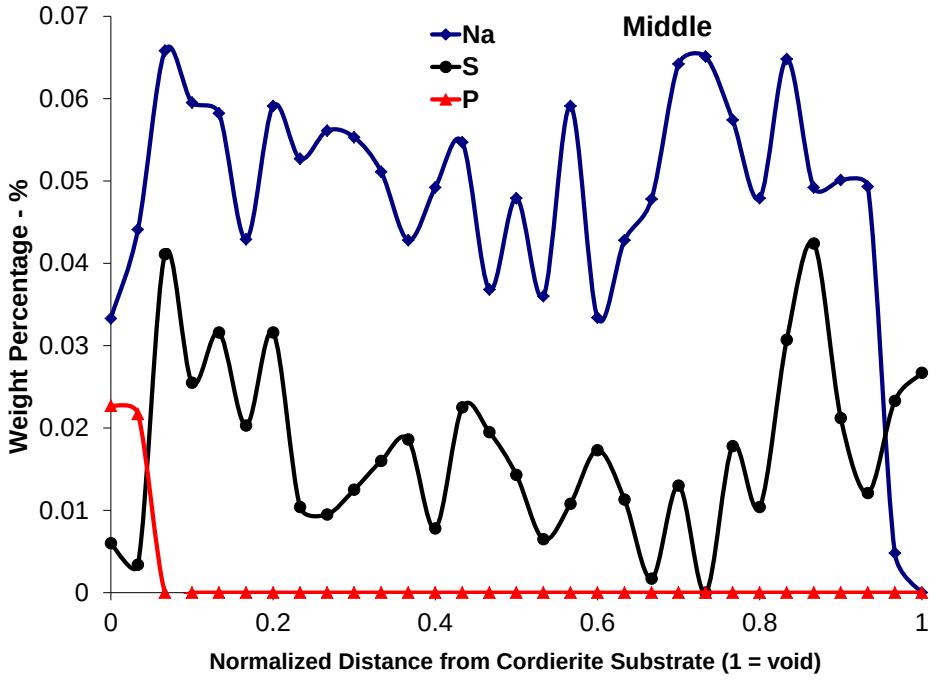

Figure 4.4.24 EPMA line scans of Na, S, and P contamination at middle of control SCR.

configuration accelerated Na-aged SCR and control SCR are similar to those observed in the light-duty configuration accelerated Na-aged SCR with the exception of S concentration at the washcoat surface, which reach values between 0.15 and 0.21% by weight.

The line scans confirm the trends observed in the EPMA micrographs for Na, S, and P. Na contamination is highest in the light-duty configuration accelerated Na-aged SCR, as illustrated by the comparison of Na concentration at the inlet of each SCR shown in Figure 4.4.25.

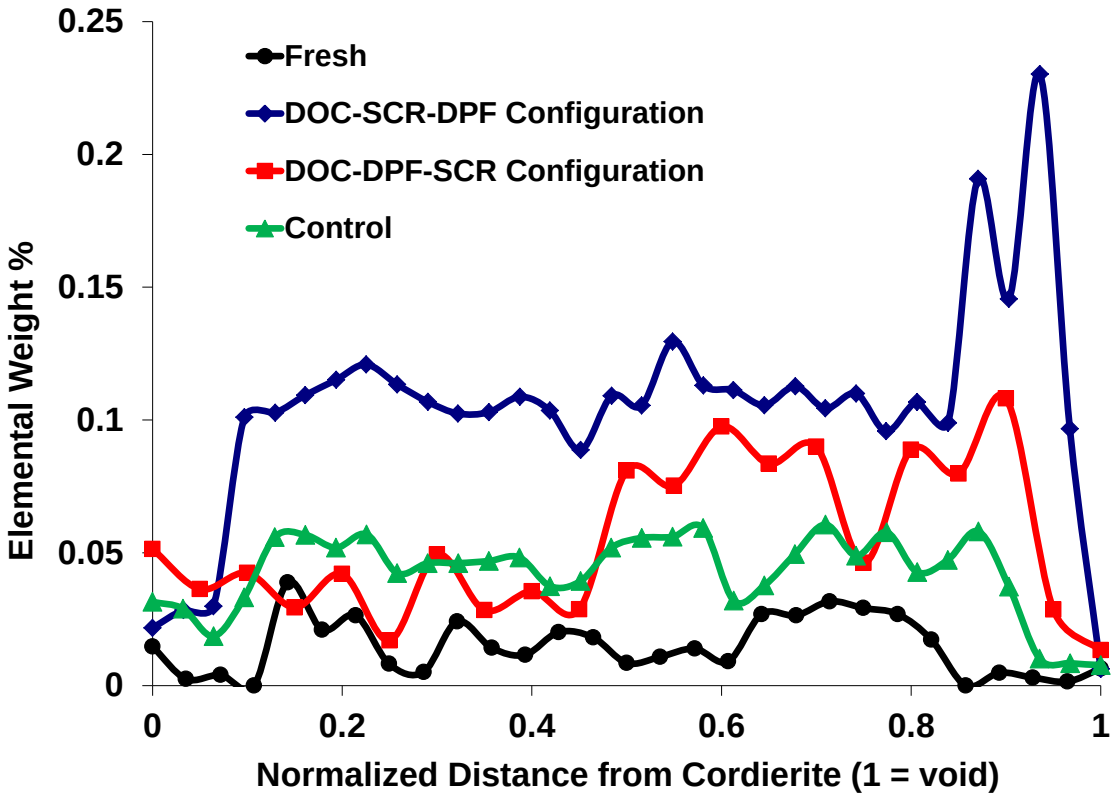

Figure 4.4.25 Na line scans at inlet of SCR samples.

The EPMA analysis of the SCR samples provides two key pieces of information. First, the arrangement of the aftertreatment system plays a significant role in the level of Na contamination present in the SCR. A DPF placed upstream of the SCR in the heavy-duty configuration shields the SCR from the majority of the Na contamination from the biodiesel fuel. Second, the distribution and concentration of Na contamination in the accelerated Na-aged SCR catalysts in the light-duty configuration are similar to that observed in the long-term engine-aged DOC catalyst. Therefore, it is believed that the accelerated Na-aging protocol provides a realistic basis for analysis regarding the impact of Na on SCR catalysts.

ICP analysis provides another method for measuring the concentration of Na in the accelerated Na-aged SCR catalysts. The content of Na in the SCR catalysts is shown in Table 4.1.

Table 4.1 ICP Measurements of Na in Fresh and Accelerated Na-aged SCR catalysts.

SCR Catalyst	Concentration of Na in ppm		
	Inlet	**Middle**	**Exit**
DOC-SCR-DPF w/ Na (Light-Duty)	929	886	1730
DOC-DPF-SCR w/ Na (Heavy-Duty)	617	427	437

The concentration of Na is significantly higher in the accelerated Na-aged SCR from the light-duty configuration relative to the heavy-duty configuration, and is

highest at the exit of the light-duty configuration accelerated Na-aged SCR. These results agree with those observed in EPMA line scans of the SCR catalysts.

BET surface area measurements were performed on fresh and accelerated Na-aged SCR samples in order to determine the impact of aging and Na contamination on the surface area of the beta Cu-zeolite SCR catalysts. The results of this analysis are shown in Figure 4.4.26. The inlet of each catalyst is relatively unchanged, but the middle and exit of the light-duty accelerated Na-aged SCR catalyst experience surface area reductions of 23 and 26 m^2/g relative to the fresh sample, respectively. When the SCR is placed downstream of the SCR in the heavy-duty configuration, no loss of surface area is observed as a result of the aging. The middle of the control SCR experiences a decline in surface area of 18 m^2/g relative to the fresh SCR, which is significant but not as drastic as that observed in the SCR from the light-duty accelerated Na-aging arrangement. While the control sample results show that high temperature exposure leads to surface area loss, this cannot be the sole contributing factor based on the fact that the maximum temperature experienced by all three SCR catalysts during aging is approximately 700ºC. Therefore, it is believed that

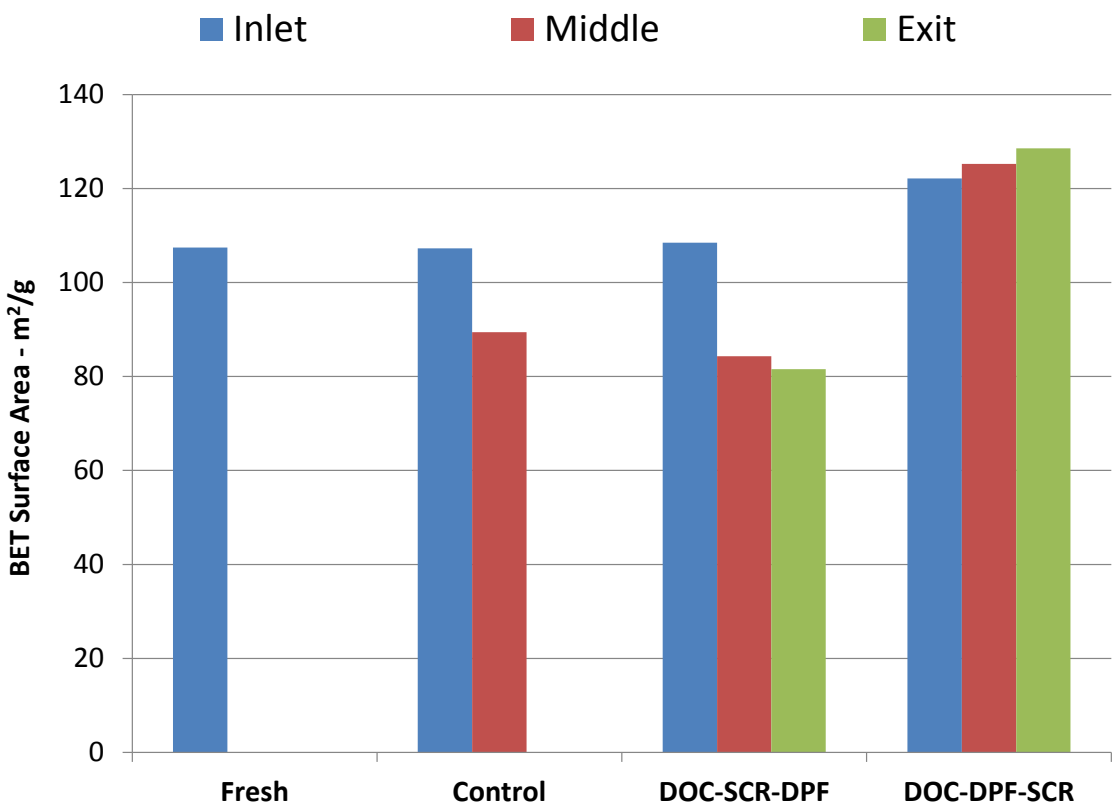

Figure 4.4.26 BET surface area measurements of fresh and accelerated Na-aged SCR catalysts.

significant presence of Na contamination observed in the light-duty configuration accelerated Na-aged SCR is the cause of the difference between that sample and the control SCR sample. This is in agreement with the results obtained by Cavataio et al. [16] that the decrease of surface area in Cu-zeolite SCR catalysts is proportional to the concentration of Na contamination in the washcoat.

The objective of DRIFTS analysis on the fresh and accelerated Na-aged SCR samples is to determine the amount of NO and NO_2 adsorbed onto the active Cu sites in the catalysts. The magnitude of the FTIR signal is strongest at lower temperatures, and therefore the discussion of DRIFTS results is focused

on experiments performed at 150ºC. Absorption spectra during NO or NO_2 exposure for the SCR catalysts are shown in Figures 4.4.27 and 4.4.28, respectively. The locations of peaks corresponding to the adsorption of NO_x onto Cu-zeolite SCR catalysts were identified in the literature [69, 93-96], and are identified in the figures. Under dry conditions for NO exposure in Figure 4.4.27 adsorption peaks for NO_2 on Cu^{2+} at a wavenumber of 1630 cm^{-1} are the most notable feature, along with small nitrate peaks around 2600 cm^{-1}. The peaks are highest in intensity for the fresh and accelerated Na-aged SCR in the heavy-duty configuration, and are noticeably smaller in the accelerated Na-aged SCR in the light-duty configuration. While these features are not distinguishable under wet conditions during NO exposure, the same trends in peak intensity for the three samples appear for both dry and wet conditions during NO_2 exposure to the SCR catalysts shown in Figure 4.4.28. In particular, NO_2 exposure under dry conditions exhibits the same peaks at 1630 cm^{-1} and 2600 cm^{-1}, along with two new nitrate peaks for NO_2 adsorption at 1157 and 930 cm^{-1}. Based on the proposed Langmuir-Hinshelwood mechanism involving the adsorption of NO_x onto active Cu sites as an active part of the SCR process [59-60], it seems likely that the decrease in peak intensity for adsorbed NO_x species observed in the light-duty accelerated Na-aged SCR sample could be attributed to a decrease in the total number of Cu sites available as a result of SCR contamination. This observation also agrees with the decreased activity of NH_3 oxidation over Cu in the light-duty accelerated Na-aged SCR catalyst. Therefore, based upon the

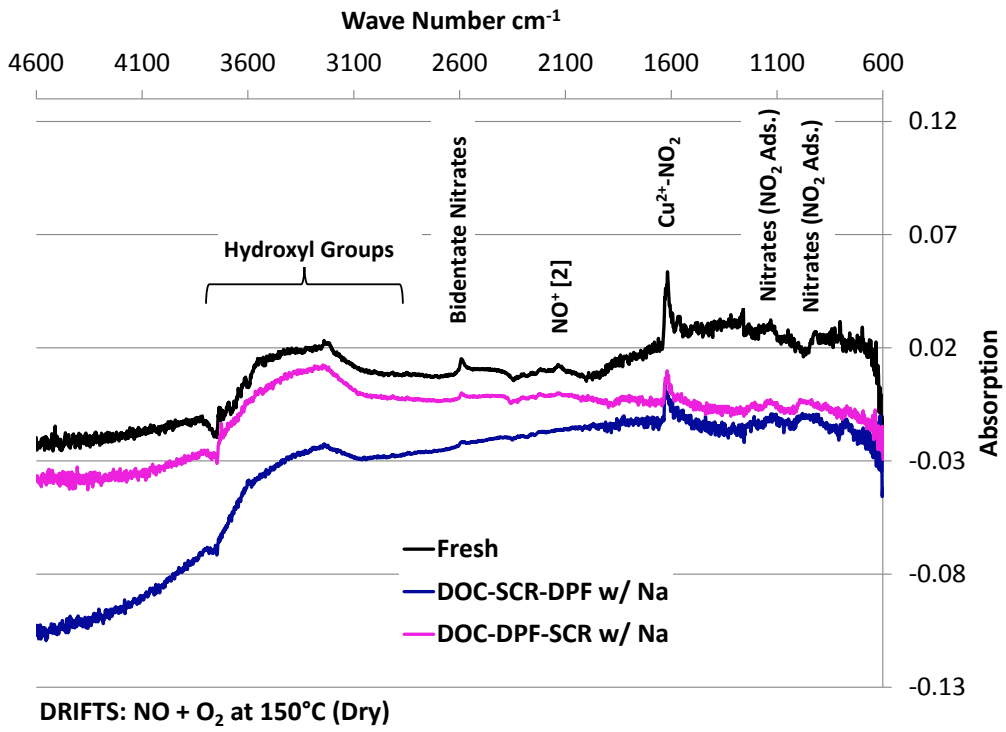

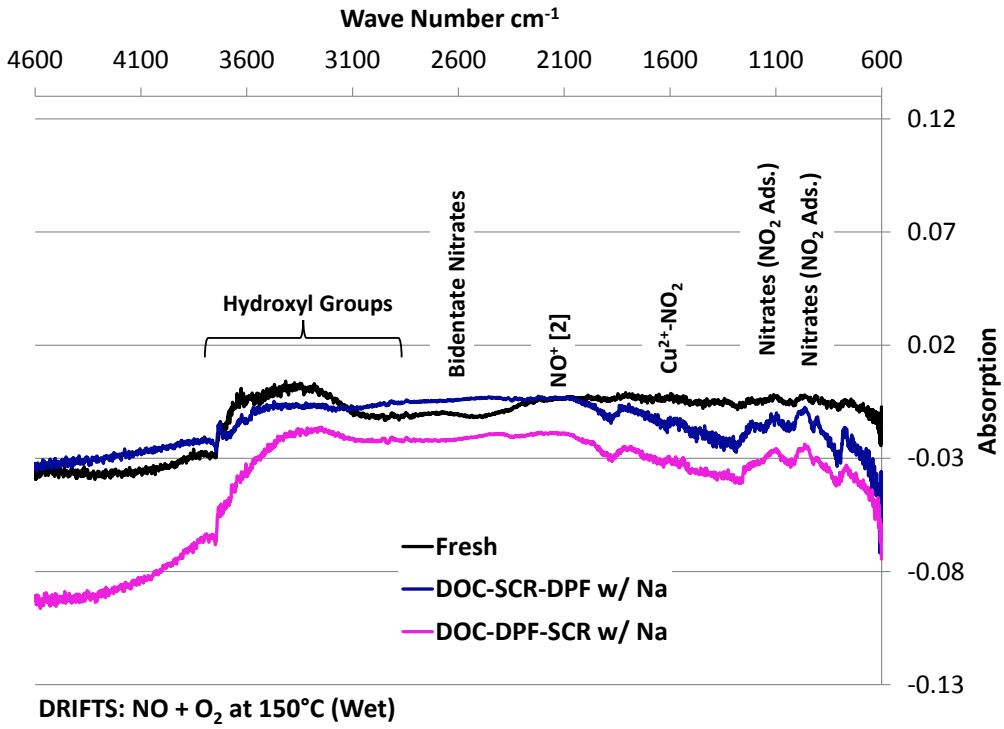

Figure 4.4.27 DRIFTS absorbance spectra for fresh and accelerated Na-aged SCRs during NO exposure for dry and wet conditions

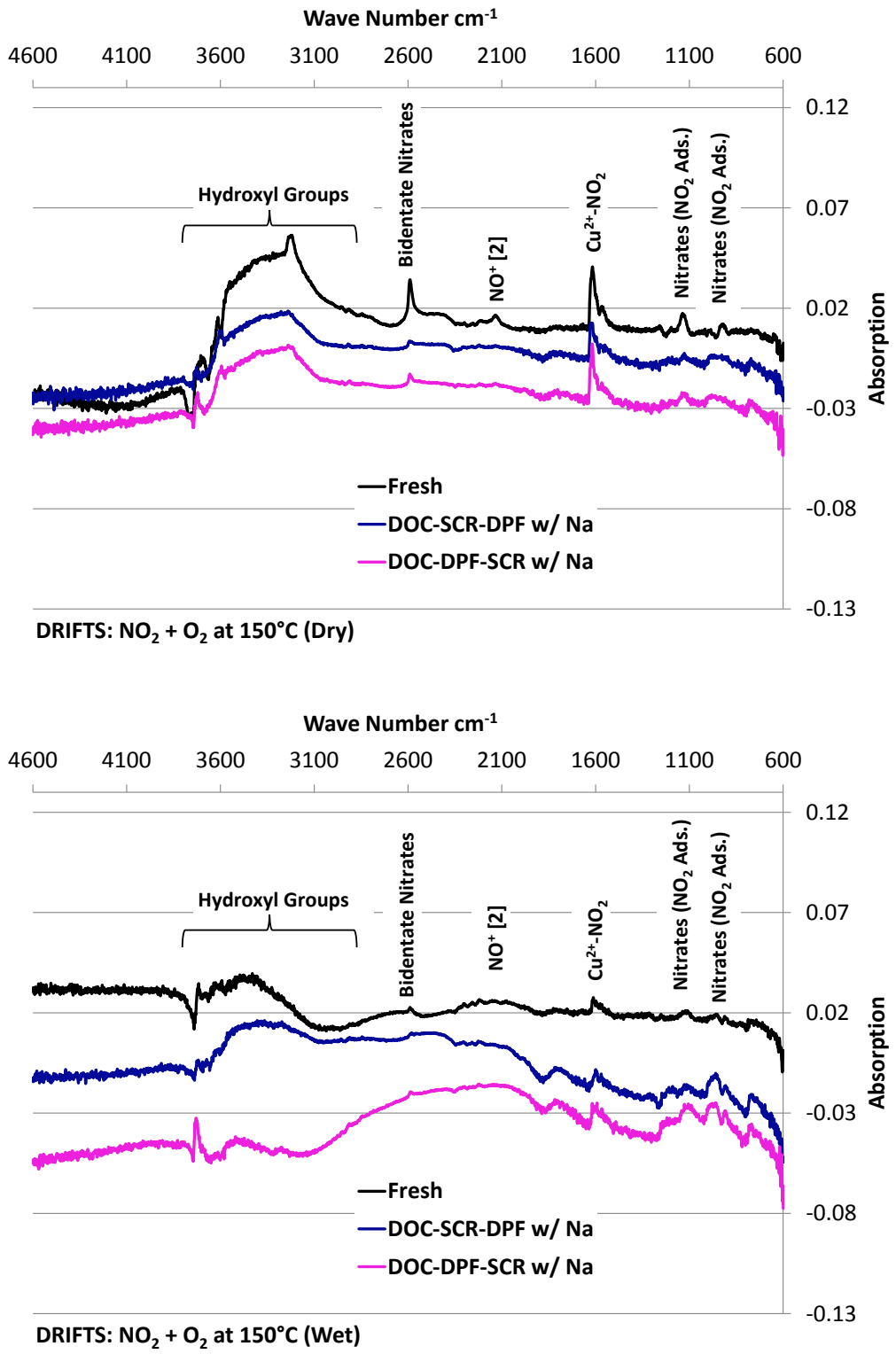

Figure 4.4.28 DRIFTS absorbance spectra for fresh and accelerated Na-aged SCRs during NO_2 exposure for dry and wet conditions

results of the DRIFTS study in conjunction with performance evaluations, it is believed that Na contamination is leading to a reduction in the number of available active Cu sites for SCR reactions.

SEM and EDS were initially performed on Cu-chabazite SCR catalysts aged by NREL with elevated levels of Na (14ppm in B20), and based on the results of that analysis the same technique was later applied to the light-duty configuration accelerated Na-aged SCR. The objective was to identify the location and concentration of Na and Cu in these catalysts. SEM and EDS were performed at channel corner locations similar to the one shown in the following EPMA images in Figure 4.4.29 for the NREL Na-aged Cu-chabazite SCR sample.

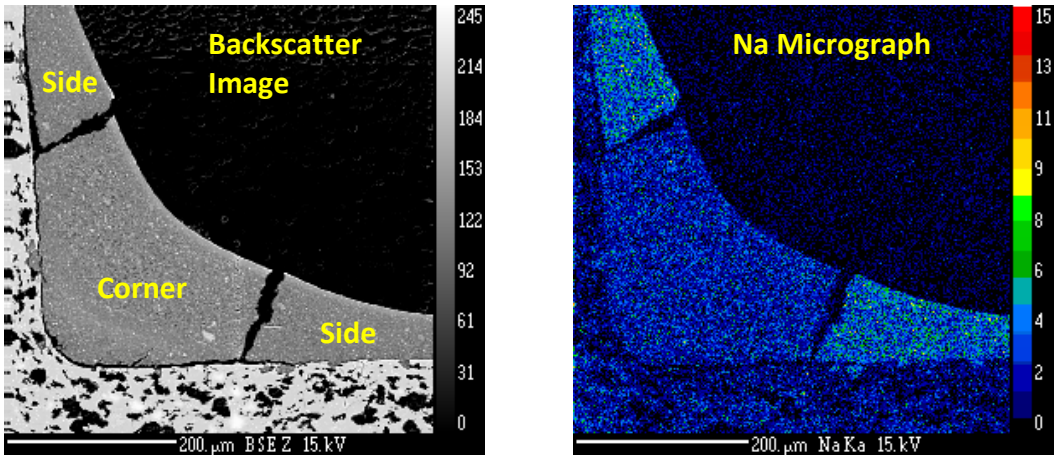

Figure 4.4.29 EPMA backscatter image and Na micrograph for NREL Na-aged Cu-chabazite SCR sample.

The ‘side’ and ‘corner’ designations are included to provide clarity on the locations discussed for the SEM and EDS results, and to illustrate that Na is

primarily located in the ‘side’ locations as seen in the Na micrograph. EDS measurements of the NREL Na-aged sample revealed that Na was present in the washcoat at concentrations of 0.17 and 0.32333% by weight in the ‘corner’ and ‘side’ locations, respectively. These concentrations are consistent with those measured by EPMA for the light-duty accelerated Na-aged SCR in the current study. Furthermore, the most interesting trend observed by EDS was the loss of Cu observed in the NREL Na-aged sample. This trend is illustrated by the comparison of Cu content in fresh, NREL ULSD-aged, and NREL Na-aged Cu-chabazite SCR catalysts shown in Figure 4.4.30.

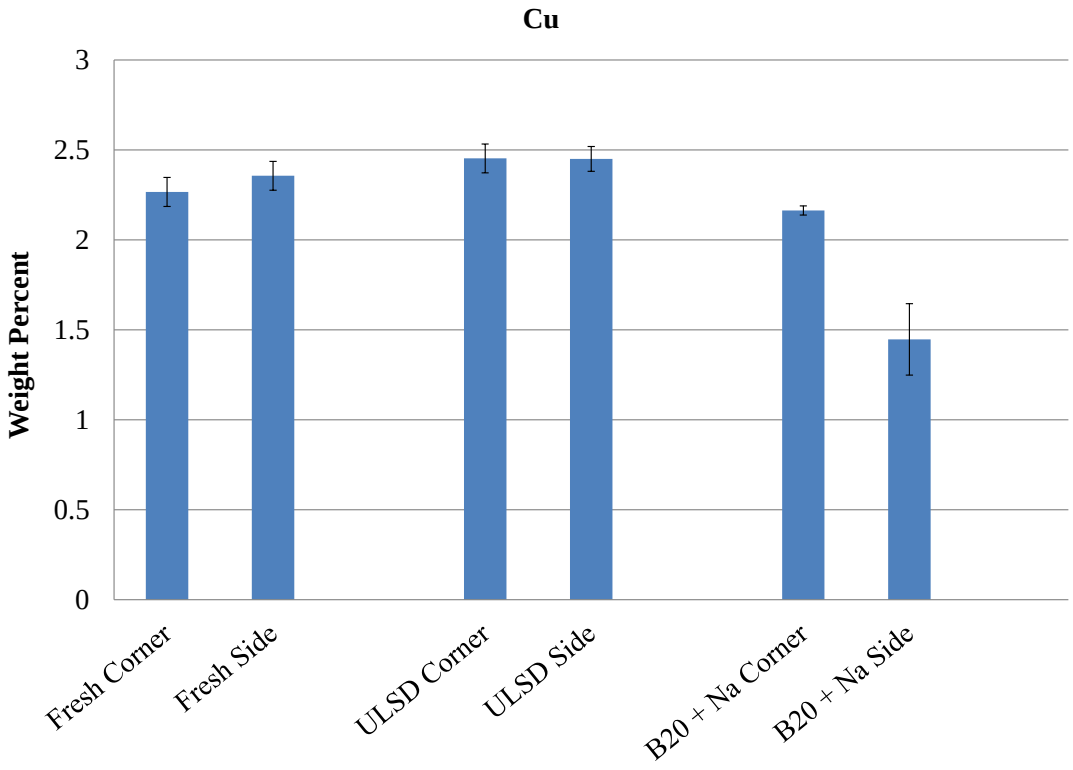

Figure 4.4.30 Cu content in fresh, NREL ULSD-aged, and NREL Na-aged Cu-chabazite SCR catalysts.

While the ‘corner’ location in the NREL Na-aged SCR exhibits a small loss of Cu content relative to the fresh and NREL ULSD-aged samples, the biggest drop in Cu content is seen at the ‘side’ location, where the concentration of Cu drops by as much as 1.0% by weight. This significant loss of Cu along with the high concentration of Na seen at the ‘side’ location in the NREL Na-aged sample suggests that Na is migrating into the washcoat and exchanging into the Cu-chabazite, thus forcing out the Cu. This phenomenon is further confirmed by the observation of CuO particles on the surface of the chabazite washcoat observed in the SEM image of the NREL Na-aged Cu-chabazite sample shown in Figure 4.4.31 and confirmed with EDS measurements. These Cu particles do not appear on the surface of the NREL ULSD-aged sample.

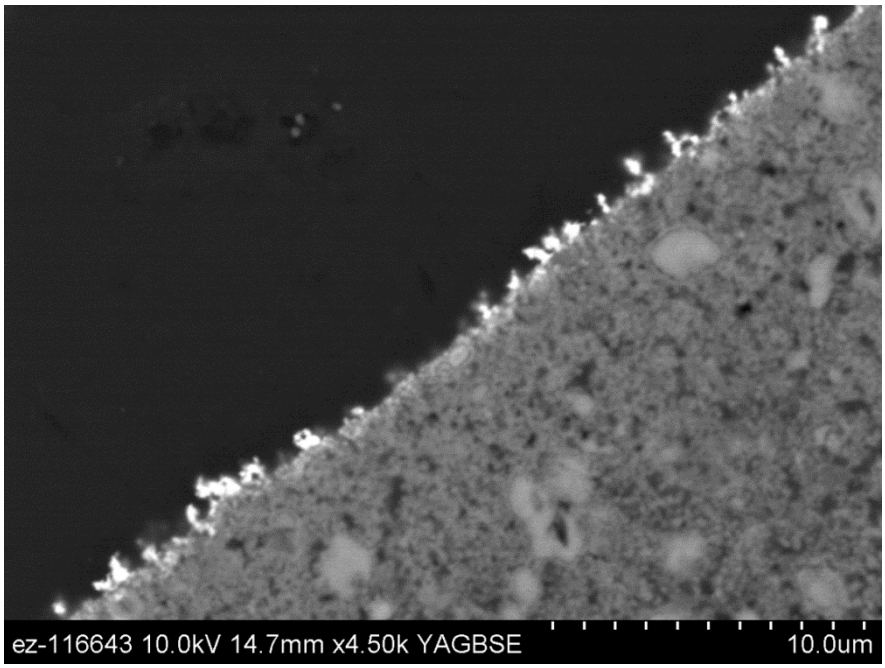

Figure 4.4.31 CuO particles on the surface of the washcoat in the NREL Na-aged Cu-chabazite SCR catalyst.

Due to the similar structure of Cu-beta and Cu-chabazite SCR catalysts, it seemed likely that the same migration of Cu out of the washcoat would occur in the accelerated Na-aged SCR samples from the current study, and therefore SEM-EDS was applied to those samples as well. An SEM image of the washcoat surface from the light-duty accelerated Na-aged SCR is shown in Figure 4.4.32, and EDS analysis of the washcoat surface where the particles are visible is shown in Figure 4.4.33. As can be seen in the figures, migration of Cu out of the washcoat in the presence of Na is occurring in the light-duty accelerated Na-aged SCR catalyst in a similar fashion to that observed in the NREL Na-aged Cu-chabazite SCR catalyst. These results confirm the loss of Cu, and consequently active Cu sites, in the light-duty accelerated Na-aged SCR catalyst and illustrate that this phenomenon occurs for multiple forms of Cu-zeolite SCR catalysts. Based on these results it is believed that loss of active Cu sites due to migration out of the zeolite washcoat is the cause of the drastic decreases observed for NO_x performance, NH_3 oxidation, and NH_3 storage in the light-duty accelerated Na-aged SCR catalyst.

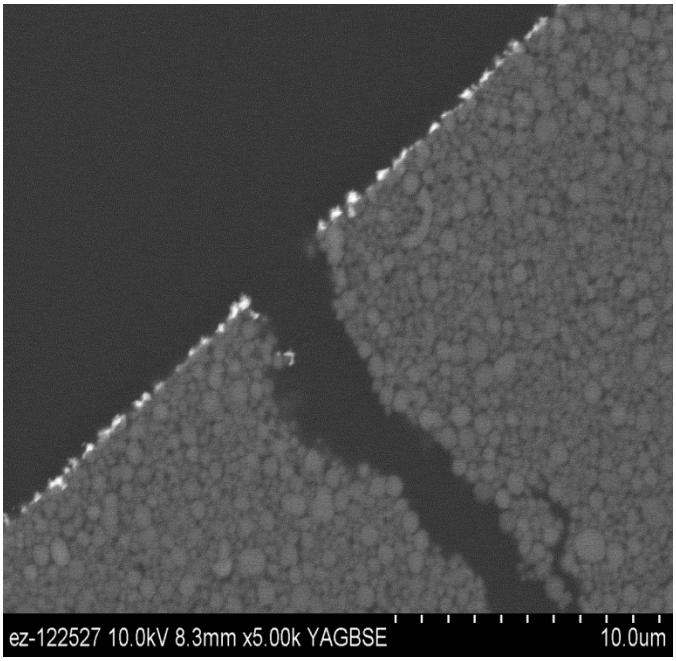

Figure 4.4.32 CuO particles on the surface of the washcoat in the light-duty configuration accelerated Na-aged SCR catalyst.

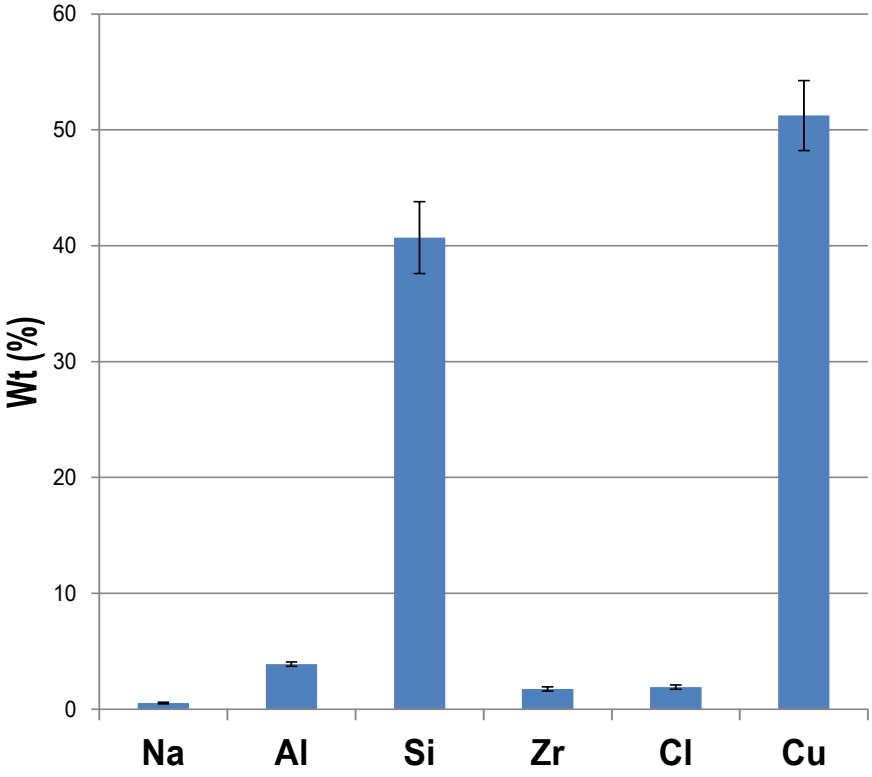

Figure 4.4.33 EDS measurement of washcoat surface in light-duty accelerated Na-aged SCR where CuO particles are present.

4.4.4 Mathematical Modeling of Cu-zeolite SCR

The Fortran model provided by Gao et al. [85] was utilized for the purpose of modeling the performance of the fresh and light-duty accelerated Na-aged SCR catalysts. Before attempting to simulate poisoning conditions it was first necessary to adjust the default kinetic parameters from the literature to ensure that the predicted performance of fresh Cu-zeolite SCR catalysts is similar to that observed. Simulations using the original kinetic rate parameters in the program exhibited excessively high oxidation of both NH_3 and NO to NO_2. Oxidation curves for NH_3 and NO are shown in Figures 4.4.34 and 4.4.35, respectively, along with the results predicted after the rate parameters were changed to better fit the experimental data.

The oxidation of NH_3 is significantly over-predicted with the original kinetics of the model at temperatures above 250ºC with oxidation values of 100% above 400ºC. Meanwhile, NO to NO_2 oxidation is as much as 20% higher than the experimental results in the 300 to 500ºC temperature range. Accurate results for the experimentally observed NH_3 oxidation in the SCR were achieved by reducing the pre-exponential coefficient and activation energy in the Arrhenius rate equation from $1.2x10^{11}$ and $162.4x10^{3}$ to $6.0x10^{12}$ and $200.0x10^{3}$, respectively. Using these values in the rate equation, the model is able to predict NH_3 oxidation to within 10% across the entire temperature range from 150 to 600ºC. The same approach was used to address the NO to NO_2 oxidation rate

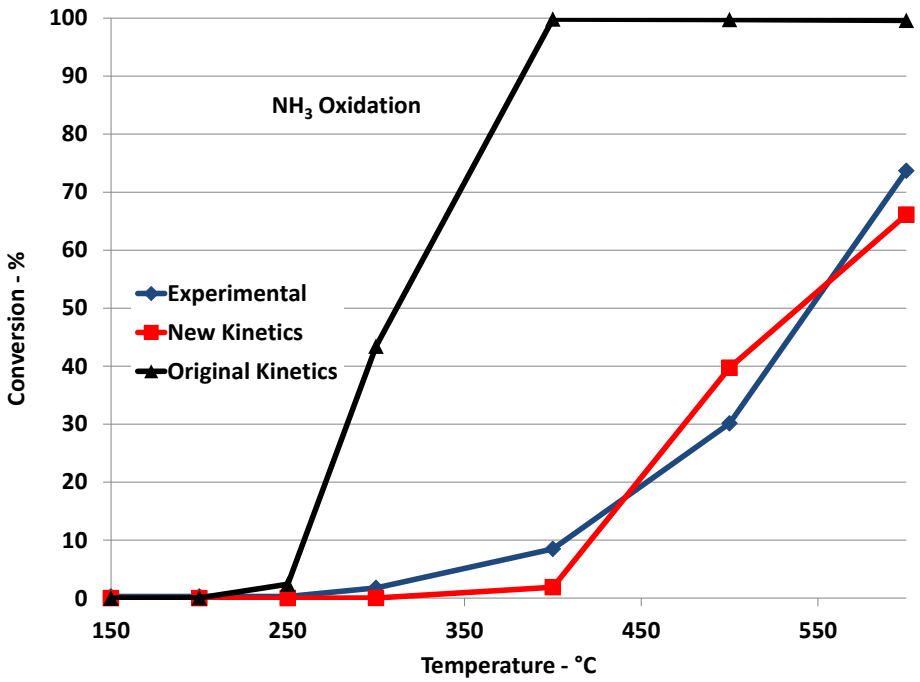

Figure 4.4.34 Fortran model simulations of NH_3 oxidation in fresh Cu-zeolite SCR.

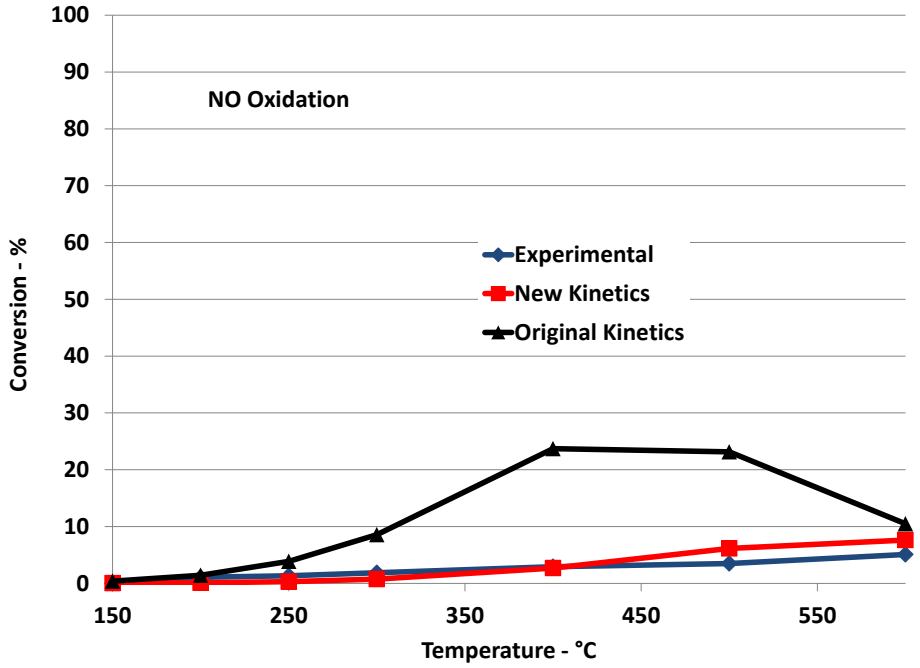

Figure 4.4.35 Fortran model simulations of NO to NO_2 oxidation in fresh Cu-zeolite SCR.

equation, where the pre-exponential coefficient and activation energy were changed from 20.0×10^3 and 48.0×10^3 to 2.5×10^3 and 50.0×10^3, respectively. Using these values the model is able to predict NO to NO_2 oxidation to within 2% of the experimental values.

After adjusting kinetic parameters for NH_3 and NO to NO_2 oxidation in the Fortran code it was possible to simulate SCR performance for Cu-zeolite using the model. The standard and fast SCR performance curves generated by the model are shown in Figures 4.4.36 and 4.4.37, respectively, along with the performance curves created by the model before any rate parameters were changed. With the original rate parameters for oxidation in place the model under-predicts SCR performance at temperatures above 400ºC due to a lack in the availability of NH_3 and/or NO caused by the excessively high oxidation. However, after the new rate values for oxidation are introduced the experimentally observed trends in both standard and fast SCR are correctly predicted by the model. The model still over-predicts NO_x conversion at temperatures above 250ºC, but the error is reduced to a maximum of less than 20% across the entire temperature range which is a drastic improvement over the 35-50% error present before the rate parameters for NH_3 and NO to NO_2 oxidation were changed.

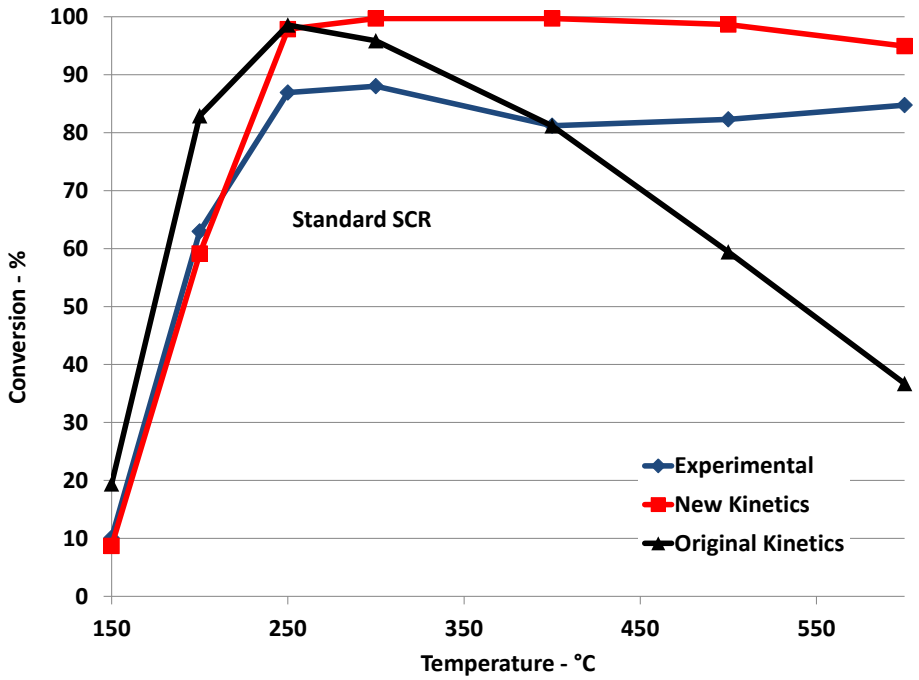

Figure 4.4.36 Fortran model simulations standard SCR performance in fresh Cu-zeolite SCR.

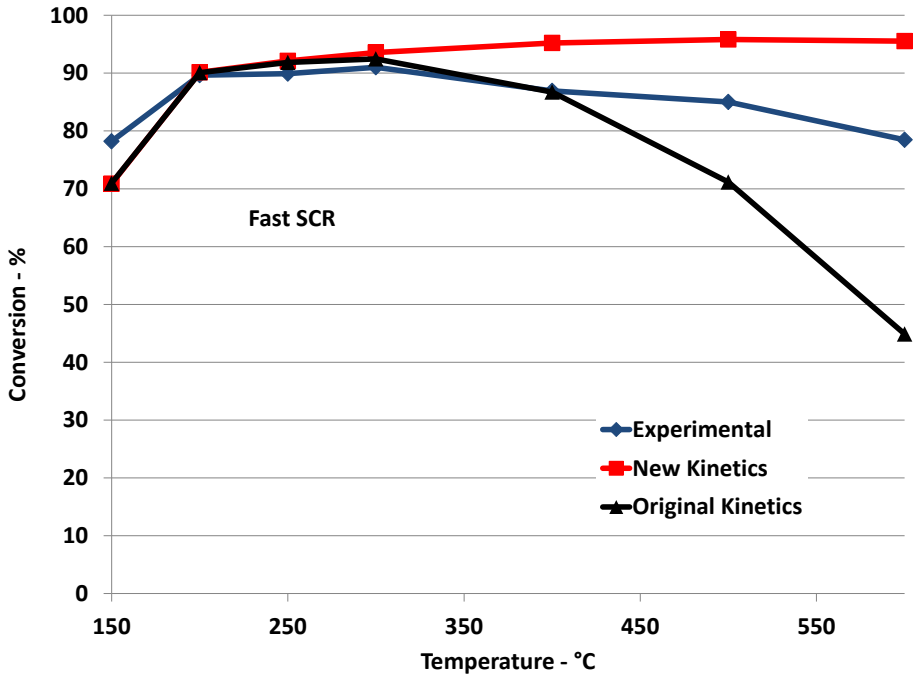

Figure 4.4.37 Fortran model simulations of fast SCR performance in fresh Cu-zeolite SCR.

After adapting the model to fit the experimentally observed fresh Cu-zeolite SCR performance, it was desirable to determine if it could also predict the performance of the light-duty configuration accelerated Na-aged SCR. To reflect the decreased surface area in the light-duty accelerated Na-aged SCR, the surface area of the catalyst in the model was reduced by 15%. The coefficient to the Arrhenius rate equation for NH_3 adsorption was also decreased by 50% to reflect decreased NH_3 storage in the Na-aged sample. The resulting model simulations for NH_3 and NO oxidation are shown in Figures 4.4.38 and 4.4.39, respectively, along with the fresh SCR data. Reducing the surface area and NH_3 adsorption in the Fortran code causes the NH_3 oxidation predicted by the model to decrease as well, resulting in NH_3 oxidation values which are within 10% of the experimentally observed values for the Na-aged SCR catalyst. However, the NO oxidation values are essentially unchanged relative to the fresh SCR model conditions. This is likely due to the fact that the NO oxidation rate parameters were reduced to values which make NO oxidation in the model kinetically limited rather than limited by surface area for reaction.

Modeling of standard and fast SCR performance in the light-duty configuration accelerated Na-aged SCR was also performed. Rate parameters for the fast SCR reaction were unchanged, but in order to reflect the drastic standard SCR NO_x performance in the Na-aged sample the original values in the Arrhenius rate equation of the standard SCR Fortran code were altered. The coefficient and activation energies were changed from 2.3×10^8 and 88.0×10^3

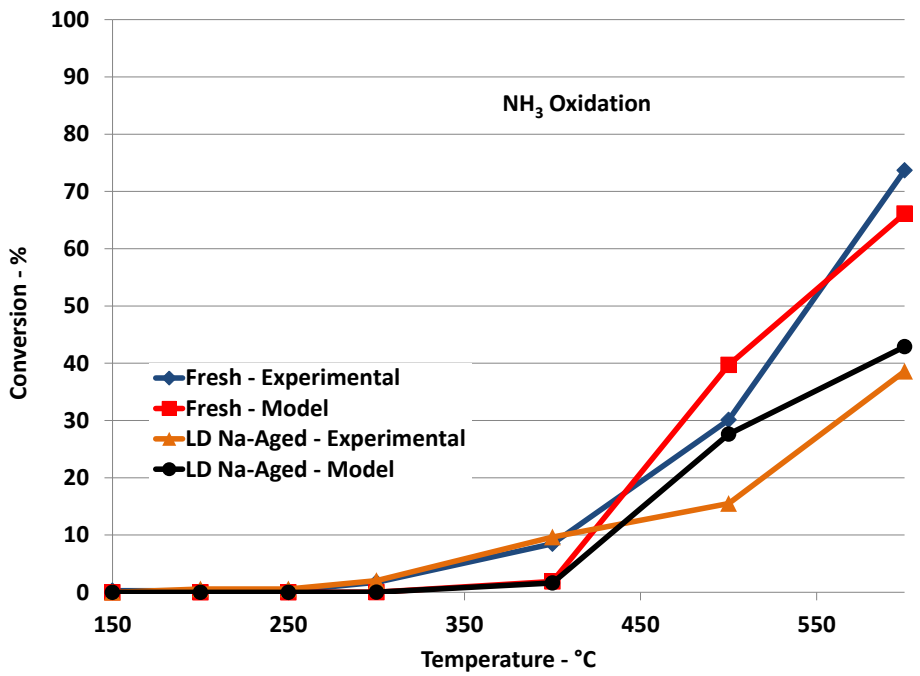

Figure 4.4.38 Fortran model simulations of NH_3 oxidation in fresh and light-duty configuration accelerated Na-aged Cu-zeolite SCR catalysts.

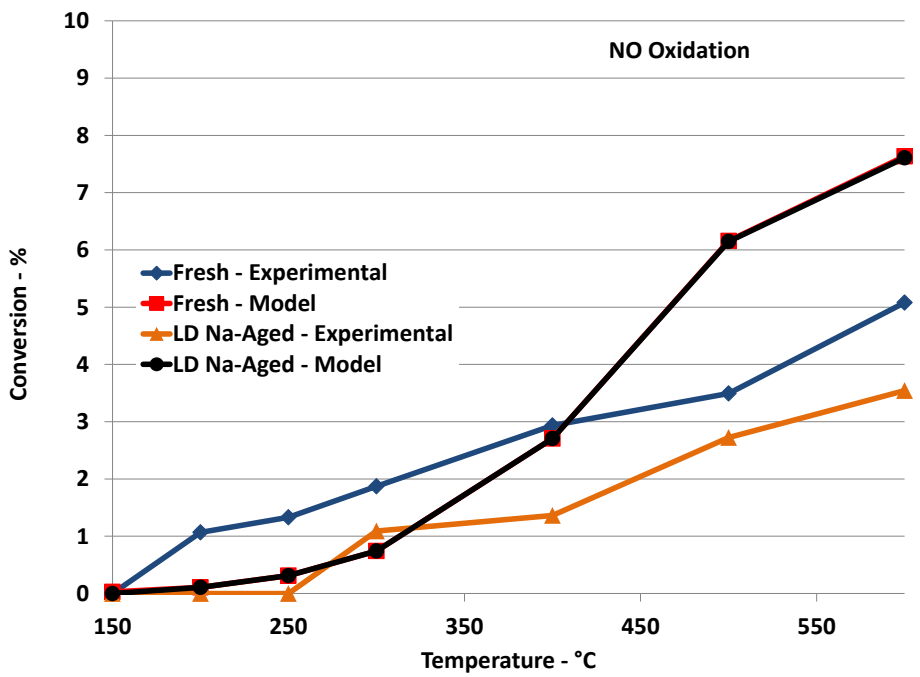

Figure 4.4.39 Fortran model simulations of NO oxidation in fresh and light-duty configuration accelerated Na-aged Cu-zeolite SCR catalysts.

to $1.0x10^4$ and $60.0x10^3$, respectively. The resulting NO_x performance curves produced by the model for standard and fast SCR in the Na-aged SCR sample are shown in Figures 4.4.40 and 4.4.41. In the case of the fast SCR performance, reduced surface area and NH_3 adsorption result in a performance curve that reflects the decreased performance and predicts the experimental results for the light-duty configuration accelerated Na-aged to within 15%. The fast SCR model is best at temperatures below 400ºC due to the fact that NH_3 oxidation in the model is more in line with the experimental results at lower temperatures. On the other hand, the mathematical model fails to provide an accurate representation of standard SCR performance in the Na-aged SCR. At temperature below 250ºC and at 500ºC the model is accurate, but at 300, 400, and 600ºC the error is as high as 30%. There are multiple factors contributing to this error. The most obvious problem is again the differences in NH_3 oxidation between experimental results and the model. However, it is also likely that the model fails to predict standard SCR behavior due to the fact that the deactivation mechanism in the light-duty configuration accelerated Na-aged SCR is extremely complex, as observed in the BFR evaluations and materials characterization. While the model can be altered to reflect decreased surface area and NH_3 adsorption, there is no way to directly account for factors such as loss of active Cu sites in the Na-aged SCR. Therefore, while the model is excellent at predicting fresh SCR performance, there are clear limitations when attempting to model the Na-aged SCR.

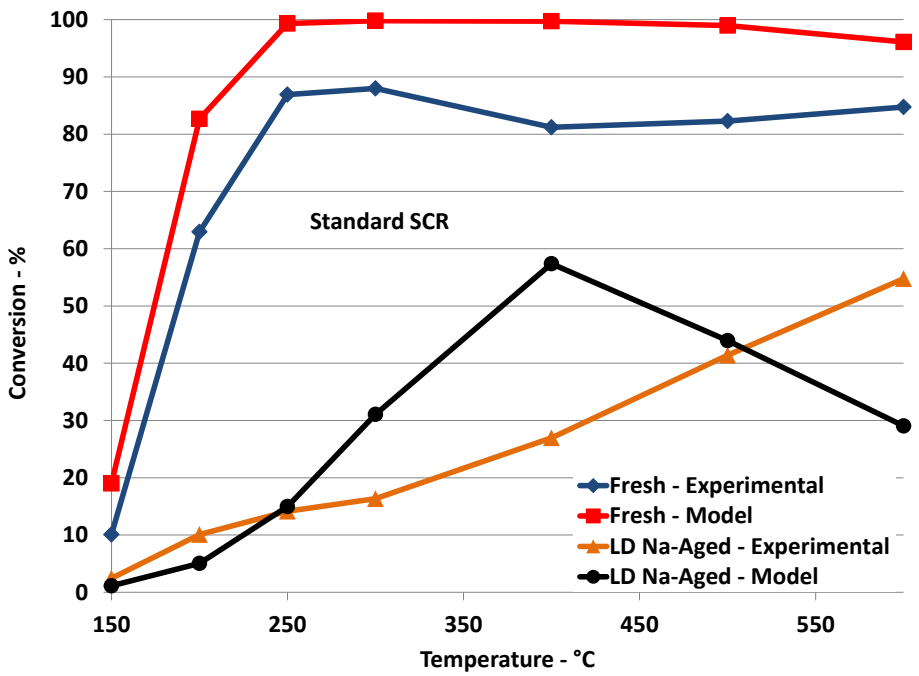

Figure 4.4.40 Fortran model simulations of standard SCR in fresh and light-duty configuration accelerated Na-aged Cu-zeolite SCR catalysts.

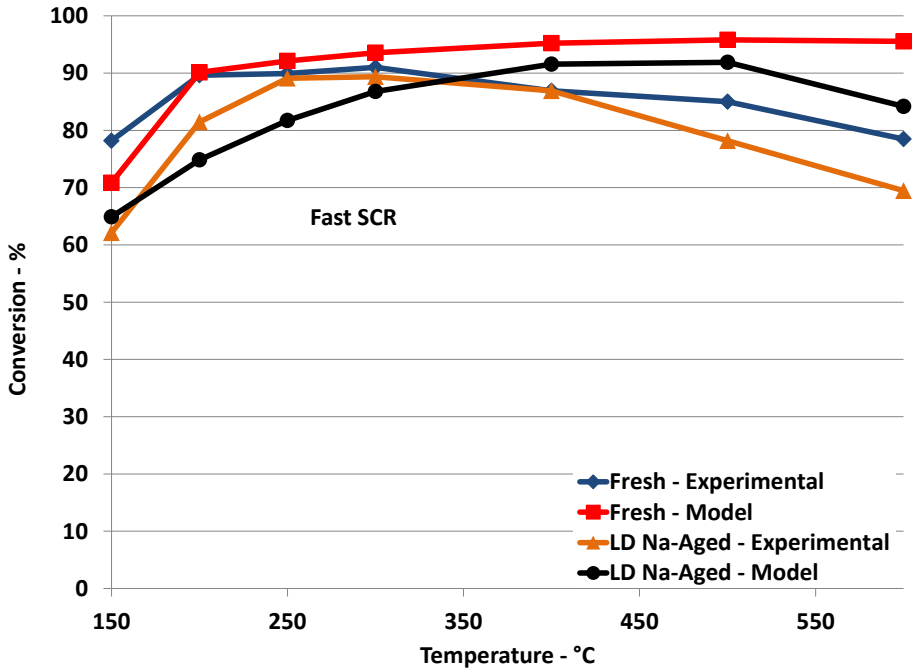

Figure 4.4.41 Fortran model simulations of fast SCR in fresh and light-duty configuration accelerated Na-aged Cu-zeolite SCR catalysts.

CHAPTER V

CONCLUSIONS AND RECOMMENDATIONS

An investigation was carried out to determine the impact of biodiesel-based Na on the performance and materials characterization of diesel aftertreatment devices, with an emphasis on Cu-zeolite SCR catalysts. An accelerated Na-aging protocol was implemented on a single-cylinder Hatz diesel engine with an aftertreatment system consisting of a DOC, SCR, and DPF to simulate 435,000 miles of equivalent Na exposure through the use of a fuel additive, while long-term engine-aged LNT, DOC, and DPF samples were provided by outside partners for comparison purposes. Performance evaluations were carried out using a bench-flow reactor (BFR) to simulate diesel exhaust conditions, and numerous materials characterization techniques were utilized including electron microprobe analysis (EPMA), scanning electron microscopy with energy dispersive spectroscopy (SEM-EDS), transmission electron microscopy (TEM), diffusive-reflective infrared Fourier transform spectroscopy (DRIFTS), and BET surface area analysis.

BFR evaluations of engine-aged LNT samples found that NO_x performance is reduced by as much as 30% across the evaluation temperature range from 200 to 400ºC. However, performance at temperatures above 300ºC can be recovered through soot oxidation and desulfation treatments to remove contaminants. While EPMA analysis identified a layer of Na on the washcoat

surface of the engine-aged LNT, it is not expected that this would inhibit NO_x performance since Na is capable of acting as a NO_x storage material like Ba. Rather, the poor performance at temperatures below 300ºC after aging is attributed to the sintering of platinum group metal (PGM) particles. TEM analysis revealed that the average particle size in the engine-aged LNT increased by 3 nm, or 33%) relative to the fresh LNT sample. Therefore, based on the results of the current study it does not appear the Na contamination from biodiesel fuel plays a significant role in the deactivation of LNT catalysts.

Performance evaluations of the DPF were not possible, so all analysis of engine-aged and accelerated Na-aged DPFs was done with EPMA to study the distribution and concentration of contaminants in the filters. In the engine-aged DPF provided by GM it was discovered that while Na is present, P and Ca are the primary contributors to the ash plugs in the filter due to increased lubricant exposure during long-term aging. Analysis of accelerated Na-aged DPFs from the light-duty (DOC-SCR-DPF) and heavy-duty (DOC-DPF-SCR) aftertreatment system configurations revealed that the arrangement of the aftertreatment system plays a significant role in the amount of Na present in the DPF. The DPF from the light-duty configuration contains levels of Na up to 3.0 wt%, but the average level is much lower and the Na is located on top of the substrate walls. However, when the DPF is placed upstream of the SCR in the heavy-duty configuration the concentration of Na increases to as high as 5.2 wt%, and the Na migrates into the cordierite substrate of the filter. Based on these results, it is

evident that in the heavy-duty configuration the DPF traps a large amount of the Na present in the exhaust.

Evaluations of the DOC on the BFR determined that both long-term engine-aging and accelerated Na-aging have a negligible impact on both HC and CO oxidation. HC conversion based on the oxidation of ethylene decreases by less than 10% across the entire temperature range, while CO oxidation is only affected at values below 150ºC. NO to NO_2 oxidation is actually shown to increase with aging, but this can be attributed to the increased size of PGM particles due to sintering which can improve NO oxidation activity. EPMA analysis on the long-term engine-aged and accelerated Na-aged DOC samples found that the Na contamination pattern in both DOCs is similar, with the bulk of the contamination appearing as a layer on the catalyst washcoat and lesser concentrations in the bulk. This result is key to the current research as it provides evidence that the accelerated Na-aging approach provides an accurate representation of long-term engine aging.

Detailed performance evaluations of the fresh and accelerated Na-aged SCR catalysts using the CLEERS transient SCR evaluation protocol provided a wealth of information regarding the effects of Na contamination on Cu-zeolite SCR performance. The SCR from the light-duty configuration accelerated Na-aging arrangement suffers drastic NO_x performance reductions as high as 70% under standard SCR conditions. The control sample, which was aged in the light-duty configuration with no Na-additive in the B20 fuel, also experiences performance losses, but not to the same extent as the Na-aged SCR. This

implies that in the light-duty accelerated Na-aging configuration both thermal deactivation and Na contamination play a role in lost NO_x conversion. When the DPF is placed upstream of the SCR in the heavy-duty configuration, the SCR performs comparable to a fresh SCR sample. This implies that the heavy-duty configuration shields the SCR from both thermal aging effects and Na contamination. Under fast SCR conditions, the aged and fresh SCR samples all perform comparably, although the light-duty configuration accelerated Na-aged SCR performs slightly worse than the other samples.

NH_3 and NO to NO_2 oxidation were also investigated for the SCR samples. NO to NO_2 oxidation is low across both aged and fresh SCR samples, making it hard to identify this as a potential source of lost NO_x conversion. However, NH_3 oxidation is significantly impacted as a result of Na-exposure and aging. While NH_3 oxidation is an undesirable side reaction, it provides insight into a possible failure mechanism for the light-duty Na-aged SCR sample, which is the loss of the active Cu sites for NH_3 storage and SCR reactions. This idea is further supported by the observation that NH_3 storage is also decreased in the light-duty configuration accelerated Na-aged SCR during BFR evaluations.

EPMA analysis of fresh and engine-aged SCR sample determined that the concentration of Na contamination is highest in the light-duty configuration accelerated Na-aged SCR sample, with concentrations as high as 0.5 wt%. This concentration is over twice as much as the maximums observed in the fresh, control, and heavy-duty configuration accelerated Na-aged SCR samples. Additionally, the distribution of Na in the light-duty accelerated Na-aged SCR is

similar to that observed in the aged DOCs, providing confidence that the accelerated aging protocol is effective in mimicking long-term aging conditions.

Surface area measurements were taken using the BET surface area measurement technique. The fresh and heavy-duty configuration accelerated Na-aged SCR samples exhibit the high surface areas, with values of 110 to 125 m^2/g. In the control and light-duty configuration accelerated Na-aged SCRs the inlet of the catalyst is unaffected, but the middle and rear experience significant surface area reductions as high as 30 m^2/g. While thermal aging clearly plays a role in the loss of surface area seen in the control SCR, there is a 10 m^2/g difference present between it and the light-duty configuration accelerated Na-aged SCR attributed to the presence Na contamination.

DRIFTS evaluations were used to study NO_x and nitrate absorption on fresh and accelerated Na-aged SCR samples. Peaks corresponding to absorption of nitrates and NO_2 on Cu sites are much more pronounced for the fresh and heavy-duty configuration accelerated Na-aged SCR relative to the light-duty configuration accelerated Na-aged SCR. This observation supports the theory that a loss of active Cu sites due to Na contamination is affecting the NO_x performance of the light-duty configuration accelerated Na-aged SCR.

SEM-EDS analysis of NREL Na-aged Cu-chabazite SCR catalysts and light-duty configuration accelerated Na-aged SCR catalysts identified migration of Na into the washcoats of both samples. This was accompanied by an observation of CuO on the surface of the washcoats. It is apparent that the Na is displacing the Cu ions in the zeolite framework and driving them out of the zeolite

washcoats, thus resulting in the loss of active Cu sites for NH_3 adsorption and SCR reactions. It is believed that this phenomenon is the primary mechanism related to Na contamination in the SCR catalysts responsible for the significant loss of performance observed in the light-duty accelerated Na-aged SCR catalyst.

Modeling of the performance of the fresh and light-duty accelerated Na-aged beta Cu-zeolite SCR catalysts was done using a Fortran program developed by Gao et al. [85] at the Oak Ridge National Laboratory. Initial values for oxidation of NH_3 and NO were too high, and therefore it was necessary to adjust kinetic rate parameters to achieve accurate results. With these adjustments in place, the model is able to predict standard SCR, fast SCR, NO oxidation, and NH_3 oxidation to within 10% of the experimentally observed results on the BFR. The model is also able to reproduce NO oxidation, NH_3 oxidation, and fast SCR performance of the Na-aged SCR to within 15% of the values obtained during BFR evaluation by reducing surface area and NH_3 adsorption in the Fortran code. However, the model fails to accurately represent standard SCR performance in the Na-aged catalyst due to the inability to completely account for the complex deactivation mechanisms caused by Na contamination. A recommendation for future work would be the extraction of kinetic parameters, in particular the pre-exponential coefficients and activation energies for the reactions in the model, from the experimental data obtained during the current study.

Overall, it was determined in the current study that exposure to Na in the levels expected for typical B20 fuel over the useful lifetime of a vehicle will not impact LNT or DOC catalysts, but will have a significant impact on both DPFs and SCR catalysts. DPFs used in the heavy duty aftertreatment configuration will experience excessive ash formation and possible migration of the Na into the substrate. Meanwhile, Cu-zeolite SCR catalysts suffer drastic performance reductions in NO_x conversion and NH_3 storage, along with losses in surface area and a decrease in the number of Cu sites active for NH_3 storage and SCR reactions. Based on these results, it appears that even at the ASTM limit of 5 ppm Na+K there should be concern about the ability of diesel aftertreatment systems to perform at the required standard for the full useful life of a vehicle.

LIST OF REFERENCES

1. **Foster, Adam L.** *Accelerated Thermal Aging of Iron-Zeolite SCR Catalysts on an Engine Bench*. Thesis. Knoxville, TN : University of Tennessee, 2008.
2. www1.eere.energy.gov. *Office of Energy Efficiency and Renewable Energy.* [Online] U.S. Department of Energy, August 2003. http://www1.eere.energy.gov/vehiclesandfuels/pdfs/basics/jtb_diesel_engine.pdf.
3. U.S. Greenhouse Gas Inventory Report. *EPA.gov.* [Online] Environmental Protection Agency, April 2012. http://www.epa.gov/climatechange/ghgemissions/usinventoryreport.html.
4. Sources of Greenhouse Gas Emissions. *EPA.gov.* [Online] Environmental Protection Agency, 2012. http://www.epa.gov/climatechange/ghgemissions/sources.html.
5. Standard Specification for Biodiesel Fuel. *ASTM.org.* [Online] 2012. [Cited: August 4, 2012.] http://www.astm.org/Standards/D6751.htm.
6. Milestones in Mobile Source Emissions. *EPA.gov.* [Online] Environmental Protection Agency, January 2012. http://www.epa.gov/oms/invntory/overview/solutions/milestones.htm.
7. Emissions Standards: Heavy-Duty Truck and Bus Engines. *diesel.net.* [Online] 2007. http://www.dieselnet.com/standards/us/hd.php.
8. Emissions Standards: Cars and Light-Duty Trucks - Tier 2. *diesel.net.* [Online] 2006. http://www.dieselnet.com/standards/us/ld_t2.php.
9. **J. F. Griffiths and J.A. Barnard.** *Flame and Combustion, 3rd Edition.* s.l. : CRC Press, 1995.
10. Auckland Regional Council- Air Quality. [Online] Auckland Council, 2010. http://www.arc.govt.nz/environment/air-quality/air-pollutants/hydrocarbons.cfm.
11. EPA - Six Common Air Pollutants. *EPA.gov.* [Online] Environmental Protection Agency, July 2012. http://www.epa.gov/airquality/carbonmonoxide/.
12. EPA - Six Common Air Pollutants. *EPA.gov.* [Online] Environmental Protection Agency, July 2012. http://www.epa.gov/airquality/sulfurdioxide/.
13. EPA - Six Common Air Pollutants. *EPA.gov.* [Online] Environmental Protection Agency, July 2012. http://www.epa.gov/airquality/nitrogenoxides/.
14. Six Common Air Pollutants: Particulate Matter. *EPA.gov.* [Online] Environmental Protection Agency, June 2012. http://www.epa.gov/pm/health.html.
15. **R.E. Hayes and S.T. Kolaczkowsk.** *Introduction to Catalytic Combustion.* Amsteldijk, The Netherlands : Gordon and Breach Science Publishers, 1997.
16. **G. Cavataio, H. Jen, D.A. Dobson and J. R. Warner.** *Laboratory Study to Determine Impact of Na and K Exposure on the Durability of DOC and SCR Catalyst Formulations.* s.l. : SAE 2009-01-2823, 2009.
17. **N. Ottinger.** *Effects of High Temperature Cyclic Aging on a Fully-Formulated Lean NOx Trap Catalyst*. Thesis. Knoxville, TN : University of Tennessee, 2008.
18. **S. Bennett.** *Modern Diesel Technology: Diesel Engines.* Clifton Park, NY : Delmar, 2010.
19. **D.W. Brookshear, K. Nguyen, T.J. Toops, B.G. Bunting, W.F. Rohr and J. Howe.** *Investigation of the Effects of Biodiesel-based Na on Emissions Control Components.* Catalysis Today, 2012, Vol. 184.

20. **J. Xue, T. E. Grift, and A. C. Hansen.** *Effect of Biodiesel on Engine Performances and Emissions.* Renewable and Sustainable Energy Reviews, 2011, Vol. 15, No.2, pp. 1098-1116.
21. **H. Hazar.** *Effects of Biodiesel on a Low Heat Loss Diesel Engine.* Renewable Energy, 2009, Vol. 34.
22. **A.N. Ozsezen, M. Canakci, A. Turkcan and C. Sayin.** *Performance and Combusion Characteristics of a DI Diesel Engine Fueled with Waste Palm Oil and Canola Oil Methyl Esters.* Fuel, 2009, Vol. 88.
23. **M. Karabektas.** *The Effects of Turbocharger on the Performance and Exhaust Emissions of a Diesel Engine Fuelled with Biodiesel.* Renewable Energy, 2009, Vol. 34.
24. **A.C. Hansen, M.R. Gratton and W. Yuan.** *Diesel Engine Performance and NOx Emissions from Oxygenated Biofuels and Blends with Diesel Fuel. Journal Transactions of the* ASABE, 2006, Vol. 49.
25. **H. Aydin and H. Bayindir.** *Performance and Emission Analysis of Cottonseed Oil Methyl Ester in a Diesel Engine.* Renewable Energy, 2010, Vol. 35.
26. **C. Carraretto, A. Macor, A. Mirandola, A. Stoppato and S. Tonon.** *Biodiesel as Alternative Fuel: Experimental Analysis and Energetic Evaluations.* Energy, 2004, Vol. 29.
27. **S. Murillo, J.L. Miguez, J. Porteiro, E. Granada and J.C. Moran**. *Performance and Exhaust Emissions in the Use of Biodiesel in Outboard Diesel Engines.* Fuel, 2007, Vol. 86.
28. **H.S. Yucesu and I. Cumali.** *Effect of Cotton Seed Oil Methyl Ester on the Performance and Exhaust Emission of a Diesel Engine.* Energy Source Part A, 2006, Vol. 28.
29. **B-F Lin, J-H Huang and D-Y Huang.** *Experimental Study of the Effects of Vegetable Oil Methyl Ester on DI Diesel Engine Performance Characteristics and Pollutant Emissions.* Fuel, 2009, Vol. 88.
30. **B. Ghobadian, H. Rahimi, A.M. Nikbakht, G. Najafi and T.F. Yusaf.** *Diesel Engine Performance and Exhaust Emission Analysis Using Waste Cooking Biodiesel Fuel with an Artificial Neural Network.* Renewable Energy, 2009, Vol. 34.
31. **D.H. Qi, L.M. Geng, H. Chen, Y.Z.H. Bian, J. Liu and X.C.H. Ren.** *Combustion and Performance Evaluation of a Diesel Engine Fueled with Biodiesel Produced from Soybean Crude oil.* Renewable Energy, 2009, Vol. 34.
32. **S. Sinha and A.K. Agarwal.** *Experimental Investigation of the Effect of Biodiesel Utliziation on Lubricating Oil Degradation and Wear of a Transportation CIDI Engine.* Journal of Engine Gas Turbine Power, 2010, Vol. 132.
33. **M.P. Dorado, E. Ballesteros, J.M. Arnal, J. Gomez and F.J.L. Gimenez.** *Testing Waste Olive Oil Methyl Ester as a Fuel in a Diesel Engine.* Energy Fuels, 2003, Vol. 17.
34. **A.K. Agarwal.** *Experimental Investigation of the Effect of Biodiesel Utilization on Lubricating Oil Tribology in Diesel Engines.* Proceedings of the Institution of Mechanical Engineers. Part D: Journal of Automobile Engineering, May, 2005, Vol. 219.

35. **A.K. Agarwal, J. Bijwe and L.M. Das.** *Wear Assessment in Biodiesel Fueled Compression Ignition Engine. Journal of Engineering for Gas Turbines and Power*, 2003, Vol. 17.
36. **A. Tsolakisa, A. Megaritis, M.L. Wyszynski and K. Theinnoi.** *Engine Performance and Emissions of a Diesel Engine Operating on Diesel-RME Blends with EGR.* Energy, 2007, Vol. 32.
37. **H. Raheman and S.V. Ghadge.** *Performance of Compression Ignition Engine with Mahua (Madhuca Indica) Biodiesel.* Fuel, 2007, Vol. 86.
38. **D. Agarwala, S. Sinhab and A.K. Agarwal.** *Experimental Investigation of Control NOx Emissions in Biodiesel-fueled Compression Ignition Engine.* Renewable Energy, 2006, Vol. 31.
39. **S. Puhan, N. Vedaraman, B.V.B. Ram, G. Sankarnarayanan and K. Jeychandran.** *Mahua Oil Methyl Ester as a Biodiesel-preparation and Emission Characteristics.* Biomass Bioenergy, 2005, Vol. 28.
40. **M. Canakci.** *Performance and Emissions Characteristics of Biodiesel from Soybean Oil.* Proceedings of the Institution of Mechanical Engineers, Part D: Journal of Automobile Engineering, 2005, Vol. 219.
41. **F. Wu, J. Wang, W. Chen and S. Shuai.** *A Study on Emission Performance of a Diesel Engine Fueled with Five Typical Methyl Ester Biodiesels.* Atmos Environ, 2009, Vol. 43.
42. **P.J.M. Frijters and R.S.G. Baert.** *Oxygenated Fuels for Clean Heavy-Duty Engines***,** International Journal of Vehicle Design, 2006, Vol. 41.
43. **Y. Kidoguchi, Y. Changlin, R. Kato and K. Miwa.** *Effects of Fuel Cetane Number and Aromatics on Combustion Process and Emissions of a Direct-injection Diesel Engine.* Society of Automotive Engineers of Japan, 2000, Vol. 21.
44. **G. Karavalaki, S. Stournas and E. Bakeas.** *Light Vehicle Regulated and Unregulated Emissions from Different Biodiesels.* Science of the Total Environment, 2009, Vol. 407.
45. **A.N. Ozsezen.** *Performance and Combustion Characteristics of a DI Diesel Engine Fueled with Waste Palm Oil and Canola Oil Methyl Esters.* Fuel, 2009, Vol. 88.
46. **J. Krahl, A. Munack, O. Schroder, H. Stein, and J. Bunger.** *Influence of Biodiesel and Different Designed Diesel Fuels on the Exhaust Gas Emissions and Health Effects.* International Society of Automotive Engineers 2003-01-3199, 2003.
47. **H. Raheman and A.G. Phadatare.** *Diesel Engine Emissions and Performance from Blends of Karanja Methyl Ester and Diesel.* Biomass Bioenergy, 2004, Vol. 27.
48. **M.S. Graboski, R.I. McCormick, T.L. Alleman and A.M. Herring.** *The Effect of Biodiesel Composition on Engine Emissions from a DDC Series 60 Diesel Engine.* National Renewable Energy Laboratory, 2003.
49. **H. Ozgunay, S. Colak, G. Zengin, O. Sari, H. Sarikahya, and L. Yuceer.** *Performance and Emission Study of Biodiesel from Leather Industry Pre-fleshings.* Waste Management, 2007, Vol. 27.

50. **G. Labeckas and S. Slavinskas.** *The Effect of Rapeseed Oil Methyl Ester on Direct Injection Diesel Engine Performance and Exhaust Emissions.* Energy Conversion Management, 2006, Vol. 47.
51. **M.E. Tat, J.H. Van Gerpen and P.S. Wang.** *Fuel Property Effects on Injection Timing, Ignition Timing, and Oxides of Nitrogen Emissions from Biodiesel-fueld Engines.* Journal Transactions of the ASABE, 2007, Vol. 50.
52. **J.P. Szybist, A.L. Boehman, J.D. Taylor and R.L. McCormick.** *Evaluation of Formulation Strategies to Eliminate the Biodiesel NOx Effect.* Fuel Processing Technology, 2005, Vol. 86.
53. **T.C. Bowen, R.D. Noble and J.L. Falconer.** *Fundamentals and Applications of Pervaporation through Zeolite Membranes***.** Journal of Membrane Science, 2004, Vol. 245.
54. **M. Guisnet and J-P Gilson.** *Zeolites for Cleaner Technologies.* London, England : Imperial College Press, 2002.
55. **H. Sjovall, L. Olsson, E. Fridell and R. J. Blint.** *Selective Catalytic Reduction of NOx with NH3 over Cu-ZSM-5—The Effect of Changing the Gas Composition.* Applied Catalysis B: Environmental, 2006, Vol. 64. 180-188.
56. **M. Devadas, O. Krocher, M. Elsener, A. Wokaun, G. Mitrikas, N. Soger, M. Pfeifer, Y. Demel and L. Mussmann.** *Characterization and Catalytic Investigation of Fe-ZSM5 for Urea-SCR.* Catalysis Today, 2007.
57. **A. Sultana, T. Nanba, M. Haneda, M. Sasaki and H. Harnada.** *Influence of Co-cations on the Formation of Cu+ Species in Cu/ZSM-5 and its Effect on Selective Catalytic Reduction of NOx with NH3.* Applied Catalysis B: Environmental, 2010, Vol. 101, 61-67.
58. **G. Qi, Y. Wang and R. T. Yang.** Catalysis Letters 2008, Vol. 121. 111-117.
59. **H. Sjovall, E. Fridell, R.J. Blint and L. Olsson.** *Selective Catalytic Reduction of NOx with NH3 over Cu-ZSM-5—The Effect of Changing the Gas Composition.* Topics in Catalysis, 2007, Vols. 42-43.
60. **N. Wilken, K. Wijayanti, K. Kamasamudram, N. W. Currier, R. Vedaiyan, A. Yezerets and L. Olsson.** *Mechanistic Investigation of Hydrothermal Aging of Cu-Beta for Ammonia SCR***.** Applied Catalysis B: Environmental, 2011.
61. **A. Goursot, B. Coq and F. Fajula,** *Toward a Molecular Description of Heterogeneous Catalysis: Transition Metal ions in Zeolites.* Jounral of Catalysis, 2003, Vol. 216.
62. **T. Komatsu, M. Nunokawa, I. S. Moon, T. Takahara, S. Namba and T. Yashiama.** *Kinetic Studies of Reduction of Nitric Oxide on Cu2+ Exchanged Zeolites.* Journal of Catalysis, 1993, Vol. 148.
63. **S. Kieger, G. Delahay, B. Coq and B. Neveu.** *Selective Catalytic Reduction of Nitric Oxide by Ammonia over Cu-FAU Catalysts in Oxygen-Rich Atmosphere.* Journal of Catalysis, 1999, Vol. 183.
64. **M. Colombo, I. Nova and E. Tronconi.** *A Comparative Study of the NH_3-SCR Reactions over a Cu-zeolite and a Fe-zeolite Catalyst***.**. Catalysis Today, 2010, Vol. 151. 223-230.

65. **G. Cavataio, H. Jen, J. R. Warner, J. W. Girard, J. Y. Kim and C. K. Lamber.** *Enhanced Durability of a Cu/Zeolite Based SCR Catalyst. Society of Automotive Engineers* 2008-01-1025, 2008.
66. **G. Cavataio, J. Y. Kim, J. R. Warner, J. W. Girard, D. Upadhyay and C. K. Lambert.** *Development of Emissions Transfer Functions for Predicting the Deterioration of a Cu-Zeolite SCR Catalysts*. Society of Automotive Engineers 2009-01-1282, 2009.
67. **J.R. Theis.** *The Poisoning and Desulfation Characteristics of Iron and Copper SCR Catalysts*. Society of Automotive Engineers 2009-01-0900, 2009.
68. **G. Cavataio, H. Jen, J. W. Girard, D. Dobson, J. R. Warner, C. K. Lambert.** s.l. : SAE 2009-01-0627, 2009.
69. **N.A. Ottinger, T.J. Toops, K. Nguyen, B.G. Bunting and J. Howe.** *Effect of Lean/Rich High Temperature Aging on NO Oxidation and NOx StorageRrelease of a Fully Formulated Lean NOx. Trap.* Applied Catalysis B: Environmental, 2011, Vol. 101.
70. **N. A. Ottinger, K. Nguyen, B. G. Bunting, T. J. Toops and J. Howe.** *Effects of Rapid High Temperature Cyclic Aging on a Fully-Formulated Lean NO_x Trap Catalyst*. Society of Automotive Engineers 2009-01-0634, 2009.
71. **Y. Cheng, J.V. Cavataio, W.D. Belanger, J.W. Hoard and R.H. Hammerle.** *Factors Affecting Diesel LNT Durability in Lab Reactor Studies.* Society of Automotive Engineers 2004-01-0156, 2004.
72. **D. Dou and J. Balland.** *Impact of Alkali Metals on the Performance and Mechanical Properties of NOx Adsorber Catalysts.* Society of Automotive Engineers 2002-01-0734, 2002.
73. **W.S. Epling, L.E. Campbell, A. Yezerets, N.W. Currier and J.E. Parks II.** *Overview of the Fundamental Reactions and Degradation Mechanisms of NOx Storage/Reduction Catalysts.* Catalysis Reviews, 2004, Vol. 46.
74. **A. Winkler, D. Ferri and M. Aguirre.** *The Influence of Chemical and Thermal Aging on the Catalytic Activity of a Monolithic Diesel Oxidation Catalyst.* Applied Catalysis B: Environmental, 2009, Vol. 93.
75. **T. Kolli, T. Kanerva, M. Huuhtanen, M. Vippola, K. Kallinen, T. Kinnenen, T. Lepisto, J. Lahtinen and R.L. Keiski.** *The Activity of Pt/Al2O3 Diesel Oxidation Catalyst after Sulphur and Calcium Treatments***.** Catalysis Today, 2010, Vol. 154.
76. **S.J. Eaton, B.G. Bunting, T.J. Toops and K. Nguyen.** *The Roles of Phosphorus and Soot on the Deactivation of Diesel Oxidation Catalysts.* Society of Automotive Engineers 2009-01-0628, 2009.
77. **M. Manni, A. Pedicillo, G. Del Piero and E.P. Massara.** *An Experimental Evaluation of the Impact of Lubricating Oils and Fuels on Diesel Particulate Filters.* Society of Automotive Engineers 2007-01-1926, 2007.
78. **A. Williams, R.L. McCormick, R.R. Hayes, J. Ireland and H.L. Fang.** *Effect of Biodiesel Blends on Diesel Particulate Filter Performance*. Society of Automotive Engineers 2006-01-3280, 2006.

79. **B. Choi, B. Liu and J. Jeong.** *Efects of Hydrothermal Aging on SiC-DPF with Metal Oxide Ash and Alkali Metals.* Journal of Industrial and Engineering Chemistry, 2009, Vol. 15.
80. **S. Eaton.** Accelerated Poisoning of Diesel Oxidation Catalysts by Zinc Dialkyldithiophosphate Derived Phosphorous. Knoxville: University of Tennessee - Thesis, 2006.
81. **Taylor, Howard E.** *Inductively Coupled Plasma-Mass Spectrometry.* Academic Press, 2001.
82. **M. Guisnet, P. Ayrault, C. Countanceau, F.M. Alvarez and J. Datka.** *Acid Properties of Dealuminated Beta Zeolites Studied by IR Spectroscopy.* Journal of the Chemical Society, 1997.
83. **S. Brunauer, P.H. Emmett and E. Teller.** Adsorption of Gases in Multimoecular Layers. Journal of the American Chemical Society, 1938.
84. **T.J. Toops, D.B. Smith and W.P. Partridge.** *Quantification of the In Situ DRIFT Spectra of Pt/K/gamma-Al2O3 NOx Adsorber Catalysts.* Applied Catalysis B: Environmental, 2005, Vol. 58.
85. **Z. Gao, C.S. Daw and V.K. Chakravarthy.** *Simulation of Catalytic Oxidation and Selective Catalytic NOx Reduction in Lean-Exhaust Hybrid Vehicles.* International Society of Automotive Engineers, 2012-01-01304, 2012.
86. **K. Radhakrishnan and A.C. Hindmarsh.** Description and Use of LSODE, the Livermore Solver for Ordinary Differential Equations. NASA Reference Publication 1327, 1993.
87. **M. Tatur, H. Nanjundaswamy and D. Tomazic.** *Effects of Biodiesel Operation on U.S. Light-Duty Tier 2 Engine and Emissions Control Systems.* Society of Automotive Engineers 2008-01-0080, 2008.
88. **M. Tatur, H. Nanjundaswamy and D. Tomazic.** *Biodiesel Effects on U.S. Light-Duty Tier 2 Engine and Emissions Control Systems – Part 2.* Society of Automotive Engineers 2009-01-0156, 2009.
89. **A. Williams, R. McCormick, J. Luecke, R. Brezny, A. Geisselmann, K. Voss, K. Hallstrom, M. Leustek, J. Parsons and H. Abi-Akar.** *Impact of Biodiesel Impurities on the Performance and Durability of DOC, DPF, and SCR Technologies.* Society of Automotive Engineers 2011-01-1136, 2011.
90. **K.M. Adams and G.W. Graham.** s.l. : Applied Catalysis B: Environmental, 2008, Vol. 80.
91. **E.C. Corbos, X. Courtiois, F. Can, P. Marecot and D. Duprez.** *Impact of the Support Oxide and Ba Loading on the Sulfur Resistance and Regeneration of Pt/Ba/Support Catalysts.* s.l. : Applied Catalysis B: Environmental, 2008, Vol. 80.
92. *The Influence of Pt Oxide Formation and Pt Dispersion on the Reactions NO2⇔NO+1/2 O2 over Pt/Al2O3 and Pt/BaO/Al2O3.* **L. Olsson, E. Fridell.** s.l. : Journal of Catalysis, 2002, Vol. 210.
93. **T. Cheung, S.K. Bhargava, M. Hobday and K. Foger.** *Adsorption of NO on Cu Exchanged Zeolites, an FTIR Study: Effects of Cu Levels, NO Pressure, and Catalyst Pretreatment.* Journal of Catalysis, 1996, Vol. 158.

94. **M. V. Konduru and S.C. Chuang.** *Dynamics of NO and N2O Decomposition over Cu-ZSM-5 under Transient Reducing and Oxidizing Conditions.* Journal of Catalysis, 2000, Vol. 196.
95. **K. Hadjiivanov, D. Klissurski, G. Ramis and G. Busca.** *Four Transform IR study of NOx Adsorptiuon on a CuZSM-5 DeNOx Catalyst.* Applied Catalysis B: Environmental, 1996, Vol. 7.
96. **T. Venkov, M. Dimitrov and K. Hadjiivanov.** *FTIR Spectroscopic Study of the Nature and Reactivity of NOx Compounds Formed on Cu/Al2O3 after Coadsorption of NO and O2.* Journal of Molecular Catalysis A: Chemical, 2006, Vol. 243.

VITA

Daniel W. Brookshear was born in Johnson City, TN on August 4, 1985. He graduated from Science Hill High School in May of 2003. In 2007, he graduated Summa Cum Laude from the University of Tennessee at Knoxville with a degree in Mechanical Engineering. After one year of work in Johnson City, TN he returned to graduate school at the University of Tennessee at Knoxville. He earned his Master of Science in Mechanical Engineering in August 2011 and completed his Ph.D. studies in May 2013.